NEHRP
Final Technical Report G18AP00058

1. Regional Panel Designation: NC

2. Project Title: ***Paleoseismic Record of Peninsula Segment Earthquakes on the San Andreas Fault near San Francisco, CA and possible NSAF linkage to Cascadia***

3. Principal Investigator(s): Chris Goldfinger (PI)

3255 NW Hurleywood Dr., Albany OR 97321
email: chris.goldfinger300@gmail.com

4. Start/End Dates: July 15, 2018-July 14, 2019
5. Year 2 Duration: 12 months and 1 year No Cost Extension

A full resolution version of this report is available at the following URL:
https://ir.library.oregonstate.edu/concern/technical_reports/ms35th18w?locale=en

ABSTRACT

Lake Merced results have established the lake as a viable paleoseismic site on the northern San Francisco peninsula. The lake records ~ 2300 years of event beds, 17 in total. Prior to that the lake was open to the ocean and contains marine shells consistent with an estuarine environment. The site was less tenable as a paleoseismic site at prior times, although that remains unexamined at present. Historic-era results from Lake Merced using bomb-carbon based age models show the site recorded three historic events, 1906, the 1957 Daly City earthquake, and Loma Prieta in 1989 with no intervening event beds. During the 20th century, these earthquakes resulted in the only three event beds in the lake during that time, providing a good test of the fidelity of the lake as an earthquake recorder. These results also show that this site records not only NSAF events, likely along the north coast and the peninsula, but also related earthquakes in the Santa Cruz Mountains, events in the probable pull apart basin at Daly City, and possibly others as well. The event bed corresponding to 1906 is ~ 1m thick, much greater than any other bed in the lake during the past 2300 years. Pb isotope data show this bed is contaminated with isotopes consistent mostly with lead based paint, and additionally tetraethyl Pb from gasoline. We interpret the thick, Pb laden deposit as likely anthropogenic material from the early development of San Francisco, and the great thickness of the bed may have been deposited over several decades as a hillslope effect following the earthquake. The Lake Merced record is largely compatible with onshore and offshore records for the north coast segment of the NSAF, and potentially with the lesser known peninsula segment. The lack of numerous "extra" events at Lake Merced relative to the north coast segment record may suggest that many, but not all north coast and peninsula segment events are one in the same, as was 1906, although numerous other interpretations are also possible.

In an effort to examine the hypothesis of a stress relationship between the NSAF and Cascadia, we re-examined the evidence from both systems. Detailed analysis of cores near the northern limit of the NSAF at Noyo Canyon and in Southern Cascadia primarily at Trinidad Canyon, have yielded improved detailed records, age models, and evidence of historic earthquakes. In southern Cascadia, several significant event beds overlie the 1700 CE earthquake bed. High-resolution age models supported by bomb-carbon ages suggest that the significant 20th century beds likely include 1906 NSAF, 1980 Eureka, and 1992 Petrolia earthquake event beds. The presence of the 1906 beds in southern Cascadia suggests that others from the NSAF should be present as well, and also suggests that event beds from Cascadia earthquakes should be expected at similar ranges south of Cascadia in Noyo Canyon. In both Trinidad plunge pool and Noyo Canyon cores, a number of unusual doublet event beds are observed. The Noyo Canyon doublets are nearly all inverted, with the coarsest components at the top. In detail, these beds are composed of two stacked fining upward sequences, with the upper unit having greater density and coarser grain size. These unusual beds are unlikely to be the result of hydrodynamic transport effects or storm or climatic events. The doublet beds correspond to periods when both the NSAF and Cascadia had significant earthquakes at similar times. In all, of the 9 major earthquakes in the Cascadia record younger than 4100 years, 7 of them have a corresponding inverted doublet bed in Noyo Canyon with significant temporal overlap with or indistinguishable from Cascadia event timings. Five other Cascadia beds have temporal equivalents in Noyo Canyon, some of which do not correlate southward along the NSAF, suggesting Noyo recorded Cascadia events. For some of the doublet beds, time intervals above and below do not allow enough time for Cascadia beds to be present in Noyo Canyon, but mis-correlated on the basis of radiocarbon. We infer

that the earthquake recurrence sequence that best explains the data is that for most Cascadia events < 4100 BP, a corresponding NSAF earthquake occurred shortly thereafter, producing the doublet stratigraphy in Noyo Canyon, and in Cascadia. The time separation between the Cascadia and NSAF ruptures is not known. We observe no interevent hemipelagic sedimentation between the two parts of the Noyo doublets, but erosion may have removed it. On the Cascadia side, the doublet for some events appears to be embedded in the tail of the first event, implying a very short time separation where the second event is settling into the still moving, waning turbidity current from the first event. The hypothesis of a stress-triggering interaction, and even partial synchronization of the NSAF with Cascadia is supported by the new stratigraphic and radiocarbon evidence of occurrence and timing. The data suggest that Cascadia ruptures first, and the NSAF thereafter. In Holocene times prior to ~ 4100 BP, the doublet stratigraphy is rare, and the weaker timing constraints available do not suggest such a relationship during that period. The 1906 event may have either ended a period of stress interactions, or is one of a small number of NSAF events unrelated to Cascadia in the past ~ 4100 years in a scenario of partial synchronization of the two faults.

Paleoseismic Record of Peninsula Segment Earthquakes on the San Andreas Fault near San Francisco, CA and possible NSAF linkage to Cascadia

TABLE OF CONTENTS

Significance of the Project

The Peninsula section of the San Andreas Fault is an obvious and significant hazard to San Francisco and peninsula cities, however the history past events on the SAF on the peninsula is poorly known. Surprisingly little is known about earthquakes and their timing prior to the great earthquake of April 18, 1906. The short paleoseismic history in this critical area means that the seismic hazard to the San Francisco Bay Area is poorly constrained, particularly so for San Francisco itself (Prentice et al., 2006).

Significance to NEHRP

This project directly addresses Elements I and II of the national ERP. Element I deals with improving hazard assessments, which we believe a good paleoseismic record near San Francisco would contribute to. It contributes to Element III by conducting research on recurrence of SAF earthquake near San Francisco, where a paucity of information presently exists. These Elements are integrated into the priorities of the regional Research areas, one of which is Northern California, focusing on the San Francisco Bay Area.

HISTORY AND TECTONIC SETTING

Lake Merced History

The history of Lake Merced, its origins and uses bear on its efficacy as a paleoseismic site. Here we examine the available historical information to address the questions of what the Lakes origins are, what connections the Lake has had with the sea, and what anthropomorphic issues may be relevant. Lake Merced was likely a small inlet which formed at the end of the last glacial period when the ocean flooded Merced Valley (Figures 1-3). It has been hypothesized that a sand bar formed and eventually blocked Lake Merced drainage to the sea, creating a lake (Fahy, 1974). The first European use of the lake's water is thought to be in the late 1700s. Fernando Rivera part of the Portola expedition that discovered San Francisco Bay, arrived overland in several expeditions in 1769-1774. Historical records show that Lake Merced was first described as an inlet, not a lake, by these early Spanish explorers. However, Fernando Rivera wrote in December of 1774 that the water was sweet and fresh, and indicated that the beach made a dam across its outlet (Shoup and Baker, 1981, and references in Fahy, 1974). At the northwestern corner of the lake, Merced and Colma formation cliffs end, and low dunes occupy a 300 m wide barrier between the lake and the ocean. Subsurface cross sections suggest that the Colma Formation units come up to sea level, and are topped by ~ 10m of dune sand in this area.

Spit Breach of 1852. As reported in the *Alta Californian*, November 28, 1852, on the stormy night of November 22, 1852, a local resident (the only one in the area) a Mr. Green reported a "loud report" he thought sounded like cannon fire, but thought it must be an earthquake. He observed that Lake Merced had broken through the spit and poured out through the narrow gap, dropping the lake surface 30' (more than its current depth). This was reported locally, and later on January 13, 1953 in the New York Times. However, there was no earthquake felt in San Francisco, 7 miles away at the time. It would appear that the lake partially drained to the ocean, breaking through the spit and the NW and of the lake during heavy rains and high lake levels (Soule, et al, 1855). This outlet has been suggested to have remained as an opening to the ocean for decades, however, historical maps show that not to be the case, and show a narrow creek outlet rather than an opening to the ocean (Figures 1-3). The description as having been

Figure 1. Perspective view of Lake Merced in 1868 viewed from the west. The distance to the ocean appears roughly similar to modern, ~ 330 m. Note also Pine Lake, just to the north, this is located at Stern Grove today. Image: George H. Goddard, Library of Congress.

open to the ocean is repeated in several public websites, but seems to be contradicted by the maps of the day. The lake was used for trout fishing as early as 1850, and this use continues today. The sensitivity of trout to salt or brackish water is high, suggesting the lake has remained fresh water from first discovery through the "spit breach" event and later.

Figure 2. Another perspective view of Lake Merced in 1868 viewed from the west. This image shows more detail of early occupancy, including houses to the east, the race track and fort to the north and northwest. From the David Rumsey collection at http://explore.museumca.org/creeks/1700-OBDCPix2.html

Figure 3. 1899 Topographic map of the Lake Merced area showing drainage patterns from the east and south. http://explore.museumca.org/creeks/1700-TopoMerced.html

There is some evidence that the surface of the lake reflects the water table of the Shallow Aquifer in this area, and may be a surface feature of it. The Spring Valley Water Company purchased the rights to Lake Merced waters in 1868 and followed this with the purchase of nearby lands, then sold the water to San Francisco residents from 1870 to 1930 (Shoup and Baker 1981). Surface runoff was diverted to the ocean, to protect the water supply from contaminants; reducing the watershed from more than 6,000 acres to under 600. The water level has varied significantly over time, from its historic maximum in 1912 of 30 feet, to a minimum of 15.5 feet in 1990. Over ~ 50 years (1889-1935) was divided into North, South, East and Impound Lakes (Shoup and Baker 1981). The lake remains an emergency supply of water for the City of San Francisco.

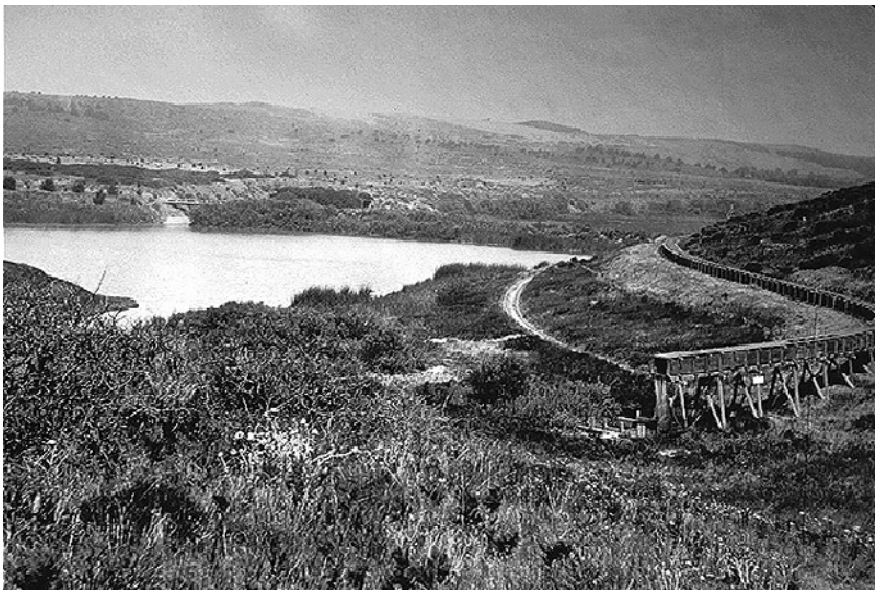

Figure 4. Lake Merced, c. 1895, with fresh water flume under construction. Photo: Shaping San Francisco: http://www.foundsf.org/index.php?title=Lake_Merced_100_years_ago

Other uses relevant to the sedimentary record in the lake include its location adjacent to several golf courses and two shooting ranges. Beginning in the 1922 several golf courses were constructed around the lake. The Lake Merced Gold Club formed in 1922 is 0.9 km southeast of the lake, and doesn't border directly on the lake. The Harding Park and Fleming courses, operating by the San Francisco Parks and Recreation Dept. on the northeast side of the main lake do border directly on the eastern shore, and were opened in 1925. The Olympic Club course borders on the southwestern shore. Formerly the Lakeside Golf Club, that course was operating before 1918. The effects of these courses on the lakes shores and sediment is not well known. The steep eastern shoreline that lies between the lake and the Harding Park course is a steep dune sand slope presently covered with Eucalyptus trees (non-native) and slash. It must be assumed that construction of these courses influenced proximal sediment input to the lake, though nothing is known at present.

Also beginning in the 1930's, the southwestern shore of South Lake has been used as the site for two shooting ranges. The Pacific Rod and Gun Club was founded in 1934, when the Works Progress Administration built the facility for a national trap and skeet shooting championship held in San Francisco that year. Trap and skeet shooting continued there until 2016 when the facility was closed due to lead contamination of the shore and lake sediments. Given until Jan. 1, 2016 by a state agency, the SFPUC then began an estimated $22 million remediation of the site. The project included the excavation and off-site disposal of 46,500 cubic yards of contaminated soil (https://medium.com/@sfbay/a-gun-clubs-final-shootout-d90da048a0e8). The city made an earlier attempt to remediate the site in 1985 when 128 tons of lead pellets and fragments were removed from the lake, where lead levels in the water exceeded State and Federal standards. Suction dredges were used and according to Tim Cohen of the Lake Merced Task force "They got suction dredges and dredged out lake sediments. … Hundreds of tons of lake sediments had accumulated decades of lead buckshot, and they remediated some of the onshore soils that were contaminated with lead and some of the soils were contaminated with lead skeets." (https://medium.com/@sfbay/a-gun-clubs-final-shootout-d90da048a0e8). The club switched to steel or bismuth shot in 1994, prior to which approximately a ton per year of lead was added to the lake between 1985 and 1994. The club has been closed and remediated above the shoreline at this point, with no further disturbance of the lake sediments. The area dredged in 1985 is not precisely known, but our mapping suggests it was limited to within 100 m of the western shore in the southwest part of the lake. Our work focused on the eastern part of the lake partially for this reason, and also because the tilt of the lake floor make the eastern section the deepest sediment sink.

A second shooting range is operated by the San Francisco Police Department and is still active in 2018. This is an indoor facility that appears to have its activities relatively well separated from any influence on the lake other than sound. The origins of this facility and potential earlier influences are not known.

Tectonic Setting

The San Andreas Fault (SAF) is probably the most intensively studied transform system in the world. Extending along the west coast of North America, from the Gulf of California to Cape Mendocino, the SAF is the largest component of a complex and wide plate boundary that extends eastward to encompass numerous other strike-slip fault strands and interactions with the Basin and Range extensional province. The Mendocino Triple Junction (MTJ) lies at the termination of the NSAF, and has migrated northward since about 25-28 Ma (Dickinson and Snyder, 1979). As the triple junction moves, the former subduction forearc transitions to right-lateral transform motion and the SAF continues to lengthen.

Geologic and Structural Setting of the Northern San Francisco Peninsula

The northern San Francisco Peninsula lies in a complex structural setting. Bounded on the west by the San Gregorio Fault, the northern SF peninsula is deformed by the San Andreas Fault, which crosses the shoreline at Mussel Rocks, by the northern tip of the associated Santa Cruz Mountains fold belt, including the blind Serra fault; a probable transtensional graben occupying a NW trending lowland through Colma and the Sunset District, and bounded on the east by the San Bruno Mountain, and Mt Sutro/Mt Davidson uplifts to the northeast.

Ryan et al. (2008) present an updated structural interpretation offshore of the northern SF peninsula using high resolution seismic reflection profiles in the area of the NSAF and San Gregorio Faults (Figure 5). Each of the profiles shows that the area between the NSAF and a fault known as the Golden Gate Fault (GG) ~ 5 km to the east is a transtensional graben (Cooper, 1973). The strata in the graben are highly deformed up to the seafloor, though the seafloor is not offset, presumably due to high current velocities and mobile surface sediment that have kept up with modest deformation rates (Ryan et al., 2008). The GG fault is well imaged west of Ocean Beach and north of the Golden Gate in high-resolution profiles.

Separation observed is primarily normal, with rollovers and drag folding consistent with extension (Figure 6). Mismatching of interval thicknesses across the GG and SAF faults strands are indicative of strike-slip separation as well. The GG fault defines the eastern boundary of the San Andreas graben of Cooper (1973), bounded on the west by the NSAF. The syntectonic fill within the San Andreas graben has not yet been dated, however Cooper (1973) inferred that the sediment is Holocene based on his assumption that prominent reflectors in the basin represent the latest Pleistocene/Holocene transgressive surface which has been dated at ~ 7700 years at Bolinas Lagoon (Berquist, 1978). Zoback et al. (1999) discuss the onshore basin as a potentially older equivalent of the pull apart basin mapped offshore. Jachens and Zoback (1999) interpreted this basin as a 2-3 km wide trough with more than a kilometer of young fill based on gravity modelling.

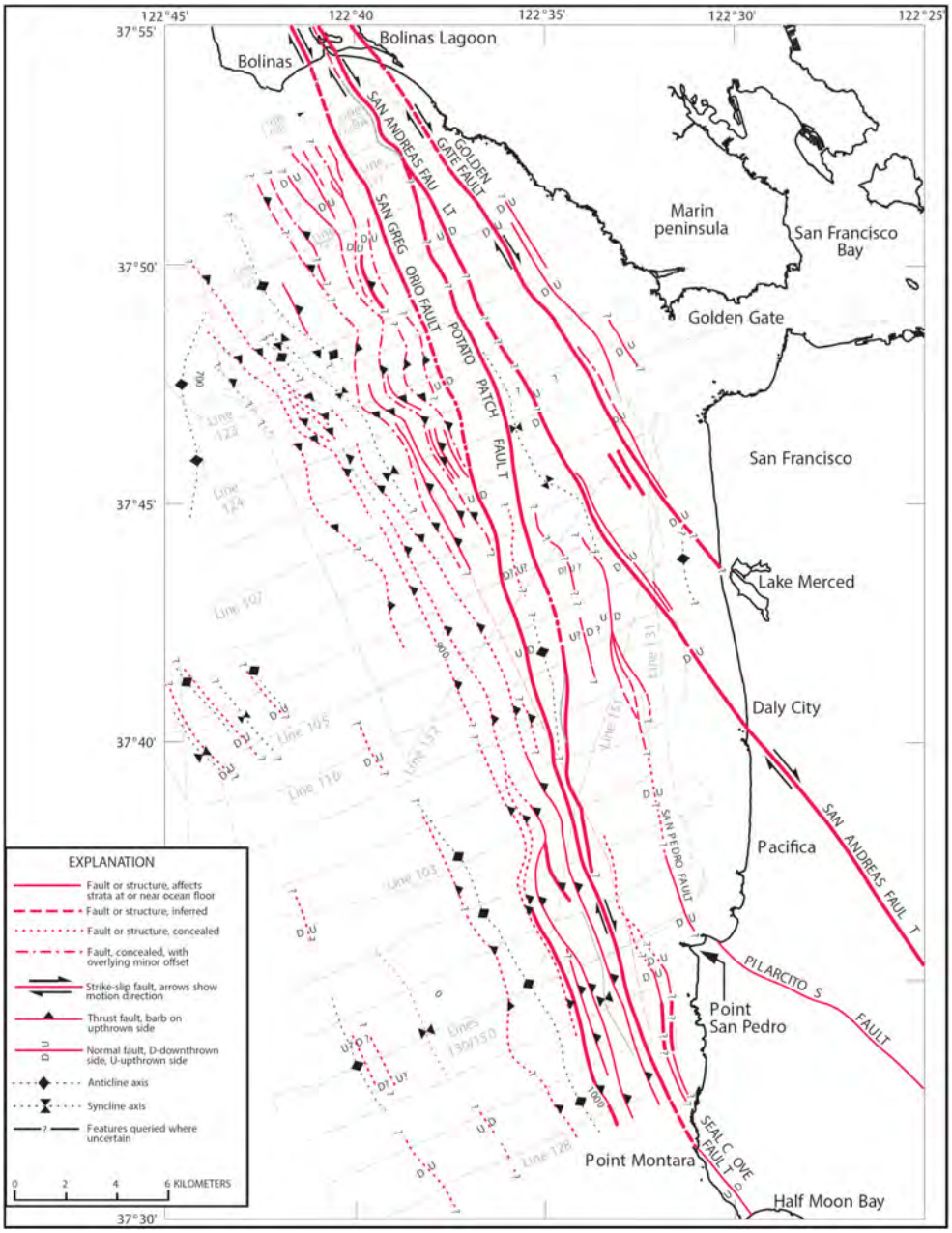

Structural Models

The San Andreas graben (Cooper 1973) has been attributed to a right (extensional) step in the San Andreas offshore of the northern SF peninsula extending to and into the area where the SAF comes ashore again at Bolinas Lagoon (Zoback et al., 1999; Jachens and Zoback, 1999, Wakabayashi et al., (2004). This is supported by a

Figure 5. Gulf of the Farallones and San Francisco Bay region, Calif., showing structure mapped from seismic reflection data. Modified after Bruns et al., 2002.

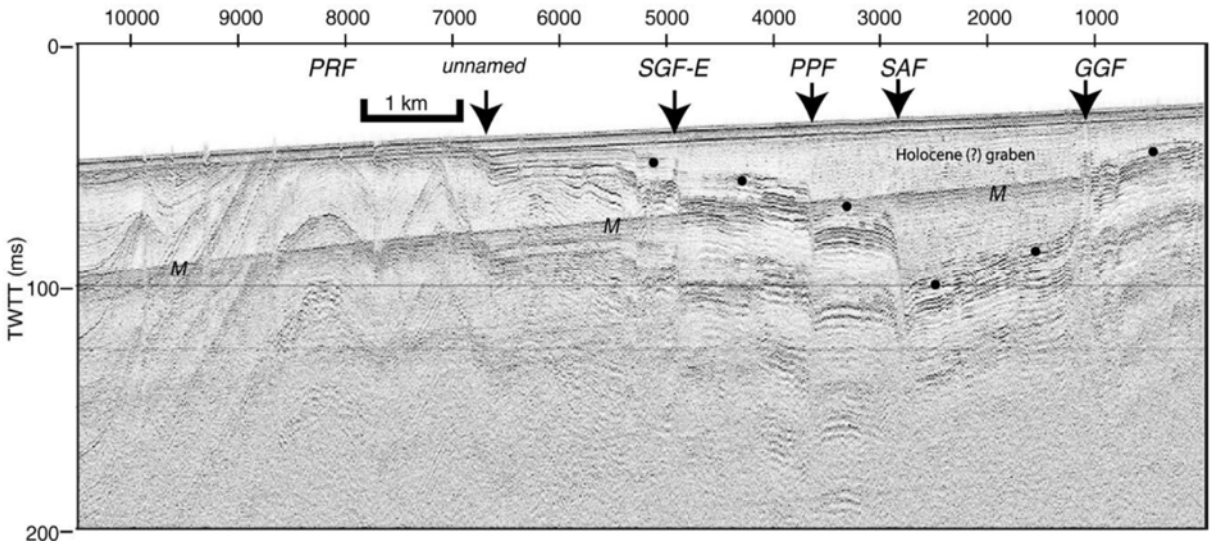

Figure 6. High resolution seismic profile across the San Andreas graben in the gulf of the Farallones. SGF-E = San Gregorio Fault east; PPf=Potato Patch Fault; SAF=San Andreas Fault; GGF=Golden Gate Fault. From Ryan et al. 2008.

significant magnetic anomaly along the GGF, implying juxtaposition of contrasting rock bodies that would require significant slip on the GGF. Wakabayashi et al. (2004) further suggest that the graben has migrated to the northwest as slip increased on the SAF strand, and decreased on the GG fault strand (Figures. 5-6). This model may explain the presence of thick shallow water sediments of the Merced and Colma formations which now lie outside the active subsiding basin. Ryan et al. (2008) present an alternative model in which the GG fault dips to the west and intersects the SAF, and thus takes a subsidiary role in which stepover of the SAF is not required to accomplish local subsidence. Nevertheless, the peninsular and north coast SAF segments are not aligned, and either a bend or stepover seems required to connect the two, and in either case, subsidence would be expected. Zoback et al. (1999) point out that this overall pattern of subsidence on the Golden Gate Platform may well be the reason that the area presently lies below sea level.

Structure and Geology around Lake Merced

The relatively shallow Lake Merced belies the extent of the structural depression it resides in. Folds mapped by Bonilla (1998), McGuire (2009), and Johnson et al. (2015) bound the west side of the lake, and trend sub-parallel to the NSAF. These folds are interpreted as the northern extremity of the Santa Cruz Mountains fold belt, and includes the blind Serra Fault, a west dipping blind thrust (Kennedy, 2002). Relatively high topography with peak elevations of 30 m (north) to 60 m (south) bound the lake to the west and south, thus the lake is not primarily a spit/barrier system as is sometimes suggested (Figures 7 and 11). Geologic mapping detail is somewhat lacking in the area, but the surficial and shallow subsurface geology is mainly the Colma and Merced formations, overlain by quaternary dunes to the west and north (Clifton et al., 1988). Along the sea cliffs west of the lake, exposures of the Colma formation and underlying Merced formation units are well exposed in the 40-60 m cliffs. An exposure of the Colma Formation at Ocean Beach investigated by Caskey et al (2005) was interpreted as having been deposited in a foreshore environment. The sandy intervals included heavy mineral laminations commonly found

Figure 7. Google Earth view across Thornton beach and the exposed ~ 60 m cliffs with NE dipping Merced (lower) and Colma formations (upper). Lake Merced, San Francisco and Sutro Tower on the skyline. (The high resolution photos have numerous overlap artifacts).

in beach environments. Cobbles were observed below the probable foreshore sediments that may represent a lag deposit that directly overlies backshore sediments of the Merced X-Sequence (Caskey et al., 2005). Stratal dips are modest (est. 7-12 degrees) to the northeast (Clifton et al., 1988, Caskey et al., 2005). The overlying terrace surface dips in the same direction at a more shallow 1-2 degrees where evident slightly to the south in Daly City, with the exception of one area just west of the center of the lake. Minor faulting evident in the bluffs is along numerous north dipping reverse faults that offset the wave-cut platform with individual offsets of 1-5 m, up to the southwest.

The structural setting indicates Lake Merced lies in a structural depression, either in a faulted syncline, or a homocline underlain by the Serra Fault, and bound by the Mt Sutro/Twin and San Bruno peaks high to the east. With stratal and terrace dips to the north and east exposed in the sea cliffs from Mussel Rocks to Fort Funston, the upper terrace surface reaches beach level near the north end of the lake, and no further bedrock exposure or terrace surfaces are observed to the north until the Cliff House area where another uplifted section exposes probable Colma formation sandstones.

McGuire (2009) used water well data to construct cross-sections in the area that show the folds to the west, the open basin in which Lake Merced sits, and the subsurface units (Figures 8 and 9).

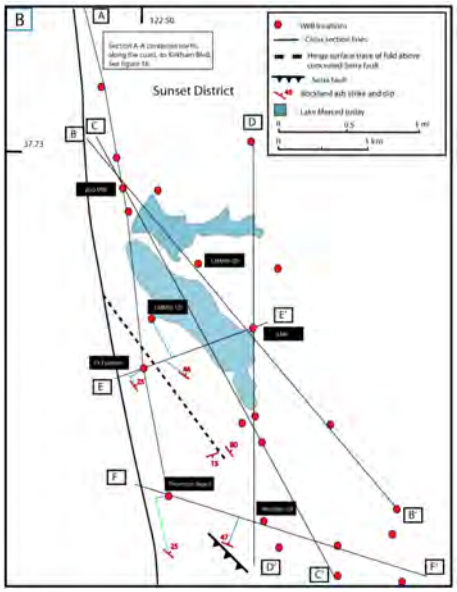

Figure 8. Location map for cross sections from McGuire (2009). Section E-E' is shown in Figure 9.

Although OSL dating was not very successful for the Pleistocene Colma formation units, general age estimates for the Colma Formation suggest uplift rates associated with deformation along the Serra fault system of 0.5-1.0mm/yr. at Thornton Beach and 0.2-0.5 at Ocean Beach (Caskey et al., 2005). Thus Lake Merced and much of the Sunset district lie in the structural depression, the western side of which is now an inverted basin which accumulated Merced and Colma formation sands during the Pleistocene.

The basin underlying Lake Merced is also Plio-Pleistocene Merced and Colma Formation units sampled and correlated from water wells by McGuire (2009). These units are interpreted as shallow embayment and nearshore sands that have been mapped in the subsurface with enough resolution to construct paleogeographic maps of the area (Figure 10). These maps, developed on each major sequence boundary, so that the area was a NW-SE trending embayment through much of the Pleistocene (McGuire, 2009). McGuire (2009) matched the sandy-embayment transitions to sea level fluctuations during the Pleistocene, showing this area was alternately flooded and drained during high stand and low stand conditions respectively.

The north end of the lake, which has had a reported outlet/inlet at one point in historic times, is bounded by dunes in the synclinal axis, with landsliding obscuring the details of the northern boundary of the lake to some extent. We estimate a minimum structural relief of ~85 m as we observe the section disappearing below the beach level from south to north. Adding to that the lake depth of ~ 8 m and estimate of the minimum Holocene sediment thickness, the minimum relief is ~ 100m. The actual structural relief, estimated by projecting the coastal dips under the lake should be on the order of 150-180m. This strongly suggests that the depression that Lake Merced sits in, is a significant structurally controlled feature that has existed for considerable time. Sediment has filled this depression up to 8 m below lake level (3 m below mean sea level), thus there may well be 150-180 m of fill in the basin. Although the lake is thought to be ~ 11,000 years in age (Holtzman, 2005), it may well by much older and we suspect that this depression has had a lake in it for much of its likely longer existence.

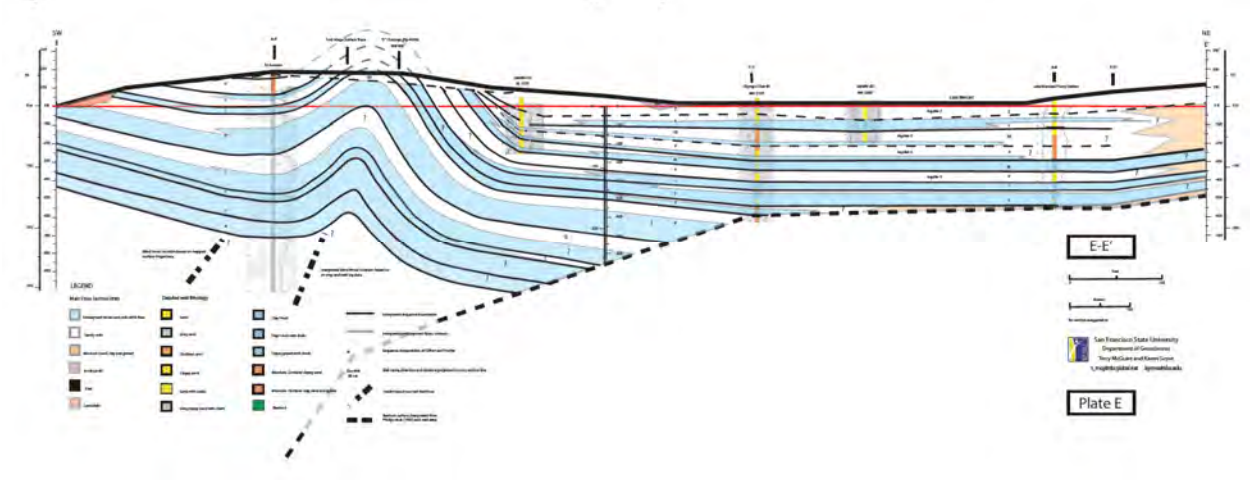

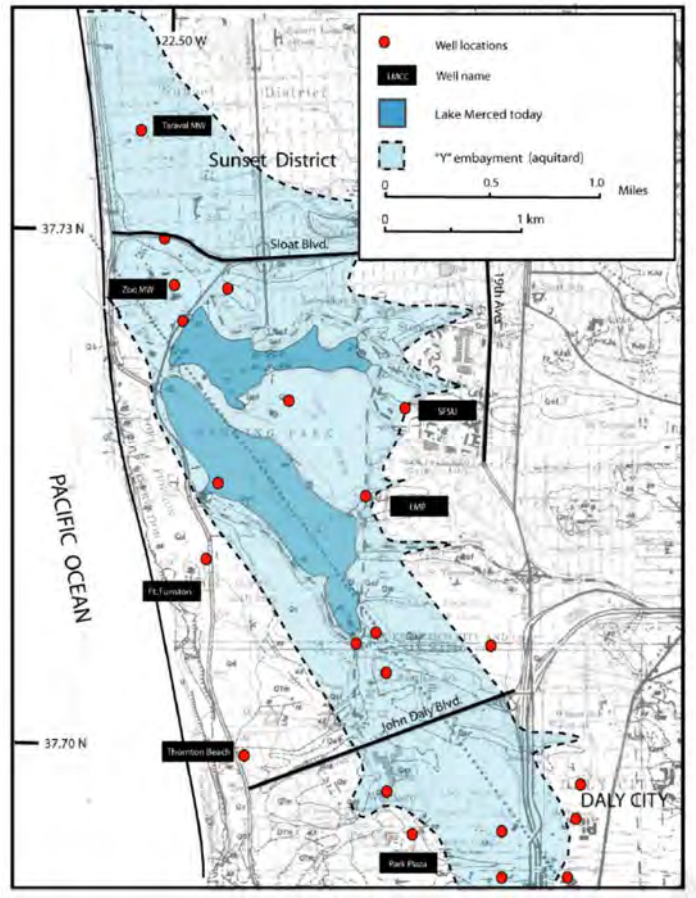

Figure 9 (previous page). Section E-E' from McGuire (2009). SW is to the left, NE to the right. This dip section shows the structural low that Lake Merced resides in at center right. Folds underlying the Fort Funston area and projecting offshore are to the left. Fine grained embayment facies are shown in blue, bounded by grey lines. Sandy units are white. See McGuire (2009) for high resolution images and well logs.

Figure 10. Paleogeographic map showing the inferred boundary of the Y embayment, which forms the aquitard for the unconfined Aquifer Z, the shallowest mapped unit. Base map from Bonilla (1971), figure from McGuire (2009).

The graben and its bounding faults observed offshore are on trend with the structural depression observed onshore (Figures 6-12), and in fact on trend with the margins of South Lake. Structural relief is at least 70 ms in two way travel time, or ~ 120 m in young materials, not unlike the our crude estimate onshore. Without age control, better comparisons are not possible, but the consistency in style and magnitude of separation in these features suggests the onshore and offshore downwarps may be one in the same. Holocene extension is also suggested by the fact that the Lake Merced bottom is ~ 3m below mean sea level.

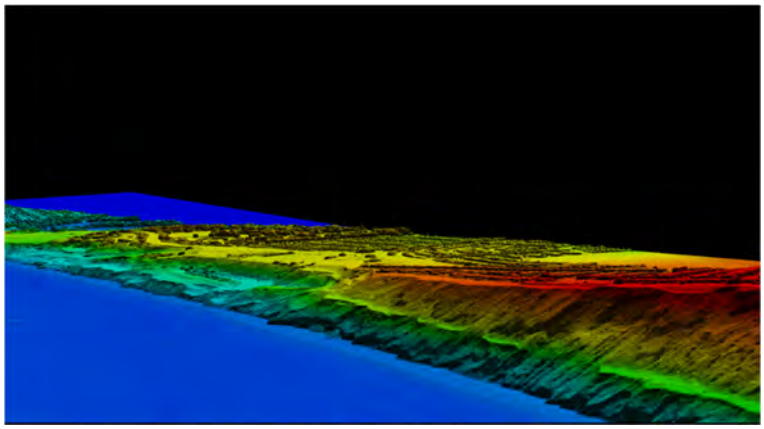

Figure 11. LIDAR Image showing marine terrace surface dipping to the north and east south of Lake Merced. Landsliding and the old coast highway are also visible.

Bürgmann et al. (2006) observe a zone of slow (0.5 mm/yr.) subsidence along the northern San Francisco peninsula using analysis of permanent scatterer INSAR data. They suggest this modern subsidence may be related to the extensional bend in the San Andreas Fault described above, and/or interaction with the offshore San Gregorio fault zone. A perspective view down the axis of the structural depression is shown in Figure 12.

Historical and Instrumental Seismicity

Seismicity post 1906 in this area has been sparse, but what there has been is intriguing. The two major faults, the San Andreas and the and the San Gregorio faults have been largely aseismic in instrumental times and since 1906, as have an intermediate fault, the Pilarcitos fault (Zoback et al, 1999). The barely historic 1938 earthquake rupture length and even the fault it occurred on are unknown at present.

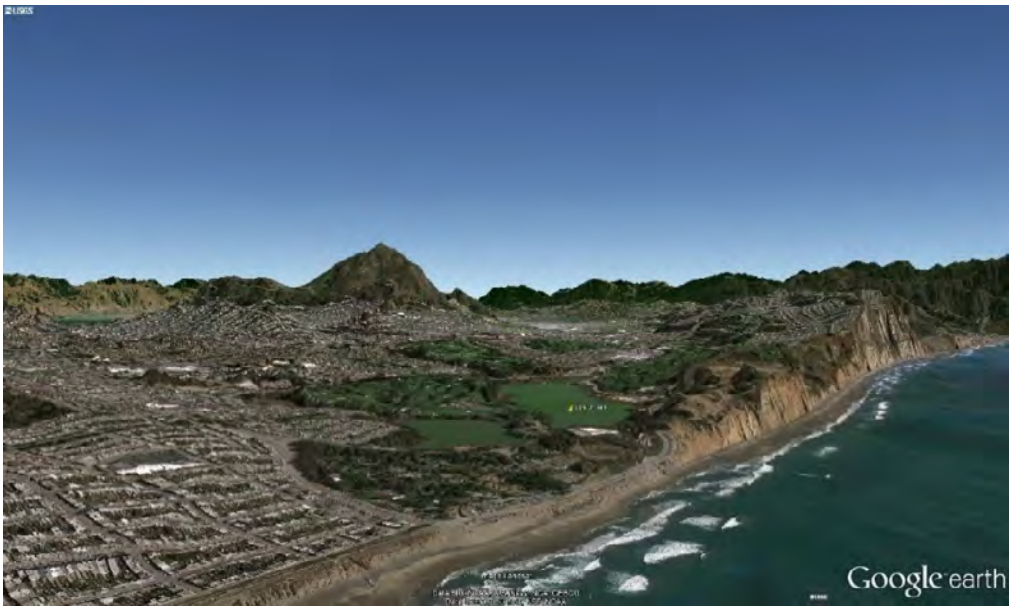

Figure 12. Perspective view along the axis of the Colma structural depression in which Lake Merced (center) resides. Uplifted terrace riser and Merced/Colma formation basin fill along the sea cliffs is to the right, and San Bruno Mountain and Mt Davidson/Sutro Hills to the left (v.e. = 3X).

Toppozada and Borchard (1998) suggest that the northern end of the rupture may have been near San Francisco. Zoback et al. (1999) suggest the previously discussed right step may represent a segment boundary, though one that is obviously not observed in all earthquakes as in 1906, but 1906 did nucleate there, another role sometimes played by segment boundaries. Further evidence of modern extension is a number of instrumental earthquakes with normal focal mechanisms in the area discussed extensively in Zoback et al. (1999). They describe these as a 30 km long zone of normal faulting mechanisms around the extensional trough striking sub-parallel to the SAF. The largest of these, the 1957 M = 5.3 normal faulting event, and other nearby events are shown in Figure 13.

Seismicity and Lake Merced

Substantial evidence exists supporting the sensitivity of this site to shaking from earthquakes on the San Andreas and perhaps other faults. In part this reflects the instability of Colma formation in which the lake is situated.

1906 Earthquake. The 1906 earthquake which nucleated just a few km to the NW had numerous effects on the lake. All following are from Youd and Hoose, (1978): "For example, the ocean shore railway grade between Lake Merced and Mussel Rock, then under construction, was almost entirely destroyed for a distance of 3 mi (5 km). The direction of the offsets was very nearly due north and south. At one break the west piece was shoved 12 or 14 feet past the other section. The west end of the intermediate piece failed to join the section a t the west bank by 6 or 7 feet. The west section that remained with the bank was from 4 to 5 feet lower vertically than the intermediate piece. On the hillside where this trestle reaches the west bank of the lake, cracks parallel to the shoreline suggest the cause of the destruction of the bridge. The displacements here are larger than any along the main fault line, and it is apparently entirely local, due to the slipping and settling of the west bank of the lake. Somewhat similar landslides were

triggered in this same area during the 1957 Daly City earthquake." "Several lateral spreads and rotational slumps, some of which were converted into flow failures, occurred around the shoreline of Lake Merced during both the 1906 and 1957 earthquakes". On Ocean Avenue, fissures were developed in the street and in the sands on either side, and water was squeezed out so as partly to flood the roadway.

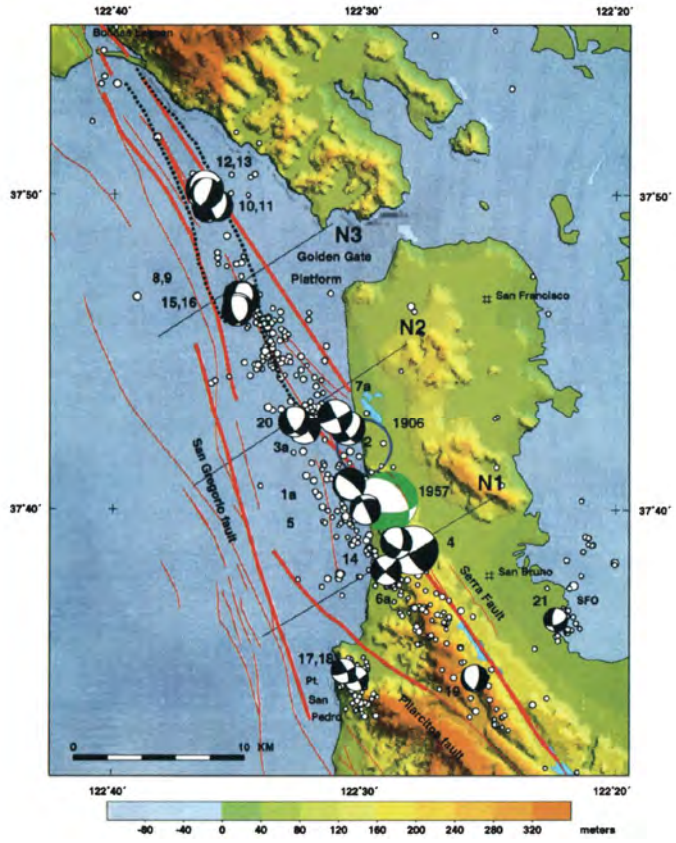

Figure 13. Instrumental seismicity in the area. 1957 normal event in green, with several other normal mechanisms shown.

1957 Daly City earthquake. "The 1957 Daly City earthquake, which generated landslides and ground cracks around Lake Merced" and "Several lateral spreads and rotational slumps, some of which were converted into flow failures, occurred around the shoreline of Lake Merced during both the 1906 and 1957 earthquakes" (Figure 14; Youd and Hoose, 1978). " State Highway 1, near Mussel Rock, was blocked by landslides; highway pavement was cracked extensively." . . . " a large reinforced concrete reservoir cracked." (Coffman and von Hake, 1973). "Landslides occurred at about a dozen different places along the shore of Lake Merced, and most, if not all, involved artificial fill. The width of the slides ranged from 75 to 300 feet and one series of slides extended along the lake shore for 800 feet. The slides produced scarps that were about 10 feet high (Bonilla, 1960).

Figure 14. Ground failures in highway fill along the margin of Lake Merced along Lake Merced Blvd from the March 22, 1957 earthquake. (Photograph by M.G. Bonilla of the U.S. Geological Survey).

Peninsula Segment San Andreas Onshore Paleoseismicity

The NSAF system has been divided into segments based on its historical record of earthquake behavior. All four northern segments (north of the creeping section at San Juan Bautista: Santa Cruz Mountain, Peninsula, North Coast, and Offshore; (Working Group, 2003) ruptured in the 1906 Mw 7.9 earthquake, extending from San Juan Bautista north to the MTJ (Lawson et al., 1908; Prentice et al., 1999; Song et al., 2008).

The onshore paleoseismology of the NSAF has been investigated at Olema, 45 km north of San Francisco; at Dogtown, close to the Olema site; at Bodega Bay, Bolinas Lagoon, Point Arena, and Fort Ross; and at several sites on the San Francisco Peninsula and in the Santa Cruz mountains. At the Vedanta site near Olema, Niemi and Hall (1992) found a maximum late Holocene slip rate of 24 ±3 mm/yr., in fair agreement with geodetic data (Segall, 2002; d'Alessio et al., 2005). They estimate that if the 4-5 m slip event recorded in 1906 is characteristic, the recurrence time for such events would be 221 ±40 yrs. The average slip per event at Point Arena similarly implies a recurrence time of 200-400 yrs. (Prentice, 1989). Ten ages from the Vedanta site (Zhang et al., 2006) and sites near Fort Ross (Kelson et al., 2006), suggest a recurrence interval of ~200 years, and timing of the penultimate event on the North Coast and Offshore segments at ~AD 1700-1750. The offshore record recorded by turbidites along the NSAF is consistent with the Vedanta record (Goldfinger et al., 2007, 2008). Knudsen et al. (2002) document probable co-seismic relative sea level changes within structural basins along the NSAF in Bodega harbor and Bolinas lagoon, 90 and 27 km north of San Francisco respectively. These data suggest two events prior to 1906, one ~ 400, and another 700-750 years BP.

A number of attempts have been made to acquire a good paleoseismic record for the peninsula segment of the SAF, with mixed results. The earthquake of 1838 produced strong shaking on the San Francisco Peninsula with an estimated magnitude of 6.8 to 7.4. It has been generally assumed that this event occurred on the SAF, but paleoseismic excavations across the fault at several sites on the Peninsula have not found evidence of 1838 surface rupture. Baldwin et al. (2011) report that in several trenches just south of Crystal Springs reservoir, they observe evidence of only two events, 1906 and a single earlier event 600-1000 years ago. Similarly, Prentice et al. (2013) working at the south end of Crystal Springs found only one pre 1906 event dated 830-930 cal BP. These results differ however from sites further south in the Portola Valley, where Baldwin and Prentice (2008) have reported 3-4 events in the past 1000 years. Prentice et al. (2016) recently reported evidence for 1906, an event dated as CE 1280-1390, underlain by another dated at CE 1020-1160 and two earlier events at a new Scarp Creek site at Filoli. Hall et al (1999) report a different record at Filoli, with one pre-1906 event estimated as < 330 BP, potentially consistent with the 1838 earthquake. Zachariasen et al. (2010) reexamined the site and suggest that other interpretations are possible at Filoli, including there being only a single event, 1906. These sparse peninsula records are very different from the Santa Cruz Mountain segment at sites at Arano flat and Hazel Dell. These sites have had many more events, probably including 1838 and a younger event (Fumal et al., 2003, 2012; Streig et al. 2014, Streig et al., 2020).

Schwartz et al. (2014) compiled all the available data on the Santa Cruz Mtns, Peninsula, northcoast and offshore segments, as well as the Hayward and San Gregorio faults and conclude that there may be a clustering or cycling of bay area ruptures suggested by a flurry of activity in the mid to late-seventeenth and late-eighteenth centuries. This was followed by a period of relative quiescence, terminated by the 1906 earthquake. They conclude that cycling of energy may be occurring, and may be manifested by both multiple fault ruptures, and or a single very large event. Continuing work on the mid-Peninsula appears to be following the same trend, with inconsistent results reported by two groups (Robert Sickler et al, and Gordon Seitz et al, presented at the USGS Norcal NEHRP meeting, January 30-31, 2018).

METHODS

Geophysical Surveys

High Resolution Bathymetry and Backscatter.

We surveyed Lake Merced using a Norbit PS-150007 wideband integrated multibeam sonar. Operating at 400 kHz, this system is a chirp system with 80 kHz bandwidth, and includes an integrated motion sensor and GNSS/INS navigation. This system covers a typical 140 deg. swath with ~ 10mm range resolution and 256-512 beams per ping. Both systems collected backscatter data, and comply with IHO specification SP 44ED5 over their full depth range. The quality of the beams may be influenced by vessel motion, surface noise, bottom hardness and roughness and other factors. The system is a stabilized system in both pitch and roll, that is, "beam steering" is employed to keep the fan array directed downward in all vessel attitudes. The system has a range resolution of less than 2 cm. Line spacing was arranged to provide at least 20% overlap in bathymetry and backscatter. The system was pole mounted on the starboard side of a 14' aluminum skiff with a 9.9 hp outboard motor (Figure 15). Solar panels and several car batteries were used and RTK position corrections broadcast from a cell network were applied in real time (Figure 17).

Figure 15. Survey vessel used for Lake Merced. Knudsen Engineering 3-20 kHz CHIRP subbottom profiler and Norbit broadband multibeam sonar were mounted on starboard pole mount. Upper part of pole carried dual GPS sensors for the motion sensing unit. Boats, motors and facilities kindly provided by the Pacific Rowing Club, Jeff Beeson pictured.

Sound Speed, Navigation and Vessel Motion Sensors

The water column sound speed profile was to be regularly monitored using casts of an AML Oceanographics Base X sound velocity profiler. High frequency of sound speed profiling is highly beneficial to the ultimate quality of any survey, and was done every few lines. Continuous 'real-time" sound speed measurements were made with a sound-speed probe at the transducer head, a particularly important place to measure sound speed due to the physics of forming multiple sonar beams.

Vessel motion was measured and recorded using a Norbit WBMS Inertial Motion Unit integrated with the Norbit iWBMS multibeam sonar unit during all surveys. This system uses multiple GNSS antennae arrayed on the vessel and an inertial system to produce Inertially-Aided Real-Time Kinematic (IARTK) attitude and position data utilizing L1 and L2 carrier phase measurements. The system was used for position, heading, and to determine roll, pitch, yaw attitude as well as heave. Antenna, Inertial Motion Unit (IMU) and sonar head positions were surveyed in place on the vessel. Small additional offsets for the sonar used in this project were measured and added to the Vessel Configuration file used in CARIS bathymetric processing. Additional positioning information was being collected with a NavCom StarFire SF 3050 GPS system. This system is a commercial satellite based differential system known as GSBAS (Global Satellite Based Augmentation System). This system provides positioning accuracy of ~ 10-20 cm horizontal, and 15-25 cm vertical worldwide (Dixon, 2006; Morales and Tsubouchi, 2007), and eliminates the need for land based base stations. The system is also provides high precision vertical control that can be used for heave corrections (unlikely in this case, but pitch changes in the vessel do occur).

Bathymetric data were acquired in real-time with the Hypack acquisition system, v. 2014. Bathymetric data from the survey were processed using Quimera data processing software (https://www.qps.nl/qimera/). This system produces motion- and sound-speed-corrected, geo-referenced bathymetry grids and imagery.

Chirp Sub Bottom Survey and Processing.

We collected a grid of seismic profiles in the lake using a Knudsen Pinger system to image the uppermost few meters at the highest possible resolution (Figure 17). Chirp has the advantage over continuous wave (CW) signals in that, properly applied, chirp signals can produce higher resolutions with lower noise levels than their CW counterparts. For FM chirp data, the frequency of the tone-burst varies linearly within the pulse itself which allows for higher resolution than a signal with a single frequency would have. Theoretical resolutions of 7-9 cm are possible, but 10-20 cm is more realistic depending on the impedance contrast of the subsurface beds, wave conditions (usually minimal for lakes), water depth (due to beam angle of the sonar insonifying a larger footprint) and other factors. The Chirp data were collected with a bandwidth of 10-20 kHz at a ping rate of 5 Hz. The Chirp dataset was processed with Sioseis (Henkart, 2006) to mute the water column, remove heave, and bandpass filtered for imaging of the shallow subsurface. Geophysical surveys were conducted using the same 14' aluminum boat with a four battery bank and 2500 watt inverter, supplemented by two 100 watt solar panels.

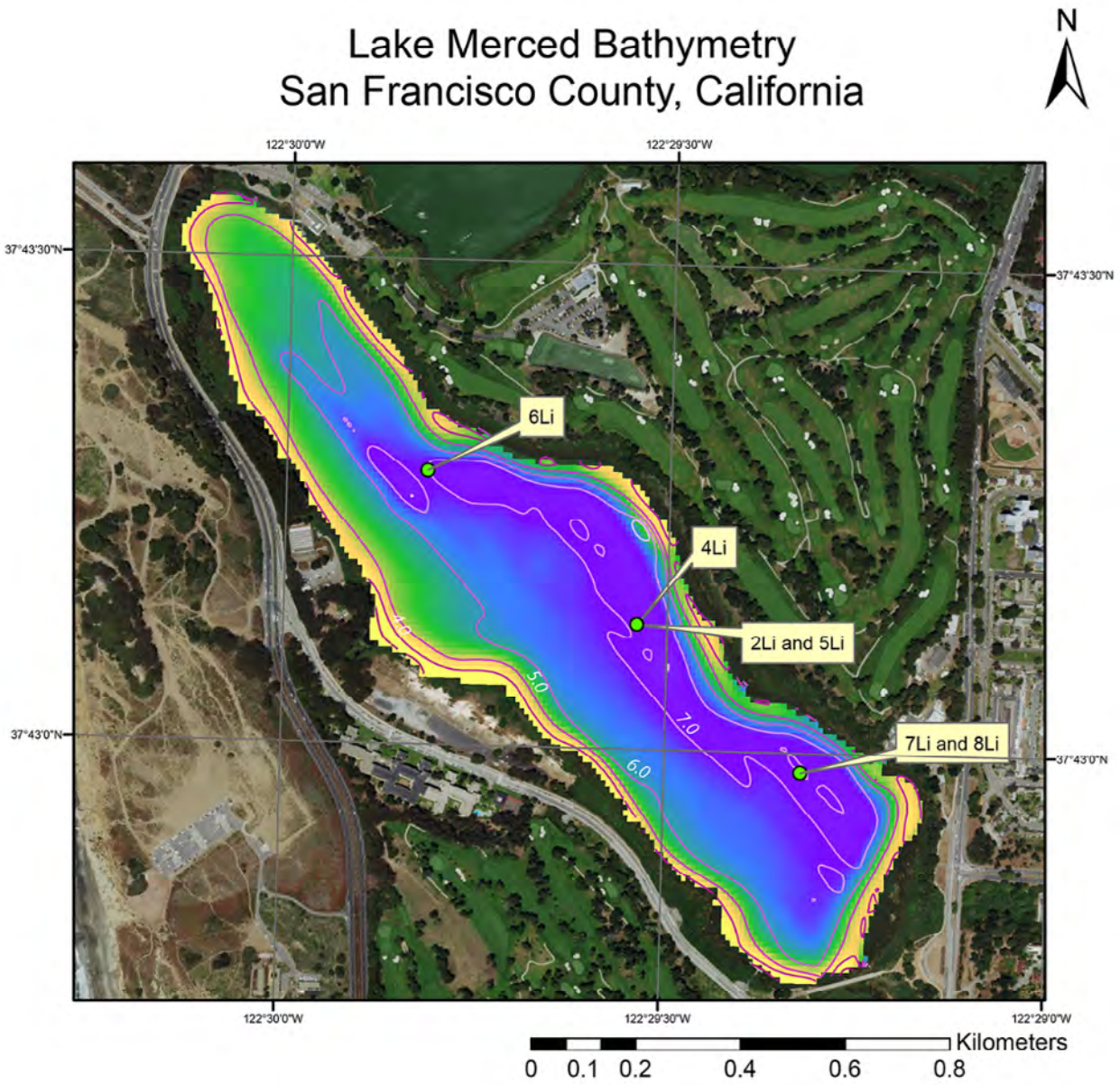

Figure 16. Initial processing of high-resolution multibeam bathymetry, Lake Merced, CA showing core sites and the east tilt of the lake floor. Contours in meters.

Figure 17. Google Earth image of Lake Merced with core sites shown in yellow, geophysical tracklines shown in black, dive/shear vane/push core sites shown as red stars. Gray shaded area is interpreted from sub-bottom profiles as the approximate limits of the 1985 remediation dredging of lake sediments adjacent to the Pacific Rod and Gun Club.

The Knudsen Engineering Pinger system was run using the optional 15 kHz transducer to obtain maximum resolution of the sedimentary record, which was expected to be relatively thin. The Knudsen system chirp bandwidth of 10 kHz was used, sweeping 10-20 kHz. Power was varied from 25-75% of the maximum of 2 kW as required to obtain good penetration. Gain was set to manual and varied as little as possible to reduce gain change induced problems in the imagery. Pulse width was 2 or 4 ms throughout the survey. Initially the multibeam and sub-bottom systems were run together to test their compatibility. While there were no problems with the multibeam bathymetry, the backscatter data were impacted by the sonar pinging, so concurrent use was discontinued. Varying the frequency and pulse lengths did not improve this enough to allow concurrent operation. When the dedicated survey began, three longitudinal lines were run and numerous cross lines. The grid was designed to look for thickness changes and reflector strength changes in the lake basin so they could then be related to potential sources of sediment input. Gas wipeout of the sedimentary section was severe however, making imaging of the sedimentary section impossible except for a few limited areas at the lake margins (Figures 18-19). Numerous lines were run in hopes of locating windows in the section where stratigraphy would be visible, but none were found.

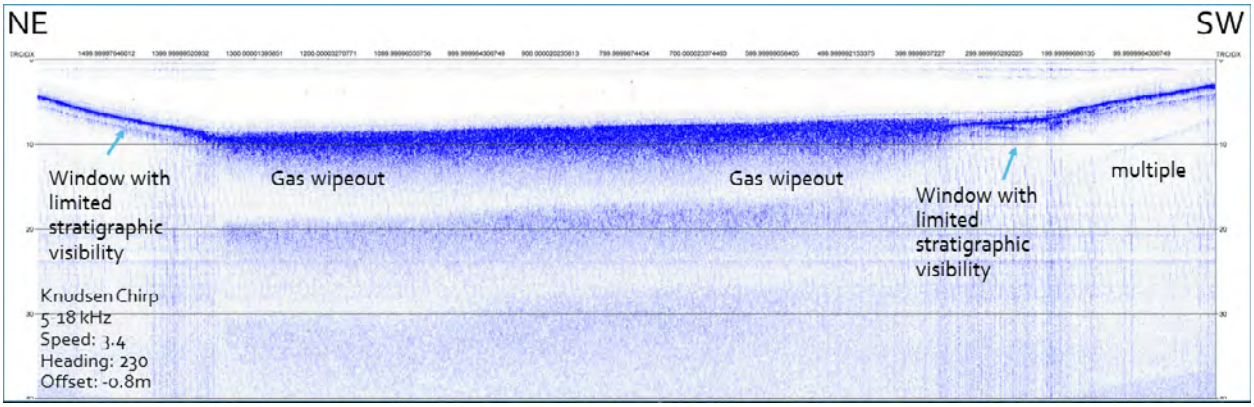

Figure 18. Typical Chirp profile across South Lake. Gap wipeout dominates the reflection section with the exception of the sandy lake walls, and very small sections of the lake floor adjacent to the walls. The east tilt of the lake for is evident in this profile. Time section converted to approximate depth using 1500 m/s velocity. Horizontal depth lines are at 5 m intervals.

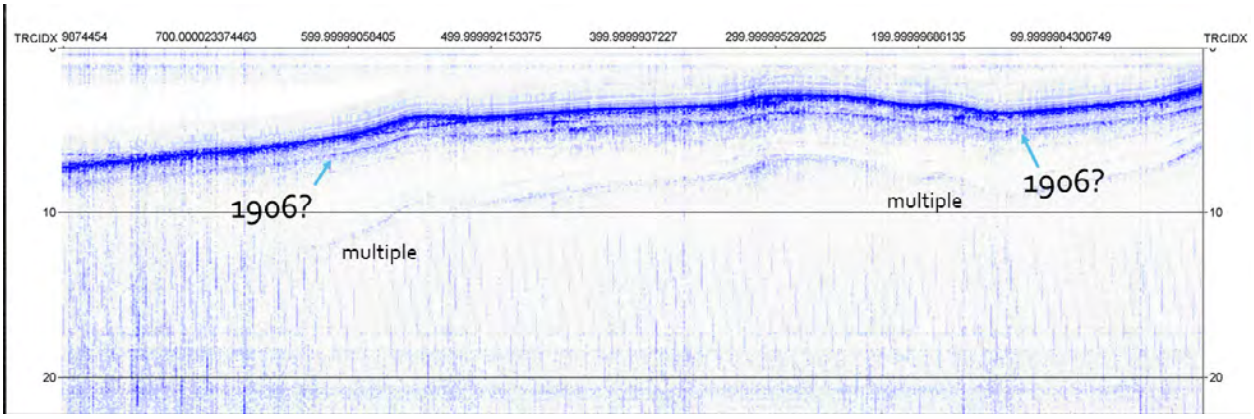

Figure 19. Visible throughout the lake in the nearshore windows is a prominent bed at 80-100cm. This matches the most prominent bed in the cores, the probable 1906 event bed. Approximate depth conversion in meters.

Core Acquisition and Analysis

Sediment coring.

Sediments in Lake Merced were cored using a 5-cm diameter, modified Livingstone piston corer using butyrate liner. These are hand driven cores deployed from a coring platform catamaran consisting of two 16' skiffs and a plywood coring deck. Cores were collected with the coring platform three or four point anchored with 6:1 scope or better, resulting in stable positioning. Casing was used on all holes to stabilize the holes and guide re-entry for each core rod section. We collected offset core pairs at each site to minimize the effects of the core section breaks that are produced every meter of core section. This allowed selection of the best core for a given site, or construction of a composite section if required. All cores were then split longitudinally and visually described. We employed several additional small vessels according to accessibility of the lakes to collect cores and conduct profiling.

Bathymetry and seismic profiles show that the lake floor is gently tilted to the east, with the deepest areas relatively close the eastern margin of the lake. That, and disturbances caused by remediation of contaminated soils on the southwest part of the lake (due to a former shooting range) prompted us to

focus on the eastern lake floor. The gently east tilted lake floor also made this the optimal target for coring, with the likelihood of an expanded sedimentary section.

Lithologic Descriptions and Physical Properties. All cores were scanned with Geotek multisensor logger that collects high-resolution visible imagery, Gamma density, magnetic susceptibility, P-wave velocity, and resistivity. Cores were then split for visual description and collection of high-resolution line-scan and CT imagery. Subsequently, high-resolution point magnetic susceptibility data were collected from each core using a point sensor (Bartington MS2E high-resolution surface sensor) at 0.5 or 1 cm intervals, and imaged with visible and Computed Tomography (CT) systems. Selected grain size analyses were performed with the laser diffraction method using a Beckman-Coulter LS 13-320 laser counter (Blott and Pye, 2006). Physical property data does an excellent job of representing properties of the sedimentary units within the core when verified with ground truth data (Wetzel and Balson, 1992; Weber et al., 1997; Rothwell and Rack, 2006). We primarily use magnetic susceptibility and both gamma and CT derived density as grain size proxies and for stratigraphic correlation, verified by grain size analyses. Further discussion of this proxy and the use of other physical property parameters can be found in Goldfinger et al. (2012). Cores were CT-scanned for density and 3-dimensional imaging of stratigraphic features using the OSU Toshiba Aquillon 64 slice CT system (0.4mm voxel resolution). We also scanned the cores with an ITRAX X Ray Fluorescence (XRF) system that collects composition information for 92 elements at 1-5 mm resolution. We have also collected numerous smear slide samples at selected intervals for lithologic and microfaunal identification.

One of the most difficult parts of modeling ages in a marine/lacustrine sequence is establishing the boundaries between event beds and background sediment. At the event bases this is typically simple, although basal erosion is an issue. At the event tops, the fine tails grade into the background material, which is commonly nearly identical to the tail material. At the same time, this boundary establishes the end of the event and the start of normal sedimentation, and drives the age model. This boundary can sometimes be distinguished visually, with grain size, with magnetics, with CT imagery, or other methods. It typically takes a lot of trial and error to find a suite of tests that are effective for a given lithology. In our work thus far, proxies for grain size include magnetic susceptibility, and coherent/incoherent scattering of the X-ray (XRF) energy.

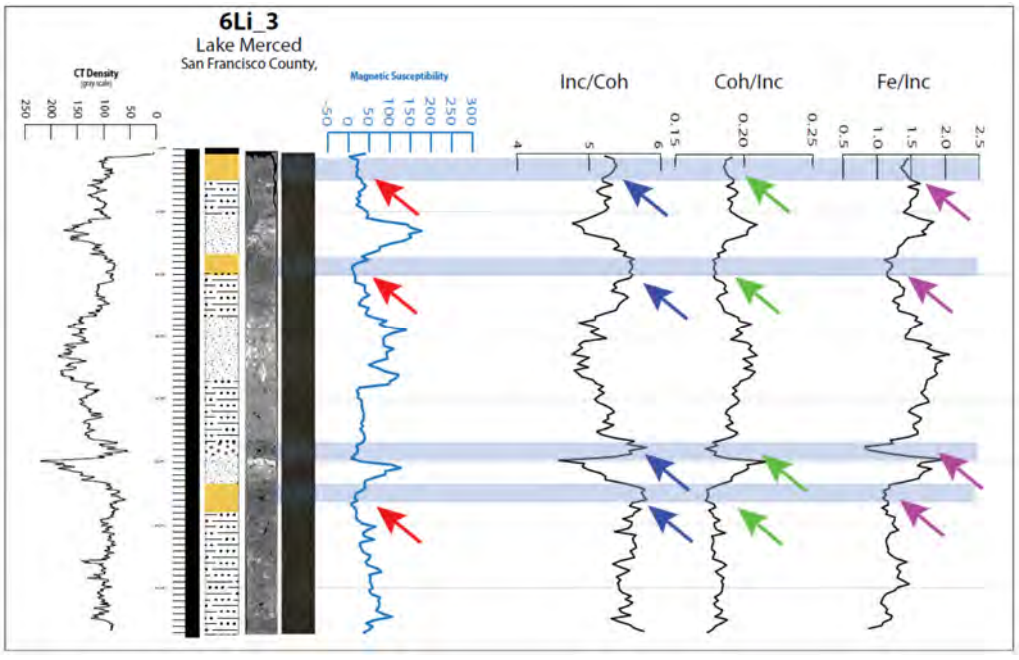

Figure 20. Example of the use of Computed Tomography (CT), magnetic susceptibility and X-Ray Fluorescence (XRF) to help define event bed-background sedimentation boundaries.

Figure 20 shows a detailed example of the use of physical property

proxies and XRF data to better define these boundaries. In Figure 20, low mag susc. and high incoherent/coherent scattering in XRF are proxies for grain size, normally low in background sediment. Lows in Fe/incoherent scattering and coherent/incoherent scattering are associated with organic content in the background sediment (Rothwell and Rack, 2006). Grey bands show the combination of these proxies to interpret background sediment in the cores, typically seen as dark (low density) in the CT image.

Age Control and Modeling

Radiocarbon ages. 22 AMS radiocarbon ages were determined at the UC Irvine Accelerator Mass Spectrometry facility on small organic samples. Raw AMS ages were calibrated to calendar years by the method of Stuvier and Braziunas (1993) using CALIB v. 7.1. Very young samples were calibrated using CaliBomb (Reimer et al., 2004) available at http://calib.org/CALIBomb/. Leaf fragments, twigs and seeds were used, picked carefully from the generally very fine organic gyttja between event beds. For some intervals we used thin (1-2) mm bulk samples where no discrete identifiable materials could be found. Using the CT imagery, we targeted intervals as close to the base of event beds as possible, though the samples were so sparse that this ideal was not common. The relative difficulty in identification of samples was a significant issue in developing good age control on the lake cores. Ages are reported as 2σ ranges, with median or mode values used for plotting as described in Goldfinger et al. (2012).

Age Models. In order to compute ages for all significant beds in the cores, we consider that the major beds that have designated event numbers were likely deposited in a very short time span, and represent zero geological time. We further assume that the background stratigraphy between event beds was deposited uniformly in time intervals between event beds. Although this is not likely in detail as there are many thin laminae, we make this approximation because heterogeneity in deposition rate is not discernable at the resolution of our data. We computed age models using OxCal, a Bayesian Markov Chain Monte Carlo calibration and age model software package (Ramsey, 2001). To compute event ages, we computed ages using the OxCal P-sequence age model, with turbidite stratigraphy removed to develop an "event free" stratigraphy. Event ages could then be extracted from the model at the appropriate depth positions in the stratigraphy (e.g. Hamilton et al., 2015). OxCal can also be used to test for coevality (at the resolution of radiocarbon) with several statistical tests (χ^2 and Acomb; http://c14.arch.ox.ac.uk/oxcalhelp/hlp_contents.html). Some ages were clearly reversed, that is older than ages below them stratigraphically. Using the lake stratigraphic correlations and all available ages, reversed ages were readily apparent, and are shown grayed out in subsequent figures.

Head to Head Age Comparisons

In the second part of this project, we compared event ages and stratigraphy between Noyo Canyon along the NSAF, and southern Cascadia sites. To do this, we compare age models from the different sites as described above, but we also consider singe event age comparisons. To do this, we use the OxCal Combine function. Normally this is used to combine ages from the same sample, and it provides goodness of fit tests and statistics. Here, we intentionally combine ages that are not from the same sample, but from Cascadia sites and Noyo Canyon sites in order to use the goodness of fit tests. The X2 test compares the two probability density functions and assumes the null hypothesis that they have no commonality. If The X2 test results in a statistic to compare to the critical values for the number of degrees of freedom involved, and rejects the null hypothesis at a given value of alpha (the confidence limit). In addition, Oxcal gives an Agreement index for the combined ages to support or reject a potential correlation, and also provides a visual plot of these comparisons.

Event Bed Correlation. Correlation between sites was attempted by integrating physical property parameters with core imagery, age data, and CT data and interactively testing alternate correlations or lack thereof. The procedure used is to match tops and bases of individual beds using all data

simultaneously, a procedure known as "flattening". The combined data set from the turbidite sequences are shifted iteratively relative to each other, using "ghost traces" to compare alternative detailed matching of wiggle traces from site to site, similar to e-log correlation in the oil industry (McCubbin, 1982; Lovlie and Van Veen, 1995; Lees et al., 1998; Morton-Thompson and Woods, 1992). These methods have also been applied in academic research with piston, gravity and ODP/IODP cores (e.g. Fukuma, 1998; Karlin et al., 2004; Abdeldayem et al., 2004; St-Onge et al., 2004, 2012; Iwaki et al., 2004; Schnellmann et al., 2002; Goldfinger et al., 2008, 2012, 2017). The methods and rationale are more completely described in Goldfinger et al. (2012).

RESULTS

In February 2014, we conducted a very brief reconnaissance survey and collected a single test core from Lake Merced using a modified Livingstone piston corer (LM-1). In FY 2016 we collected five more long cores ranging from 5-7 m in length, and several shorter ones along the central/eastern part of the lake. We also collected high-resolution multibeam bathymetry, backscatter data, and numerous CHIRP seismic reflection profiles. The objectives were to explore the Lake Merced area and examine it for paleoseismic potential.

Geophysical Results

Bathymetry

The lake has a maximum depth presently of ~ 8 meters, with the western arm (South Lake) shoaling somewhat toward the north end. The lake floor is sloped to the east at a relatively steep average angle of ~ 3-4 degrees. The surface slope angle gradually increases southward in South Lake. We found the lake walls to be visibly failure prone with a number of small failures around the shore in the bathymetry data and along the subaerial shore. The 1957 failures were still visible as they are in Google Earth.

The bathymetry data from Lake Merced is shown in Figure 21. Several features are obvious in the image. There are clear bathymetry artifacts in the data running parallel to the tracklines. These are due to changing water velocity structure that was not fully captured with the sound velocity profiles done during the survey. We do not observe surface expression of any faults in the lake, although such faults running parallel to the survey lines might be difficult to note. There are several other features, including the pipes and intakes for the San Francisco backup water supply along the southeastern deep sections of the lake. There are also three other unidentified objects on the lake bed and the southeastern area as well. The most notable feature is the slop of the lake bottom. Despite a high sedimentation rate, the lake floor has a strong tilt to the northeast, averaging ~ 0.27 degrees (Figure 21). Given the high sedimentation rate in the past 2000 years, and the prior history of an inlet or open lagoon with an opening to the sea, the tilted lakebed suggests a relatively rapid tectonic origin. This in turn is compatible with previous interpretations that Lake Merced might be part of a pull-apart where the main San Andreas slip steps to the right onto the Golden Gate strand. This interpretation is also consistent with the 1957 Daly City earthquake its normal faulting mechanism. There is evidence of lake wall failures are several point along the lake walls. Figure 22 shows one of these locales.

Although we do not observe a surface fault in the lake, we suggest that the tilt strongly suggests the presence of one. If such is the case, we can estimate a slip rate. If we assume that prior to ~ 2000 years when the stratigraphy indicates ocean conditions existed, then a maximum limiting slip rate would be the down-dropping of the eastern lake of 1.5 m over that time, or ~ .75 mm/yr. The lake floor at its deepest is ~ 1.8 m below mean sea level. We suggest also that given the high sedimentation rate, the lake would rapidly fill that accommodation space, and that the relatively deep lake floor also suggests a tectonic origin.

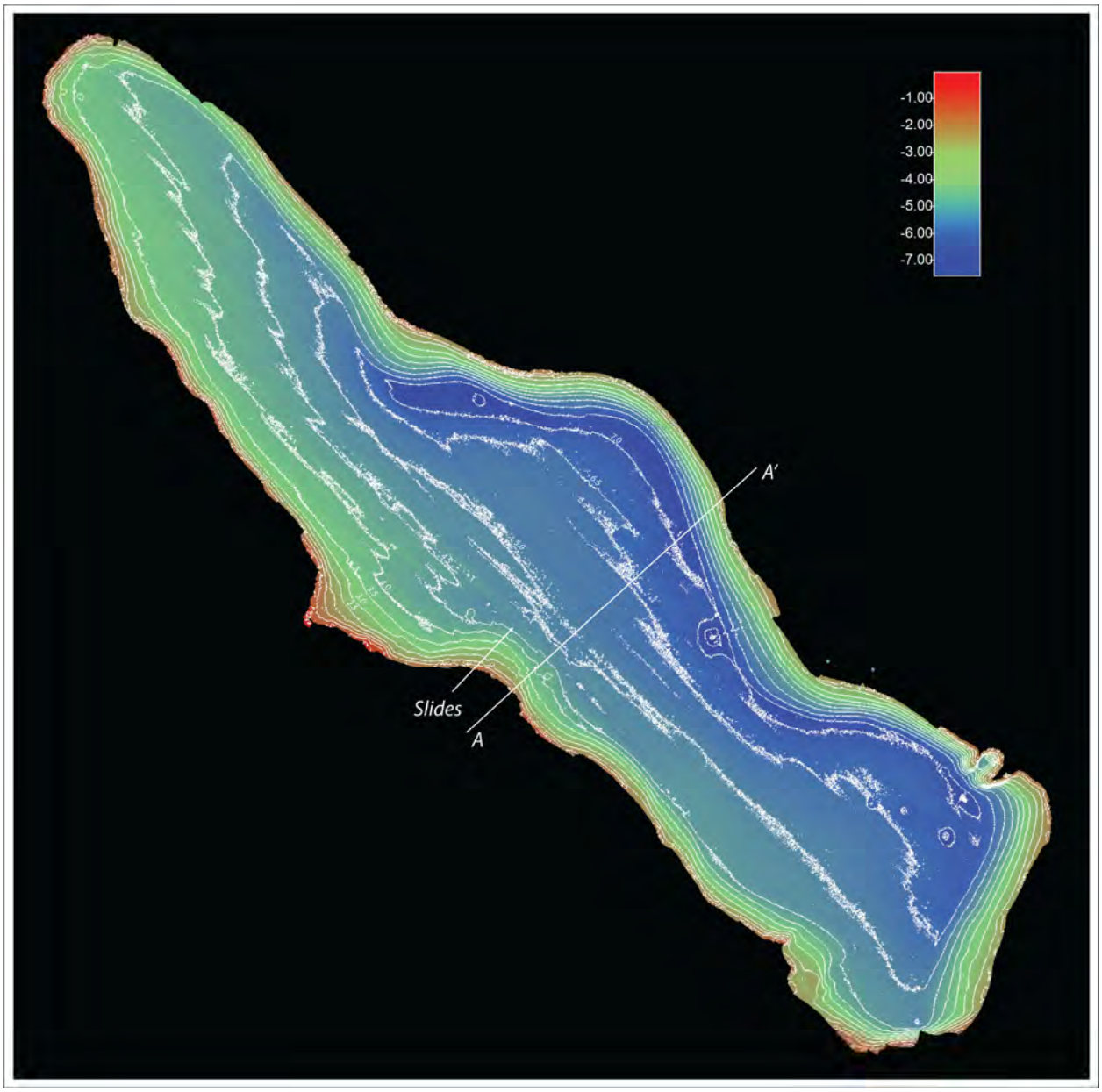

Figure 21. Shaded relief image of Lake Merced multibeam bathymetric data. Contours are meters. The NE tilt of the lake floor is readily apparent. The depocenter closer to the eastern shore is the reason most of the cores were collected there. The lake generally deepens to the SE. A singular "pothole" feature is observed with several m depth below the lake floor in the middle of this depocenter, and another anomaly associated with the adjacent pumping station is seen at the SE part of the lake. Location of the following two figures are shown.

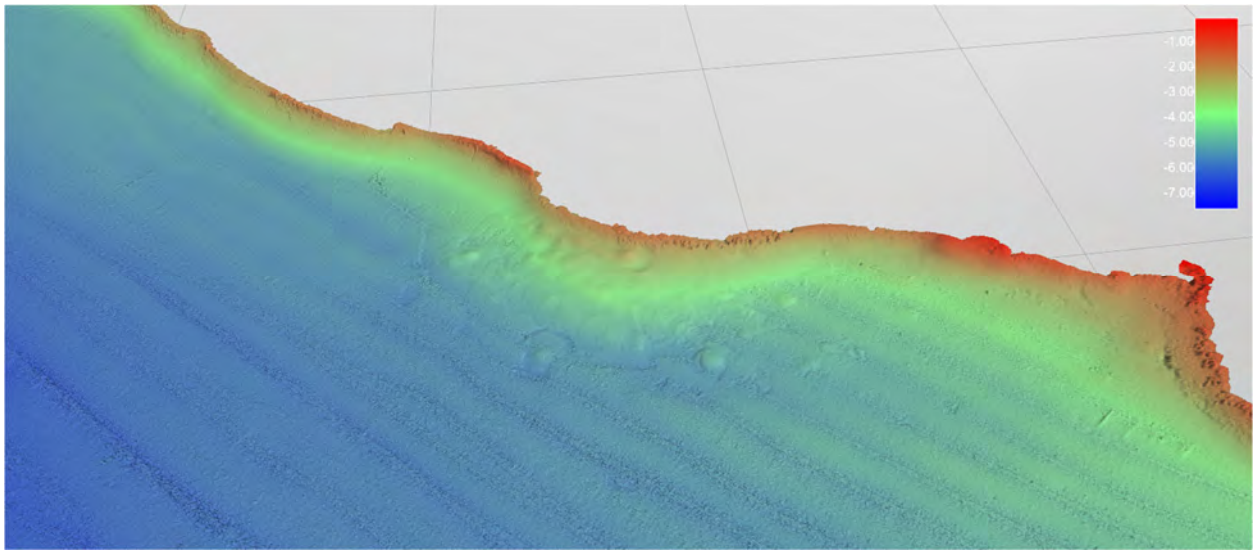

Figure 22. Slides and slide blocks on the western shore of Lake Merced at the location shown in Figure 21, west is up in this image.

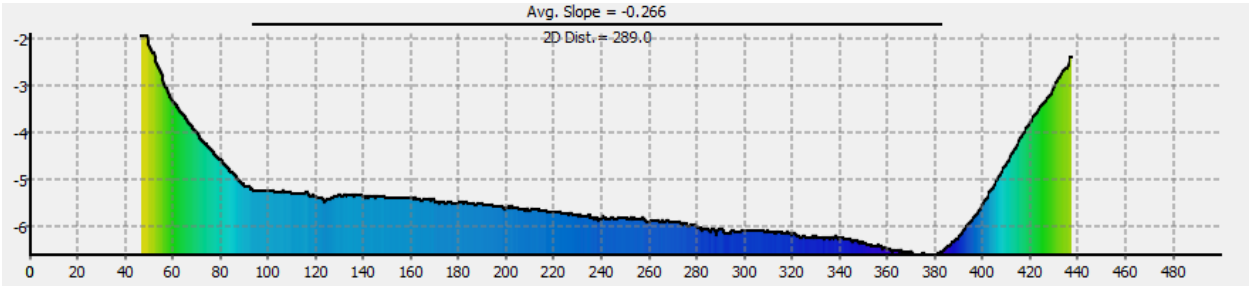

Figure 23. Profile across Lake Merced at the location shown in Figure 21. A strong tilt to the east is apparent. The lake floor drops almost 1.5 meters across the middle 290 m of this profile.

The subbottom profile grid as noted above were designed to look for thickness changes and reflector strength changes in the lake basin so they could then be related to potential sources of sediment input. Gas wipeout of the sedimentary section was severe however, making imaging of the sedimentary section impossible except for a few limited areas at the lake margins (Figures 18-19). At this stage of analysis, very little can be interpreted from the subbottom profiles. Visible throughout the lake in the nearshore windows is a prominent bed at 80-100cm. This matches the most prominent bed in the cores, which may be the1906 event bed as described below.

Sub-Bottom Profiles

The subbottom profile grid as noted above were designed to look for thickness changes and reflector strength changes in the lake basin so they could then be related to potential sources of sediment input. Gas wipeout of the sedimentary section was severe however, making imaging of the sedimentary section impossible except for a few limited areas at the lake margins (Figures 18-19). At this stage of analysis, very little can be interpreted from the subbottom profiles. Visible throughout the lake in the nearshore windows is a prominent bed at 80-100cm. This matches the most prominent bed in the cores, which is likely the1906 event bed as described below.

Core stratigraphy

The stratigraphy observed in the core set show a coherent stratigraphy of sharp-based turbidites that correlate throughout the lake. This event bed stratigraphy includes 15 lacustrine turbidites ranging in thickness from a few cm to an upper unit of ~ 1m thickness, interbedded with very fine interevent sediment. This stratigraphy lies above a lower unit containing numerous shells of probable marine origin. This suggests a history involving a late Holocene lacustrine period preceded by an estuarine episode of unknown length. A typical bed with CT imagery, lithologic log, RGB image and CT density and magnetic susceptibility traces is shown in Figure 24. These relatively fine grained beds are for the most part, not visible to the eye in the cores.

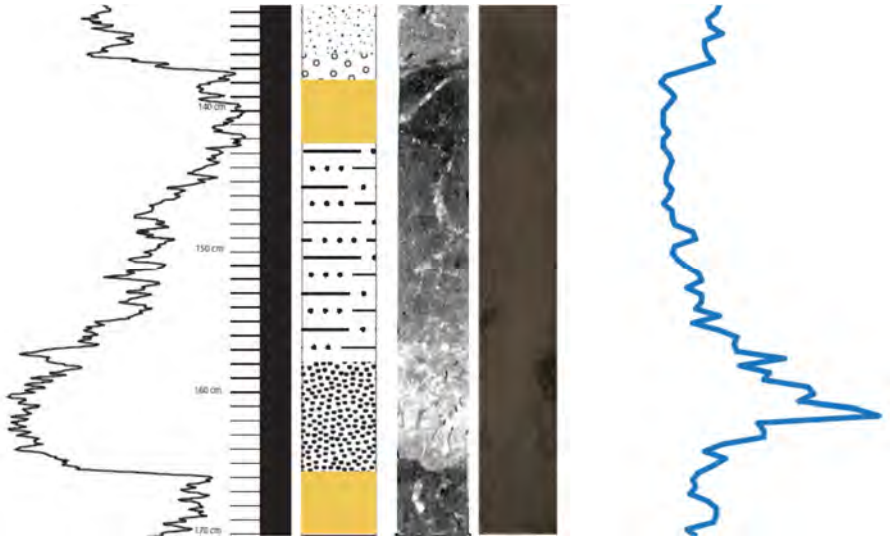

Figure 24. Typical event bed stratigraphy of the upper lacustrine unit of Lake Merced in core 5Li. Lithology, CT image, and RGB image are shown, with magnetic susceptibility trace (right) and CT density trace (left). Sharp based fining upward turbidite is visible (light tones), overlain by interevent bed (dark tones). Density and magnetic traces mirror the fining upward bed structure. See Figure 27 for Explanation, scales and context.

In detail, a thin surface sand is present (Bed 1), below which a small diffuse turbidite is present in some, but not all cores (Bed 2). Below that, all cores contain a thick unit ranging from 80-110 cm in thickness (Bed 3; Figure 27). In places, this thick bed eroded into and in some case removed the bed below.

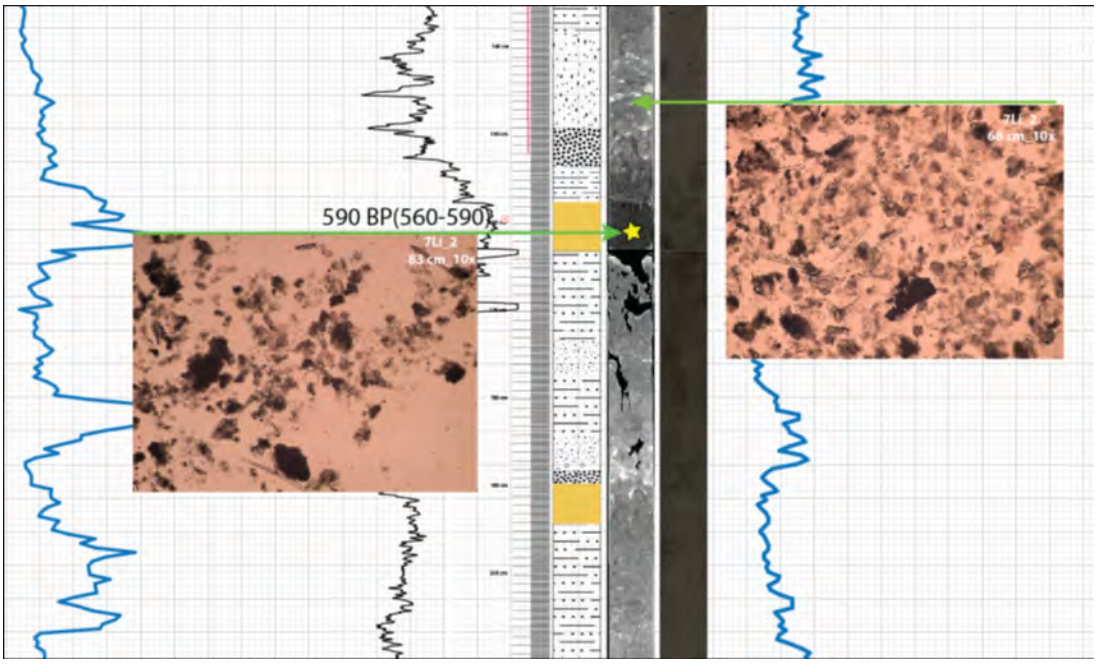

Figure 25. Comparison of smear slides from and interevent bed (left) and an event bed (right). Similar lithology is observed, with an increase in lithics in the event beds. Green arrows indicate sample locations, yellow star is a radiocarbon sample location. See Figure 27 for Explanation, scales and context.

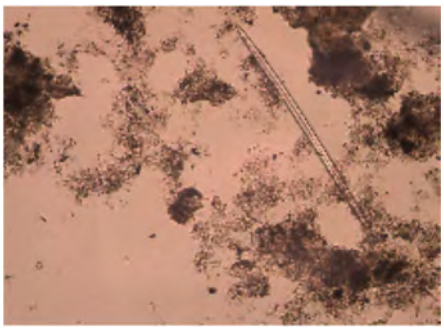

Figure 26. Fresh water sponge spicules like this one are common on the interevent background sediment of Lake Merced

The cores show a correlated stratigraphy of 17 beds, and several uncorrelated beds, above a sharp contact. Below the contact is a shelly-silty clay mixture, grey in color that extends to the bottom of the cores. This contact is at a depth of 3.5-4 m. This lower unit is also characterized by the absence of any magnetic variability in the magnetic susceptibility data, indicating a major change in sedimentation at that time (Figure 27). We interpret this contact as one between a lower estuarine unit, and an upper lacustrine unit, though this is not yet confirmed.

In the upper, likely lacustrine unit, smear slides show the event bed stratigraphy and interevent sediment are similar (Figure 25). Flocculated clays, lithics and relatively sparse diatoms are the dominant constituents, with greater lithic content within the event beds (Figure 25). Between the event beds are thin units of gyttja which we interpret as the background sediment of the lake. The turbidite beds are composed of mostly this same material, with more silt and very fine sand. This it appears that the event beds are similar to the diatom-rich gyttja forming between events, and suggests that the event beds are derived from materials internal to the lake. While the diatoms have not been investigated as of this writing, fresh water sponge spicules are apparent in the lacustrine section (Figure 26).

Intra-Lake Correlation

The preliminary correlation of the beds was performed jointly using the radiocarbon ages, well log correlation methods with the geophysical traces, and CT imagery. Our preliminary correlation of all lake cores is shown in Figure 27. Notable is that the event beds make up ~ 3.5 meters of a composite ~ 4 m stratigraphy of the lake above the estuarine (?) contact, with the background gyttja representing only ~59 cm. Thus it appears that 87% of the lake fill post ~ 2400 cal BP is composed of internally derived event beds. The surface sand was captured in some of the cores, and is not presently dated using radiocarbon, but its age is estimated with sedimentation rates (below).

Correlation of the beds within the lake is relatively straightforward over the short distances within this relatively small lake. However more variability from core to core is observed that we would expect, and we suspect that this may be due to deformation of the very soft samples during coring and from handling of the relatively soft butyrate liners. We interpret 17 beds in the lacustrine section, and find that no significant beds pinch in or out within the area covered by the core set, while there are many minor changes between sites. And several minor beds that are uncorrelated. Beds within the estuarine section are not correlated or used further in our paleoseismic analysis due to the unknown sedimentary environment. Correlation of physical properties follows trends similar to those observed in offshore cores, with grain size positively correlated to density trends and magnetic susceptibility with primary difference being the very low absolute values or magnetic susceptibility, at times actually negative. We attribute this to a low occurrence of mafic minerals in the lake sediments (Goldfinger et al., 2008, 2012).

Bed thickness variability shows that turbidite thickness does not clearly show a spatial correlation to the physiography of the lake (Figure 27). Stream input is mainly at the north end of the lake feeding from the western hills of San Francisco into eastern Lake Merced. This drainage has been highly modified, and presently does not feed western Lake Merced (South Lake) directly. For example, Beds 2, 7, 8, and 10 are most robust in the middle part of the lake where there is no stream input (cores 2Li and 4Li); Beds 5, 6 and 11 are most robust in the northern part of the lake (Core 6Li), and only beds 13 and 15 are most robust at the south end of the lake, with the greatest depth by a slight margin and near a secondary stream input.

Correlation using the physical property traces, CT imagery and radiocarbon ages was done iteratively through many cycles to establish the likely reversed ages, after which the final result in Figure 27 resulted. Interval thicknesses of the interevent beds were then collected using the best available intervals or averages of the best available if multiple good intervals were available. In this way, we were in most cases able to avoid poorly defined or deformed intervals by using the full core set to develop a composite stratigraphic section.

Table 1. Lake Merced radiocarbon results.

ID #	Core section	Interval in section (cm)	sample type	Empty bag (g)	Wet sediment without bag (g)	Dry sediment without bag (g)	UUCIAMS #	Radiocarbon Age	uncertainty	Notes
1b	5Li_5	22.5-23.3	Humics	2.3	3.1	0.8	187615	1975	20	
2b	5Li_5	45-46	Humics	2.2	3	0.8	187616	2425	20	
3b	5Li_3	x	Humics	X	X	X				Discarded. Sandy.
4b	5Li_3	74-75cm	Humics	2.6	3.5	0.9	187617	1525	20	
5	5Li_6	22.5 -22.8	Humics	2.3	3.5	1.2	187618	2820	30	
51	6Li_3	54-54.5	Humics				198158	1150	20	
6	6Li_4	62-63	Humics	2.3	3.1	0.8	187619	1450	20	
7	7Li_2	83-82.5	Humics	2.5	3.8	1.3	187620	645	15	
8	7Li_3	69.5-70	Humics	2.1	2.9	0.8	187621	1545	15	
9	7Li_5	11.5-12	Humics	1.3	2.1	0.8	187622	2355	15	
10	8Li_2	20-20.5	Humics	2.2	3.3	1.1				
11	8Li_2	20.5-21	Humics	1.8	2.9	1.1	187623	645	15	
12	8Li_2	57-57.5	Humics	1.3	2.1	0.8				
13	8Li_2	48-48.5	Humics	1.9	2.7	0.8	187624	1065	20	
131	8Li_2	83.5-84.3	Humics				198159	1540	15	
14	6Li_3	47.5-48	Humics	1.6	2.1	0.5				
15	8Li_3	33.5-34	Humics	1.5	2.3	0.8				
16	8Li_9	24.5-24.8	Humics	3.4	4.2	0.8				
17	8Li_9	24.8-25	Humics	2	3	1				
18	8Li_9	25-25.3	Humics	2	2.9	0.9				
19	8Li_9	25.7-26.2	Humics	1.6	2.3	0.7	187625	3325	20	
20	8Li_9	27.2-28	Humics	1.7	2.6	0.9	187626	3385	20	
201	2Li_4	27-27.5	Humics				198156	1515	20	
202	2Li_4	28.5-28.9	Humics				198157	1505	15	
203	2Li_4	45-45.5	Humics				198155	1540	15	
21	2Li_4	53-53.3	Humics	1.7	2.8	1.1				
22	2Li_5	19.5-20.2	Humics	4.5	6.5		187627	1700	15	Dry weight with bag 4.8
23	2Li_5	31-31.2	Humics	4	5					Dry weight with bag 4.0
24	2Li_6	22-23	Humics	2	2.9	0.9	187628	2410	15	
25	2Li_6	23-23.4	Humics	1.8	2.6	0.8	187629	2405	15	
26	2Li_10	27-27.5	Humics	1.6	2.3	0.7	187630	3700	20	
27	7Li_1	27-28.2	Humics	1.9	4.2	2.3				
271	8Li_5	13.7-14.3	Humics				198160	1990	20	
28	8Li_5	39-39.3	Humics	1.9	2.7	0.8				
29	8Li_5	37-37.4	Humics	1.5	2.2	0.7	187631	2375	20	
30	4Li_1	42-43	Humics	1.7	4	2.3	187632	Modern		
31	4Li_1	60-61.3	Humics	1.6	3.9	2.3	187633	Modern		
310	5Li_1	17.8-18.4	Humics				198161	Modern		
311	5Li_1	13-13.5	Humics				198162	Modern		
32	5Li_2	55.5-56.5	Humics	1.8	2.5	0.7	187634	720	15	
33	6Li_2	40.5-41.5	Humics	1.4	2.8	1.4	187635	700	15	*Check CT. Could be 41-42 if core moved 0.5cm above beginning of liner. 40.5-41.5cm interval taken when core top/liner start is at 0. But CT might be off by ~0.5cm from compiling.
34	2Li_3	46-46.5	Humics	4	6					
? LM 340	2LI-2	~ 10 cm					?	925	15	OSU sample number re-assigned 4/20/21
? LM 341	2LI-2	~ 10 cm					?	1095	15	OSU sample number re-assigned 4/20/21

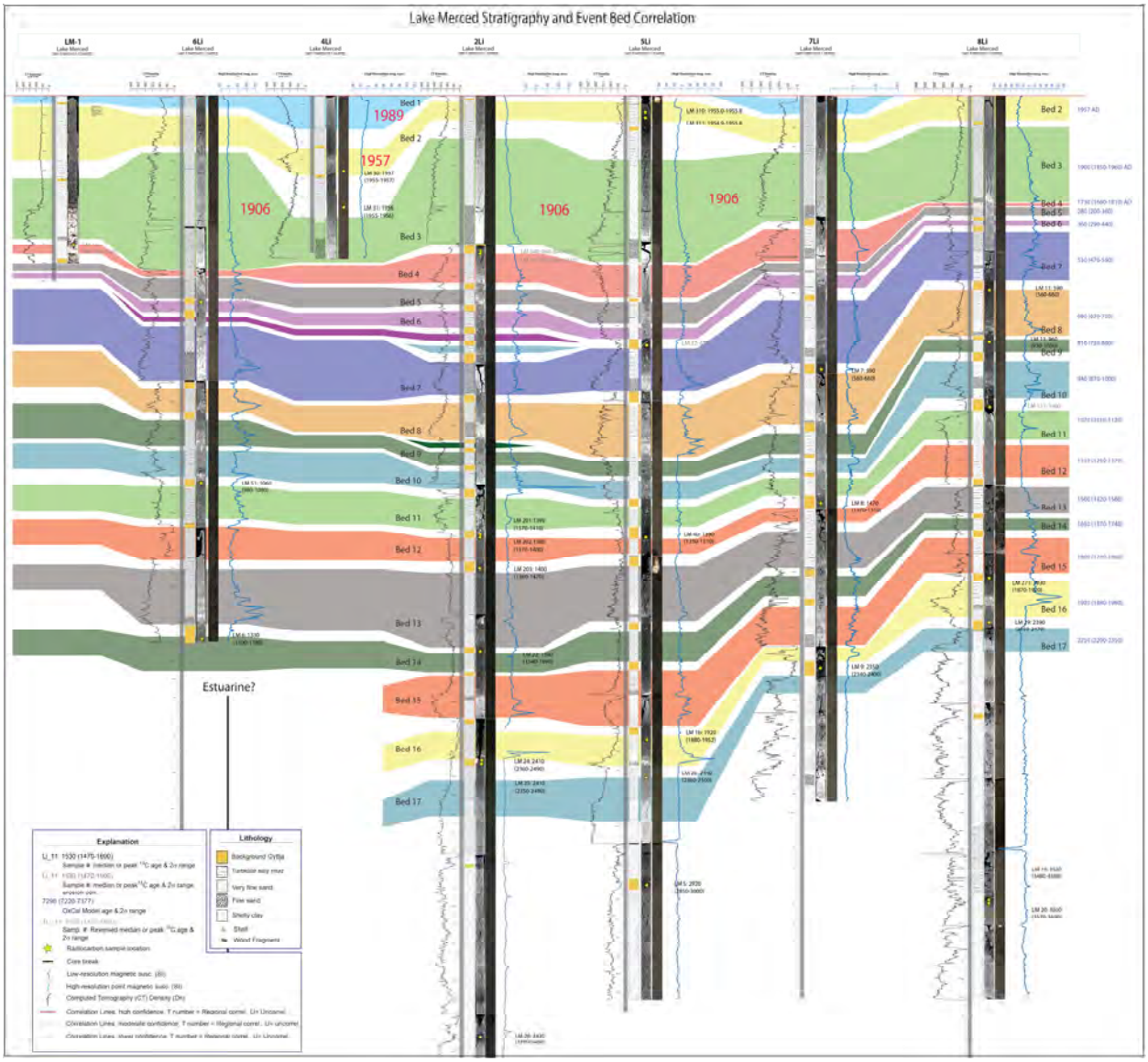

Figure 27. Final correlation diagram and radiocarbon results from Lake Merced. Radiocarbon ages are shown in black, and are grey if considered reversed in the context of all ages. OxCal model ages shown in blue at right. Core sites shown in Figures 17 and 18.

Historic Beds

Figure 28 shows the upper part of core 4Li, and three very soupy turbidites. Not all cores captured the uppermost surficial unit (Bed 1). Only the upper part lower bed, (bed 3) is shown. The uppermost bed is atypical in that it shows a coarsening upward structure, as it does in two other examples (Figure 27), while in the LM-1 core, it has a sharp base. Bed 2 two has a sharp base and an upper internal contact as opposed to a smoothly fining upward structure. This is a common observations in bypassing with turbidite structures when a large fraction bypasses a given location and deposits further downslope (e.g. Lowe, 1982; Stevenson et al., 2013). Bed 3 is a very thick bed, the thickest bed in the lacustrine stratigraphy, and has a sharp and erosional base, likely with missing interevent section below it.

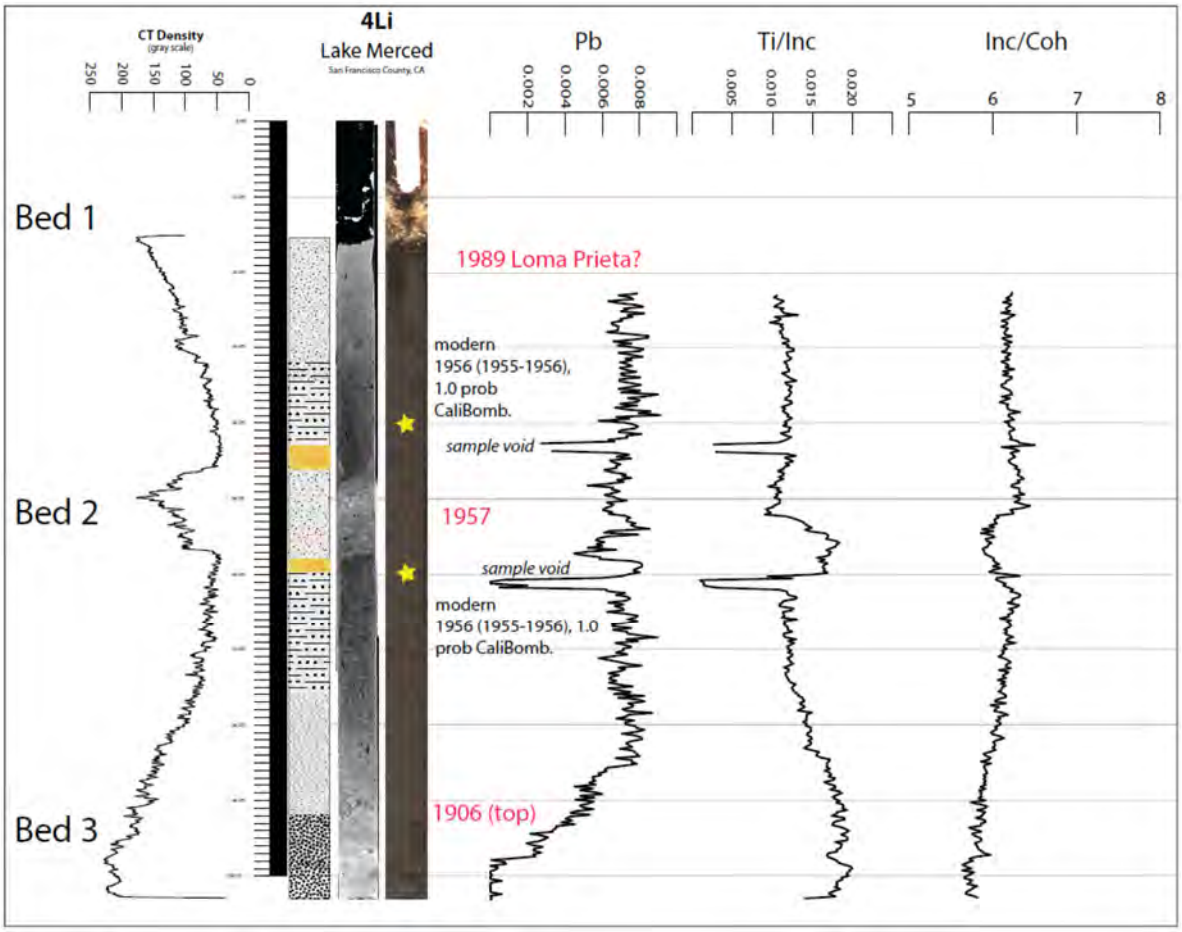

Figure 28. Upper section of core 4Li. This core was a short core taken to capture the surface as carefully as possible. The CT imagery reveals three beds 1) an upper surface silt, Bed 1; 2) a silty bed dated at 1955-56 just above and just below the event bed with CaliBomb, likely the 1957 earthquake turbidite, and the upper part and tail of the thick likely 1906 deposit. The 20th century ages are supported by high levels of Pb shown in XRF data (3 black traces to right of core), possibly corresponding to leaded gasoline and lead paint in the debris from the 1906 earthquake. Titanium is a proxy for lithics and grain size, and Incoherent/coherent scattering is a proxy for organic material, low in the turbidites and high in interevent beds.

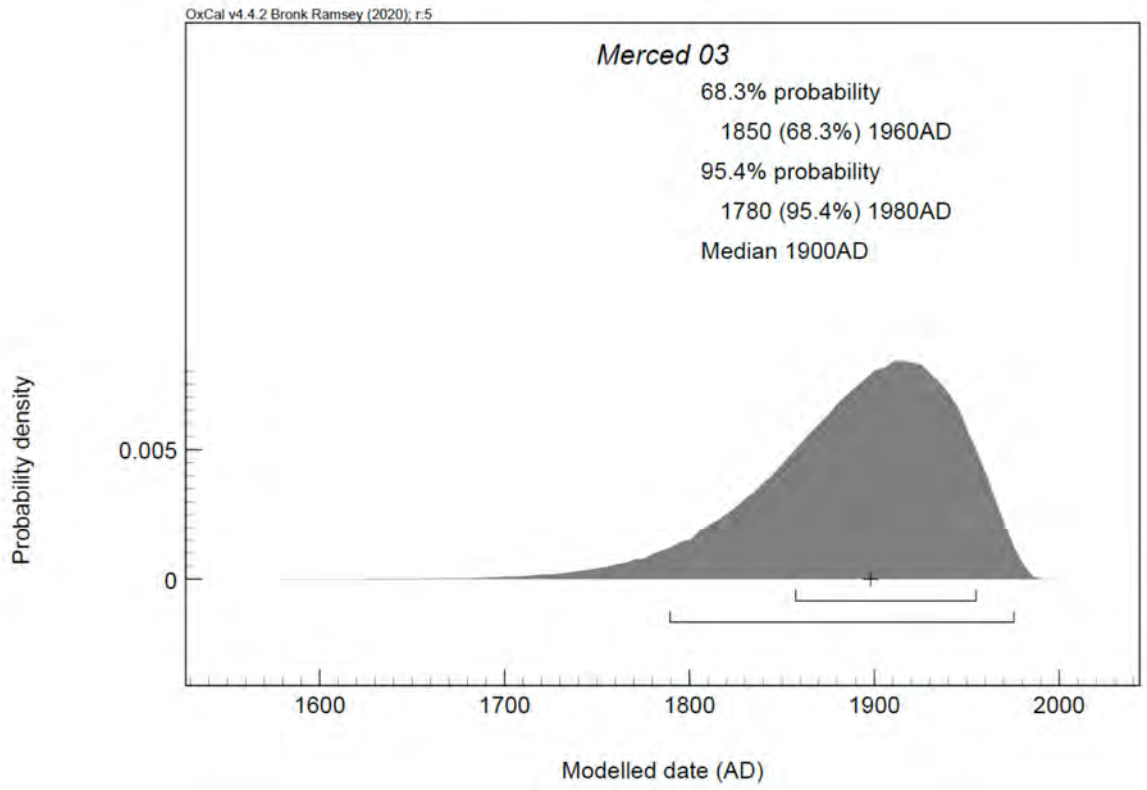

Figure 29. OxCal modelled probability function for Lake Merced Bed 3, interpreted as the 1906 earthquake disturbance bed.

The age of the very thick and robust Bed 3 is difficult to obtain directly. The bed is ~ 1 m thick, several times thicker than the other event beds, and has an irregular and almost certainly erosional base. Three

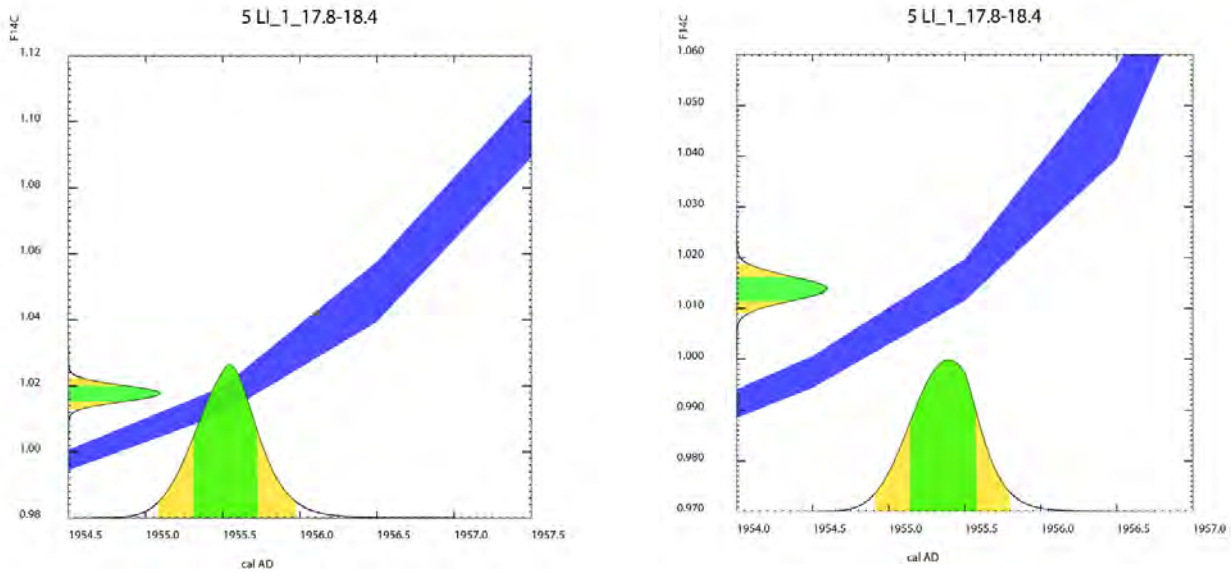

Figure 30. Two replicate ages for Bed 2 calculated with CaliBomb. Very narrow age ranges are due to very steep calibration curve with samples containing bomb carbon (post 1952).

attempts to date this interval yielded ages of ~ 440-1100 Cal BP (Figure 27). Given that ages much deeper in the cores were considerably younger, we interpret these ages as reversed, mostly likely due to contamination by reworked material. No high-quality interevent bed material was available for dating this unit, which is merged with the tail of the underlying bed in CT imagery. We thus use the overall age model, discussed further below, to estimate the age of Bed 3. Figure 29 shows the probability density function for the OxCal model age for Bed 3. At the 2 sigma level, the 1852 spit breaching event is excluded (barely) as an origin for this bed, while at the 3 sigma level it is not excluded. Mean and median values are within 16 years of the 1906 earthquake.

Bed 2 was dated with radiocarbon, and yielded a "modern" age. Two replicate samples were dated, and were then recalibrated using Calibomb. These ages yielded nearly identical ages spanning 1955-1956. The very narrow 2 sigma rages are due to the very steep calibration curve in the post 1952 bomb carbon era (McKay et al., 1986). These ages very narrowly date Bed 2, which we interpret as most likely the result of the 1957 local earthquake (Figure 31).

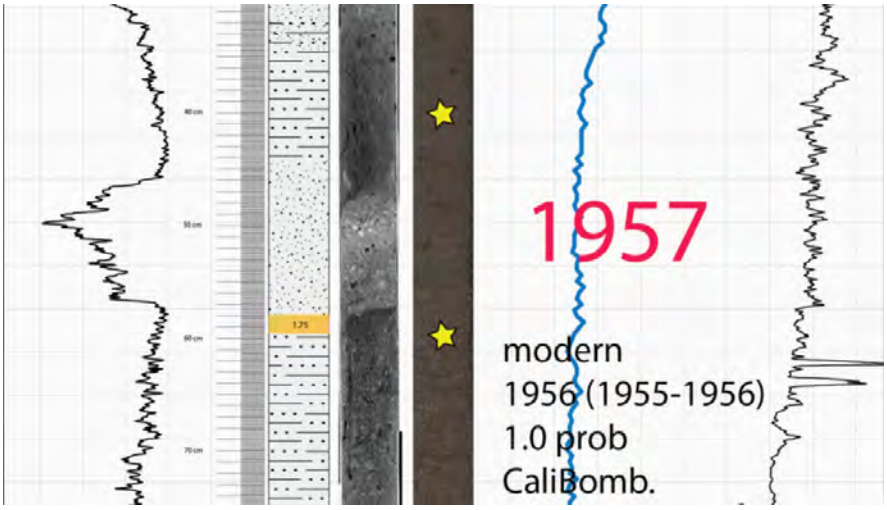

Figure 31. Close view of Bed 2 and radiocarbon sample locations above and below the bed.

Bed 1, the surficial bed, is dated using sedimentation rates from the two underlying 20th century beds. The interval thickness of interevent sediment between bet 3 and Bed 2 was obtained from the clearest examples, 1.75 and 2 cm. These two intervals were averaged and yield a sedimentation rate of 0.0376 cm/yr., assuming 1906 and 1957 as the ages of beds 3 and 2 respectively. The interval between Beds 1 and 2 is 1.1 cm, yielding an age of 1986 +/- 8 rms (1978-1994) AD assuming the sedimentation rate was similar to the earlier rate. While there is less certainly for this event, it is the only event above 1957, and there was only one significant earthquake in that time period. We therefore interpret Bed 1 as most likely associated with the 1989 Loma Prieta earthquake.

Age Model

We have created a preliminary OxCal P-Sequence age model encompassing the pre-1989 and post estuarine (~ 2200 cal BP) period (Ramsey 2009; Figure 32), that includes the 16 beds below 1989.

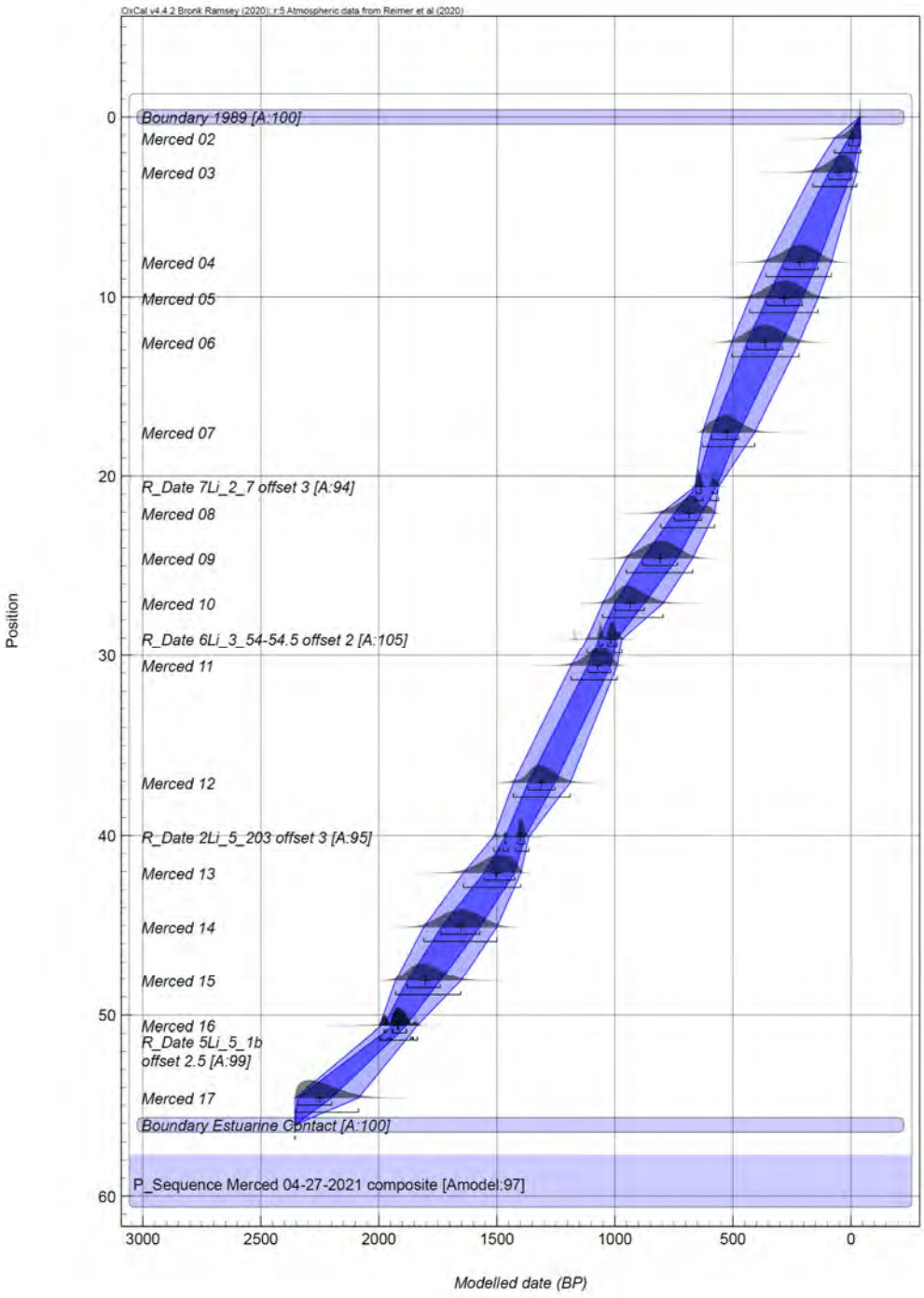

Figure 32. *OxCal P Sequence model. This is an event-free model developed from the interevent sediment composite, in which the ages of 17 events are modeled. The upper boundary is established at the well determined 1989 event, the lower boundary is located at the well-dated estuarine contact. Composite core section assembled from best preserved inter-event intervals (turbidites removed) across the core set. Radiocarbon ages selected from those shown in Figure 27 to eliminate several obvious age reversals. Interevent intervals interpreted visually from CT imagery in this model. OxCal model (AModel) fit is 97.3%, Aoverall is 97.1%. Model input and output data are given in Appendix 1 and 2.*

The OxCal Agreement Indices for the model were mostly 90-100% (minimum acceptable value is 60%) except the T10 and T12 beds. The low agreement for Bed 10 may be due to unobserved basal erosion, an undetected problem with one of the age, or could in part be related to a multiple peak issue in the calibration curve that statistically includes a broad time range. Bed 12 had a low agreement index of 88 which while statistically acceptable, indicates a problem perhaps similar to that for bed 10, though it cannot be attributed to a calibration curve region with multiple probability peaks. There are no reversals or significant kinks in the depositional curve implying a reasonably coherent model with low variability in sedimentation rate over the past ~2000 years. The overall model index is a reasonably good 97%, but impacted as a result of the poor agreement for beds 10 and 12 as discussed. OxCal model input is given in Appendix 1, and model output given in Appendix 2.

The 1906 Event and Lake Sedimentation

One of the most striking observations from our Lake Merced cores is that the presumed 1906 turbidite in Lake Merced is very thick and robust in all cores relative to all prior events of the previous ~ 2000 years. This bed is ~ 1 m in the cores and difficult to date directly as it has eroded materials at its base. Although it's possible also that this could be a sand bed related to the spit breaching of Lake Merced in 1852, we observe that the event bed does not coarsen or thicken toward the northern part of the lake (core 6Li) where the breach occurred, and does not contain any marine shells. It also does not overlap with 1852 at 2 sigma, though it does at the 3 sigma level. Thus we favor and interpretation of the 1906 earthquake as having triggered deposition of this event bed. This could have important implications for the long-term earthquake hazards in the area, but the meaning of the observation is not at all clear. One simple explanation could be that ground motions from 1906, at least on this part of the northern peninsula, were much greater in the 1906 event than other events in the past ~ 2000 years. However, the stratigraphy associated with the 1906 event is entangled with the development of San Francisco itself, and so anthropogenic effects could be considerable.

Little was known about sedimentation of the lake prior to our 2016 coring. Generally, it is assumed that turbidity and sediment flux into the lake has increased substantially since settlement of the area and development of the drainages to the east. This however has not been formally documented in any detail. One bit of data that does exist is from water quality studies of the lake, which include turbidity along with a suite of chemical analyses. Figure 33 shows a plot of turbidity from 1960 to 1999 showing the generally increasing turbidity trend. The drainage system is to the east in the Ingleside area is now urbanized, and the drainage bypasses Lake Merced, however older maps show it to be a well-developed system leading into the broad saddle along what is now Ocean Avenue, between San Bruno Mountain and the Mt. Davidson area.

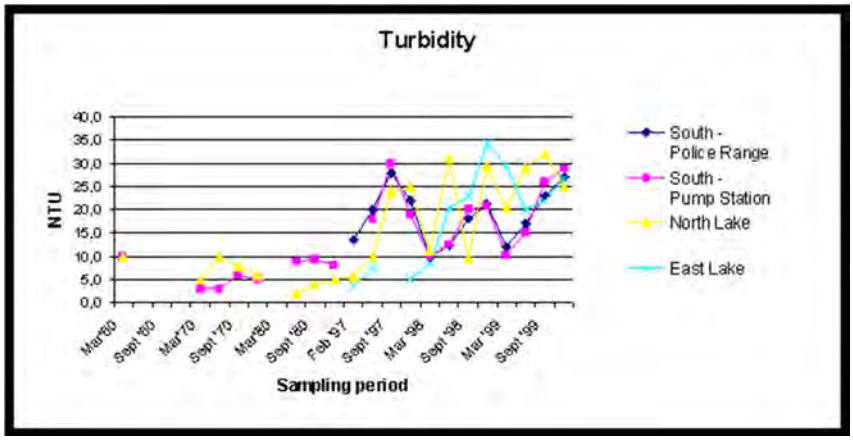

Figure 33. Turbidity at the surface in lake Merced, 1960-1999. Data reported in an informal report at http://online.sfsu.edu/bholzman/LakeMerced/water.htm

The question then is how much has development of the lake Merced watershed influenced the sedimentation and surficial materials available to fail under earthquake loadings? Determining which hypothesis explains the thick 1906 bed is not straightforward, particularly when the hypotheses are not mutually exclusive. One avenue is to look at the Pb isotopic signatures within the 1906 bed. Figure 28 shows the XRF signature of the tail of the 1906 bed, including Pb. The Pb date show a ramp up of Pb in the tail of the 1906 bed. The Pb data below 1906 are flat line at low value of ~ 0.0-0.001 ppm. That Pb increases in this bed is not surprising, given the construction of San Francisco in the half century prior to the great earthquake.

The historical narrative of the 1852 lake draining (rather than spit breaching) event shows that San Francisco did not extend to the west of San Bruno mountain at that time, so at issue is most likely the 54 years between 1852 and 1906. During that time at least one source of Pb would have been introduced into the watershed, that being from lead in paint. Lead based paint existed well before the turn of the century. Lead as an additive in paint was used to resist moisture, accelerate drying and increase durability and included lead(II) chromate (Pb Cr O_4, "chrome yellow"), Lead (II,IV) oxide, (Pb_3 O_4, "red lead"), and lead(II) carbonate (Pb C O_3, "white lead") as the most common forms. These additives have been used for centuries and were common in that time range, even though its recognition as a hazard also began about that time.

Another source of Pb is tetraethyl lead additive in gasoline. Tetraethyl lead abbreviated TEL, is an organolead compound with the formula $(CH_3CH_2)_4Pb$. TEL was discovered to be a useful antiknock additive and octane booster in automotive gasoline by the General Motors research lab in 1921 (Kitman, 2000). Manufacturing of TEL began in 1923, and introduction in production gasoline began in 1924 (Nriagu, 1990).

Considering these two sources of Pb introduced at different times, it may be possible to deconvolve the Pb spike in the tail of the 1906 bed to determine the timing of sedimentation. Was the tail deposited all at once, or was it deposited over decades of watershed input post-earthquake? Several primary observations are relevant to this question. First, the tail of the 1906 bed shows a very smoothly diminishing density and grain size. The tail is almost entirely without internal variations, bedding, lamellae or features of any kind, though it is somewhat bioturbated. This is notable as most turbidite beds in other settings show more variability than the 1906 bed in Lake Merced. This in itself argues against an extended watershed

response to 1906, as such a response would be expected to be modulated by storm events and minor landsliding, which should be represented in the structure of the post 1906 sediment accumulation.

Figure 34 shows an example of Pb isotopic ratios used to discriminate the approximate era in which the Pb additive was used.

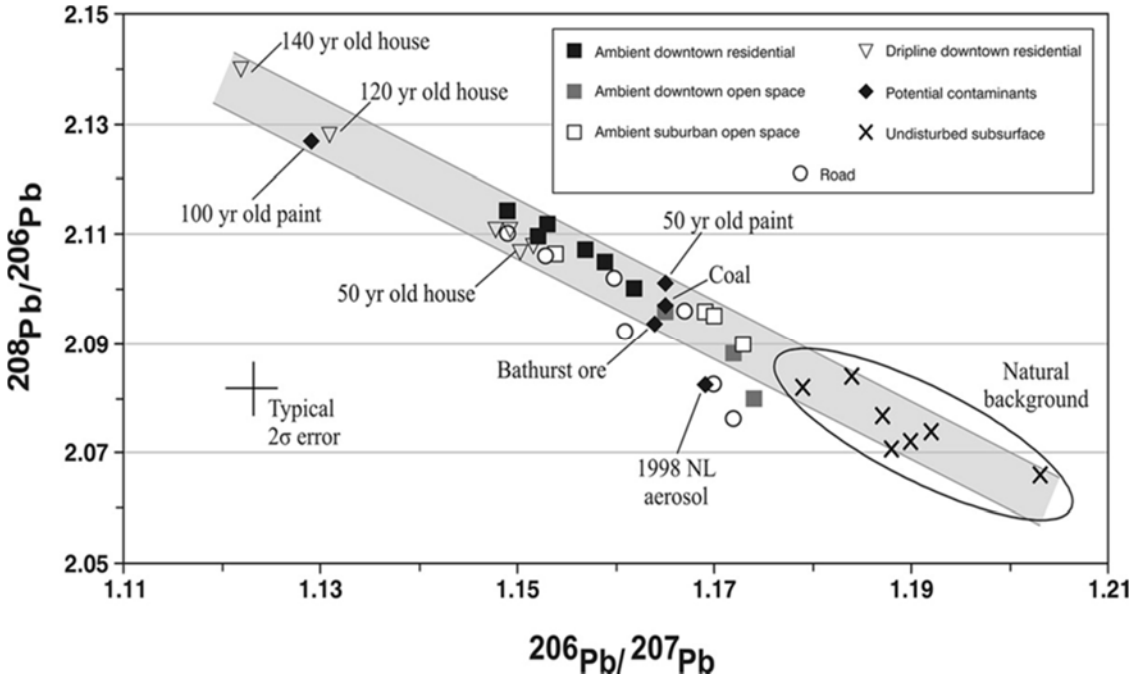

Figure 34. Lead isotopic discrimination of lead based paint by era. Isotopic ratios are capable of discriminating older paint from more recent samples, and may be capable of determining the approximate age of the paint additives (if present) in the probable 1906 event bed tail. From Bell et al., 2010.

Pb isotopes are also capable of discriminating TEL and the approximate age of the additive. Figure 35 shows an example of such discrimination typical of TEL (Ritson et al., 1999). From the introduction of TEL until it's banning from gasoline, isotopic rations varied according to ore sources used by the sole producer of TEL (Rabinowitz and Wetherill, 1972; Shirahata et al., 1980; Ritson et al., 1994. Gasolines and aerosols in the San Francisco Bay area from 1972 and later have lead isotopic compositions higher in $^{206}Pb/^{207}Pb$ (Rabinowitz and Wetherill, 1972; Hirao and Patterson, 1974) than those in the period from 1923-1972 (Chow and Johnstone, 1965; Chow and Earl, 1972; Rabinowitz and Wetherill, 1972. This is shown in Figure 32 which shows Pb isotopic values from cores in San Pablo Bay. This situation is a bit more complicated as Pb sources include hydraulic mining in the Sierra foothills. Nevertheless, pre and post 1972 gasoline aerosols are readily distinguished.

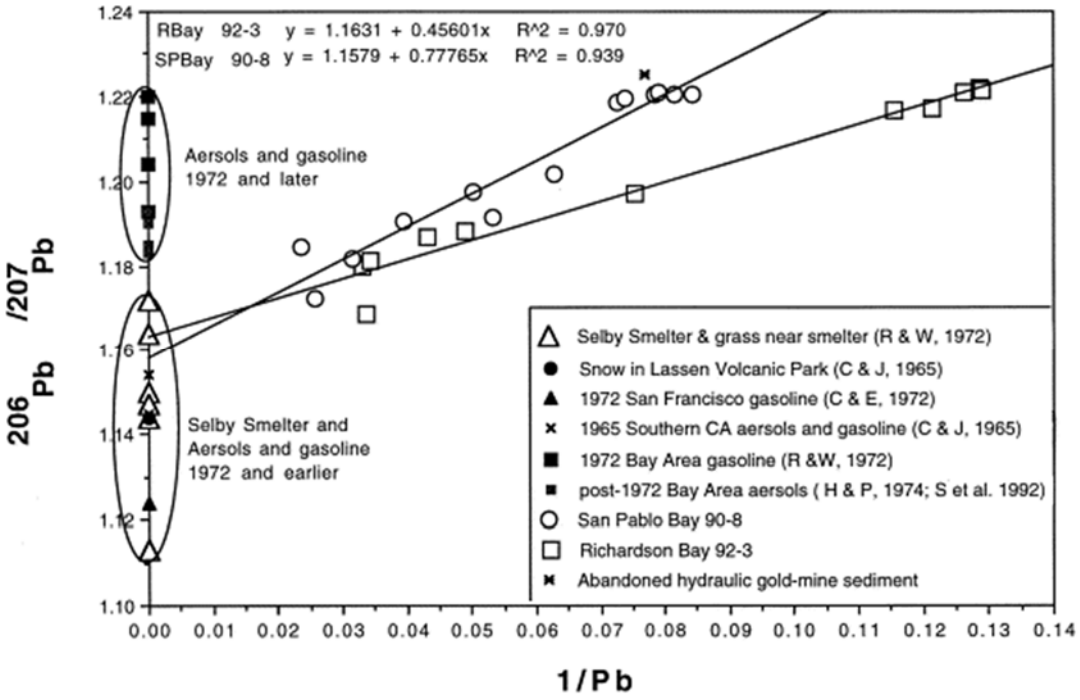

Figure 35. *A plot of lead isotopic composition ($^{206}Pb/^{207}Pb$) vs. concentration (1/Pb) for core sediments in RB92-3 and SP90-8. Mixing lines suggest a common end member contaminant for both Bays that is lower in $^{206}Pb/^{207}Pb$ than recent (post-1972) aerosols. C & J = Chow and Johnstone, 1965; C & E = Chow and Earl, 1972; R & W = Rabinowitz and Wetherill, 1972; H & P = Hirao and Patterson, 1974; and S et al. = Smith et al., 1992. Abandoned hydraulic gold mines = You Bet Pit and Malakoff Diggings. From Ritson et al., (1999).*

Figure 36 shows the sharp increase in the late 1800's-early 1900's attributable to multiple sources of Pb contamination in sediment in San Pablo and Richardson Bays. A confounding element of this problem could be the Pb contamination from the shooting range that was established in 1933 on the southwestern lake shore, however this is long enough after the 1906 earthquake that it may not play an important role. On the other hand, appearance of this Pb source in the long tail of the 1906 bed would confirm a long term hillslope effect was operative long after 1906.

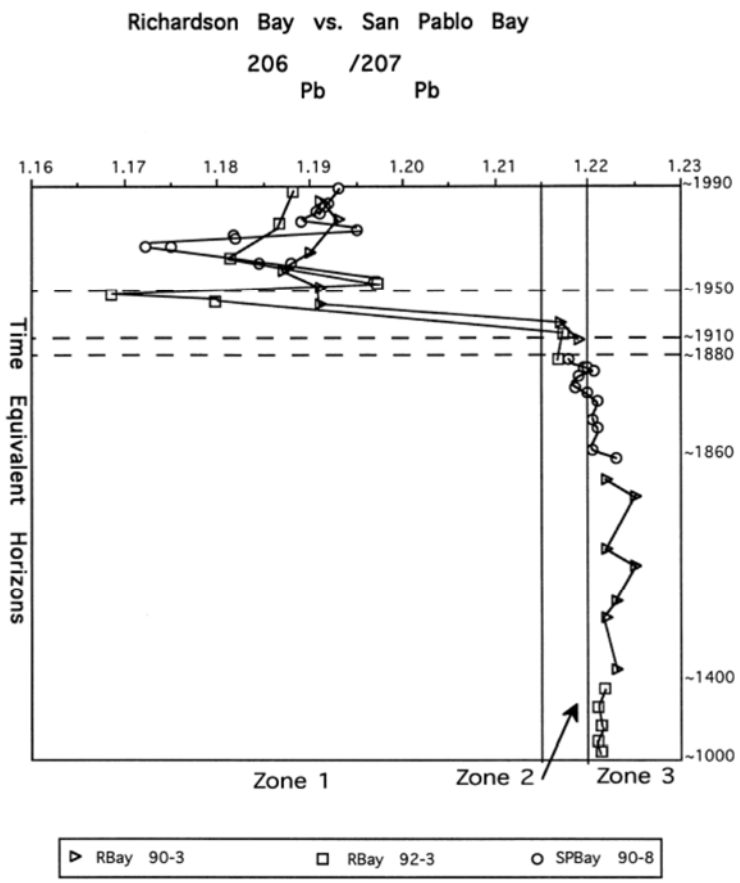

Figure 36. *A plot of the lead isotopic composition _206Pbr207Pb. of the San Pablo Bay core 90-8 and Richardson Bay cores 90-3 and 92-3 in time equivalent horizons. The zones are differentiated by isotopic composition and represent changing sources of lead. Zone 3 = natural background, Zone 2 = slight shift in Pb isotopic composition in late 1800s, Zone 1 = horizons highly contaminated with lead. The dates are interpreted in other papers on these cores. The dates shown are: ~1990, for the year cores were collected; ~1950, for the first appearance ^{137}Cs (Fuller et al., 1999); 1910 is from a mixing model for Richardson Bay core 92-3 based on a combination of radioisotopes Cs, ^{210}Pb, ^{234}Th, $^{239,240}Pu$ (Fuller et al., 1999); 1880 and 1862 are from a comparative bathymetry study in San Pablo Bay (Jaffe et al., 1998); and ~1400 and ~1000 are from ^{14}C dates on a mollusk shells (van Geen et al., 1999). From Ritson et al., 1999.*

In order to investigate the timing and composition of the historic era sediments, including the 1906 deposit, we collected 29 samples from cores 5Li and 6Li from the surface down to 150 cm, well below the 1906 deposit. We performed ICP-MS Pb isotopic analysis to extract isotopic ratios from the samples at the University of Washington Isotope Geochemistry Laboratory supervised by Dr. Bruce Nelson.

The Pb208/Pb206 ratios are typical of background, rising slightly toward the top of the core. The transition to late 20th century values is gradual, and the most recent values in the upper core are similar to those reported for urban spaces reported in Bell et al. (2010). They do not appear to be consistent with lead-based paint of any time period when comparing to the values of Bell et al. (2010; Figure 34 and Figure 35). The results of these analyses are shown in Figures 37 and 38. The results for these cores are similar, and support a similar isotopic pattern in the upper section of these cores. In both figures, we see a

Pb206/Pb207 ratio of ~ 1.17-1.19 in the upper ~ 50 cm of the cores, then a transition down to ~ 100 cm, and below that, and consistent value of ~ 1.21-1.22. The values mirror almost exactly the observations from cores in nearby San Pablo Bay of Ritson et al. (1999) shown in Figure 35. The background value corresponds to pre-1906 lake sediment. We cannot say exactly what decade this value corresponds to, nor what depth in the core, as we expect that some erosion of the lake bed likely occurred with deposition of the 1906 turbidite. Nevertheless, the background value is consistent with the pre-1910 value of Ritson. For the youngest section, ~ 50 cm and above, values are similar to the post 1950 observations of Ritson, based on the initial appearance of Cs137. They are also generally consistent with the 1972- and later isotopic ratios for gasoline in the Bay Area from shown in Figure 36 from Ritson et al. (1999), though the range for this value is not diagnostic. The timing implied by the isotopic ratios is also consistent with the age models and appearance of bomb carbon contamination and the likely 1957 turbidite at and above ~ 20 cm in the cores. The transitional values between these two zones reflect a detailed sampling of the period ~ 1906-1950, and are more puzzling. The rather smooth transition is similar to the XRF transition shown in Figure 28, and to the smooth waning of the dense turbidite tail shown in the XRF Pb trace in Figure 28. The structure of the turbidite is fairly smooth in the grain size and density in the upper part of the event bed, suggesting a single event bed with a fining upward waning turbidity current. The alternative would be a post-event watershed response that provided a high sedimentation rate for a number of decades post-1906. In that case, we might expect some storm related inputs that could be differentiated sub-events in the bed, which are not clearly observed. However the transition of isotopic ratio would appear to support this scenario as tetraethyl lead contamination increased with time and increasing automobile traffic. Pb also adsorbs preferentially to finer sediment grains, so the steady increase could also be driven by the fining upward structure of the 1906 bed. Perhaps definitive is the presence of bomb carbon and the 1956 calibomb age that appears to be in the "tail" of the 1906 event. This shows that the hillslope effect following 1906 extended over five decades. We prefer the latter interpretation, and the lack of more discrete event beds may be the result of the core location at the southern part of West Lake, farthest from the stream input.

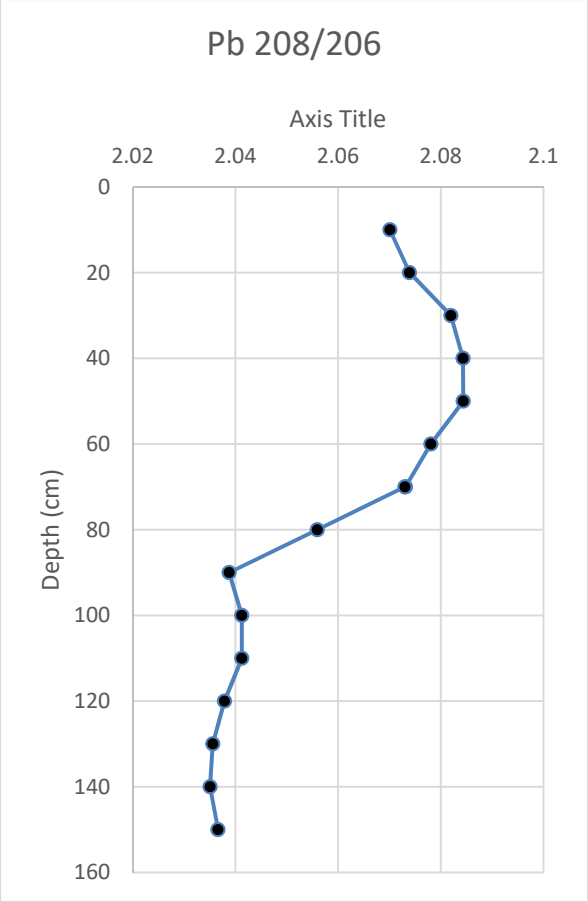

Figure 37. Pb 208/Pb206 isotopic ratio for core Li6.

The thick event bed this does not necessarily imply stronger ground motion from 1906 than previous events and most likely represents both pre-seismic sediment supply increases due to development of San Francisco and outlying areas, followed by a watershed response to the earthquake, perhaps enhanced by disposal of earthquake debris and further development. The isotopic ratios for lead shot from North American sources (e.g. Scheuhammer and Templeton, 1998) varies through the Pb206/Pb207 range observed at Lake Merced, and thus is not diagnostic in this instance. We are thus uncertain of the role in may have played in contamination of post 1933 sediment in the lake, but the Pb spike began at the base of the turbidite, suggesting Pb contamination from 1933 and later was not a factor initially, but could have contributed later during a watershed response.

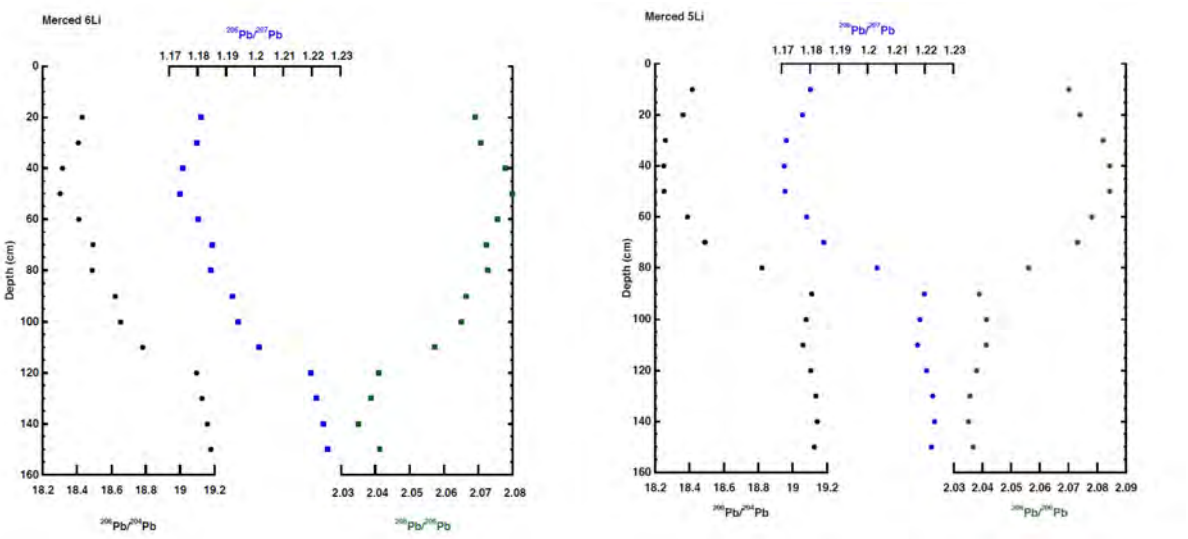

Figure 38. Pb isotopic ratios for the upper 1.5m of cores 5Li and 6 Li. Pb isotope compositions normalized to NIST-981 values of 208Pb/204Pb=36.7006, 207Pb/204Pb=15.4891, 206Pb/204Pb=16.9356 from Todt et al., 1996. Pb isotope external reproducibility at 2 sigma = ± 125, 150 and 200 ppm for 206/204, 207/204 and 208/204, respectively

Assessing the Northcoast NSAF Along-Strike Paleoseismic Record

NSAF Turbidite Record: Noyo to San Francisco

As part of this project, we re-examined the turbidite record along the North Coast segment of the NSAF between San Francisco and Noyo Canyon. Preliminary assessments of this record and were published in Goldfinger et al. (2006, 2008). At that time, they had significant difficulties in several respects. First, while correlation of the event beds based on log signatures was performed, and iterated many times, there was significant disagreement between the radiocarbon ages among samples that appeared to come from beds likely to be the same, as they were well-correlated between sites. Nonetheless, the results were published with the best fitting interpretation, accepting a certain level of noise in the age data. Second, there was an apparently significant drop off in the turbidite record in the late Holocene, with fewer beds, and those became quite thin or absent for times younger than about 3000 years. It was clear that the sediment supply was diminishing during this time, and the reason was not entirely clear. Third, the linkage between the very high-resolution record at Noyo Canyon, and the much less well resolved record to the south was weak due the extreme difference in sedimentation rates, and also possibly due to the unique inverted doublet pattern observed in many Noyo turbidites, which appeared to not be replicated further south. Together these difficulties resulted in a relatively poor linkage between the Noyo Canyon record and the San Francisco area.

In this project, we address these three issues to improve the core records south of Noyo, and examine the linkages (if any) between Noyo Canyon and sites to the south. We have acquired new CT imagery from many of the cores, and revised the correlation along strike to this end. In prior work, CT imaging was not available generally in the years 2002-2008, but became available after that time. Figure 39 shows that trackline and core locations for the NSAF core series. In Figure 40 we present the results of a

revised correlation of the North Coast segment, with the addition of CT data and revised radiocarbon ages. All of the ages have now been recalibrated using interpolated reservoir values along strike, the Marine 20 reservoir database, and sedimentation rates which are used to correct the ages for sample depth below the event bed (if any) and the sample interval used.

With the addition of CT data, some of the issues with the original radiocarbon data became apparent. Without CT data, sample for radiocarbon in fine-grained turbidite sequences is problematic, as contamination may not be apparent visually. In our Cascadia work, this was much less of a problem as the hemipelagic sediment was of a more contrasting color, and easily observed. This color difference fades southward, and is essentially not observed along the NSAF. The CT data reveal that many of the suspected problematic radiocarbon samples were recovered from areas in the core that were contaminated with fine grained reworked material from the event bed of interest, or other event beds. These ages are now greyed out in the compiled correlation figures. Unfortunately, this close examination revealed that many of the NSAF ages (excepting Noyo Canyon) were contaminated, explaining the high variability from site to site. While evaluating these ages and correlations, iterative attempts were made to find consistency with both ages and correlations tie points, and this resulted in elimination of more ages as reversed in comparison to clear nearby correlatives. Another major age reversal was revealed by the CT data to be due to double–penetration of the piston for in RR0207-13PC. This is a rare occurrence, but can occur while coring in large seas when the ship lifts the core upward when it is partially penetrating the seabed, and then drops it back into the seabed. The core disturbance and reversed age in this core are confirmed by a repetition of the section as observed in the physical property data.

The correlation made significant use of the CT imagery in a search for unique depositional features that could help to assess possible correlations or lack thereof. This process was much more difficult than the equivalent process for the Cascadia subduction zone as presented in Goldfinger et al. (2012, 2017). In Cascadia, the correlations were much more obvious, likely the result of much larger earthquakes, and very short epicentral distances between the rupture plane and failure zones. The maximum distance would be on the order of 15 km for the CSZ, but as much as 100 km for the NSAF, with its ~Mw 8 (or less) earthquakes, as opposed to Mw 8.8-9.2 for Cascadia. The CSZ also had a very low failure or reversal rate for radiocarbon ages, which we attribute mostly to the contrasting color of the hemipelagic sediment, non-existent along the NSAF. The contrast between these two fault systems illustrates the way in which the log correlation and radiocarbon ages are used. Neither one can be considered the “primary” dataset, with the other in a supporting role. Instead, the reliability of each must be considered as the analysis proceeds, and may shift spatially and temporally. Overall, the correlation is similar to the previous publications, but he ages of the event beds are now much more uncertain due to the contamination issue.

We closely examined the linkages of the North Coast cores to Noyo Canyon using several newer cores collected in 2009. The newer cores, TN0909-15 and 16JC were collected at the base of the slope adjacent to the original and newer cores in Noyo Channel. These cores are in close proximity to the Noyo cores, but are out of the channel and monitor the adjacent continental slope. Using the physical property data from these cores, we were able to establish a stronger linkage between the high-resolution Noyo cores and their associated radiocarbon chronology, and the lower resolution North Coast cores. The best of these cores in TN0909-16 JC/TC. By comparison to the full set of cores, this core captured the surface and has the most complete record. We correlate this core to our original Noyo cores, M9907-49PC, and RR0207-14JC. This linking core currently does not have age control, which is pending, however the correlations to both other Noyo cores, and to cores to the south is quite strong nonetheless. The surface was captured in this core, based on fresh, soupy oxidized material in the core tops. The lower part of the core clearly penetrated the same high frequency turbidite strata at the Holocene-Pleistocene transition as observed in M9907-49PC in Noyo Channel. The slope base cores clearly captured only the larger events, but the downcore pattern can be linked to the Noyo cores based on these larger events. In particular the NT9, NT 11 and NT19 large events link to the slope base cores and establish the continuity of the record in this

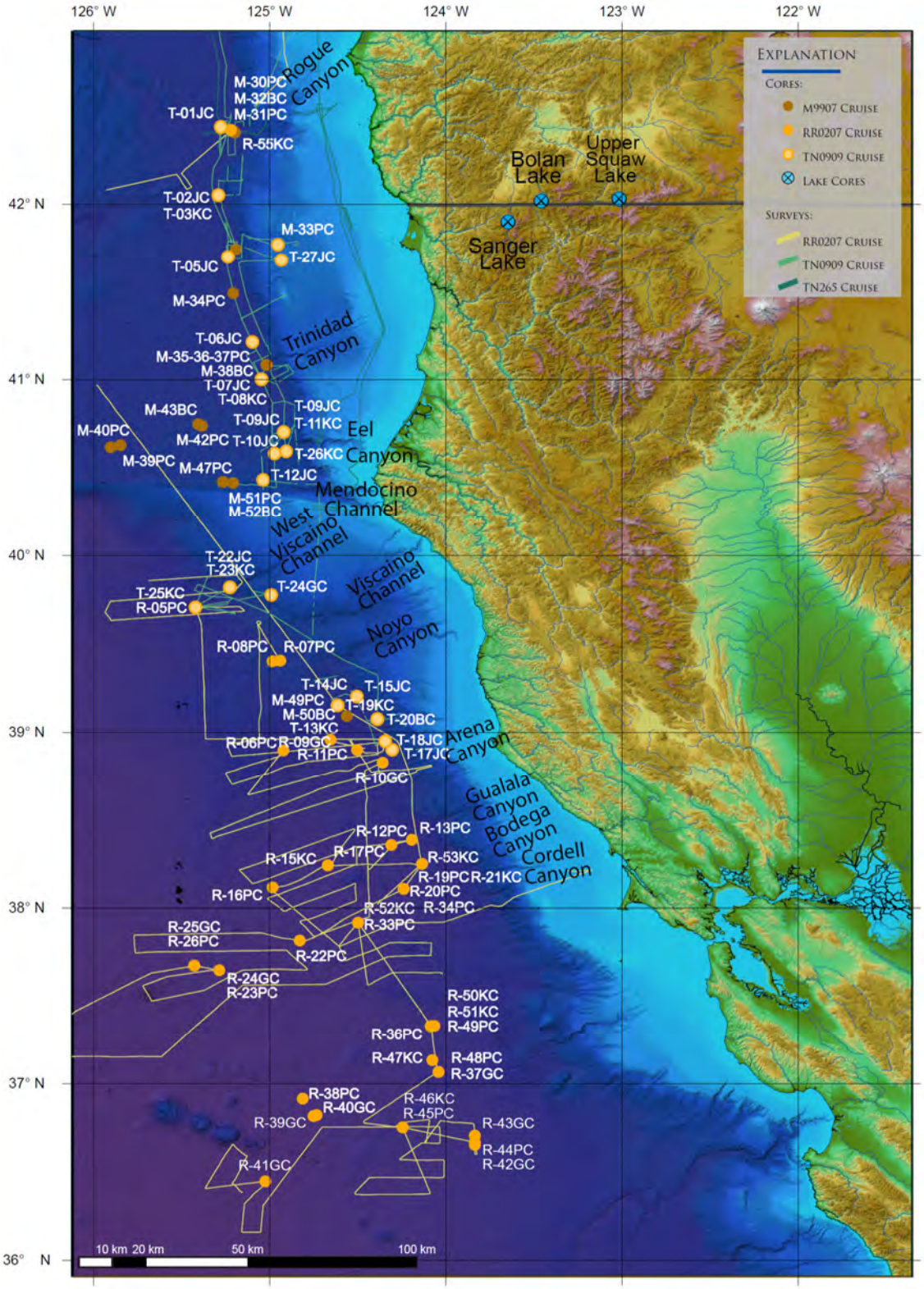

Figure 39. Site map showing M9907 (prefix M), RR0207 (prefix R), and TN0909 (prefix T) cores along the northern California margin in the Mendocino triple junction region. Chirp subbottom tracklines are shown in yellow and green by cruise.

area in the latest Holocene for the past ~ 2500 years or so, and with somewhat less reliably down to ~ 5100 years BP.

Having linked the slope base cores to Noyo Canyon, we found that linking these cores to the North Coast cores from further south at Gualala, Albion, Cordell, Pioneer and Farallon Canyons was then relatively straightforward with the aid of CT imagery, and flattening and correlation of pairs and groups of these cores. This is important because with this linkage, we can then use the chronology established at Noyo Canyon to examine the southward correlation of many key events between Noyo Canyon and the San Francisco area. The full correlation diagram is shown in Figure 40. The records are shown in colored swaths down to about ~ 5000 years BP, and more tentative linkages shown in thin lines below that. These primary linkages are described below.

1906 bed (NT 1). One might expect this bed to be prominent along the interval from Noyo Canyon to the San Francisco area at Pioneer Canyon, however that is not the case. The bed is prominent at Noyo Canyon, but quickly fades southward. We interpret a weak surface bed to be present at all core sites southward except Farallon Channel sites at which the uppermost stratigraphy is absent (Figure 40). We attribute the weakness of this bed to the declining late Holocene sediment supply, and southward increase in epicentral distance from the Canyons to the NSAF. However that may not fully explain the prominence of the first prominent Late Holocene bed, NT-6, at only ~ 820 BP.

Beds NT 3-4: These beds are form prominent inverted doublet at Noyo Canyon sites. This doublet is a prominent at Noyo Canyon, and can be correlated robustly along the full length of the Northcoast section. The doublet has an age indistinguishable from 1700 AD, the age of the uppermost Cascadia earthquake, and the penultimate northcoast event reported at land sites. The lower part of the doublet fades southward, as does the overall thickness of the bed.

Beds NT 5-5a: These beds are form prominent inverted doublet at Noyo Canyon sites. This doublet is a prominent at Noyo Canyon, and can be correlated the full length of the Northcoast section albeit as a faint bed to the south of the Noyo area. However, the correlation of these faint beds southward from Noyo is not robust and based mainly on stratigraphic position. The beds are indistinct and not unique in their faint character. The bed has an age of ~ 700 BP, identical to an uncorrelated Cascadia bed, T2g.

Bed NT 6. This bed is a typical Noyo Canyon bed; it is not particularly prominent at Noyo, but is present in all cores. The best age for this bed is 820 (690-940), with a second age ~ 100 years older; the younger age is preferred. This bed however is very prominent and easily correlated southward to Pioneer Canyon (Figure 40), being one of the best late Holocene beds linking Noyo Canyon along the Northcoast segment to the latitude of San Francisco. This bed does not have a doublet character, nor does it thin southward. The bed has an age indistinguishable from Cascadia T3.

Beds NT 7-7a: These beds form a doublet at Noyo Canyon sites. This doublet is a prominent at Noyo Canyon, is not inverted, and the lower unit can be correlated the full length of the Northcoast section, with the upper bed identified only within the Noyo area. The bed has an age of ~ 1200 BP, indistinguishable from well-correlated Cascadia bed, T4.

Bed NT 8. This bed is a typical Noyo Canyon bed; it is a not particularly prominent single bed at Noyo, but is present in all cores. This bed however is very prominent and easily correlated southward to Pioneer Canyon (Figure 40). This bed does not have a doublet character, nor does it thin southward. The bed has an age of ~ 1370 BP, indistinguishable from Cascadia T4a.

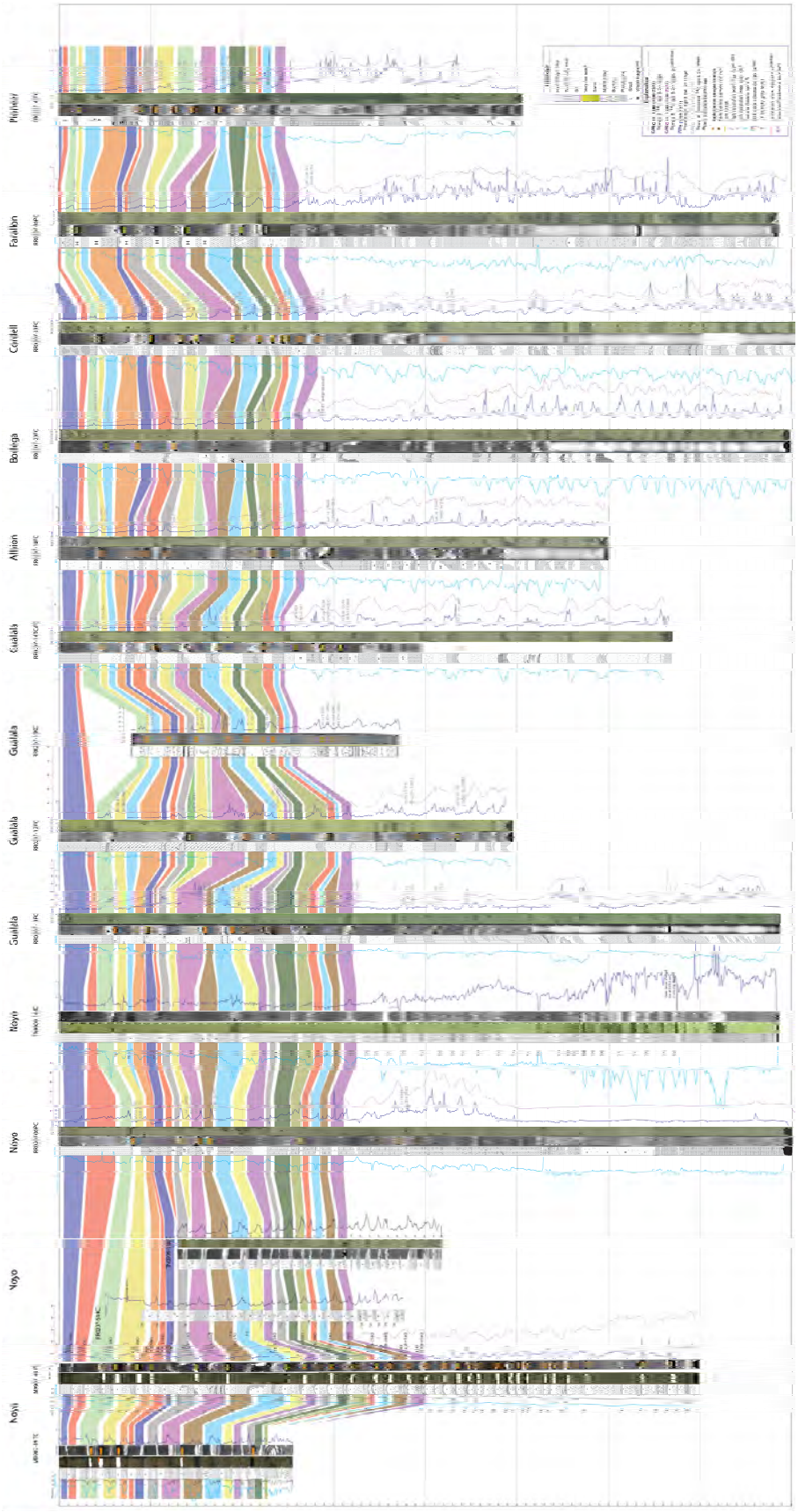

Figure 40 (previous page). *Correlation diagram for the Northcoast segment of the NSAF from Noyo Canyon to Pioneer Canyon. Core name prefix "M" = Melville 1999, Prefix RR = Roger Revelle, 2002, TT = Thompson, 2009. CT imagery, and analog X ray imagery shown where CT is not available. See Figure 39 for map location of cores and canyon/channel systems.*

Bed NT 9: This bed is a prominent inverted doublet at Noyo Canyon sites. This doublet is prominent at Noyo Canyon, and can be correlated robustly along the full length of the Northcoast section. The doublet has an age indistinguishable from 1580 BP, the age of Cascadia T5. The lower part of the doublet fades southward, as does the overall thickness of the bed.

Bed NT 10: This bed is a prominent inverted doublet at Noyo Canyon sites. This doublet loses that characteristic outside the Noyo area, and can be correlated intermittently along the length of the Northcoast section, apparently terminating between Farallon and Pioneer Canyons. The doublet has an age of ~ 1900 BP, ~100 years younger than the poorly constrained age of Cascadia T5b. The lower part of the doublet fades southward, as does the overall thickness of the bed.

Bed NT 11: This bed is a prominent inverted doublet at Noyo Canyon sites. This doublet is prominent at Noyo Canyon, and can be correlated robustly along the full length of the Northcoast section, losing its inverted doublet character south of Gualala Canyon. The doublet has an age indistinguishable from 2300 BP, the age of Cascadia T5c. The lower part of the doublet fades southward, as does the overall thickness of the bed.

Bed NT 12. This bed is a typical Noyo Canyon single bed; it is a not particularly prominent single bed at Noyo, but is present in all cores. This bed is intermittently and weakly correlated southward to Albion Canyon (Figure 40). This bed weak doublet character at Noyo only, and does thin southward. The bed has an age of ~ 2500 BP, indistinguishable from Cascadia T6.

Bed NT 13. This bed is a not particularly prominent single bed at Noyo, but is present in all cores. This bed becomes faint and is weakly correlated southward to Gualala Canyon (Figure 40). This bed does not have a doublet character, nor does it thin southward. The bed has an age of ~ 2730 BP, indistinguishable from Cascadia T6a.

Bed NT 14. This bed is a not particularly prominent single bed at Noyo, but is present in all cores. This bed becomes faint and is weakly correlated southward to Gualala Canyon (Figure 40). This bed does not have a doublet character, nor does it thin southward. The bed has an age of ~ 2860 BP, indistinguishable from Cascadia T6b.

Bed NT 15. This bed is a not particularly prominent single bed at Noyo, but is present in all cores. This bed becomes faint and is weakly correlated southward to Gualala Canyon (Figure 40). This bed does not have a doublet character, nor does it thin southward. The bed has an age of ~ 3130 BP, similar to Cascadia T7.

Beds NT 15a-16: These beds are form a doublet at Noyo Canyon sites. This doublet is a prominent at Noyo Canyon, is not inverted, and the upper unit, and likely both units can be correlated the full length of the Northcoast section. The bed has an age of ~ 3280 BP, ~100 years older than the poorly age-constrained Cascadia bed, T7a.

Bed NT 17: These beds form a doublet at Noyo Canyon sites. This doublet is a prominent at Noyo Canyon, is not inverted, at least the lower unit can be correlated intermittently the full length of the Northcoast section, with the upper bed identified only within the Noyo area. The bed has an age of ~ 3400 BP, indistinguishable from well-correlated Cascadia bed, T8.

Bed NT 18: This bed is a weak doublet bed at Noyo, and is present in all cores. This bed becomes faint and is weakly correlated southward to Gualala Canyon (Figure 40). This bed's weak doublet character

weakens and thins southward. The bed has an age of ~ 4560 BP, overlapping with two Cascadia ages, T9a and T9b.

Bed NT 19: This bed forms a doublet at Noyo Canyon sites. This doublet is not inverted, at least the lower unit can be correlated intermittently the full length of the Northcoast section. The bed has an age of ~ 5020 BP, indistinguishable from Cascadia bed, T10a.

NSAF Stratigraphic Summary

The results of the new correlation show that, as before, many event beds can be correlated over much or all of the 280 km between Noyo and Pioneer Canyons. Of the 19 correlated beds extending southward from Noyo Canyon, 11 of them are interpreted to correlate to Pioneer Canyon, with 1 just short. 4 beds are interpreted to extend between Noyo and Bodega Canyon. ~ 160 km, and 1 bed terminating at Gualala Canyon, a distance of ~ 130 km. Three beds correlate much of the full length, just dying out at Noyo Channel, and several other beds a limited to smaller sections of the middle part of the northcoast transect. The quality of the correlations is highly variable from very strong, to weak. Typically the thick doublet beds observed in Noyo Canyon tend to correlate robustly along much or all of the full transect length After re-assessment of the earlier radiocarbon ages south of Noyo Canyon, and linking the northcoast beds to the Noyo Canyon chronology, we find that there is not a sharp drop off in sedimentation rate as previously suggested by Goldfinger et al. (2008). While we do see a gradual falloff in sedimentation rate and grain size in the late Holocene, this transition is gradual, much like that observed in Cascadia (Goldfinger et al., 2017). We note that this trend may be reversed at some sites along the northcoast transect post ~ 1800 CE. The uppermost two events in this interval are diffuse and thicker than typical. These are the 1906 bed and the penultimate event dated in the age model (discussed below) at ~ 1820 CE along much of the northcoast section. Given the gradual decrease in sediment supply, we suggest this historical increase could be related to logging activities along the northcoast transect in the last two centuries.

Southern Cascadia Stratigraphic Sequence

As part of this project we wished to re-examine possible linkages between the Cascadia event time series and that of the NSAF as proposed by Goldfinger et al. (2008). This required extensive improvement of the stratigraphic record of southernmost Cascadia, similar to the re-analysis of the NSAF northcoast transect.

Goldfinger et al, (2012) presented initial stratigraphic correlations for southern Cascadia, extending southward from Rogue Canyon to the Eel Channel system. However, it was obvious that the region south of Trinidad Canyon and plunge pool included a much higher frequency turbidite record. The high frequency turbidite record was not addressed in that paper, and only preliminary connections between the largest events were presented. The earthquake model presented by Goldfinger et al. (2012) did not include the numerous events evident in the southernmost cores. Most of these events did not pass the criteria for being included as plate boundary earthquakes as they could not be correlated over the minimum 150 km distance using the abyssal core set as one of the criteria for inclusion in that record. Turbidite beds correlated over at least that distance were thought to be spatially extensive enough such that crustal earthquakes and slab earthquakes would be unlikely to generate synchronous beds across multiple canyon systems over distances that great. Other criteria used in Goldfinger et al. (2012) included correlation across multiple site types (canyon, fan, apron, isolated slope basins). Some of these site types included slope basins such as Hydrate Ridge (central Oregon) which had no possibility of terrestrial input from storms, river systems etc. Inclusion of this site (and subsequently several others, Goldfinger et al.,

2017) allowed testing of the record and key sites which could have included terrestrially derived beds from large storms. Using the isolated basin sites as comparators, it was clear that these sites, notably Rogue Canyon, had nearly identical event bed records, reducing sharply the possibility of storm sourced event stratigraphy during the Holocene. In southernmost Cascadia, south of Rogue Canyon, the ability to apply these criteria that worked well elsewhere in Cascadia, was reduced. There were no completely isolated slope basins that could be used, and additionally, the width of the continental shelf is narrower, increasing the possibility that storm events could deliver sediment to the deep abyssal plain.

With these difficulties in mind, Goldfinger et al. (2013), Morey et al. (2013), and Black (2014) attempted to address the recurrence of plate boundary earthquakes in southern Cascadia in various ways. Goldfinger et al. (2013) improved on the stratigraphic correlation between Rogue Canyon and Trinidad Canyon using the newer 2009 cores more fully than was possible in the then nearly completed 2012 paper. They used cores from three cruises, new CT scans, new radiocarbon ages and detailed correlations with well-log geophysical correlations to show that the stratigraphic record was relatively straightforward to correlate in that region. They also used Chirp subbottom profiles to show that the main series of Cascadia earthquake beds could be individually traced over that region (minimum strike length of 170 km). This demonstrated that there were no observed significant deviations from the stratigraphy best represented at Rogue Canyon. Goldfinger et al. (2013) also showed that the thinner beds that correlated over shorter distances mostly increased in thickness, density and grain size southward in keeping with the general southward increase in sediment supply. Termed "mud turbidites" based on their character at Rogue Canyon, many of these became silty and or sandy in some cases southward. Black (2014) built on the investigation of the southern Cascadia event beds by making more use of the Chirp sub-bottom profiles, generating synthetic seismograms which were used to test for bed correlations with core data, and supported the Rogue to Trinidad correlations of Goldfinger et al (2013). Other relevant observations along the N-S core transect in the filled trench showed that that the overall sedimentation rate, along with the grain size and density of the event beds all increased on the aprons and outboard of the canyon mouths. Also noted in these papers is the absence of Mazama ash in any core south of Rogue Canyon. The sedimentation rate dramatically increases in Trinidad plunge pool, the overall sedimentation rate being just over 200% greater that adjacent cores to the north (TN0909-06JC). These observations show several things. First, that while mostly relict, some material is being transported from the canyon heads to the abyssal plain, demonstrated by the presence of the Mazama ash. The ash distribution also demonstrates the lack of significant trench-parallel transport. The higher sedimentation rates adjacent to the canyon mouths show that canyon transport is important, even if they canyons are not significantly recharged during the Holocene, something also noted for Washington by Goldfinger et al. (2017). Hill et al. (2020), based on subbottom profiling and multibeam bathymetry, suggest that canyon transport is less important, but the abyssal and plunge pool core set indicate otherwise. We infer from the previous studies and this study, that both canyon and sheet flow transport under seismic loadings are likely operative.

Black (2014) also created a table of global observations of turbidity current distances and a figure to show the likely triggering range for both southern CSZ events, and the NSAF. Like earlier efforts, the difficulties in working south of the Trinidad Canyon area proved too difficult to overcome in Black (2014). Morey et al. (2013) made the surprising discovery that it was possible to correlate event stratigraphy between offshore cores and onshore lakes in southern Cascadia. Using the same well-log correlation methods used offshore, Morey et al. (2013) made preliminary correlations between offshore southern CSZ cores and Squaw Lakes, Bolan Lake, Sanger Lake and Triangle Lake. While preliminary, this work showed that the general size patterns observed offshore were replicated onshore, including many or all of the smaller events noted offshore for time periods for which there was temporal overlap. Subsequent work has more recently demonstrated that lake stratigraphy commonly records CSZ events and upper plate earthquakes in some cases (Goldfinger et al., 2014, 2016, 2020; Leithold et al., 2018, Morey, 2020).

Revised Southern Cascadia offshore Event Stratigraphy

Previous work avoided using cores from the Trinidad canyon and plunge pool area, and from the Eel Channel and its tributaries further to the south. This was primarily due to the high frequency record that clearly had numerous uncorrelated events. Given the multiple fault sources in the Gorda plate, the Blanco and Mendocino fault systems, the proximity of the NSAF, and the possibility of Eel River storm events in the record, the prospects for further advances in that region appeared limited. However, recent efforts to test this assumption have yielded some promising results outlined in this section. In Figure 41, we show an improved correlation of the Trinidad plunge pool site. This site is key to understanding southern CSZ event stratigraphy, and has a set of very high-resolution records well-recovered in the cores. The fact that Trinidad plunge pool captures much of the output of the canyon is largely responsible for the very high resolution records. This figure incorporates several cores not previous incorporated, mainly because their records are nearly identical, but are shown here for their value as sample replicates at this important site. The high frequency event bed record is clearly apparent at the Trinidad site, as are most of the main sequence CSZ beds, the majority of which are clearly thicker beds than the average. The combined radiocarbon and well-log correlation shown here is an improvement on the Trinidad site figure in Goldfinger et al. (2012). The Trinidad site also best captures the high-resolution record of several beds younger than the CE 1700 event, CSZ event T1. This figure also shows several interesting elements. Most obvious is the large number of additional beds located between CSZ T2 and T3. In most of Cascadia, there is nothing between these two event beds. In the region between Rogue and Trinidad, there are two small events, T2a and T2b, very faint beds that can be traced over most of that distance. In the Trinidad pool however, there are ~8-10 beds, 4 significant, in that interval. These beds are not generally observed outside the plunge pool, or in onshore or lacustrine paleoseismic records. We cannot attribute these beds to any source, and suspect they may be limited to the Trinidad canyon, and could be a spate of local earthquakes from any number of sources, or have some other origin. This sequence has a normal radiocarbon age progression during that time range, and from this we can rule out seiches within the pool. Much of the Trinidad section younger than about 2500 BP shows a more normal Cascadia sequence, with a modest number of additional beds. Below that age, the bed frequency increases dramatically, and becomes uninterpretable. This was discussed in Goldfinger et al. (2012), and is likely the result of the "turn on" of terrestrial sediment sources. This is apparent in all Cascadia cores, and is youngest in the southern Cascadia margin, reaching essentially a zero age at the Eel Channel system. Also notable are several beds above Cascadia T1. The figure shows five of them, two significant and three minor. These beds are replicated in all of plunge pool cores that captured the surface: two trigger cores and one box core (Figure 41) showing that these events are persistent at the Trinidad site. The third trigger core, M9907-35TC has a partial record above T1, and failed to capture the surface. The piston cores M9907-35PC, and 36PC are each missing parts of the uppermost section, as is common for piston cores, while M9907-37PC appears to have captured the surface. The young events are best represented in core M9907-36TC.

In Figure 42, we present an updated stratigraphic correlation for the southern CSZ. This figure is based on a more detailed version with many more cores given in Appendix 4. The improved correlation builds on Goldfinger et al. (2013) using additional CT data, additional cores not previously used, additional radiocarbon ages, and takes advantage of the synthetic seismogram work of Black (2014).
We note, as did Goldfinger et al. (2012) that the stratigraphy thickens southward due to the Eel River sediment supply, making the highest resolution records recoverable with 10cm piston cores about 3000 years in length, as opposed to the > 10,000 years recoverable elsewhere in the CSZ. This limits our ability to assess paleoseismic records older than Cascadia T6 or T7. Figure 43 shows a representative pair of these cores "flattened" on bed tops and bases to assist on visualizing the correlation. A flattened diagram showing the uppermost stratigraphy in this area is shown in Figure 44.

The correlation of beds along strike is fairly well supported by the spatial density of core sites and replicate cores. Nevertheless, there are notable uncertainties in the process of lithostratigraphic correlation, even when supported by radiocarbon ages. The primary difficulty in this region stems from the uneven sediment supply. The abyssal plain, which represents the position of the filled Cascadia "trench" is nearly flat, sloping southward a total of 28 m (3087-3115m) between Rogue and Klamath canyons over 110 km, a slope angle of 0.015 degrees. Given the flat bottom, little sediment transport in either direction would be expected once turbidity currents exited the lower slope and canyons. The slight right turning tendency from the Coriolis force (e.g. Wells, 2007) would oppose the very weak bottom slope. The lack of sediment transport along strike was demonstrated by Goldfinger et al. (2012) who found no evidence of the Mazama ash, delivered to the Rogue Apron in significant quantity by the T14 turbidity current, in any cores south of Rogue Apron (there are no nearby cores to the north with which to test northward transport). The sediment supply, as indicated by the thickness and grain size of event beds, is moderate near Rogue Canyon, low adjacent to Smith and Klamath Canyons, and rises sharply at Trinidad Canyon and southward to Eel Canyon and Channel. This evidence is generally compatible with modern river discharge of these systems, suggesting that while most of these systems are effectively relict during the Holocene (Eel and possibly Trinidad excepted, Goldfinger et al., 2017), the long-term sediment supply, which is tapped by earthquakes, retains a long-term linkage to the nearby river systems in that sediments delivered during the Pleistocene are still available on the slope and in canyons (Goldfinger et al., 2017). The Trinidad system is not linked directly to a river system, and is thought to receive some sediment from the Eel system via the north-flowing Davidson current in the winter months (Puig et al., 2003) much as some of the Washington canyons are supplied by the Columbia River (Nittrouer et al., 1981, Sternberg, 1986). Alternatively, recent mapping suggests little activity in upper Trinidad Canyon, and attributes turbidity current sourcing to failures in the lower slope and canyon (Hill et al., 2020).

Recent work in several settings has shown that while mapped submarine failures clearly are major contributors (e.g. Mountjoy et al., 2018) they are not the only sources, and may not be required as the source of typical seismically triggered turbidity currents, as thin failures of surficial material are all that is required to supply sufficient material (Moernaut et al., 2014, Okutsu et al., 2019). Indeed, mappable slide failures are insufficient in number and volume to supply the observed volume of material observed in seismoturbidites from Washington canyons (Goldfinger et al., 2017). Those authors also infer broad thin failures of surficial materials must occur, in addition to canyon loaded and wall failures, to account for the missing material volume. For purposes of submarine paleoseismology, Goldfinger et al. (2012; 2017) have shown that the consistency of the CSZ turbidite record across multiple site environments, both with and without sediment recharge, is a robust feature of the stratigraphy, and in fact is used directly as a test of seismic origin.

The thinner and finer grained beds found off the Smith and Klamath systems is reflected in another common way, increased bioturbation. As noted by Goldfinger et al. (2012; 2017), fine-grained turbidite tails are commonly heavily bioturbated due to their high organic content. In cases where the entire turbidite is fine grained, the entire bed is also bioturbated. The net effect is more obscuration of stratigraphic relationships and difficulty in intersite correlation. These effects can best be seen in Figure 44 and related figures in Goldfinger et al. (2013) which show the weaker, finer grained and bioturbated event beds adjacent to Smith and Klamath Canyons, and at an abyssal site with no adjacent canyon (TN0909-02PC).

Another important observation relates to Cascadia T1 and T2. Goldfinger (2012) observed that across seven cores at the Rogue Apron site, only one core reliably revealed the time separation between these two events. The rest of the cores showed these two events amalgamated, with the thin hemipelagic interval obscured. Similarly, we find the same sort of relationship in many of the southern CSZ cores. At the best sites, such as Trinidad plunge pool, these events are clearly separated by the high sedimentation rate and therefore high resolution cores. At other sites between Rogue and Trinidad, many of them do not

show this clear relationship, and in fact appear to be missing one of the two events. For example, the event originally labelled T2 in Goldfinger et al. (2012) was interpreted as such by the radiocarbon ages at

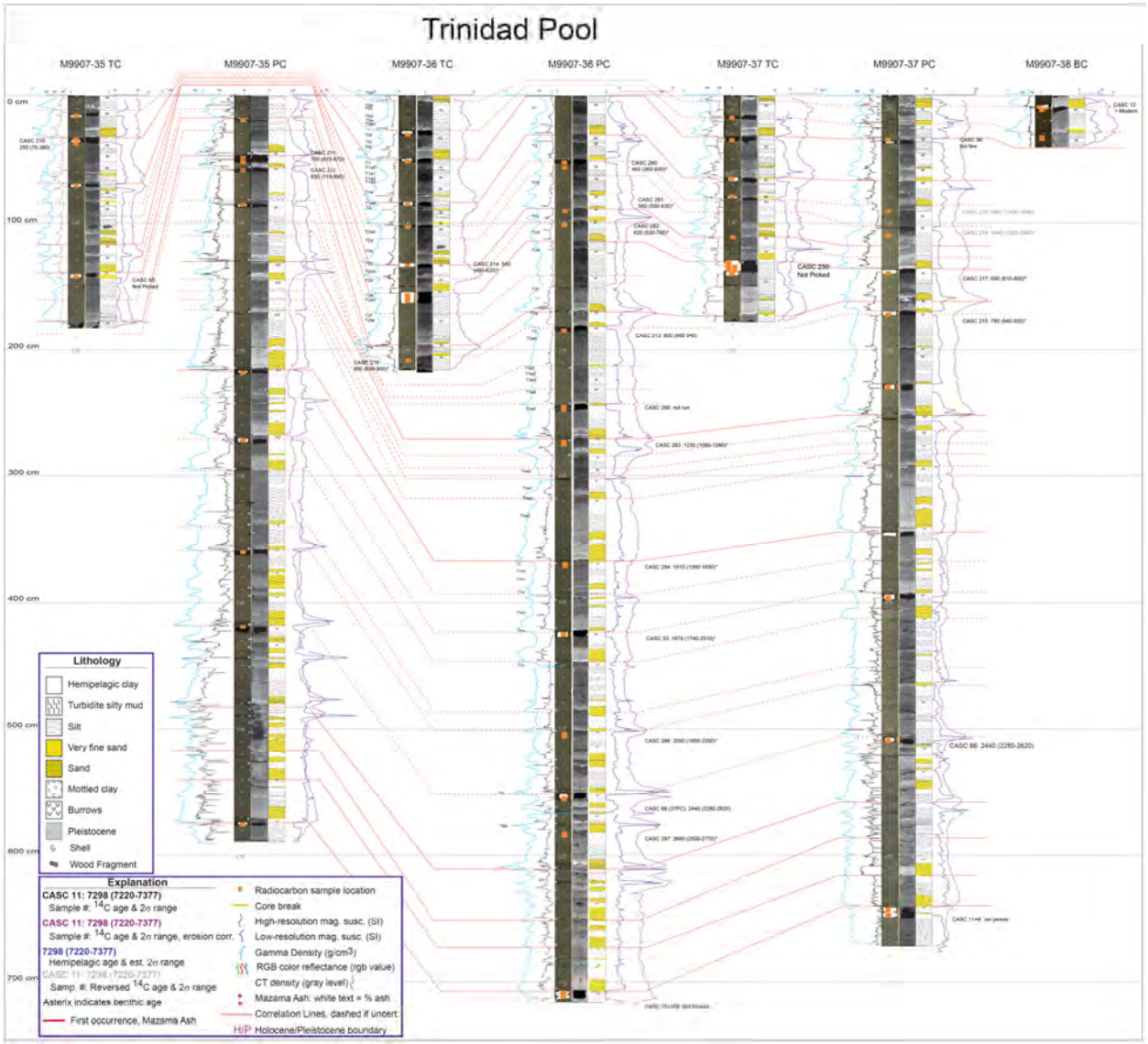

Figure 41. Correlation diagram for Trinidad plunge pool, modified with additional petrophysical and CT data after Goldfinger et al. (2012).

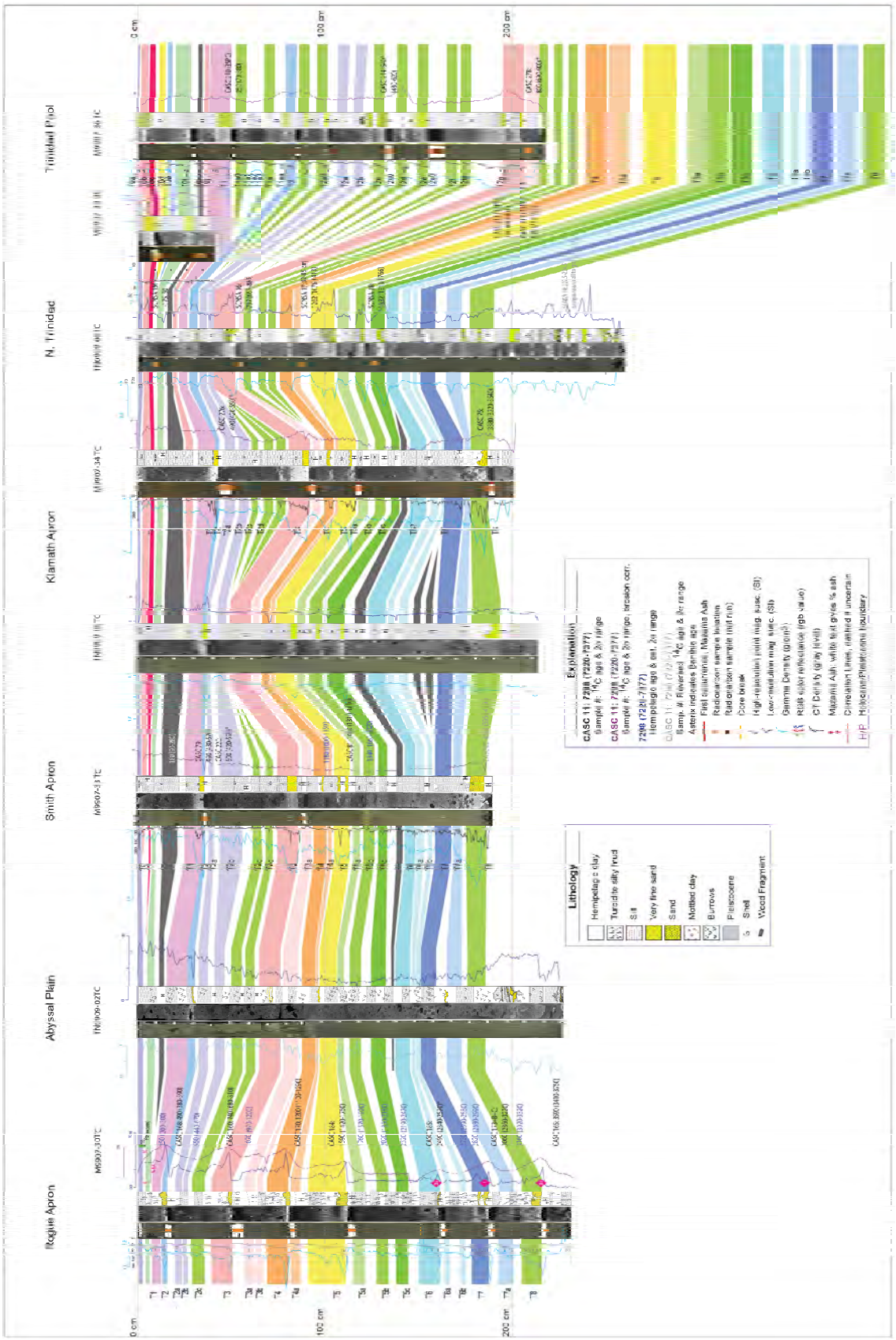
Rogue Apron
Abyssal Plain
Smith Apron
Klamath Apron
N. Trinidad
Trinidad Pivot
Lithology
Hemipelagic clay
Turbidite silty mud
Silt
Very fine sand
Sand
Mottled clay
Burrows
Pleistocene
Shell
Wood Fragment
Explanation
Hemipelagic age & sed. rate range
Turbidite age & sed. rate range
Asterix indicates Benthic age
First Occurrence, Malaspina Ash
Radiocarbon sample location
Radiocarbon sample (not rim)
Core break
High-resolution point mag. susc. (SI)
Low-resolution mag. susc. (SI)
Gamma Density (g/cm³)
RGB color reflectance (rgb value)
CT Density (gray level)
Malaspina Ash: white to tan gray % ash
Correlation Lines, dashed if uncertain
H/P Holocene/Pleistocene boundary

Figure 42 (previous page). Simplified and revised correlation diagram, Rogue Apron to Trinidad plunge pool for the late Holocene. See Appendix 4 for full diagram.

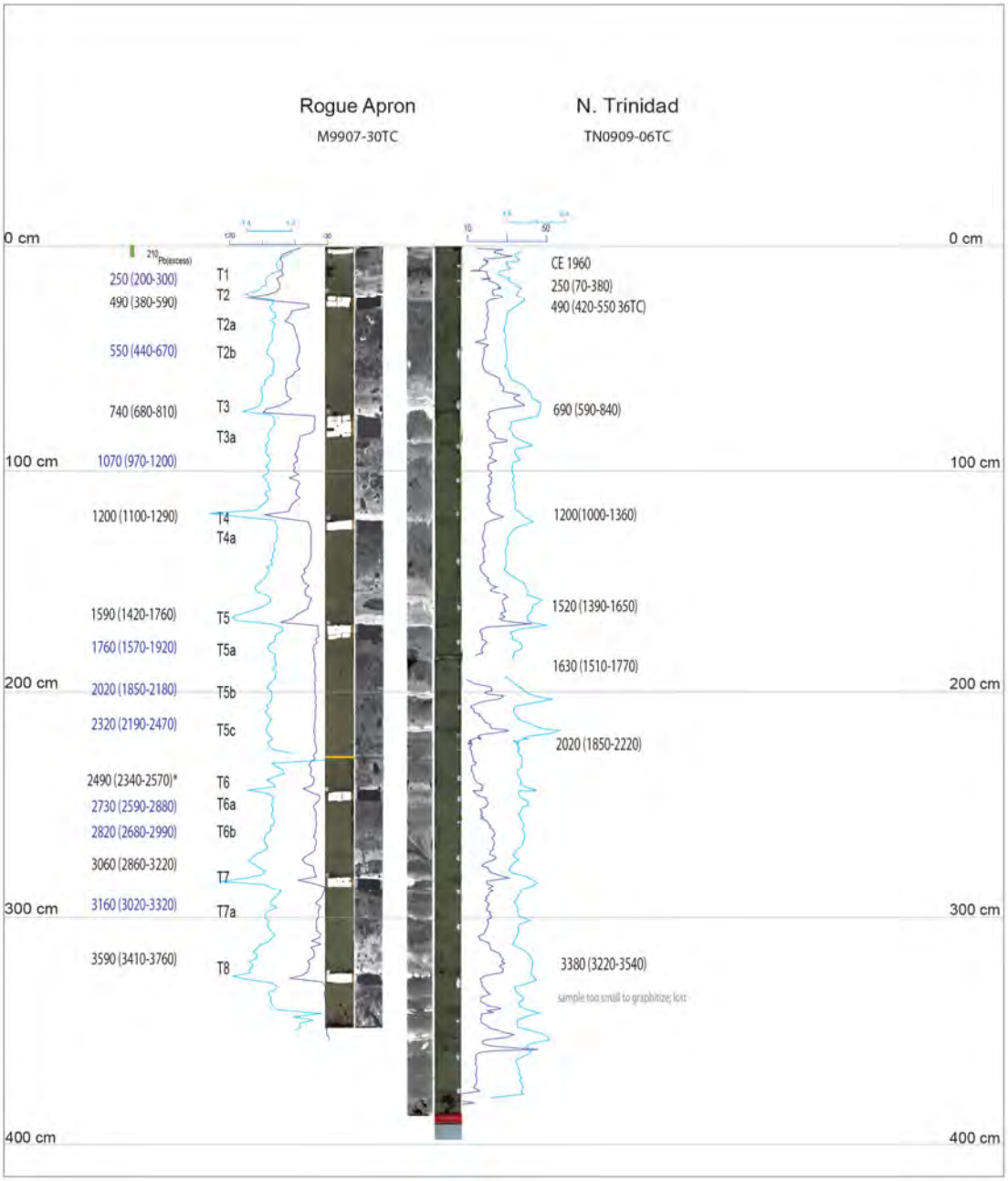

Figure 43. Flattened core diagram comparing Rogue apron core M9907-30TC to core TN0909-06TC, just north of the Trinidad plunge pool. The major event beds and their proposed correlations are apparent in this figure. Other southern CSZ event beds vary along strike, with most weakening northward in thickness, density and grain size. Compare the robust T5B and T5c in the right core (TN0909-06TC) to the weak diffuse correlatives at left (M9907-30TC).

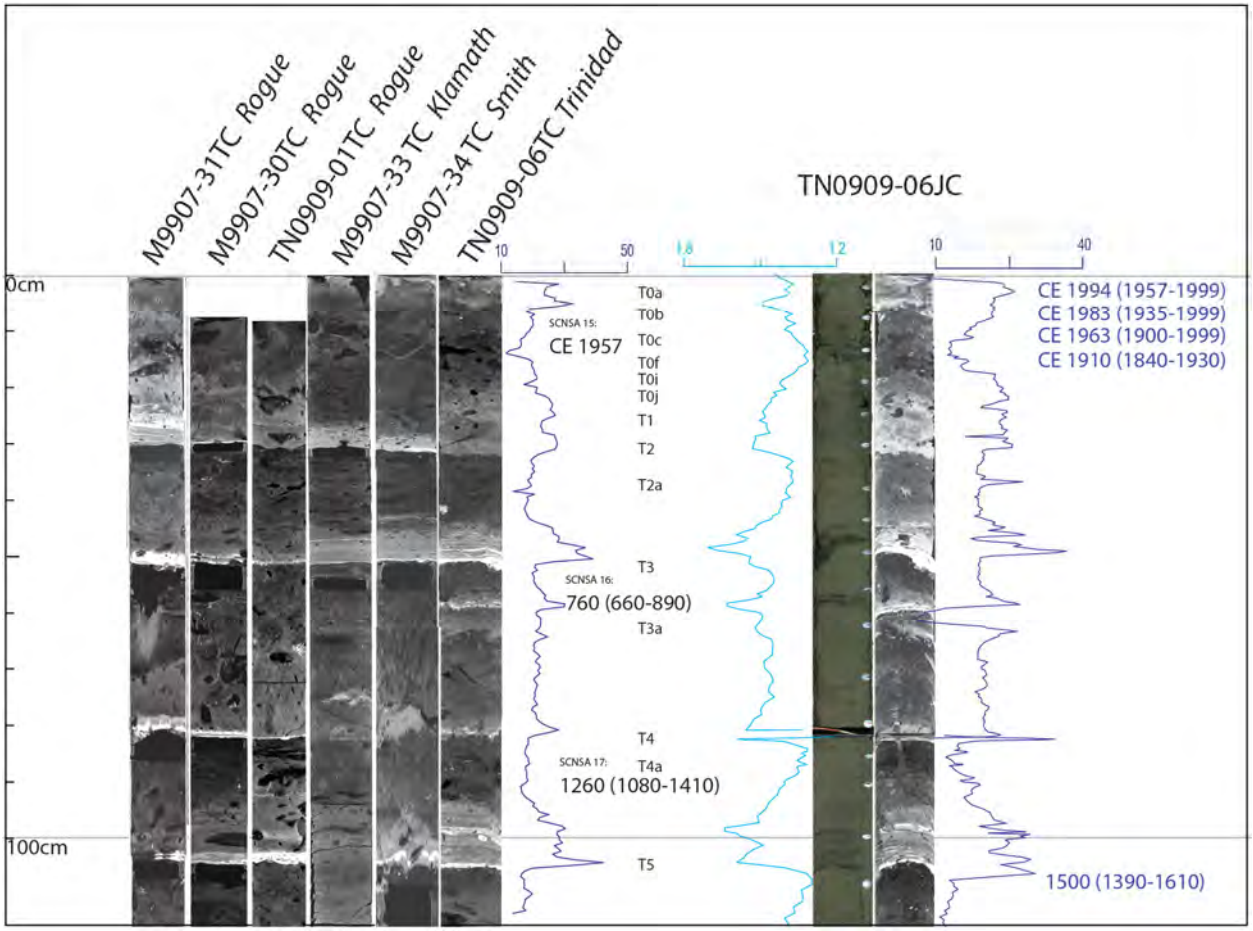

Figure 44. Plot of CT data for representative cores between Rogue and Trinidad Canyons, showing the upper meter of section, and extending downward to Cascadia regional event T5. At right, core TN0909-06JC is shown with magnetic susceptibility (right) and Gamma density (left), and model ages at right, and radiocarbon ages at left adjacent to trigger core TN0909-06TC, which is shown with magnetic susceptibility data. The upper age "CE 1957" is the bomb carbon determination, the others are shown with median and 2 sigma. At left, equivalent sections are shown for other cores as noted. These cores have been flattened to match event bed tops and bases to TN0909-06TC.

Klamath and Smith Canyons which were compatible with the mean age of T2 (~ 480 +/- 95) margin wide. However this meant that T1 would have to have been the very small event above that. The problem with that interpretation was that T1 is robust throughout Cascadia, both onshore and offshore, and observations in the southern CSZ of subsidence and tsunami deposits did not support a very weak CE 1700 event at those latitudes (Garrison-Laney et al., 2002, Kelsey et al., 2005, Valentine et al., 2012). In this report, we reinterpret the large event with the T2-like age, and the amalgamated T1 and T2, representing effectively one bed where much of T2 has been eroded, but the base remains T2 and has that age. This is consistent with Rogue Canyon observations, onshore paleoseismology, and newly developed age models for historic events discussed below.

Post CE 1700 Stratigraphy

The post CE 1700 core stratigraphy at Trinidad Canyon shows three significant and seven minor beds. The uppermost significant bed is effectively a surface sand, and little or no hemipelagic material is observed above it (Figure 44). In several cores, it appears that this uppermost bed is likely to be two

separate beds spaced closely, as in M9907-37TC (Figure 44), but this is not clear in all cores, partly because not all captured the surface. This observation includes cores M9907-36TC, M9907-38BC, and M9907-37PC, and M9907-37TC. The uppermost beds are consistent between the 1999 cores, and the 2009 cores just outside the plunge pool, suggesting no event beds were deposited in that decade at that latitude. These plunge pool cores were collected in 1999, and the lack of hemipelagic material observed, even in the box core with near perfect preservation of the seafloor, indicates that little time had elapsed since that event bed was deposited, prior to the date of collection in 1999 (Figure 44). The third bed from the top, one of the faint ones, returned a post-bomb radiocarbon age at two sites, indicating all three of the uppermost beds are post 1952 (Reimer et al., 2004, and references therein). Those ages were calibrated with Cali-Bomb (Queen's University Belfast http://calib.org/CALIBomb/ accessed 07/15/2020) and incorporated in the age models discussed below.

Historic Era Age Models

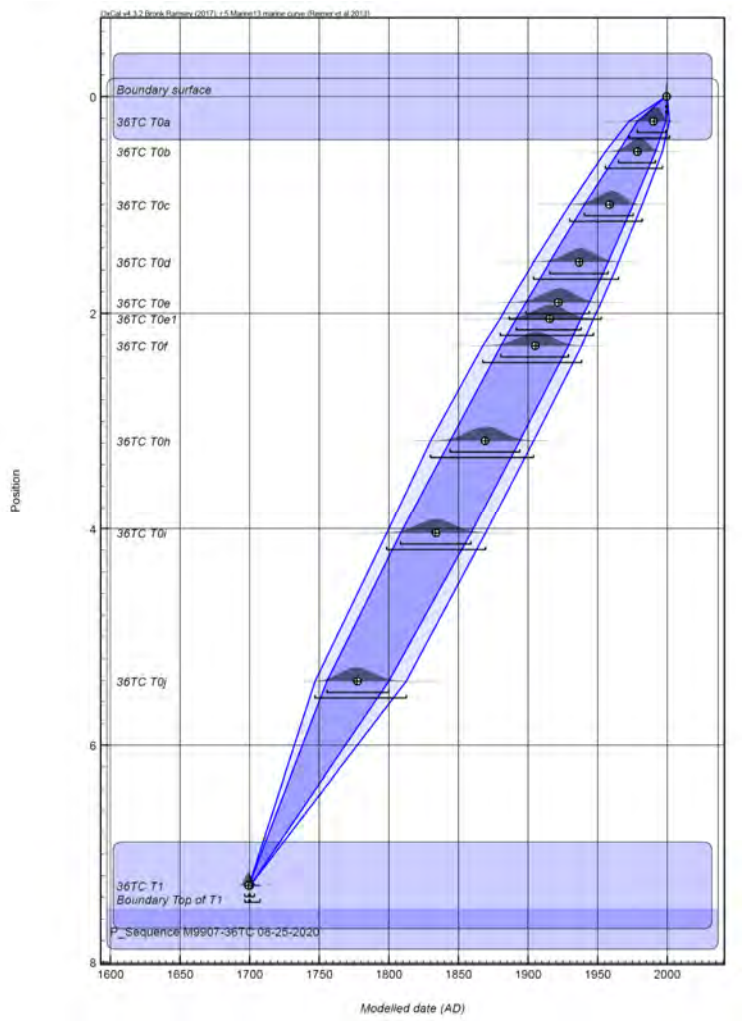

Figure 45. OxCal P-Sequence age model for post 1700 BP time in Trinidad Canyon, cores M9907-36TC and M9907-38BC. For this model, the well-correlated T1 event is fixed at 1700 CE to allow closer examination of the timing of historical events.

OxCal P-Sequence depositional age models anchored by bomb-carbon and AMS ^{14}C ages (Figure 45) were calculated for the section above 1700 CE. We calculated two models, one with the local radiocarbon age of the T1 bed, and one assuming that the T1 bed had an exact age of 1700 CE. The difference between these two models was negligible, the latter is shown in Figure 45. These models suggest the ages of the three beds younger than 1952 are ~1960 (1930-1980) ~1980 (1955-1996), and ~1990 (1972-1999). The upper two beds are significant, and can be traced 140 km and 155 km to the north respectively (Figure 42). The third bed, one of the more faint ones, can nevertheless also be correlated 155 km north to Rogue Apron (Figure 42). The next three beds down are faint and only one, the ~ 1920 bed can be correlated 120 km to the north at Smith Canyon. The next bed down is significant and is dated at ~1910 (1870-1940) and can be correlated 155 km to the north (Figure 42). The next bed down is dated at ~1870 (1830-1900). Two faint beds with ages of ~1780 (1750-1810) and ~1830 (1800-1870) lie just above the 1700 CE T1 event bed. Except for the two mentioned, the other five faint beds cannot be traced outside the Trinidad plunge pool reliably or at all. The post

1700 CE beds likely continue south of Trinidad plunge pool, and are tentatively correlated southward to the Eel system in the figures. For the purposes of determining spatial extent and age modeling, we consider the southward extent likely, but unreliable due to the much higher turbidite frequency, and difficulty in radiocarbon dating. While some ages exist, hemipelagic intervals, and thus datable material is sparse, reducing age control for the Eel system.

The post 1700 CE beds include five beds that can be correlated over multiple canyon systems for distances of 120-155 km, and five that cannot. The flat abyssal plain inhibits along strike sediment transport via turbidity currents, suggesting appearance of these events is likely due to independent delivery via the nearby Rogue, Smith, Klamath and Trinidad canyon systems. This is supported by several cores collected between canyon systems that show a much weaker, finer-grained turbidite stratigraphy (TN0909-02 JC/TC). The correlation across multiple systems excludes locally sourced events, including random failures and very small local earthquakes. At the same time however, correlation over ~ 150 km is not sufficient to exclude slab and large crustal earthquakes as very long correlations do in Goldfinger et al. (2012). It is also not long enough to exclude large storm events, though none of the canyon systems in question are favorable conduits for storm related deposition, with the exception of Eel Canyon as shown in the analysis by Goldfinger et al., (2012). The sites along the southern Cascadia margin also lack isolated basin sites from which terrestrially sourced turbidity currents could be excluded (Goldfinger et al., 2012; Patton et al. 2013). Given the weaker constraints available with which to discriminate event beds between earthquake types and storm related events, we rely more on the frequency and timing of events to interpret their most probable origins.

The upper two beds are significant, and correlate over 150 km. The uppermost bed has no detectable post event deposition the median age corresponds well with is most likely associated with the 1992 Petrolia Mw 7.2 earthquake, one of the four largest events of the 20th century. The second event similarly is a good match for the 1980 Mw 7.2 Eureka earthquake, which was very close to Trinidad Canyon. There were also Mw 6.9 and 7.0 earthquakes off southern Oregon and northern California, at ranges of 60-70 km respectively from the lower reaches of Rogue and Smith Canyons. While these smaller events might potentially trigger small turbidity currents, the trends observed for the upper events are not consistent with this hypothesis, as they steadily increase in thickness, density and grain size to the south toward the Eureka and Petrolia earthquakes (Figure 42). The third event is less significant, but nonetheless persistent over ~ 130 km. The third bed appears to terminate north of Smith Canyon near core TN0909-02PC, although thus is very uncertain as the sedimentation rate is low, and the bioturbation is extensive. There was an earthquake of Mw 6.2 only 17 km west of the plunge pool in 1959. There was also a large flooding event in 1964, and we cannot effectively discriminate between these two possibilities. The three faint beds below the ~1960 bed are dated at 1940 (1900-1970), 1920 (1890-1950), and 1920 (1880-1950). The ~ 1920 bed is more significant and can be correlated for ~ 120 km to the north. We suspect this bed may be related to the 1922 Mw7.3 Gorda plate earthquake located 41 km to the NNW of the plunge pool. The other two events could be linked to earthquakes in 1941, a Mw 6.8 event in the Gorda plate 48 km to the southwest, and a Mw 6.9 event on the Mendocino Ridge, 79 km to the southwest. Other smaller earthquakes at both greater and lesser ranges are also possible. The next event down, the 7th from the top is a significant event, traceable 155 km to the north among multiple systems. This event closely matches the age of the NSAF 1906 Mw 7.9 earthquake which is observed in multiple cores in nearby Noyo Canyon offshore northern California. The next event down is faint, and has a model age of 1870 (1830-1900), and could potentially be either the 1861-62 major storm, or the Mw ~ 6.8 1873 slab earthquake (Brocher, 2019). We are unable to discriminate these possibilities with present data, however this event strengthens toward the area of this earthquake adjacent to Smith Canyon, an area where all other event beds weaken due to lower sedimentation rates there, suggesting the earthquake is the more likely source, although it's expression is weak for the Mw estimated for this event (Brocher et al., 2019). The two faint beds with ages of ~1780 (1750-1810) and ~1830 (1800-1870) that lie above T1 at 1700 CE are not well

explained. The ~ 1830 event however could correspond to a possible Cascadia event at about that time (Carver and Plafker, 1999, Carver, 2000).

Implications of the Historical Event Stratigraphy

The historical event bed stratigraphy represents one of the first observed offshore record of known historical records in Cascadia. The only other is in Effingham Inlet (Enkin et al. 2013). This record offers several clear opportunities. Turbidite records of known earthquakes offer the possibility of improving estimates of Cascadia earthquake magnitudes of smaller sizes. Currently, the only ground truth is the 1700 CE event of Mw 9.0 based on a transoceanic tsunami record (Satake et al., 2003). The magnitude of this event could be lower as suggested by recent tsunami modeling by Melgar (2021). Estimates were made from rupture area and interevent time by Goldfinger et al. (2012) using the 1700 event as a control point. These estimates were very crude, and really intended only for comparison within the turbidite dataset rather than actual estimates of Mw. Rong et al. (2014) improved on these estimates using turbidite mass per event and developing a relationship to make this estimate. However, these very rough estimates may now be tested against the historical record. While beyond the scope of this report, we include a brief assessment here as this is an outcome of this work and bears on the issue of NSAF and Cascadia interaction.

From the historic era results, we construct an improved triggering range vs Mw plot for turbidity currents large enough to leave observable beds in multiple systems. Figure 46 shows a plot with the results of this project. These Cascadia results comprise four points: Mw=7.3: 120 km; Mw= 7.2: ~150-210 km; and Mw= 7.9: ~ 240 km. For comparison, Figure 47 shows a compilation of global observations of triggering distances, modified from Black (2014) with the addition of the Cascadia data from this project.

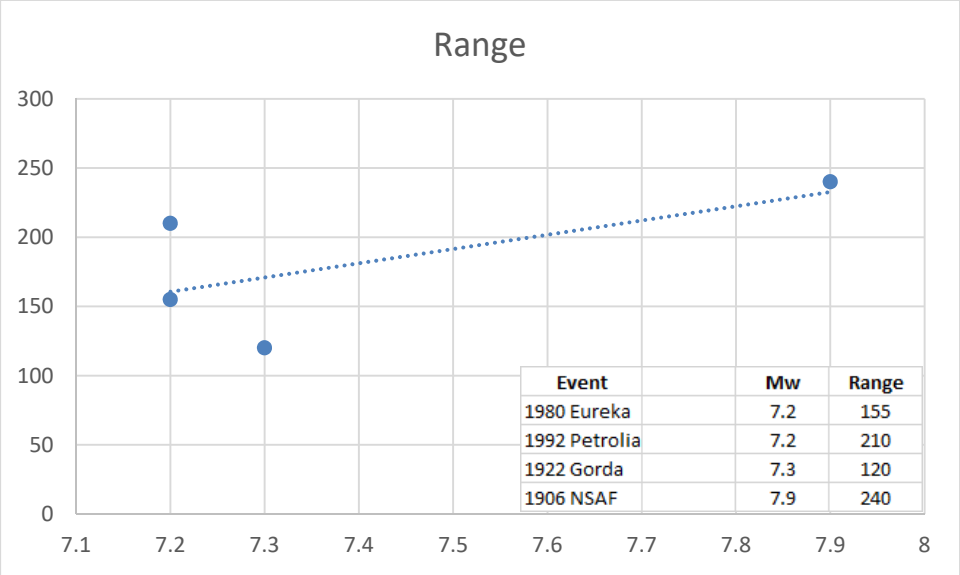

Figure 46. Triggering range vs. MW for four historic Cascadia and NSAF earthquakes in the 20th century.

These approximate (and minimum) values allow refined consideration of the smallest Southern Cascadia turbidites attributed to the plate boundary by Goldfinger et al. (2012, 2017). Previously, the criteria used for to discriminate plate boundary earthquakes was a minimum strike length correlation of ~ 150 km. Slab and crustal earthquakes were assumed not to be capable of generating correlated event bends over that distance, given the high attenuation of the accretionary wedge. However, the historical crustal and probable slab events just described are apparently correlated over this distance, thus the criteria used was too short for this setting, and some of the events attributed to the southernmost CSZ which met the previous criteria could in fact be sourced from crustal or slab earthquakes as well as plate boundary events. We also conclude that that previous rough magnitude estimates (Mw 7.5-8.4) for the smallest events that do not extend north of Rogue Canyon, and are not found in the tsunami record at Bradley Lake (Kelsey et al., 2005; Priest et al., 2014) may be overestimated. Some of these events are similar in extent, thickness, mass and grain size to the event beds associated with the probable 1906,

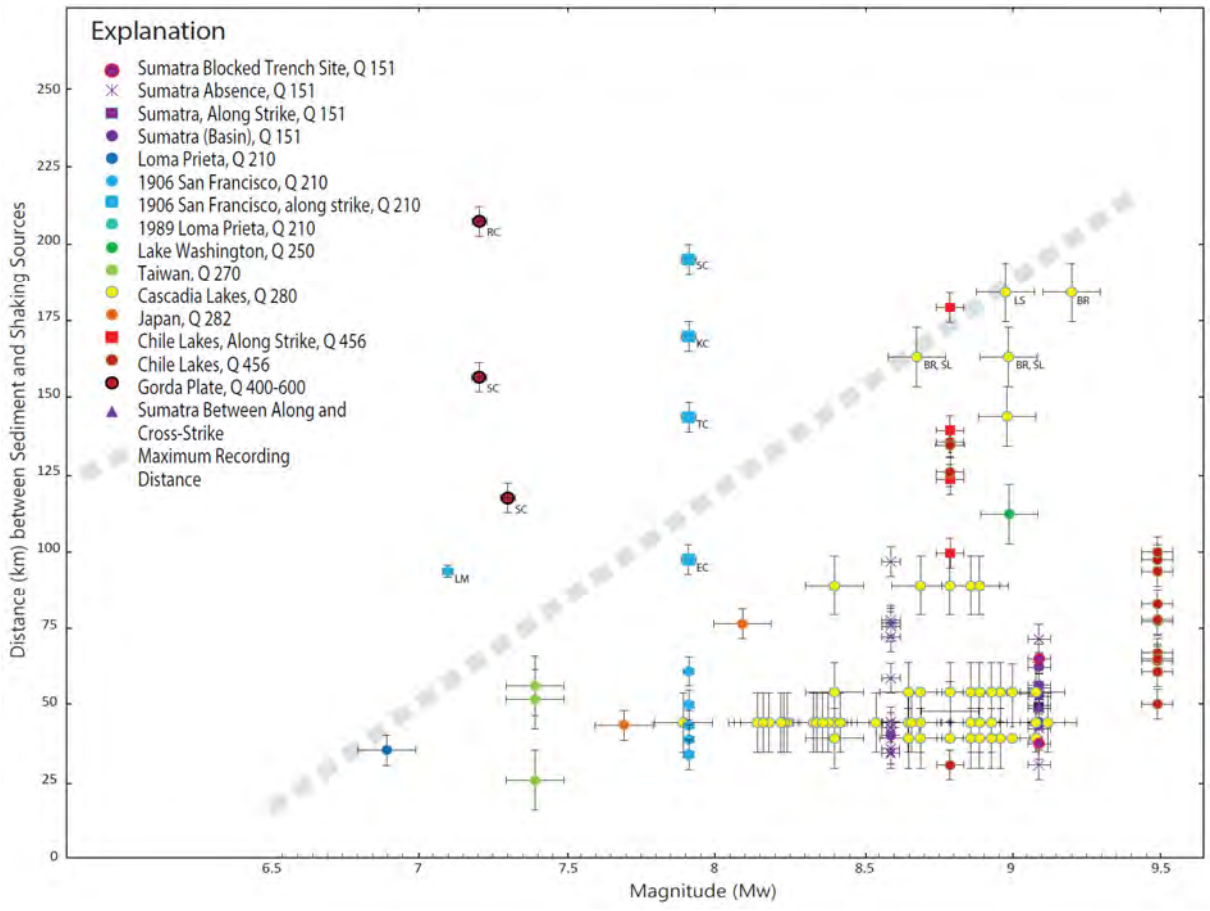

Figure 47. *Global observed triggering ranges for turbidity currents from source earthquakes vs. Mw. Marker colors denote both site locales and cool to warm colors indicate Q value increase, also indicated in the Explanation. Square markers denote along strike measurement; round markers denote across-strike measurement; triangles denote along and across-strike measurement. Dashed grey line represents maximum observed across-strike triggering range. Individual controlling maximum range sites are: LM = Lake Merced; EC = Eel Canyon, TC = Trinidad canyon; KC = Klamath Canyon; SC= Smith Canyon; RC = Rogue Canyon. Modified after Black (2014).*

1922, 1980 and 1992 (Mw 7.2-7.9) earthquakes. Interpreted CSZ beds that could be affected by this are T2a, T6a, T7a, T8b, T9b, T10d and T15a of Goldfinger et al. (2012), and several others added in Goldfinger et al. (2017): T6b, T12a, T14a, and T16a, several of which were downgraded to Segment D southern ruptures. Several more that were added in a new "Segment E": T2b, T2c, T9c, and T10e (Goldfinger et al., 2017). There are additional correlated and uncorrelated events that are un-attributed, these are shown in Figure 42. With the observed greater triggering ranges from multiple earthquake sources, at least some of these events are very likely not CSZ sourced, however they likely remain evidence of significant earthquakes.

NSAF events in Cascadia

The second opportunity, the one most relevant to this work, stems from the observation that at least one NSAF earthquake, 1906, appears in the Cascadia record, ~ 100 km north of the Mendocino Triple Junction. In previous work we considered this possibility unlikely, however this observation is robust in the age models, and the lack of other large historical earthquakes in the area at that time. One anomaly with the proposed 1906 bed is that it appears in Trinidad plunge pool as a doublet of two tightly spaced elements, while at the same time dying out rapidly northward, and yet not thickening southward toward the San Andreas. This seeming anomaly contradicts what would be expected from a San Andreas event, although it could be attributed to local earthquake effects and sediment supply. Perhaps a better explanation is that there was a possible triggered aftershock of the April 18 1906 earthquake on April 23, five days after the mainshock. This Mw 6.4 event was approximately located just north of Arcata CA, and could be responsible for the doublet bed in Trinidad plunge pool as well as the anomalous thickening of the event bed at only that site.

The apparent presence of NSAF triggered turbidites in southern Cascadia is an intriguing if unsurprising result that offers opportunities. First, if this happened once, it almost certainly happened numerous times in the past. Second, of the Trinidad Canyon and pool sites are in range for NSAF triggering, then Noyo Canyon, a similar distance south of the CSZ, would likely be in range for triggering Noyo Canyon turbidites from typically much larger Cascadia earthquakes. We first construct detailed age models deeper in the section for Cascadia, and for the NSAF record at Noyo Canyon and finally compare the stratigraphic sequences.

Southern Cascadia and NSAF Age Models

Noyo Canyon Age Model

We developed an age model for Noyo Canyon using cores M9907-49PC and TC, TN0909-14JC and TC, and box core M9907-50BC, and Kasten core RR0207-54KC. These cores allowed a detailed site correlation for the upper Noyo Channel site, with all cores located within a few hundred meters of each other at most. The Noyo Channel site correlation diagram is shown in Figure 48. Having a large number of cores to use to characterize a single site helps to overcome local variability and coring artifacts to arrive at a composite stratigraphy that represents the site as closely as possible. Even so, the local variability was significant, most likely due to the proximal position of the Noyo cores in the upper part of the abyssal channel system. Some of this variability is apparent in Figure 48. Coring artifacts are observed at NSAF events T7, T8, and T10 in M9907-49PC. All three of these are suction artifacts from the piston coring process. But all three are also recovered in the other cores without artifacts, pointing out the importance of multiple cores at a given site. Also observed is a difference between the two piston cores, M9907-49PC, and TN0909-14JC. These two pairs of cores were taken 10 years apart, and in the intervening time, the mechanical couplers between core barrels were revised, adding external couplers for the latter core. The external couplers (as opposed to smooth barrel joints in 1999) resulted in more barrel drag on penetration of the sediments, and thus a more compressed section as can be seen in Figure 48.

Another result of this equipment change is that significant compression of TN0909 core relative to the M9907 cores is common. For this reason, we chose to create an age model based only on the M9907-49PC/TC cores.

We primarily relied on the stratigraphic data from M9907-49TC as it has limited suction deformation, and was less compressed that the 2009 cores. The upper part of the model, above event NT3-4, came from M9907-50 BC, which had a number of pristeen subsamples collected. The ages come mainly from M9907-49PC, 1 meter away. The tabular input and results of the OxCal model are given in Appendices 5 and 6 respectively. We describe here some of the results of the model and their implications. The Noyo age model shows some key tie points. The model age for T1, the third event down is 1880-1950, with a mean of 1920. This age compares favorably to the 1906 NSAF earthquake, as previously described in Goldfinger et al. (2006, 2008). This is not the uppermost event in these cores however, the compilation of Figure 48 shows that that there are two more faint events above the probable 1906 event, T0 and T0a. The upper event, T0, had a range of 1975-2003, trimmed by the date of collection to 1975-1999. The mean is 1990 (rounded to 5 years). We suspect that this event may be the 1992 Petrolia Mw 7.2 event, the largest event in that time period. The second faint event has a mean and median of 1960, and could be

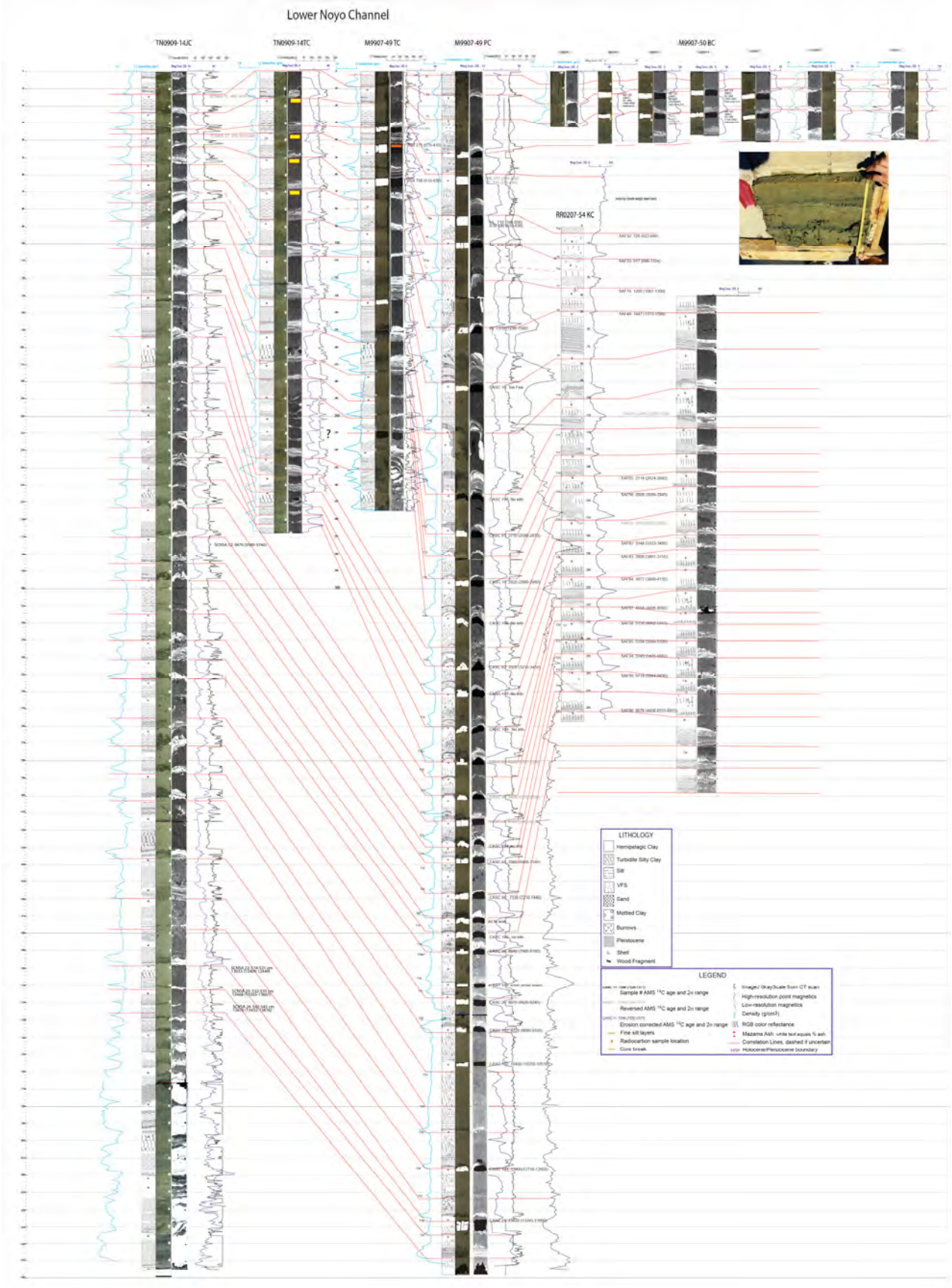
Lower Noyo Channel
TN0909-14JC
TN0909-14TC
M9907-49 TC
M9907-49 PC
M9907-50 BC
RR0207-54 KC
LITHOLOGY
Hemipelagic Clay
Turbidite Silty Clay
Silt
VFS
Sand
Mottled Clay
Burrows
Pleistocene
Shell
Wood Fragment
LEGEND
Sample # AMS 14C age and 2σ range
Reversed AMS 14C age and 2σ range
Erosion corrected AMS 14C age and 2σ range
Fine silt layers
Radiocarbon sample location
Core break
Imaged Gray Scale from CT scan
High-resolution point magnetics
Low-resolution magnetics
Density (g/cm3)
RGB color reflectance
Mazama Ash: white text equals % ash
Correlation Lines, dashed if uncertain
Holocene/Pleistocene boundary

Figure 48 (previous page). Correlation diagram for Noyo Channel cores, northern NSAF.

related to the 1964 floods. The mode for this age is younger, ~ 1970-1975, and we consider it equally likely that this bed is a result of the 1980 Mw 7.2 earthquake, although it is at a range of 165 km to the head of Noyo Canyon. Below the probable robust 1906 bed (Figure 49), another faint bed T1a is found to have a mean age of 1865, and median of 1870. This faint event could be the result of the 1861-1862 ARC flood event. One additional robust bed, NT2, is found between the 1906 and CE 1700 beds, with a model age of ~1810 (1720-1890). This is a robust bed similar to others in the NSAF turbidite stratigraphy and attributed to NSAF earthquakes. This event however has no NSAF earthquake known or observed at lake or onshore paleoseismic sites. A weak event is also observed at about this time on the Cascadia side in Trinidad Canyon. Nothing further is known about this event, which could have a number of origins. One additional faint event, NT2a, with an age of ~ 1740 (1640-1830) overlies the ~1700 CE doublet bed.

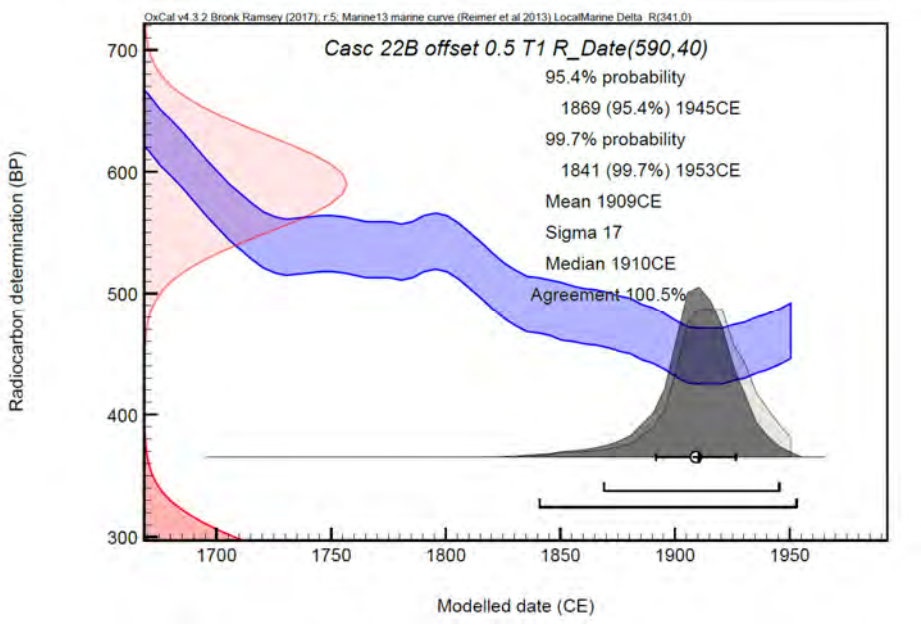

Figure 49. Single plot from the Noyo P-sequence age model. The event, locally called T1, is the likely event bed from the NSAF 1906 earthquake. The 99.7% probability range extends slightly outside the 1950 limit for non-bomb carbon ^{14}C dating, and is noted as "out of range" in the table output, but nevertheless yielded a valid age for this event.

The doublet event at about ~1700 CE is separated in time from events above and below. Figure 51 shows the PDF's of the event and its overlying and underlying neighbors. We show both the P-sequence ages and the analytical ages for T3-4, and T5, which were dated directly. In many cases the direct analytical ages are more accurate when available due to the uncertainties inherent in the P-sequence models where erosion and bioturbation are factors that can rarely be quantified. For the ~ 1700 CE event we prefer the modal age as shown in Figure 48 based on dating similar events on the Cascadia side, where the modal age of this particular event could be independently verified against the AD 1700 Cascadia earthquake. Figure 51 show the relatively minor radiocarbon overlap, and none at all for the overlying and underlying beds respectively. A wispy minor bed, T02a, overlies the ~ 1700 CE event, but is considered an unlikely candidate for confusion with the major plate boundary earthquakes that took place around that time.

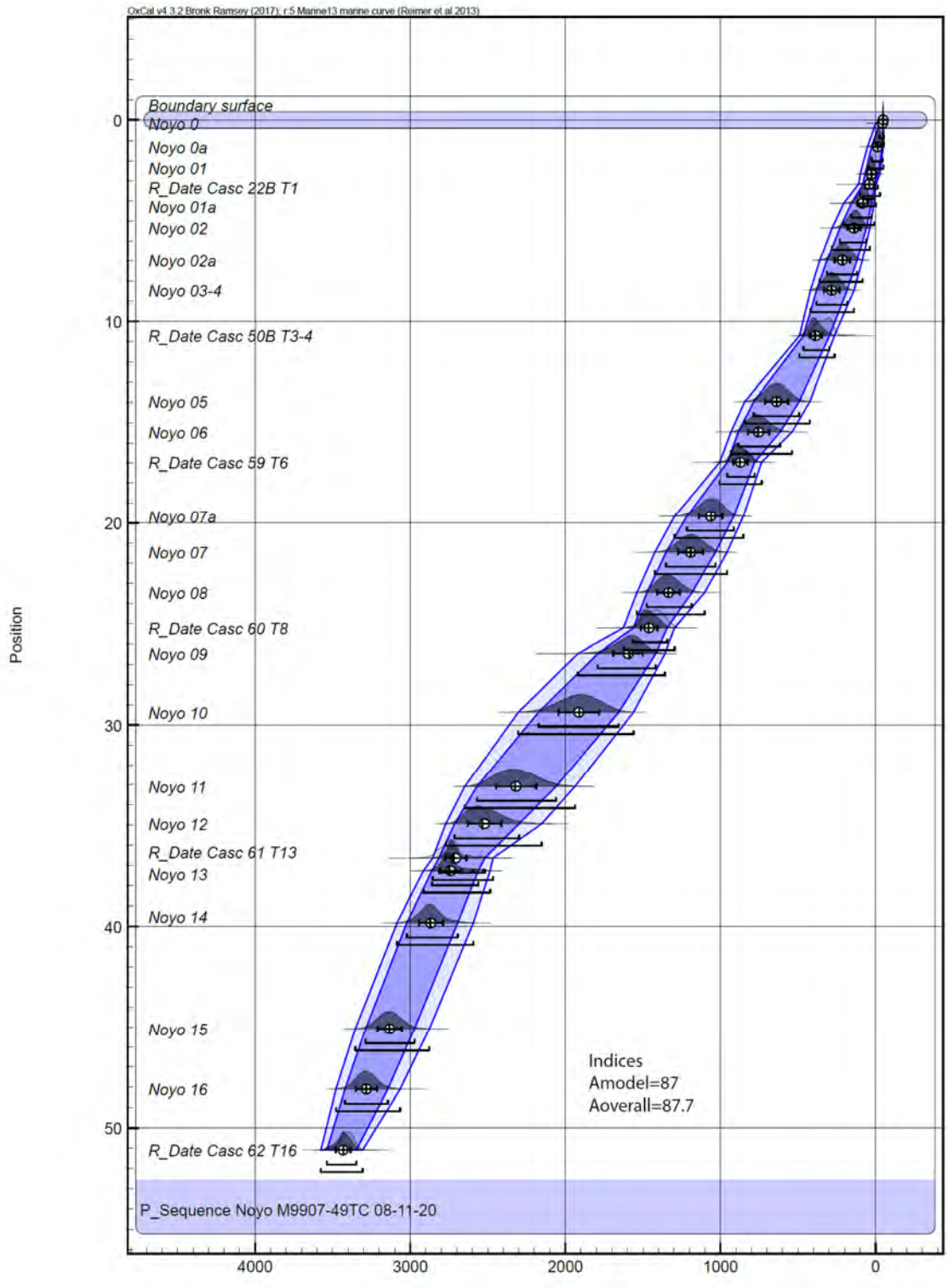

Figure 50. Post 3300 cal. BP Oxcal P-sequence age model for Noyo Canyon. Upper beds utilize box core M9907-50BC, subcores 6 and 7, beds below Noyo event NT3-4 use core M9907-49TC. These cores have similar compaction and are suitable for this composite age model. See Appendices 3 and 4 for the model code and tabular output.

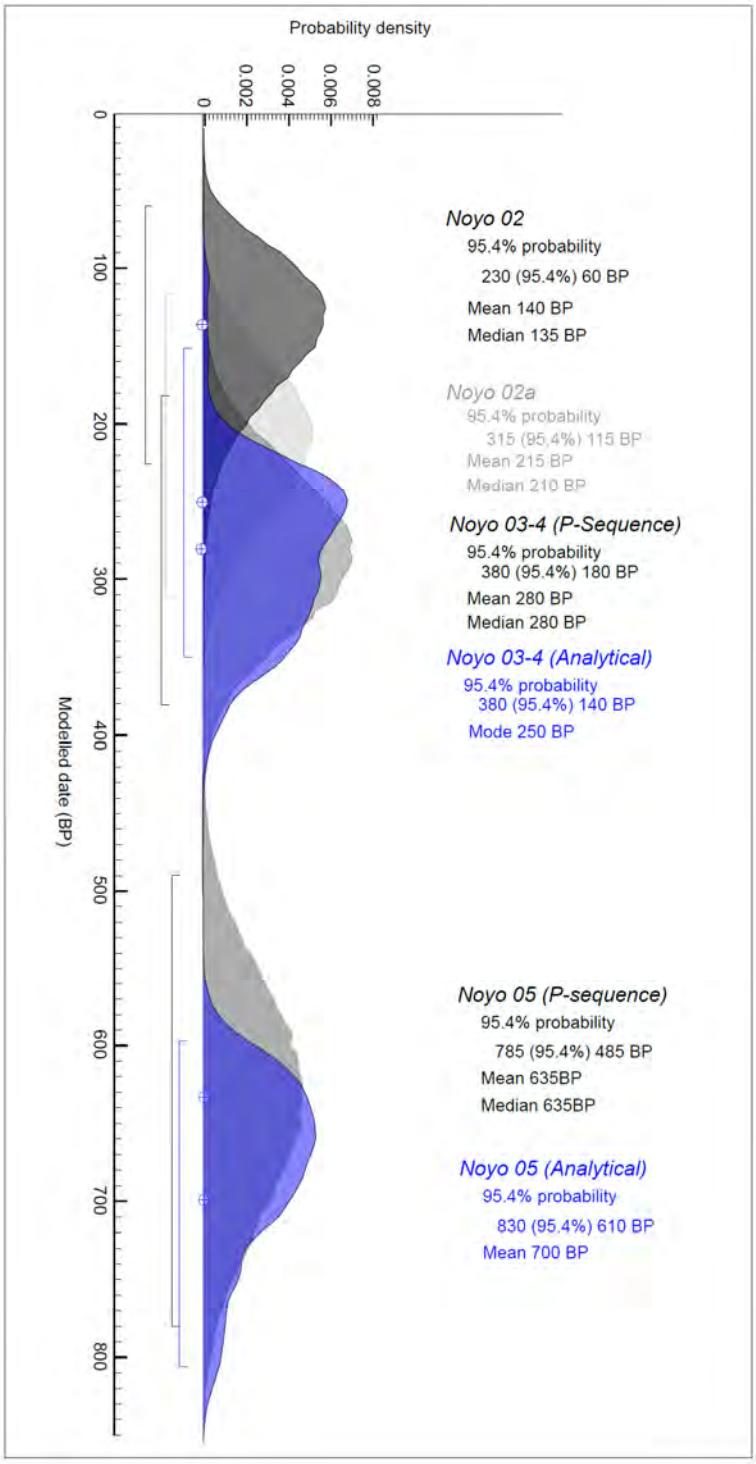

Figure 51. Age model detail of the ~ 1700 CE doublet, and its immediate neighbors. The ~ 1700 event is shown with a P-sequence model age, and a preferred analytical age (in blue) for that event which was directly dated. Similarly, the Noyo T05 event is also shown with a P sequence model distribution, and a preferred analytical age (in blue). 2σ ranges are shown. Minor event T02a shown in grey due to the low probability this small event would be confused with the major events above or below.

The complete post 3300 BP age model for Noyo Canyon/Channel is given in Figure 50.

Southern Cascadia Age Model

To model the ages of late Holocene event beds in Southern Cascadia, we investigate the core set available in detail. Cores were collected in 1999 (cruise M9907), and 2009 (cruise TN0909). Of these there are wide differences between the numerous sites. As described in Goldfinger et al. (2013), turbidite beds between the major event beds, termed "mud turbidites" become coarser, thicker and more dense southward. The increasing thickness and grain size trends increase southward to the southern limit of Cascadia, but not universally so. Some individual beds fade southward, while others remain similar to their characteristics at their Rogue Canyon location. The bed thickness and grain size characteristics are modulated by other factors as well, partly described in Goldfinger et al., (2013). In the vicinity of Smith and Kamath Canyons, all beds become more fine-grained. This trend was interpreted as a result of distance from sediment sources, as these two canyons are low volume sources of sediment in comparison to those to the north and south. The southernmost Cascadia systems, Eel and Mendocino Channels have been sampled extensively and found to have very high turbidite frequency, as well as a somewhat chaotic stratigraphy. Paull et al. (2014) found the turbidite frequency on Eel Fan is ~ one event per ~36 years for the mid to late Holocene, nearly identical to the value of 39 year recurrence found in the post 1500 BP section of the TN0909 Eel cores. This high-frequency record may consist of all earthquakes, or a mix of storm events and earthquakes. Eel Canyon has a very narrow shelf between the mouth of the Eel River and the canyon head, this relatively direct input to that system is possible during storm events, where a wider shelf precludes this possibility from most, if not all other Cascadia canyon systems. This aspect of sediment transport is discussed extensively in Goldfinger et al. (2012) and Paull et al., (2014). The Eel cores may also contain earthquakes from numerous sources, including the Gorda Plate, Mendocino Fault, CSZ interplate events, and the NSAF. We conclude that the high-frequency turbidite record contained in the Eel cores, while potentially useful, would require a very high level of effort to be useful as paleoseismic record, and likely would not be able to resolve the variety of earthquake sources adequately. We turn then to Trinidad Canyon, a unique site with a very high resolution record.

Trinidad Canyon Age Model

Trinidad Canyon is a unique system comprised of a large drainage basin with multiple feeder canyons that merge and drop steeply down the lower slope into a plunge pool (Lee et al. 2002). The plunge pool in turn has no well-defined exit, and is surrounded by a concentric wave-field that indicates flow out of the plunge pool. We sampled the plunge pool and the areas immediately to the north and south to characterize this site in detail. The plunge pool cores include M9907-35-37PC-TC, and box core M9907-32BC. This gives us a seven cores at this site with which to characterize the stratigraphy in detail. We focus on Trinidad Canyon because its record is of excellent quality, without obvious core disturbances, and does not appear to suffer from the disadvantages of the very-high turbidity current frequency of the Eel system to the south, or the lower sediment supply conditions to the north. The plunge pool likely is responsible for the very high-resolution record given that there is no large river system directly related to the Trinidad Canyon system. We infer that sediment plumes from the Eel River system indirectly supply the Trinidad system during winter storm conditions, similar to, with a the recharge of the SW Washington canyon recharge from the Columbia River (Sternberg, 1986).

We used the best available intervals from the Trinidad Plunge pool core set between the beds from the surface down to the well correlated CSZ T1. This event was dated directly in M9907-35PC, one of the cores used in the age model, resulting in a 2 sigma age of 100-410 cal BP. The depth corrected model of this age is 250 cal BP (70-380) The broad range is common for ages in this range, but this event has yielded similar ages throughout Cascadia basin (Goldfinger et al., 2012). While radiocarbon alone obviously cannot distinguish the age of this bed more precisely due to the radiocarbon "flat spot" in this

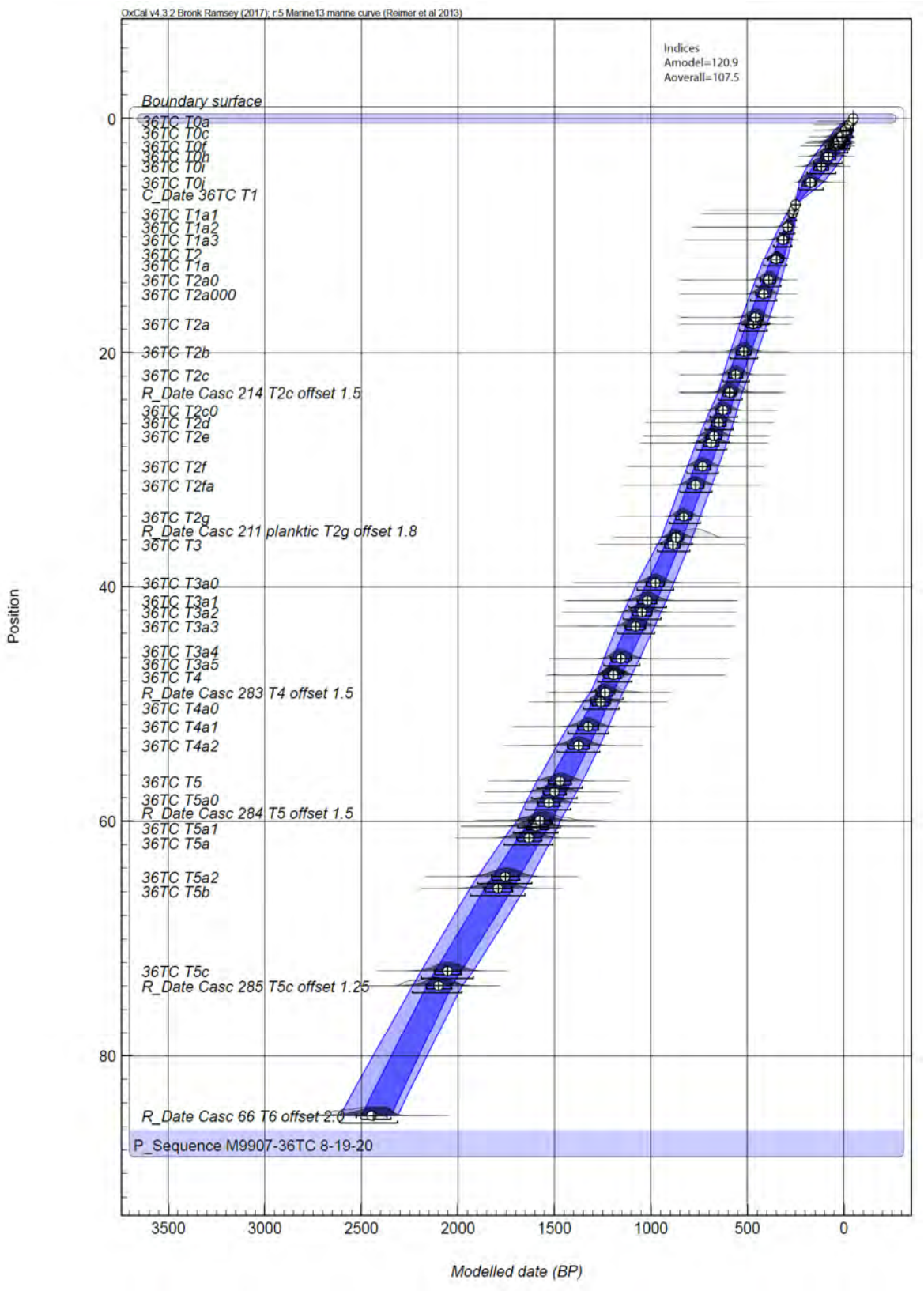

Figure 52. OxCal P-Sequence age model for post 2500 BP time in Trinidad Canyon, cores M9907-36 PC and TC. Upper 250 years of model are shown in more detail in Figure 45.

age range, we assume this is the 1700CE event based on the ^{14}C ages and log and seismic correlation of this bed in much of Cascadia (Goldfinger et al., 2012; 2017).

We constructed an age model for the stratigraphy above T1 to the surface, using the assumption of the exact 1700 CE date for T1, the surface age of core collection of 1999, and the constraint that the upper three beds must all be post 1952, based on the bomb carbon age in bed T0c, the third bed from the surface. There are six beds correlated to other sites, and several smaller uncorrelated beds seen in the detailed CT imagery. An "event-free" stack was created by compositing the best hemipelagic intervals available between each pair of events across the Trinidad plunge pool core set. Even with seven cores, uncertainty exists that can be reduced by compositing the full set. Multiple measurements of interevent thicknesses were collected from the full 3D CT imagery using the Osirix Dicom imaging system. The depth of each radiocarbon age sample was calculated based on sample thickness and position below the bed base as discussed in Goldfinger et al. (2012). The resulting age model table is shown in Appendix 5 and the depth figure from OxCal is shown in Figure 52. The input event free stack and OxCal code are given in Appendix 6. This simple model has no significant errors, and no sharp links in sedimentation rate suggesting a relatively straightforward result. The results are discussed below.

We constructed a second age model extending to the base of the clearly interpretable section at Trinidad Canyon, which is just below regional event T6 (Figure 52). This model uses the same top section above regional event T1, and makes the same assumption that that dated event is the 1700 CE event. It uses the well-dated event T6 as the base of the model. Both models are incorporated in to a southern Cascadia-NSAF space-time diagram presented in the Discussion section.

Doublet Stratigraphy in Noyo and Trinidad Systems

Cascadia Doublets

In our original publications (Goldfinger et al., 2003; 2008, 2012, 2013), we noted but did not attempt to interpret a number of odd doublet turbidites, mainly in Noyo Canyon, but also in Trinidad plunge pool. The Noyo doublets are more pronounced, and give the event beds the appearance of coarsening upward sequences. The Cascadia doublets are less pronounced, and where present, have the odd appearance of a late pulse of coarser material embedded in the event bed tail, or in some cases, a separate event with some passage of time between the two. For example, the probable T1 event bed is shown in Figure 53. This bed has a typical coarse base and rapid fining upward sequence, but then appears to have a second coarse base with loading structures embedded in the tail of the bed. Above that, a second fining upward sequence is observed. Multiple pulse turbidites are common in Cascadia (Pastor et al. 2013), and form the basis in many cases for intersite correlation (Goldfinger et al., 2012). This bed differs from most multipulse Cascadia turbidites in that the second pulse does not appear to be co-genetic with the first. There is not a high energy signature of laminar and cross beds commonly observed in typical multi-pulse beds, but rather a clear second base (Bouma A) embedded in the fining tail of the first event. The load casts imply rapid deposition into a soft, low-energy substrate rather than a dynamic high-energy hydrodynamic event.

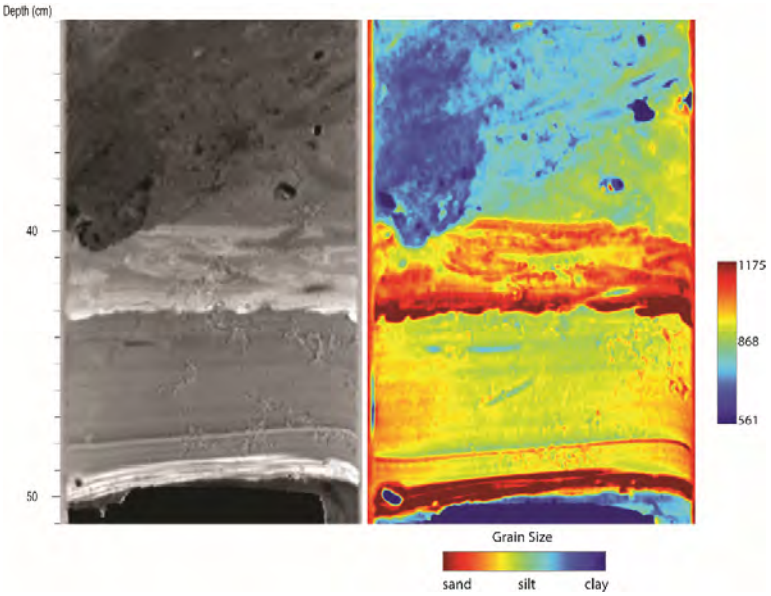

Figure 53. CT imagery from core M9907-36TC. Grey scale and color CT images are shown, with Hounsfield units (CT density) and approximate grain size scales shown. Different CT slices are shown in each panel to illustrate the character of the bed. This event bed is interpreted as Cascadia T1, with a radiocarbon age of 250 (70-380) cal BP. The upper unit of this atypical doublet appears to have load casts set into the upper silt tail of the basal sand.

Within the interpretable time range of the Trinidad Plunge pool (< 2500 BP), there are three other doublets that have similarities and differences with the T1 doublet (Figure 54). In all Trinidad (and southward) cores, Cascadia event T3, another well-correlated event, there is a second event just above it that does not correspond with any known Cascadia event, or correlate northward, T2g. The age of T3 at Trinidad is similar to the age elsewhere in Cascadia, 800 (660-940) cal. BP, with multiple ^{14}C ages. The overlying event is dated at 750 (610-870) cal BP. While the difference in age is not very significant, there is a thin hemipelagic layer between the two, confirming that the age difference is present, and the model ages support this result. The next main series event down, T4, also has a doublet that does not correlate northward. The T4 bed is actually a triplet, and has three coarse elements. The second one has load casts similar to those observed for T1. The third pulse is a weaker silty pulse showing some flow structure. Like T1, the load casts in the second element of this bed suggest a low energy tail deposition following deposition of the basal bed, with loading of the second pulse into the tail of the first. The third example is Cascadia T5, also a well-correlated regional bed, with a Trinidad ^{14}C age of 1510 (1380-1650) cal. BP, similar to the ages reported regionally. This bed had multiple internal pulses, and a small doublet event just on top of the tail. In this case, likely a short time elapses between the waning of the T5 tail and the doublet bed (Figure 54).

Noyo Doublets

In Noyo Canyon, many of the late Holocene turbidites, younger than about 3500 years BP have and odd inverted doublet appearance. Most of these beds are not in fact coarsening upward in the strict sense, but rather are two fining upward sequences, closely stacked, with the upper unit typically denser, thicker, and coarser in grain size than the lower unit. Commonly also, the upper unit has a sharp upper contact, implying bypassing of at least some of the medium and fine grained components expected in the event tail. This feature is not uncommon in a setting like the proximal cores on Noyo Canyon/Channel. Figure 55 shows a typical example of this stratigraphy. The geophysical traces suggest a coarsening upward unit, but the CT image reveals a coarse sandy bed deposited on top of a silty fining upward bed. The magnetic and CT density data were collected after the 1999 core was sampled, and are disrupted by the sample void, but the Gamma density was collected from the core onboard before splitting). This unusual stacking is common in the late Holocene record of Noyo Canyon, though not all beds show this structure. This particular bed was sampled for radiocarbon, and the calibrated age at the base is 250 (140-380) cal. BP, or ~ 1700 CE. An interval between the two coarse units was thought to be hemipelagic sediment and also sampled and dated. The interval was silty mud and clearly not the fine hemipelagic clay required for reliable dating. This date was reversed: 500 (430-580), showing that the foraminifera collected from between the coarse units were reworked, and part of the turbidite rather than hemipelagic sediment.

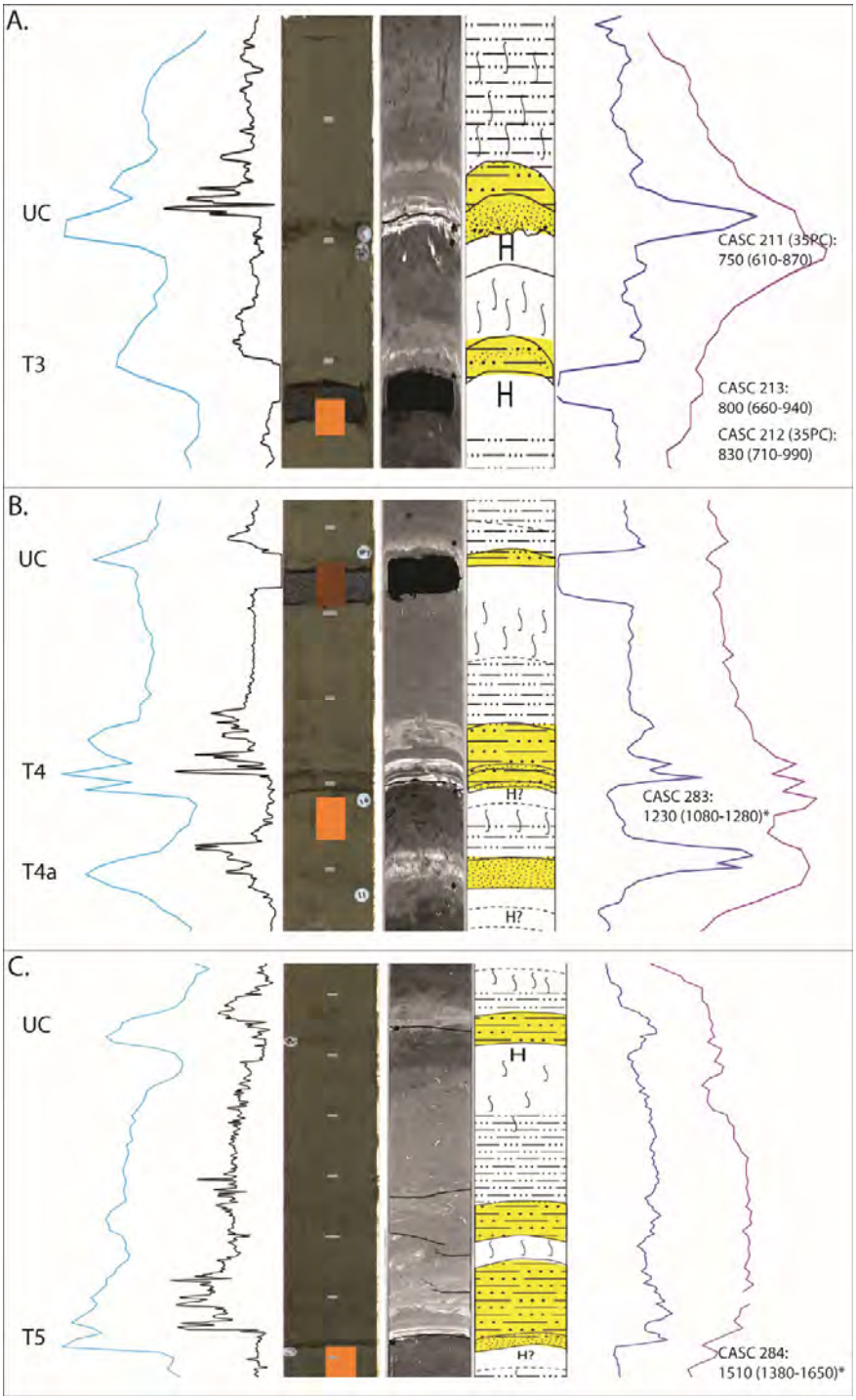

Figure 54. Three complex late Holocene turbidites from Trinidad Plunge Pool. A. Cascadia T3 is overlain by a bed labeled "UC (uncorrelated), with a thin interval of hemipelagic and a median age slightly younger than T3. B. Cascadia T4 is a complex triplet, the middle interval of which shows load casts into the basal unit. C. Cascadia T5 is a complex multi-pulse bed, directly overlain by a second event labelled UC. Radiocarbon median ages with 2σ ranges are shown. Grey ticks are 10 cm depth markers.

Eleven other examples of this doublet are available, seven from the 7 subsamples of box core M9907-50BC, M9907-49PC, and TN0909-14PC and TC (Figure 48).

All of the doublets show similar structure, and no evidence of hemipelagic sediment between the two coarse pulses. Inverted structures such as this are sometimes invoked for storm related turbidites, which may show a coarsening upward, then fining upward sequence that corresponds to the waxing and waning of the event over a period of days (Figure 56, Mulder et al., 2001; see discussion in Goldfinger et al., 2012). These beds however are not similar to the hyperpycnal beds as they are formed of two fining upward sequences. Additionally, Noyo Canyon is not closely connected to a river system. The nearest river is the Noyo River, a small coastal river 16 km to the south of the closest part of the upper Noyo Canyon. The canyon and river may have been connected during the last Pleistocene lowstand, but are currently separated by a wide, mostly flat-lying sedimented shelf with no channel pathway connecting them during the Holocene (Beeson et al., 2017).

The other late Holocene doublets in Noyo Canyon are shown in Figure 57. Comparing to the overall stratigraphy of the site, it can be seen that several events do not have the doublet structure, while several either cannot be determined or are intermediate types.

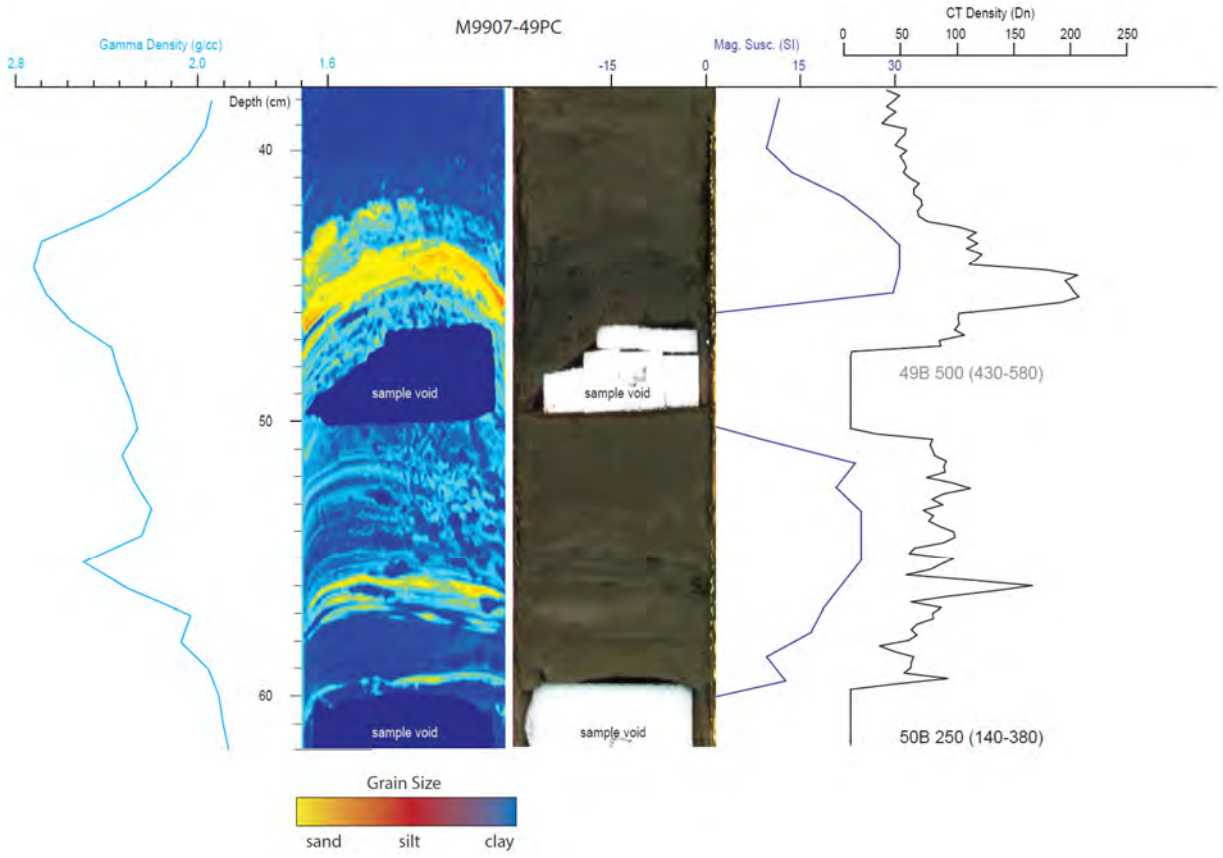

Figure 55. An example of the doublet stratigraphy commonly observed in Noyo Canyon event beds. This unit was thought to be two separate turbidites and 14C dated, yielding the upper greyed out, reversed age. The stacking of a dense, sand-rich unit above a finer grained unit is evident. The age obtained from below the doublet is similar to the ages for this event to the south, and to the AD 1700 event in Cascadia.

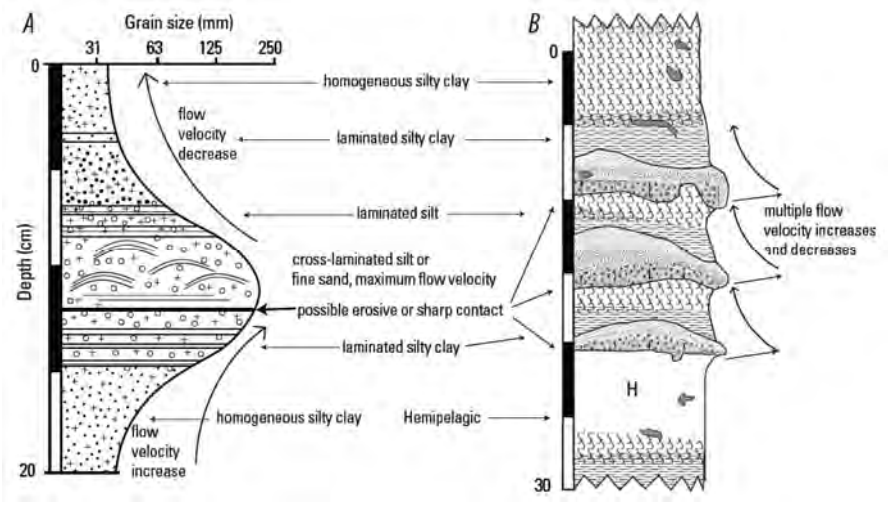

Figure 56. A, Idealized stratigraphy resulting from hyperpycnal flow, characterized by a coarsening-upward sequence followed by a fining-upward sequence, attributed to a waxing, then waning, hydrographic profile during a storm event (after Mulder and others, 2001).

Other events with similar hydrographs, such as a gradual dam breaching, may produce similar stratigraphy. B, Typical stratigraphic sequence from a turbidite with multiple fining-upward pulses from core M9907- 12PC in Juan de Fuca Channel. This turbidite and nearly all others in the Holocene Cascadia Basin turbidite sequence exhibit multipulsed stratigraphy, with no waxing phase. Multiple fining-upward sequences are capped by a fine mud tail, signaling the final waning of the turbidity current.

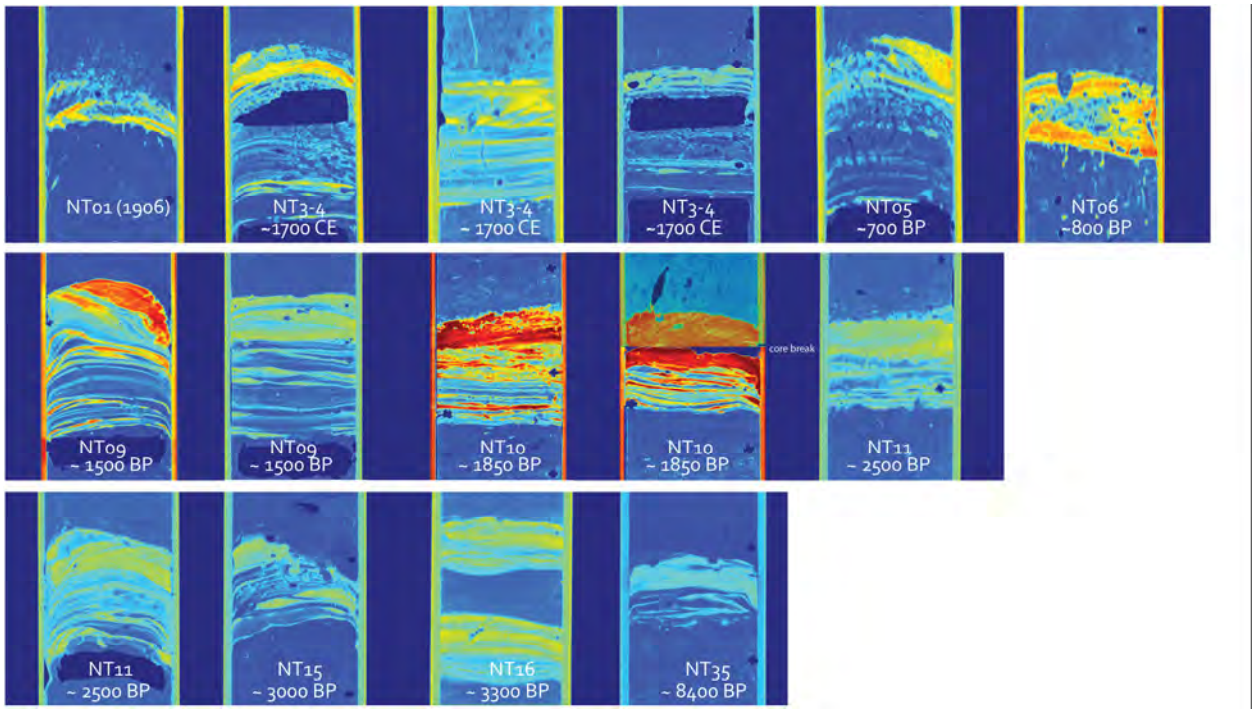

Figure 57. Examples of the Noyo Canyon/Channel inverted doublet stratigraphy, their local bed designations and approximate ages B are shown. Warmer colors indicate increasing density and grainsize, dark areas are radiocarbon sample voids. The 1906 bed is one of the few in the past ~ 4000 years that does not have the inverted doublet sequence, although it does have a thinner poorly developed doublet. The bottom right event is one of the few inverted doublets observed prior to ~ 4000 BP.

DISCUSSION

Lacustrine and Estuarine History of Lake Merced

The issue of the long term history of the lake and its access to the sea is an issue of some concern. Much like fluvially fed lakes where climate/storm events may result in a thin silt layer, a beach sand event may occur during periods when the lake spit is breached and open to the sea. The methodology to address this possibility has developed with lake paleoseismic work in Alpine settings (e.g. Schnellmann et al., 2002; Strasser et al., 2006), and also used in Lake Washington by Karlin and Abbella (1992) and Karlin et al., (2004). Beds deposited by either spit breaching or from upslope weather events are expected to thicken toward their sources, the spit or river inlet respectively. Earthquake sourced, internal lake turbidites however would thicken and coarsen toward failed wall sources, which may or may not coincide with inlet sources. In other settings, inlet sourced bets have generally proven to be thinner and less spatially significant than even modest earthquakes. As noted above, we did not observe thickening or coarsening of beds toward either the north (primary input) or south end (secondary input) of South Lake (Figure 58). The thickness and coarseness of beds (using CT density proxy) appears to be random, with similar numbers of beds more robust near stream inputs, or away from stream inputs. Only two beds are more robust near the southern end of the deep section of the lake, at the lakes deepest point and a secondary stream input point. The issue of potential spit breaching during the late Holocene, which is somewhat ambiguous in historical records, seems excluded by the lack of thickening and coarsening toward the northwestern part of South Lake, where spit breaching would have to be located. The general shoaling of the lake in that direction could be related to spit openings earlier in the Holocene, or it could be related to faulting around the lake, which may control the origin and geometry of the lake. This result suggests strongly that bed thickness and grain size is more likely modulated by wall sourced failures rather than proximity to external sediment input at least in the last 2300 years, following an obvious estuarine period. Unfortunately the lack of usable Chirp seismic data precludes a second test of this issue using reflectivity as a proxy for bed thickness and impedance contrast.

Figure 58. Portion of the Creek and Watershed Map of San Francisco and Vicinity. Creek inputs are from the south, the southeast, and from the northeast. From Ramirez-Herrera et al., 2007).

With respect to spit breaching events in general, the historical documents are ambiguous, but seem to indicate a fully fresh water system despite the report of breaching of the spit. Lake Merced also differs significantly from typical barrier spit lagoons found elsewhere in northern California. Along the northern California coast, such lagoons such as Big Lagoon and Stone Lagoon typify the barrier-spit configuration. These lagoons are drowned estuary systems with narrow sand spits supported by longshore transport. Their levels are a function of rainfall and permeable drainage to the ocean, punctuated periodically by spit

breaching events when the impounded lakes reach very high levels. The well-documented spit breaching of Stone Lagoon in 2002 typifies this process (Kraus et al., 2002). In such cases the lagoon may be open to the sea for some period of time before the barrier reforms.

Lake Merced however appears to lie in a structural basin, bounded on the seaward (west) side by bedrock bluffs of the Merced formation. The South Lake shorelines parallel strands of the Golden Gate Fault and San Andreas, and may controlled by these fault strands. The low area in the bluffs at the NW point of South Lake is the point at which the lake has drained historically, and is likely the buried low-stand arroyo from Ingleside Creek, which now bypasses Lake Merced. This area is ~ 330 m wide from mean tide level to the lake shore, and roughly 600m wide parallel to the coast. The historical maps show a narrow creek draining Lake Merced to the ocean, and the 1852 report indicates a broad area of this narrow zone was breached. We suspect that this area is not a spit at all, but sand filling of a former canyon, and thus distinct from typical barrier spit systems, though longshore transport may still contribute to maintenance of this barrier.

Structural origin of Lake Merced?

The coincidence of the strike of the lake margins paralleling the Golden Gate and San Andreas faults, while crossing the drainage trends, suggests a connection. In our investigation we had hoped to actually image a fault in the lake, but the gas content of the sediment precluded that. Other evidence of faulting exists, while some has been refuted in recent years. Notable is the relatively recent investigation of the San Bruno Fault. This fault was originally proposed by Lawson (1895, 1914), and its trace lies 3 to 4 km northeast of the San Andreas Fault. This fault has been included on all subsequent maps and has been considered important in the structural geology of the Peninsula. Lawson based the existence of the fault on sediments were cut off the fault that uplifted the Franciscan rocks to the northeast. However, later investigation into this structure, prompted by extension of a BART line to the San Francisco airport failed to confirm the existence of the San Bruno Fault (USGS., 1997; Bonilla et al., 2000). The fault had never been observed, and later investigation failed to locate evidence to support it. USGS (1997) found that the thick sections of Merced formation were either eroded or never deposited, thus no fault was required to explain their juxtaposition against San Bruno Mountain. Borings and geophysical data also failed show evidence of this fault. Seismicity however does support an interpretation of a right step in the San Andreas to the Golden Gate Fault, a model that does not require a long onshore extension of the Golden Gate Fault which might have been linked to the San Bruno Fault (Jachens et al., 1996; Zoback and Jachens, 1996; Jachens and Zoback, 1999).

While the San Bruno Fault likely does not exist, another fault the Serra Fault likely does exist and may play a role in the physiography of Lake Merced. The Serra Fault is thought to be a southwest dipping blind thrust responsible for uplift of Merced Formation sediments west of the lake, and is mapped to project under the lake (McGuire, 2009, Hengesh et al., 1995, Kennedy, 2002). This fault may be responsible for inversion of the former Merced depocenter, and the structural subsidence of the basin in which Lake Merced resides today. The fault shows Holocene activity in trenches several km to the SE of the lake (Hengesh et al., 1995). We suggest that the east tilt of the lake floor of ~ 4 degrees is consistent with growth of the Serra Fault anticline just to west, although other interpretations are not excluded. The tilted lake floor would be expected to fill in rapidly given the overall fairly high sedimentation rate of ~ 1.6 mm/yr. At that rate, the ~ 400 cm Holocene section was deposited in ~ 2500 years, more than twice the differential height of ~ 200 cm across the lake with a 4 degree east tilt. We conclude that the there is a high likelihood that the lake is structurally controlled.

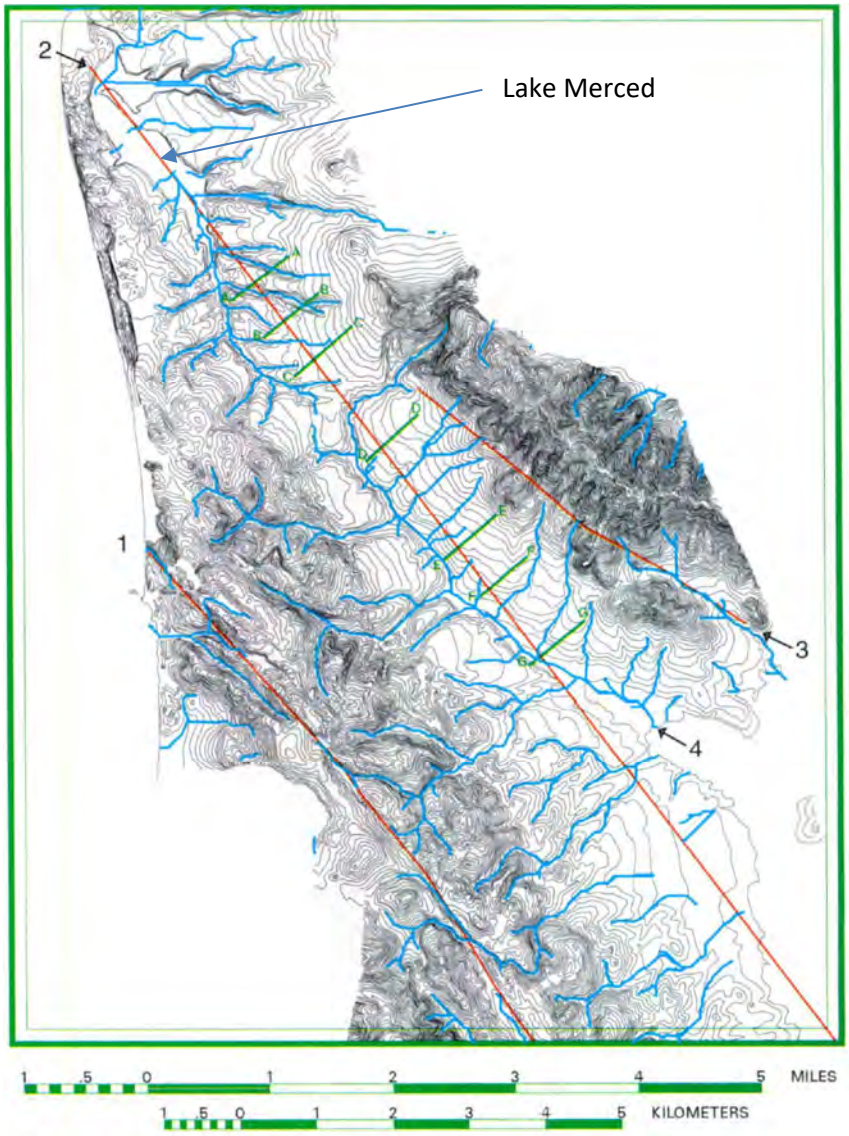

Figure 59. *Map showing the digitized vector contours of the 1800s U.S. Coast Survey topography, the drainage network (blue) derived by digital processing of that topography. 1, San Andreas Fault; 2, Bonilla trace of the San Bruno Fault; 3, Hillside Fault; 4, mouth of Colma Creek. Figure from Bonilla et al., 2000.*

Relationship of Correlated Northcoast Beds to Lake Merced and Other Land Sites

Despite problematic correlations along the northcoast segment, we can make several observations regarding these beds and their connections to other paleoseismic sites in the late Holocene. The revised correlation in Figure 40 shows that most of the northcoast beds between Noyo and Pioneer Canyons can be correlated along strike. The uppermost of these beds is the 1906 bed. While this bed is thin, it appears consistently along the northcoast segment. Comparing to land sites offers little more information. Noyo bed NT3-4 (280, 180-380 BP) can also be correlated along strike, and has temporal correlatives at numerous land sites including Alder Creek, Fort Ross, Bodega, Vedanta, Dogtown, Bolinas and Lake Merced. Beds NT 5 through NT 11 can similarly be correlated southward to Pioneer Canyon as interpreted in Figure 40. There is permissive correlation of these beds at the Northcoast land sites as

shown in Table 2, however the radiocarbon based correlation is not sufficient to demonstrate unequivocal linkage. Beds NT12-NT14 do not appear to correlate south of Albion Canyon. Beds NT12 and NT 13 or 14 do have radiocarbon overlap with the oldest events at Vedanta, but are older than all other land sites. Where they overlap, the offshore Northcoast record is very similar to that of the onshore sites, suggesting that these records may be evidence of the same series of NSAF northcoast segment earthquakes (Figure 40). At Lake Merced, Bed 4, the event below the large probable 1906 bed (Bed 3), has a 2 sigma age of AD 1660-1770, with a median of 1720, indistinguishable from the northcoast segment ages reported at Noyo Canyon for turbidite NT 3-4 (2 sigma AD 1780—1660, median 1720). The penultimate event age for Vedanta Marsh is similar at 1670-1740, median AD 1710. Bed 5 has a model age of AD 1520-1650, median of 1590. This does not match events at either Vedanta or Noyo Canyon, but is similar to the Peninsula segment penultimate event with a median of ~ 1620 shown in Schwartz et al. (2014). Other age matchups are preliminary, but suggest that trenches on the Peninsula as reported by Prentice et al. (2013, 2016, 2019) may have temporal correlatives with Beds 3, 8 and 9 at Lake Merced. Given the proposed recording of both 1989 Loma Prieta and the 1957 Daly City earthquakes, it is not surprising that Lake Merced has more event beds than can be found on the peninsula or northcoast segments of the SAF. A table of the median ages and 2 sigma ranges for the Merced preliminary model as compared to those for the offshore site at Noyo Canyon and Vedanta is shown in Table 2.

Table 2 shows that in comparing Noyo Canyon with Lake Merced, including 1906 and the 14 prior event beds in Lake Merced, 10 of them have significant radiocarbon overlap with Noyo Canyon beds, and all but one of these has a potential correlative at Vedanta marsh. Four beds at Lake Merced are not observed at Noyo Canyon or Vedanta marsh, with one other not observed at Noyo, but has a correlative observed at Vedanta. Of these 10, 8 are statistically indistinguishable between the two sites, and the other 2 have significant temporal overlap. No beds are observed at Noyo Canyon without temporal correlatives at Lake Merced.

This comparison is very preliminary as much work remains to better define boundaries in the Lake Merced stratigraphy, and incorporate sample thickness and other factors into the rough age model (see below). Nonetheless, the comparison suggest that Lake Merced may well have captured most or all NSAF northcoast segment earthquakes over the past ~ 2300 years. The Lake Merced record also clearly captures local events such as the 1957 event, and Santa Cruz Mtn. events such as the Loma Prieta earthquake. At this stage, it is not clear what the recurrence intervals are for such events, nor the recording fidelity of them at Lake Merced.

The good correspondence between Lake Merced and Noyo Canyon suggests that 1957 and Loma Prieta events could be relatively rare if Lake Merced is recording northcoast events. In Table 2, we suggest one simple scenario of event linkage. Events in green represent events that link Northcoast and Peninsula segments as in 1906. Events in yellow (5) represent possible Peninsula segment events at Lake Merced that also have potential correlatives in the Santa Cruz Mts. segment as reported in Streig et al. (2020) and shown in Figures 62-63. One of these events, Merced bed 7 also has a temporal correlative at Vedanta, but not at Noyo Canyon. Four of these five do not have good correlatives at other land sites on the northcoast, or at Noyo Canyon. Correlation along the Peninsula segment is difficult at present, and ongoing work there may help test rupture models for this segment. Alternatively, these beds could represent local or Loma Prieta type events. At southern offshore sites such as Pioneer Cordell or Farallon Canyons the younger of the potential Peninsula events do not appear to have temporally correlative event beds, suggesting these events were beyond the triggering range for these canyons. These southern Canyons do have several event beds that correlate along part of the northcoast segment, but do not appear to have onshore correlatives (Figures 62-63).

In Figure 60 we show a direct comparison between Cordell Canyon core RR0107-33PC and Lake Merced core 7Li. Cordell was chosen because it better captures the surface among the southern NSAF offshore cores. The Lake Merced core was flattened to match tops and bases of events beds in multiple iterations to investigate possible fits to the offshore record. Figure 60 represents the best fitting option for this comparison. The upper part correlated poorly as the 1906 bed is very thick, and is just a faint bed offshore at mist sites except Noyo. There are also several young beds just below that that do not appear, or are very faint offshore. But from CE 1700 and older, the correlation appears to improve. The prominent ~ 1700 CE bed offshore and in the lake line up well, as do several other prominent beds.

Table 2. ^{14}C ages from Noyo Canyon, Vedanta marsh and Lake Merced

	Noyo Canyon	**Vedanta marsh**	**Lake Merced**	**Lake Merced**	
Noyo bed	This study*	Zhang et al. (2006)	This study	This study (AD)	Merced bed
	not observed	not observed		1986 (1976-1996) AD	Bed 1
	not observed	not observed		1957 AD	Bed 2
T1	50	E1 44	50 (-10-80)	1900 (1780-1980) AD	Bed 3
T3-4	**250 (170-390)**	**E2 250 (210-280**	**220 (80-370)**	**1730 (1580-1870) AD**	Bed 4
	not observed	not observed	280 (140-430)	1670 (1520-1810) AD	Bed 5
	not observed	not observed	360 (220-510)	1590 (1440-1730) AD	Bed 6
	not observed	E3 560 (510-600)	530(400-630)	1420 (1320-1550) AD	Bed 7
T5	**630 (410-860)**	**E4 620 (570-660)**	**690 (570-810)**	**1270 (1140-1270) AD**	Bed 8
T6	**780 (560-980)**	**E5 770 (720-810)**	**810 (670-960)**	**1140 (990-1280) AD**	Bed 9
T7a	940 (770-1130)	E6 820 (790-850)	940 (790-1060)	1010 (890-1160) AD	Bed 10
T7	**1080 (860-1330)**	**E7 1100 (1070-1130)**	**1070 (990-1190)**	**880 (760-960) AD**	Bed 11
T8	**1280 (1040-1500)**	**E8 1270 (1240-1300)**	**1310 (1180-1440)**	**640 (510-770) AD**	Bed 12
T9	**1550 (1340-1810)**	**not observed**	**1500 (1390-1650)**	**450 (300-560) AD**	Bed 13
	not observed	not observed	1650 (1500-1810)	300 (140-450) AD	Bed 14
T10	**1820 (1510-2170)**	**E9 1880 (1730-2020)**	**1800(1650-1930)**	**150 (20-300) AD**	Bed 15
	not observed	not observed	1920 (1830-2000)	30 (-50-120)	Bed 16
T11	2170 (1810-2520)	E10 2190 (2070-2300)	2250 (2080-2360)	-300 (-130--410)	Bed 17
T12	2570 (2250-2810)	not observed			
	not observed	E11 2390 (2190-2580)			
	not observed	not observed			
T13	2760 (2590-2390)	E12 2780 (2610-2940)			
T14	2900 (2700-3120)				
T15	3190 (2960-3400)				
T15a					
T16	3350 (3150-3530)				
T17	3620 (3150-3530)				
T18	3850 (3620-4160)				
T19	4100 (3760-4560)				

* (revised from Goldfinger et al., 2008)

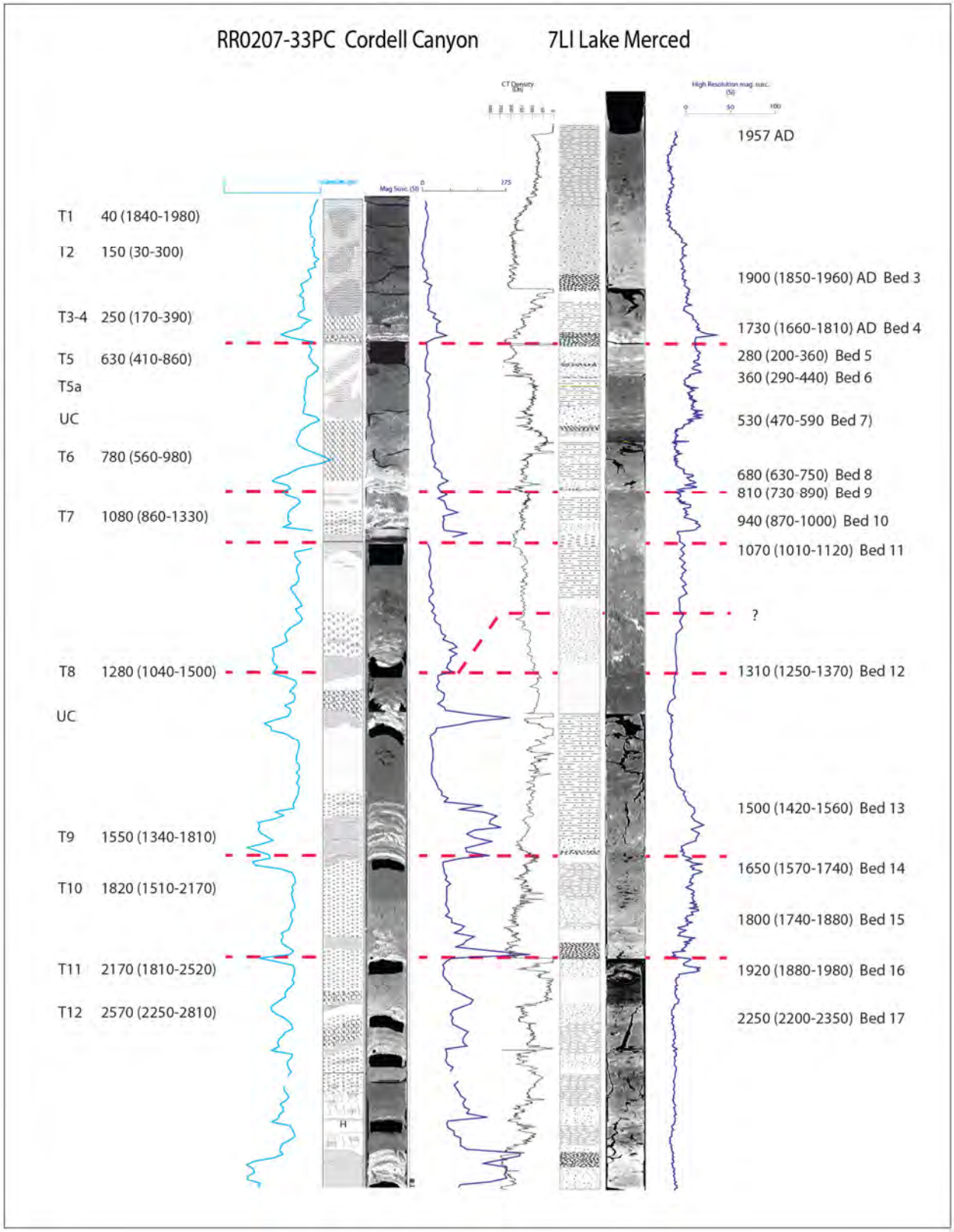

Figure 60. Preliminary attempts to correlated representative core RR0207-33PC from Cordell Canyon, to core 7Li at Lake Merced. While the records are quite different, some similarities and possible correlations are shown in red dashed lines.

The wiggle matching of the geophysical traces is only fair, but it appears that at least some of the primary sequences can be matched, including many of those shown in Table 2, in which the proposed matches are shown in bold. Beds in Table 2 that do not have good matches between land and marine sites for the most part also do not have good matches in the direct comparison in Figure 60.

We suggest the simplest explanation is that these beds could be related to Peninsula segment or Santa Cruz Mtn. segment events that do not correlate northward or appear offshore at the latitude of our southern cores. At this stage, the possibility that Lake Merced is recording both Northcoast and Peninsula segment earthquakes is our preferred hypothesis. In this scenario, the segment boundary between these two segments is not commonly utilized, as it was not in 1906, and many events could rupture across the Golden Gate. If this scenario were uncommon, and the two segments commonly ruptured independently, we would expect to see both segments as separate event beds in Lake Merced, offset in time, which appears unlikely based on the Lake Merced data. Even rupture pairs spaced very closely in time would most likely leave a doublet signature in the turbidite data, which we do not observe. The younger of the potential Peninsula segment ruptures have potential correlatives in the Santa Cruz mountain segment data. At this time, this must be considered one of many scenarios permitted by the data. We also note that of the 10 events suggested to correlate along the northcoast segment, 8 of them also have temporal correlatives in Cascadia. Potentially this could suggest that a Cascadia linkage as proposed in Goldfinger et al. (2008) and discussed below, could play a role in the rupture mode of the NSAF Northcoast and Peninsula segments, and also suggests southward directivity may be common.

Sources of the Historical Turbidites in Northern California.

One of the key observations about the post-1700 Cascadia turbidites is that they are more extensive than initially thought. With additional data, it became possible to correlate some of them for significant distances of 50-170 km with reasonable confidence. This raises a number of questions, and offers opportunities. With very large distance correlations, such as the main series of CSZ earthquakes, local crustal earthquakes are very unlikely sources. However, smaller CSZ plate boundary earthquakes, and slab earthquakes with their greater spatial effects as just described, are candidates. Also, very large storms are candidates as well given that the criteria used for major plate boundary earthquakes (1000 km correlation across numerous site types) are not applicable to this more spatially limited setting.

Goldfinger et al. (2012) discuss the criteria for distinguishing storm and earthquake generated turbidites in Cascadia. Primarily they used regional correlation, and inclusion of sites with no possibility of terrestrial input to make this determination for events that correlated over hundreds, and up to nearly the full 1000 km length of Cascadia. The distance between Hydrate Ridge basin and Trinidad Canyon is ~ 390 km of strike length, and is sampled by numerous cores and includes the fully isolated Hydrate Ridge basin. Turbidite beds correlated over this distance have some of the criteria used for full length events, 1) At least one fully isolated basin, which eliminates storm related effects as well as distal tsunami as sources; 2) long strike length, likely too long to be related to crustal or slab earthquakes. In the Cascadia record, this would include 15 events (T3a, T4a, T5a, T5b, T5c, T8a, T9a, T10a, T10b, T10c, T10f, T12a, T14a, and T16a. Event beds that could not be extended north of Rogue Canyon are: T2a, T6a, T7a, T8b, T9b, T10d, and T15a. While the correlation criteria for these events is reduced in comparison to the main series events due to their lack of robust and unique log signatures, they nevertheless have consistent stratigraphic position and ages. When looking at the shorter ~140 km strike length between Rogue and Trinidad Canyons, far fewer such criteria apply. Large storms can easily cover this relatively short distance, and no isolated basins exist to ground truth the stratigraphy by eliminating terrestrial sources. The tools available at present are reduced primarily to assessing the age models against historic events for historic times, and the more general arguments regarding storm sourcing given in Goldfinger et al. (2012). The storm sourcing arguments essentially rest on the width of the continental shelf and the depth of the shelf edge. For all but the Eel system, the shelf width and depth are too great to accommodate either storm disturbance though wave action, or direct cross-shelf transport. Goldfinger et al. (2012)

address these issues at length, and conclude that canyon heads may be loaded in cases where active river systems are proximal, through indirect shelf transport events, but that they are largely decoupled from storm events by shelf width and depth. Earthquakes on the other hand, shake the entire continental slope, and can supply sediment for a turbidity current from any part, or all parts of a canyon system, or from the open slope, and do not require Holocene reloading from rivers in Cascadia (Goldfinger et al. 2012; 2017). For the pre-historic turbidite beds included in Segment D, as described above, and others included in this report, these remain the primary arguments. Hill et al. (2020) show that little activity in the upper parts of Trinidad Canyon can be discerned with multibeam sonar and Chirp profiles. While these observations are somewhat resolution limited as the data sources lacked cores, this nevertheless suggests that at least the principal sediment sources for the Trinidad plunge pool were likely in the mid-to lower canyon. If correct, this makes the Trinidad plunge pool what might be regarded as a semi-isolated paleoseismic site, subject to further evaluation.

The plunge pool is also isolated in that turbidity currents that might have margin parallel flow components are somewhat inhibited by the elevated levees around the plunge pool. The plunge pool levees are steep and ~ 75m in height on the north side, high enough to limit ingress by slow moving turbidity currents from the abyssal plain, and likely would inhibit some turbidity currents from escaping the pool. On the south side, facing the Eel Fan, the fan has elevated the abyssal plain, reducing the vertical height of the levee to ~ 95 m on the south side. Turbidity currents would be inhibited from the Eel fan on the southern side, given the free downhill slopes available to the west, though flow into the Plunge Pool could still occur. Figure 61 shows that the constructional Eel Fan presently ends 22 km south of the plunge pool levees, and that fan channels are directed to the west, thus we consider the isolation of the plunge pool from the south to be highly likely during the Holocene. At the same time, the ~ 80 m depth of the plunge pool and steep interior walls restrict the flow of weak turbidity currents, trapping much material inside the plunge pool. That turbidity currents escape is evidenced by the levees and sediment waves surrounding the pool, but these were likely constructed largely during the Pleistocene and may be somewhat, or entirely relict during the late Holocene.

Given this context for turbidite sources, we consider some of the larger disturbance events known in historic times.

The Petrolia and Eureka Earthquakes of 1992 and 1980

The Mw 7.2 Eureka and Mw 7.2 Petrolia earthquakes are the two largest earthquakes in northern California in the post-1952 era. The Eureka event is thought to be a Gorda Plate earthquake with a left-lateral motion on a northeast striking fault plane (Lay et al., 1982), and is compatible with the rapidly deforming Gorda plate structure (Chaytor et al., 2004). The Petrolia earthquake is a shallow east dipping thrust that is either on the plate boundary, or just above it on a splay thrust (Oppenheimer et al., 1992). Shake maps for these two events are shown in Figure 62. The 1980 event generated moderate intensities up to MMI VI at Brookings Oregon, and the 1992 event somewhat lower intensities to the north, with MMI III felt at Brookings, although the ground motions were higher locally in the epicentral area.

The 1906 NSAF Earthquake

The Mw 7.9 NSAF earthquake of 1906 is of particular interest for this study, as the NSAF is the focus, and presence of paleoseismic evidence of 1906 north of the triple junction has not previously been reported. The shake map for this event is shown in Figure 63, and it can be seen that shaking of MMI intensity VI extends north to about the latitude of Trinidad, CA, ~ 100 km north of the triple junction. Felt reports suggest intensity IV extended to about Brookings, Oregon, with I-III felt even farther north (Stover and Coffman, 1993).

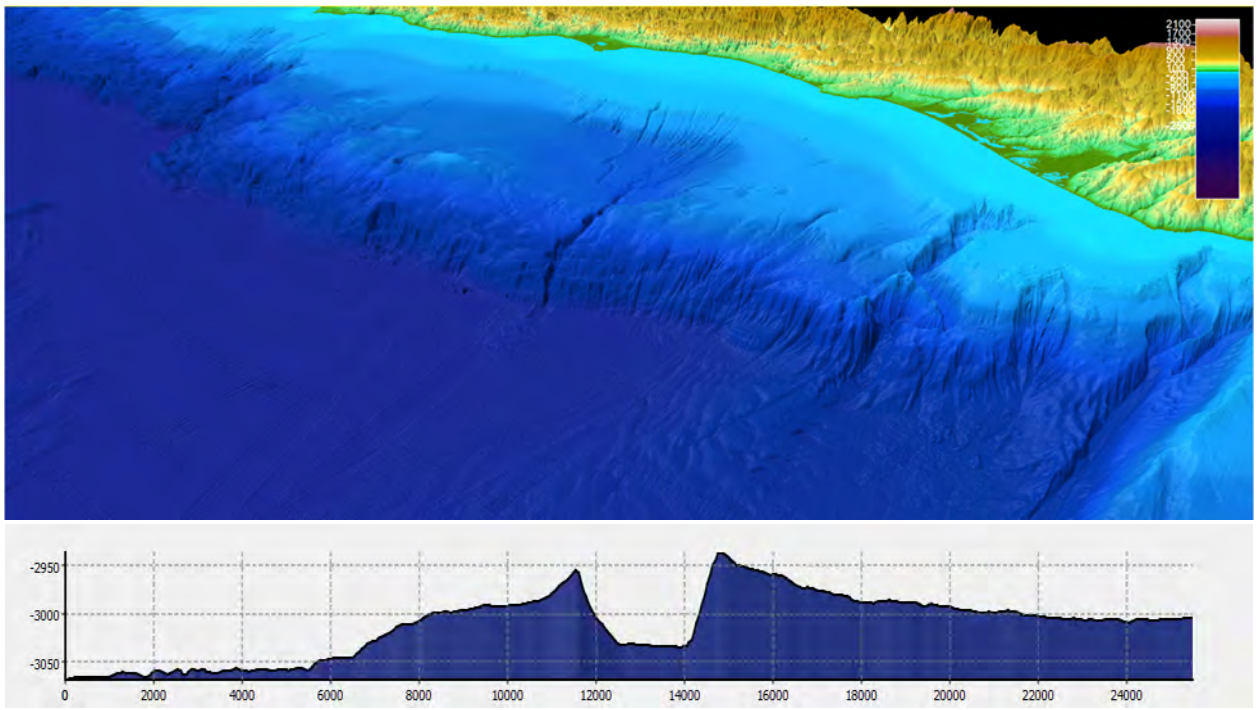

Figure 61. Shaded-relief perspective view of southern Cascadia, looking northeast. At center is the Trinidad Canyon system, at right is the Eel system and at far right is Mattole Canyon. Lower panel shows a margin parallel profile across the Trinidad plunge pool. Depths and horizontal ticks in meters.

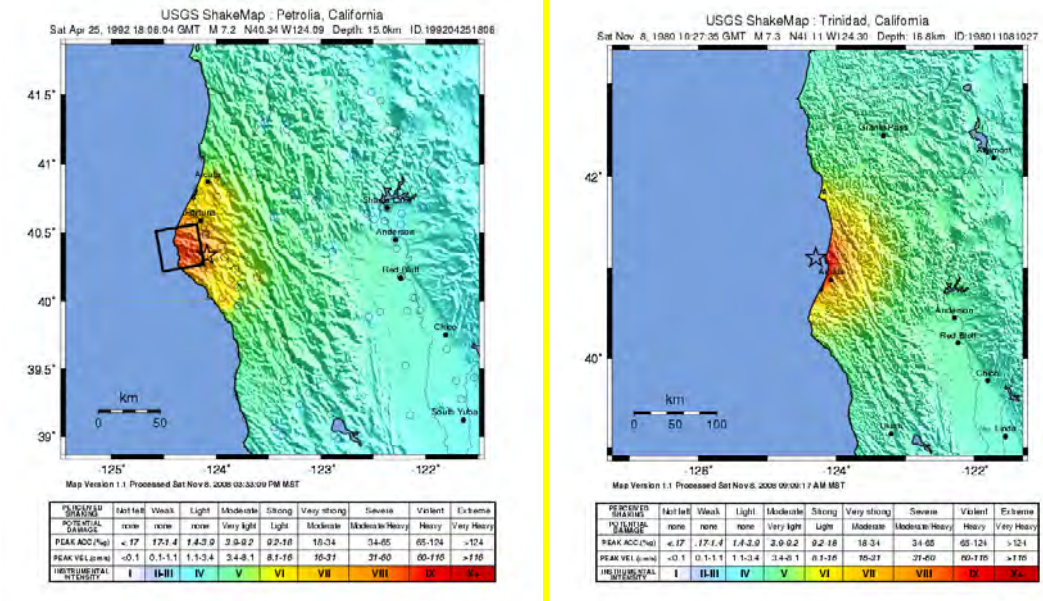

Figure 62. Shake maps showing Mercalli intensities for the 1992 Petrolia mw 7.2 event (left), and the 1980 Mw 7.2 Eureka event (right).

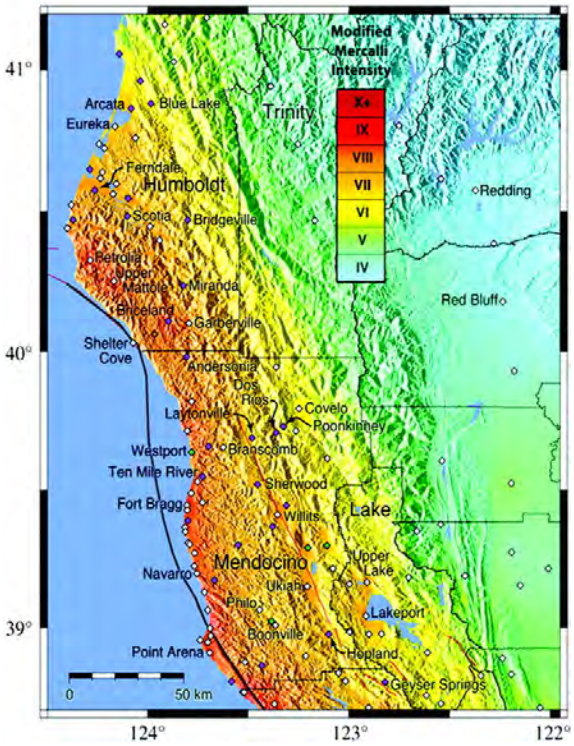

Figure 63. Modified Mercalli intensity for the 1906 Mw 7.9 event. (From Bundock et al., 2006).

The 1964 Flood Event

The 1964 "Christmas flood" was the largest in recorded history in northern California (USGS, 2014). The discharge of the Eel, Klamath Trinity and Smith Rivers set records for years recorded continuously later than ~ 1922-1931.

The 1861-62 Flood Event

Detailed discharge data do not exist for this event, however the 46 day storm of the winter of 1861-62 likely ranks as one of the largest of the past several hundred years (Dettinger and Ralph, 2011). This event must be considered as a viable sediment source for offshore northern California as it inundated most of the west coast.

The sources of the historic earthquakes in the southernmost CSZ record are good matches for the timing of the uppermost turbidites, constrained by high resolution depositional age models and precise bomb-carbon ^{14}C ages. They additionally pass the same broad criteria for earthquake sourcing that the larger events do, less the presence of a definitive isolated basin site, but with the inclusion of the Trinidad plunge pool, which is likely at least partially isolated during the late Holocene high-stand. We therefore interpret the historic events prior to 1999 as follows (2 sigma ranges in parentheses): The 1992 Petrolia Mw 7.2 earthquake is interpreted as our event T0a, with a median model age of 1990 (1978-1999) extending northward to near Rogue Canyon. The 1980 7.2 Eureka earthquake is interpreted as our event T0b, with a median model age of 1980 (1665-1991, although it could also be an Mw 6.3 event 7.5 km to the south). This bed appears to extend northward to Rogue Canyon. The third bed down, T0c, is much more faint than the two above and yields a model mean age of 1960 (1940-1975) and could be the 1964 flood event, but could also be the 1959 Mw 6.2 Gorda earthquake 30 km to the west of lower Trinidad Canyon, and 19 km west of the plunge pool. T0d, T0e, and T0e1 have the following median ages respectively: 1937 (1915-1957), 1922 (1896-1944), and 1915 (1891-1838). An Mw 6.8 event occurred in 1941 that might have triggered T0d; a Mw 7.3 Gorda earthquake 47 km to the west in 1922 could have triggered T0e. The next event down, and the closest earthquake in time and space to T0e1 is a 1923 Mw 6.9 event on the Gorda Ridge, 87 km to the southwest, or a 1920 event on the Pacific Plate 127 km southwest. Locally the most significant historic bed at the Trinidad site, T0f is most likely the 1906 Mw 7.9 NSAF earthquake, with a model age of 1905 (1880-1929). In some cores, this bed appears to be a doublet, with no intervening time between the twin beds, and perhaps coincidentally, there was a second 1906 earthquake just north of Arcata CA, on April 25, 1906, five days after the NSAF event. This second earthquake was ~ 42 km from the Trinidad Canyon head, and 70 km from the canyon midpoint. Inclusion of a small turbidity current from this second event could explain why the 1906 bed is so prominent in Trinidad plunge pool, and less so both to the north and south. There are three faint beds between the 1906 bed and the 1700 CE bed with the following model ages: T0h 1870 (1840-1890), T0i 1830 (1810-1860), and T0j 1780 (1760-1800). The

first of these could be several events, including an earthquake in 1898, or the 1861-62 flood event. A small subduction event was reported in the early to mid-1800's by Carver (2000) and Valentine et al. (2012) in the lower Eel River valley where the main series of Cascadia earthquakes is also observed. That 1800's event could potentially be recorded as our event T0i, leaving T0j in the late 1700's uninterpreted.

Implications for the CSZ Paleoseismic Record

The proposed linkage of the southern CSZ records to several historic crustal and slab earthquakes has several implications for the CSZ paleoseismic record which we touch on briefly. The first is that the triggering distances for turbidity currents specific to the southern CSZ, previously unknown, now can be estimated with several data points in the Mw-7.1-7.9 range. The 1992 Petrolia Mw 7.2 event, T0a, appears to correlate at least 140 km, and potentially as much as 230 km along strike. The 1980 Mw 7.3 event, T0b, correlates at least 140 km along strike. These lengths are data limited as there are no core sites and marine paleoseismic data between Rogue Canyon and the next site to the north at Hydrate Ridge, 250 km to the north. This remains a significant data gap in the CSZ marine paleoseismic record. The small event underlying these two, T0c dies out 110 km north of Trinidad, though its origin is unknown. The interpreted 1906 NSAF event, T0f, is a major event at Trinidad, but extends as a fine grained event to Rogue Canyon, 230 km north of the triple junction. The mid 1830's event, T0i, extends to Smith Canyon, 80 km north of Trinidad, but its origin, or slip distribution if an earthquake, is also unknown.

The general implication of this result is that triggering distances of 150-230 km can be expected in the southern CSZ from Mw 7.1-7.9 earthquakes. In the case of the Petrolia event, directivity effects are approximately normal to the margin, while for 1906 and 1980, they are parallel to the margin and would have enhanced ground motions to the north and north-northeast respectively. These values are more than double and could be triple the estimate of Goldfinger et al. (2012) who used 90 km as a preliminary range estimate. The follow-on implication of this increase in triggering range is that it could imply that the strike lengths of some of the southern CSZ events, and thus their magnitudes could be overestimated. The general characteristics of the 1980 and 1992 turbidites are on par with the smaller of the Segment D and E CSZ events included in the Goldfinger et al. (2012; 2017) catalogue. The magnitude estimates therefore could be lower, reduced from Mw7.8-8.3, to the Mw 7.0-7.4 range. Additionally, it has become less clear what some of the smaller Segment D and E events actually are. Assuming earthquake origin, as discussed above, it may be that the subset of events that do not correlate as far as Hydrate Ridge, as well as additional southern events are almost certainly a mix of Gorda, NSAF and CSZ earthquakes. Distinguishing these sources for times earlier than the historic events may well be very difficult. Additionally, the triggering distance increase should be applied to future CSZ paleoseismic catalogues and models for the segmented partial ruptures. Another obvious implication is that NSAF events clearly can be recorded in Cascadia, and if 1906 is present, we must assume that at least some of the previous NSAF events are present as well. Given that, we expect that Cascadia events should also be recorded at similar ranges south of the CSZ, for example in Noyo Canyon at 90 km range.

Finally, we discuss below the presence of NSAF triggered turbidites in the southern CSZ.

Possible explanations for the Noyo and Trinidad Canyon Doublet Event Beds

Previous work along the Cascadia and northern California margins (Goldfinger et al., 2003, 2012, 2006 2008, 2017, Hamilton et al., 2015) show that the doublet stratigraphy described here for Noyo and Trinidad Canyons is not common elsewhere along either margin, although there are a few examples. Inverted doublets such as those of Noyo canyon are very rare, except as discussed above for Noyo and Trinidad in the Late Holocene. Some possible explanations for this could include hydrodynamic

complexities of these two systems, aftershock sequences, triggered earthquakes, directivity of multi pulse events, or sequential failures feeding the turbidity currents.

Hydrodynamics

Hydrodynamics are commonly cited as the source of bed structures in turbidite deposits (Walker, 1965, Komar, 1985, Kneller and McCaffrey, 2003), and are the most commonly cited explanation for the Bouma sequence observed in waning flows. Additional hydrodynamic complexities could come in the form of bathymetric pathway complexities, longitudinal flow variability due to a complex source, flow density dynamics, or multiply sourced turbidity currents that merge along their travel paths. Upper Trinidad Canyon certainly has numerous tributaries, far more than average, that merge on the mid-slope terrace to form a simple lower canyon pathway to the abyssal plunge pool (Figure 61). If these numerous pathways are influencing the event bed structure, one might expect to see 10 or more coarse pulses in the beds, but this is not the case. Noyo Canyon is quite different, it has a simple pathway that only has two tributaries on the uppermost slope, and is otherwise a simple single pathway (Figure 64). This two headed canyon configuration might provide a relatively simple explanation of the Noyo doublets.

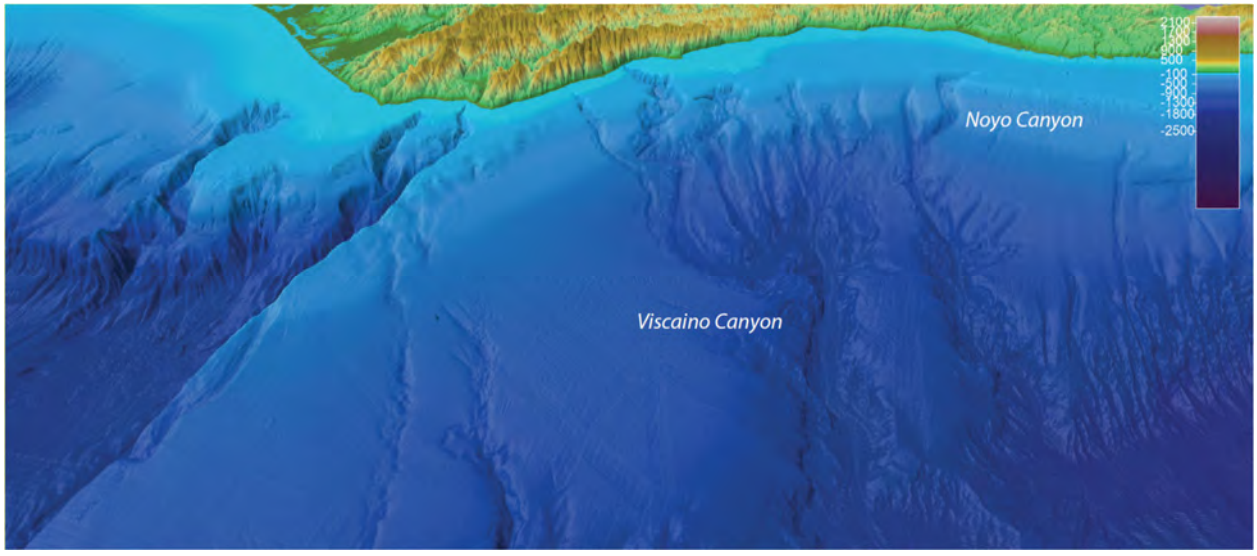

Figure 64. Shaded relief perspective view of the multibeam bathymetric data near Cape Mendocino showing Viscaino and Noyo Canyon systems.

However we have found that such complexities seem not to generate matching stratigraphies at the scale of a single canyon (Gutierrez-pastor at al., 2012, Goldfinger et al., 2012, 2017). The same appears to be true of canyon systems where numerous failures likely occur along the full length of the system, and yet the turbidite structure does not reflect these individually, though they do commonly thicken downstream (Goldfinger et al., 2017). Instead, the deposits linked to great earthquakes remain remarkably uniform above and below such proximal confluences, and begin to show evidence of stacking only in distal confluences in the NSAF system, but not in the Cascadia systems (Gutierrez –Pastor et al., 2012). This suggests that shallow confluences seem not to be represented in event deposits near the canyon mouths, while they can be represented below distal abyssal confluences with very different travel path distances. The Noyo turbidite doublets are also largely restricted to a narrow time range in the late Holocene, which if hydrodynamics are invoked, would require a sudden change in canyon configuration or pathway bathymetry at around 4000 BP. In this interval, some but not all events have the doublet structure. While we cannot rule this out, it seems unlikely that such a rapid change in the canyon would occur, affect a number of events, and then revert back to the previous configuration in time for the 1906 event which is not a doublet. The presence of doublets also seems to be associated with the Mendocino Triple Junction

region, and this association is unlinked to any particular hydrodynamic condition in that area that we are aware of. While adjacent Viscaino Canyon is quite complex, it is not used for paleoseismology due to the input of littoral sand from the nearshore; at the same time, adjacent Noyo Canyon is quite simple in configuration (Figure 64). We therefore consider hydrodynamics a relatively poor candidate for explaining either the Noyo or Trinidad doublets.

Aftershock Sequences

Aftershock sequences could potentially contribute to the paired stratigraphy observed on both Canyon systems. Late pulses of coarse material, even within the tail of a settling turbidite bed would not be a surprising result, and has been suggested (though not demonstrated) for at least one case from the 2011 Tohoku earthquake (Kioka et al., 2018). In Trinidad Canyon, several of the event bed doublets could be compatible with this scenario. Even so, the log-correlation of the Cascadia basin turbidites shows that the structural variability from site to site is relatively low, which is inconsistent with significant input from aftershocks that are random in space and time following each major event. Current information about the lower threshold of triggering and recording as discussed above, suggest that in Cascadia basin, aftershocks below Mw 7.0 might not be reliably recorded, although this threshold remains poorly known and subject to wide variability. The one example presented here of an aftershock or triggered event several days after 1906 that may have resulted in a local and subtle doublet in Trinidad Canyon. This could be an example of this mechanism, and would set the lower triggering/recording threshold for that site at Mw 6.4 with a range inside 50 km. In Noyo Canyon however, the doublets are almost universally coarser in the upper unit. While this configuration could be explained as an artifact of variability of ground motions, or other factors, the observation that nearly all of the event beds have this configuration makes this explanation unlikely. We also note the lack of such evidence in Cascadia cores, with the exception of those noted here in Trinidad Canyon, making this a site that is unusually susceptible to either proximity or recording of such aftershocks, or both. Overall we infer that aftershocks, while they are likely represented sporadically in the stratigraphic record, are not a highly likely explanation for the Trinidad and Noyo Canyon doublets.

Triggered Earthquakes

Goldfinger et al. (2008) proposed triggering of one fault by the other based on the similarity in timing of events in both systems over the same time range as described here. While the timing was not constrained to values better than the radiocarbon age uncertainties, the sequence of numerous age overlaps seemed a plausible explanation and a remarkable coincidence at the very least. Now, with better age models and stratigraphic evidence, we re-examine this hypothesis.

Figure 65 shows the time series of Cascadia and NSAF earthquakes (modified after Witter et al., 2014) that includes southern Cascadia marine and onshore age data, and the same for the northern NSAF. Figure 66 shows an expanded view of the most recent ~ 3500 years near the triple junction. We have modified the diagram in several ways: 1) we have added new analytical ages based on sedimentation rates for several events at Hydrate Ridge, which did not previously exist; 2) we have used the slightly modified ages for Bradley Lake, modified as discussed with the original authors and described in Goldfinger et al. (2012) and Nelson et al. (2021); 3) we have added the OxCal age model results presented here for Trinidad Plunge Pool and Noyo Canyon; 4) we have added the onshore age data for Lake Merced, Vedanta Marsh, Dogtown, Bolinas lagoon Bodega Bay, Alder Creek/Point Arena and Fort Ross along the NSAF; 5) we have adjusted the best fitting age picks for each event using the new data detailed in this report; 6) we have symbolized the stratigraphic evidence or absence of evidence of the stratigraphic doublets; and 7) we have added symbolization for the use of well-log and sub-bottom profile correlation where available.

When we compare the new age and correlation data across the triple junction, we see that many of the events that are correlated northward along the Cascadia and southward along the NSAF margins have

similar radiocarbon overlaps to those noted in the earlier work of Goldfinger et al. (2008). We also note that these event pairs overlapping in time between both fault systems for the most part also correspond to stratigraphic doublets observed in Noyo Canyon, Trinidad Canyon, or both in some cases. These parings are noted with "=" symbols in the figures and given in Table 2.

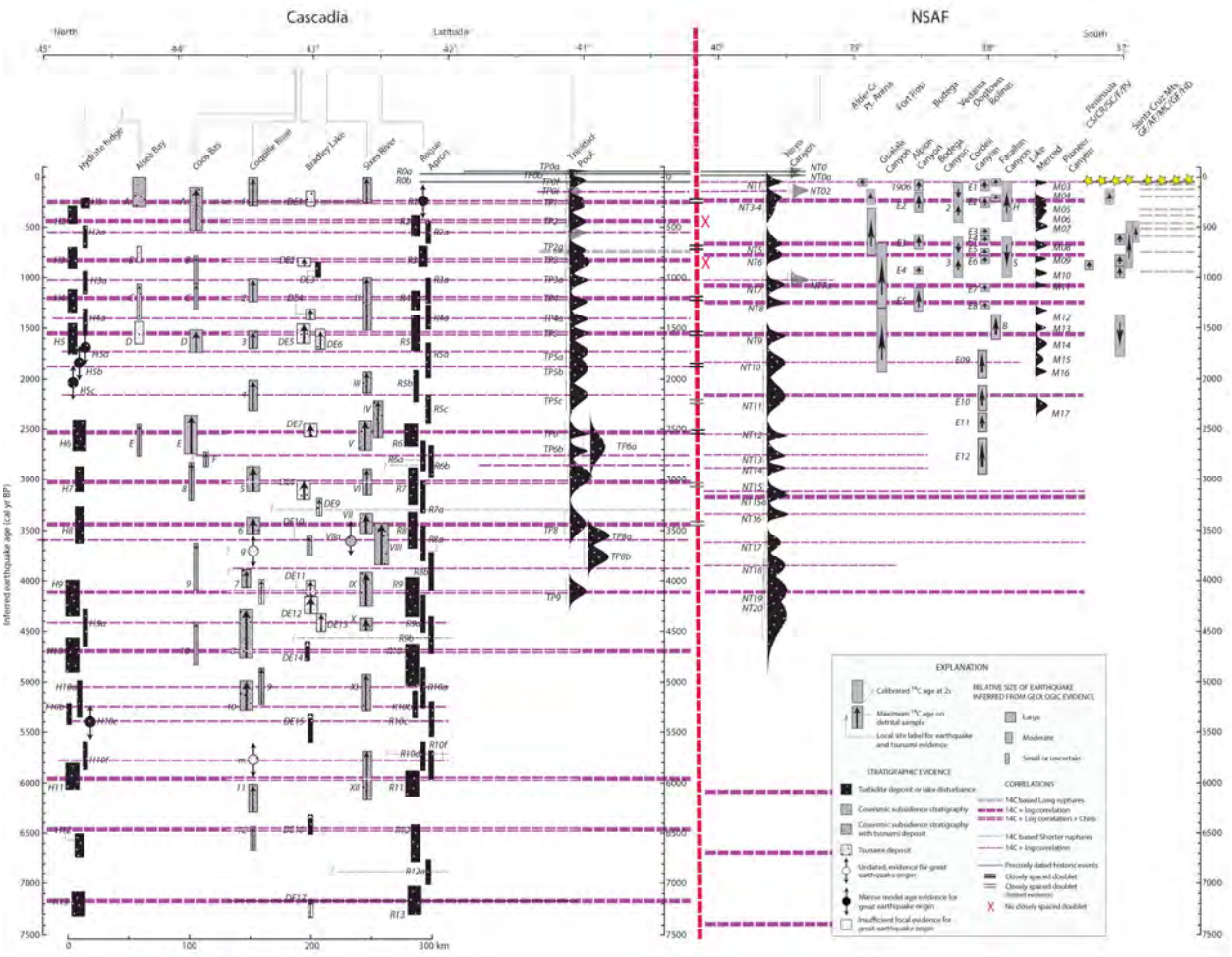

Figure 65. Space-Time diagram for southern Cascadia and the northern NSAF. Onshore and offshore age data are shown for both fault systems, with the triple junction represented by a red vertical dashed line. Stratigraphic correlations of Cascadia turbidites from Goldfinger et al. (2012) shown to reflect long (>500 km) fault ruptures (bold dashes) of most of the megathrust, as distinguished from shorter (<500 km) fault segment breaks (thin dashes). Correlation supported by well-log methods and or sub-bottom profiling are symbolized as shown in the explanation, heavier lines indicate thicker beds. Up arrows denote maximum age estimates on detrital samples. Symbol width represents relative size of earthquake inferred from deposit thickness or amount of subsidence evident in change in microfossil assemblages. Rectangles represent inferred earthquake age ranges in calendar years before 1950, calibrated from radiocarbon dates as discussed in Methods. The age ranges presented here have been recalibrated from the original laboratory reported age and are compiled in Appendix 1 of Goldfinger et al. (2012). Original age data for Cascadia earthquake records from coastal sites are reported in studies at Alsea Bay (Nelson et al., 2008); Coos Bay (Nelson et al., 1996, 1998); Coquille River (Witter et al., 2003); Bradley Lake (Kelsey et al., 2005); and Sixes River (Kelsey et al., 2002). Doublets are shown with double lines, absence of doublets shown with red X's at the triple junction. Modified after Witter et al., 2014. Peninsula and Santa Cruz Mts. data from Weldon et al. (2013), Prentice et al., 2019, Streig et al. (2020) and references therein, particularly their Figure 8.

The comparison shows that with improved age models, the similarity in event sequences is striking. One key element however, is that the presence of NSAF events such as 1906 in the Cascadia Canyons was not previously known. Furthermore, it must be expected that Cascadia events should also generate event beds in Noyo Canyon at a similar 90 km range. This alone might explain much of the temporal correspondence between Southern Cascadia stratigraphy and the NSAF sequence at Noyo Canyon. In that scenario, many of the ages in Noyo Canyon could simply be replicate dates of Cascadia earthquakes. But examination of the time series shows that this explanation is alone is unlikely. Our ground truth event is 1906, which is clearly represented in both systems and is a simple turbidite on both the Noyo and

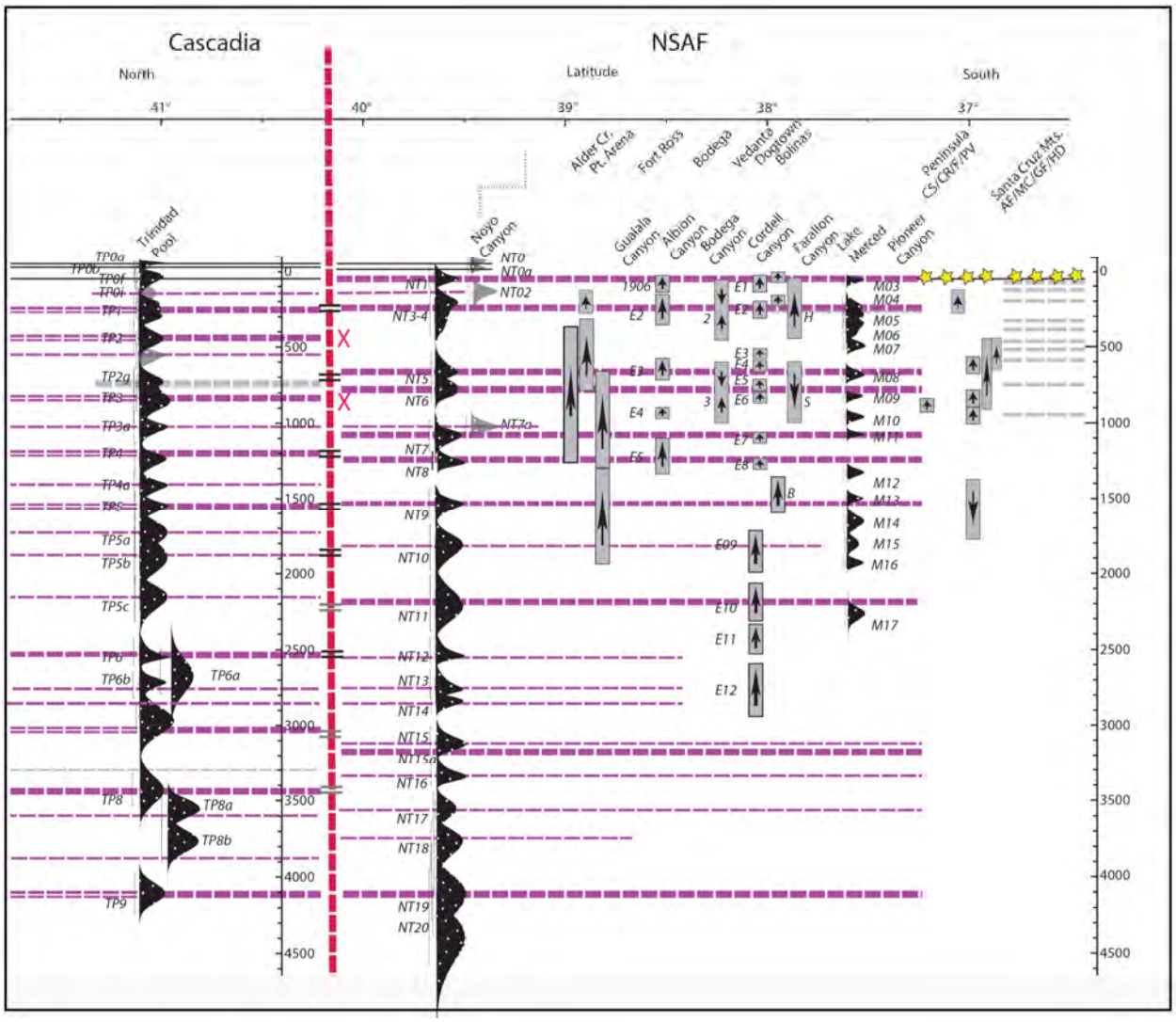

Figure 66. Space-Time diagram for southern Cascadia and the northern NSAF, zoomed to show the past ~ 3500 year time span near the triple junction. Explanation and symbology is given in Figure 65.

Cascadia sides, in fact it is much thinner and simpler in structure than the thick doublets earlier in time, and lacks the doublet character. Comparing to the next significant event in time, in the 1700 CE time range, we see a doublet in both systems, and indeed both faults are known to have had an earthquake at or

approximately at that time. With the expectation that each fault should be able to trigger turbidity currents in the opposing system, we expect to observe two events in that time range, and would normally expect to see a time separation represented by hemipelagic sediment between the two event beds. What we observe however is a doublet in both systems, neither of which shows any evidence of time separation. The nearest events in time in Trinidad Canyon are the overlying event around the 1830's, and the next underlying event at about 750 BP. On the Noyo side, we also see an event at ~ 1830, and the nearest underlying bed is ~ 700 BP. With this ~ 550-600 year time span, no other events are observed, and have no overlap with the lower bounding unit, and moderate overlap with the upper bounding event bed. On the Noyo side, the radiocarbon age ~ 1700 CE (250, 170-390 BP) is from the base of the doublet, and the larger overlying second pulse could easily erode into the finer bed below, erasing any evidence of time separation. On the Cascadia side, in Trinidad Canyon however, the weaker upper unit of the doublet is embedded in the tail of the lower, more robust bed. This is unambiguous evidence of a very short time separation, possibly as short as a few hours, to a few days if the second pulse is indeed the NSAF earthquake turbidite. The ~ 1700 event is observed southward at all sites along the NSAF including Lake Merced, a strike length of at least 280 km, and thus is a significant event. On the Cascadia side, the event is thought to be Mw ~ 9.0 with ~ 1000 km of strike length (Goldfinger et al., 2012, 2017). Given the stratigraphic evidence, the lack of alternative event beds near enough in time, and the robustness of both events, we suggest that the simplest explanation for the observed the stratigraphic evidence is that the 1700 and possibly other doublets represent both the NSAF and Cascadia Earthquakes, closely stacked, with minimal but unknown time separation. The inverted character of the Noyo doublet suggests that the more distant Cascadia megathrust could have triggered the finer lower unit, while the robust sandy upper unit was triggered shortly thereafter by the proximal NSAF earthquakes. The NSAF cuts and offsets the upper part of Noyo Canyon, and thus has an essentially zero epicentral distance to the upper canyon. On the Cascadia side, the lower unit is more robust, and the upper part of the doublet is weaker, consistent with a smaller earthquake or a more distant fault. In neither case can a more local explanation for the doublet relationships be ruled out however.

Some, but not all of the other post ~ 4100 BP doublets shown in Figure 66, appear to have a potentially similar explanation to that of the two 1700 CE events. Progressing downsection, the next event down on the Noyo side is the ~ 700 BP event, NT5, for which there is a temporal equivalent on the Cascadia side, Trinidad event T2g. In Noyo Canyon, this event is much like the other doublets, with an upper unit that is coarser. And no apparent time separation between it and the lower unit. The temporal equivalent on the Cascadia side is a complex bed with multiple coarse pulses arranged in a fining upward sequence. This event or pair of events, at ~ 700-750 BP has no known Cascadia earthquake associated with it, either in onshore or offshore data. The Cascadia side turbidite is only found in Trinidad plunge pool and other Eel Fan cores, but does not extend northward. On the NSAF side, there is a pair of events at ~ 700 and 800 BP, as on the Cascadia side, and a similarly aged pair exist also at Vedanta Marsh and Lake Merced. Fort Ross has an event that overlaps with the younger, but not the older of these two. The next event, Cascadia T3 at ~ 800 BP/ Noyo NT6, is represented in both fault systems, but is a simple single event bed in both systems, with no doublet or inverted structure. This is one of the most perplexing event pairs, with the Cascadia event T3 extending northward the full length of the subduction zone and recorded onshore, offshore and in lakes (Goldfinger et al., 2012; 2017. 2017a, Hamilton et al., 2015). On the NSAF side an event of this age is present and correlated southward in offshore cores, and with temporal correlatives at Lake Merced, Vedanta Marsh, and Noyo Canyon, but not Fort Ross (Figure 66). This event pair in both fault systems has 500 years of time above and ~ 200 years below without intervening events on the Noyo side, but the upper gap is filled on the Cascadia site by T2 and T2a. This is a pair of events that simply does not fit the model proposed.

The next sequence is Cascadia T4, which includes the previously described T4 doublet on the Cascadia side, with robust linkages northward, and a temporal equivalent in inverted doublet NT7, on the Noyo side (Figure 66). Intervening event T3a in Cascadia has no doublet equivalent in Noyo Canyon, although

there is a weak turbidite, NT7a in that stratigraphic position with that approximate age. This event has possible equivalents along the San Andreas in Lake Merced and Vedanta Marsh and Fort Ross. The lack of a doublet suggest that at Noyo Canyon, NT7a could also be the remote record of the Cascadia T3a event. Downcore, the next events in Cascadia are a series of events between T4 and T5. In much of southern Cascadia, that stratigraphic position is occupied by T4a, a weak single event. In the Trinidad pool, there are 4 event beds in that interval. We were unable to determine which of these (if any) correlate with regional T4a. On the Noyo side, event NT8 is a minor singlet with a temporal equivalent only at Lake Merced (M12). Temporally, on the Cascadia side the interval without other events is ~ 200 years above, and ~ 170 years below. On the Noyo side, the gaps are ~ 150 years above and below, not enough in either case to rule out other interpretations.

The next event downcore is Cascadia T5, a major event correlated along the length of Cascadia. This event is commonly a doublet at most sites in Cascadia, thus the doublet character at Trinidad is not diagnostic. Its age at Trinidad is 1510 (1380-1650), similar to the Cascadia margin-wide average of 1550 (1380-1730), and indistinguishable from onshore ages for this event (Goldfinger et al., 2012, Valentine et al., 2012, Padgett et al., 2021, Nelson et al., 2021). The NSAF temporal equivalent is NT9, which is a robust coarse inverted doublet (Figure 57) with a similar P-sequence model age of 1580 (1300-1830). The time intervals are ~150 years above and ~180 years below on the Cascadia side. On the Noyo side, the intervals are ~ 200 years above, and 350 years below, excluding the possibility of mis-assignment of the matching beds. NSAF temporal equivalents are observed at Dogtown and Lake Merced (M13).

The next three events are a ubiquitous series of beds present in much of central and southern Cascadia, T5a, T5b, and T5c. At all correlated Cascadia sites, T5a is faint, and T5b and T5c relatively robust, much more so in southern Cascadia. The same is true at Trinidad Canyon, with T5b and T5c unusually robust, rivalling some of the margin wide events in thickness, grain size and density. At Trinidad, all three of these events could be considered weak doublets, though the evidence is not particularly strong. On the Noyo side. T5a has no temporal equivalent there or at Vedanta, but one exists at Lake Merced (M14). T5b and T5c on the Cascadia side do have robust temporal equivalents on the Noyo side, NT10 and NT11, and both are inverted doublets (the example in M9907-49PC is deformed by coring, but the TC shows these characteristics). The NT10 age (1820, 1510-2170) is similar to the model age for Trinidad (1820, 1710-1940), and the single age for that event 1870 (1740-2010) in M9907-36PC. The NT11 age at Noyo (2170, 1810-2550), differs from the Cascadia mean of 2310 (2170-2460), but within a modest range that we think is likely radiocarbon noise. The new model age for this event at Trinidad is 2100 (1980-2220), improving the fit considerably. Adding the new model from Trinidad to the margin average for T5c generates a modified margin average of 2230 (2280-2370), still with significant overlap of Noyo NT11. Based on the strong doublet character, we prefer matching these events and think the differing times are the result of model and radiocarbon uncertainties. Both T5b and T5c have approximate temporal equivalents at Vedanta Marsh, but are too old for the Fort Ross and Lake Merced records.

Below this depth, the Trinidad record becomes more difficult to interpret due to higher turbidite frequency and increased uncertainty of correlation of event beds to the north, and therefore their association with regional seismo-turbidites. This frequency change may have resulted from possible terrestrial influence, or perhaps a spate of earthquakes from multiple sources. In any case, we attempt to correlate the margin wide events to include T6, T7, T8 and T9 primarily based on log correlation, the age models, and the thicker denser beds at Trinidad, but this linkage has increased uncertainty and should be treated with caution. Cascadia T6, if interpreted correctly at Trinidad, has a model age of 2520 (2380-2710), similar to onshore ages, the marine average (2540, 2390-2680) and to the direct age from Trinidad of 2440 (2280-2620). On the Noyo side, NT12 is a simple singlet, with a similar model age of 2570 (2260-2800). This event has a temporal correlative in E11 at Vedanta, but is too old for Fort Ross and Lake Merced. Cascadia event T6a has an age of ~ 2730 (2580-2870) derived from the Rogue analytical model, and has a potential Noyo temporal equivalent in NT13 at 2770 (2600-2930). This event is also not

a doublet, and has a temporal equivalent in E12 at Vedanta, the oldest event at that site, and is too old for Fort Ross or Lake Merced. Cascadia major event T7 has a mean age of 3030 (2870-3160) in Cascadia, and has a Noyo temporal equivalent in doublet NT15, which has a model age of 3190 (2970-3400). While significantly overlapped at 2 sigma, this age difference is greater than most of the other doublets (Figure 66). Cascadia T8, with a margin average of 3440 (3270-3610), but no direct Trinidad age or model age, has temporal overlap with both Noyo beds NT16 and NT17. NT16 has a direct age of 3320 (3210-3450), and model age of 3350 (3150-3530). This age is one of the larger doublet misfits with Cascadia, and with the Noyo OxCal model as well. NT17 is a singlet with similar offset in time to NT16, but older on the Noyo side. Finally, Cascadia T9 has an average age of 4110 (3940-4300). On the Noyo side, potential correlative event is NT17, with a model age of 4100 (3760-4560) and is a doublet bed, though not inverted or unusually thick.

In the remainder of the Noyo record, which extends to ~ 13,400 BP in core M9907-49PC, there are few inverted doublets, and none with the robust thickened character noted above. This change in character suggests either a change in character of NSAF earthquakes, a change in the hydrodynamics of the Noyo turbidity currents, or possibly that Cascadia and the NSAF were not partially synchronized as they seem to have been after ~ 4000 BP.

Table 3 summarizes criteria for evaluating the triggering hypothesis. In addition to radiocarbon overlap, and the presence of the unusual doublets, we further suggest that in the event that one fault triggers the other producing doublet stratigraphy, these doublets should fade with distance from the triple junction. Additionally, the additional bed thickness created at sites proximal to the triple junction should also thin away from the triple junction. Local factors and sedimentation rates of course would modify these expected trends. These criteria are included in Table 3, and we note the many, but not all the doublet event beds are consistent with these criteria.

Table 3. Turbidite characteristics along strike, Northcoast NSAF

Noyo Event	Doublet?	Inverted?	Thick?	Noyo Doublet Fades southward?	Noyo Bed Thins southward?	Casc. Doublet Fades northward?	Casc. Bed Thins northward?	Along-strike extent	Cascadia radio-cabon overlap	NSAF onshore overlap?	Lake Merced overlap?	Cascadia Doublet?
T1 (1906)	No	NA	No	NA	No	NA	Yes	full	No	All	Yes, M03	No
T3-4	Yes	Yes	Yes	Yes, lower	Yes	Yes	possible*	Full	Yes, T1	FR-E2, B-2, V-E2, Bo-"H"	M04	yes
T5-5a	Yes	Yes	Yes	Yes	Yes	Yes	Yes*	Full	Yes, T2g	Yes, FR-E3, B-3, V-E4, B-"S"	M07	Yes
T6	No	NA	No	NA	No	NA	Yes*	Full	Yes, T3	Yes, B 3, V E5, E6, Bo "S"	Yes, M8	Yes*
T7a-7	Yes	No	Yes	Yes, Upper	Yes	Yes	Yes*, T4	Full	Yes, T3a, T4	Yes, FR E5, VE7	Yes, M10	Yes**
T8	No	No	No	NA	No, thickens	NA	no*	Full	Yes T4a	Yes, V E8, FR E5	Yes, M11	?
T9	Yes	Yes	Yes	Yes, Lower	Yes	No	Yes*	Full	Yes, T5	No	Yes, M12	Yes
T10	Yes	Yes	Yes	Yes, Lower	No	NA	Yes*	Nearly Full	Yes, T5b	Yes, V 09	Yes, M14	No
T11	Yes	Yes	Yes	Yes, lower	No	NA	Yes*	Full	Yes, T5c	Yes, V E10	Older than LM	No
T12	Yes	Yes	Yes	No	No	?	No*	Bodega	Yes, T6	older than all land sites	Older than LM	?
T13	No	NA	No	NA	No	?	Ye*s	Bodega	Yes, T6a, T6b	older than all land sites	Older than LM	?
T14	No	NA	No	NA	No	?	Yes*	Bodega	Yes, T6a, T6b	older than all land sites	Older than LM	?
T15	No	NA	No	NA	Yes	?	?	Bodega	Yes, T7	older than all land sites	Older than LM	?
T15a-T16	Yes	Yes	Yes	Yes	Yes	?	?	Full	Yes, T8	older than all land sites	Older than LM	?
T17	Yes	No	No	Noyo only	No	?	?	Full	Yes, T8a	older than all land sites	Older than LM	?
T18	Yes	No	No	, terminates at Gual	No	?	?	Gualala	Yes, T8b	older than all land sites	Older than LM	?
T19	Yes	No	Yes	Yes	Yes	?	?	Full	Yes, T9	older than all land sites	Older than LM	?

FR= Fort Ross; B=Bodega; Bo=Bolinas; V=Vedanta; LM = Lake Merced
*if T2g is the pair
**This may be consistent with NSAF rupture preceding Cascadia

Colors indicate fit to the triggering model. Green = Best Fit; Yellow = good fit; Blue = poor or no fit

In all, in the last 4100 years, we suggest that 6 Cascadia-Noyo pairs are the most likely candidates for a stress triggering relationship, having both the inverted doublets in Noyo, good temporal match, and for three of them, a clear doublet on the Cascadia side. There are three other possible matches, with reduced temporal overlap but with Noyo inverted doublets, and two pairs with temporal overlap, but no doublet character. This represents 8 of 16 significant Cascadia events having good temporal match and doublet character in one or both fault systems, and excludes none of the major margin-wide Cascadia events with the single exception of T2, the smallest of them. It includes 12 of 16 events considering temporal overlap with 8 having doublet character. Of the smaller southern segment events, this includes of 6 of 8 events. On the Noyo side, there are 8 significant events with both close overlap and doublet character of a total of

13. Of those, 10 of them have temporal equivalents at one or more land sites to the south, 7 of them observed at multiple sites.

The abrupt change at ~ 4100 years BP from variable simple or complex event beds in Noyo Canyon at earlier times, to complex inverted doublets at about that time corresponds with no known change in the NSAF, although the Lake Merced and Vedanta records do not extend to earlier times. As Noyo Canyon is not directly connected to any river system, we consider it is unlikely that climate change and or sediment supply could account for this abrupt character change. During the period where the doublets are observed, the average recurrence time on the NSAF is ~ 250 years in Noyo Canyon. For the remainder of the Holocene, the recurrence average is greater, at ~ 370 years. At the same time, the recurrence period decreases significantly on the Cascadia side, some of which might partially be attributed to recording of asynchronous NSAF events. One might expect that the Noyo Canon record to increase in bed frequency for periods where the faults were not partially synchronized, our preferred interpretation. That they are not is perplexing, since both faults should then be recorded asynchronously, decreasing the recurrence time. This suggests either problems with our model, or longer-term energy cycling that is influencing one or both faults.

Head to Head Age Comparisons

We further address direct comparisons between potential correlatives on the Cascadia and Noyo Canyon sides of the triple junction by performing simple statistical comparisons of the radiocarbon ages. Age models are powerful tools for comparisons of sequences as shown in the previous sections, but may be somewhat compromised in comparing single event ages as they can be shifted away from their associated radiocarbon ages in order to arrive at a best fitting sequence in the Bayesian p-sequence models. In comparing head to head ages we give up some of the advantages of the depositional models in order to focus on comparing individual events. In the following analyses, we compare event ages of temporal correlatives statistically. The ages are recalibrated, and a simple correction applied to each to offset the age for its correct depth below the event bed. This is the same correction used in the OxCal P-Sequence models to position the sample correctly in the vertical sequence. The method uses the OxCal combine function and is as described in the methods section. As simple metrics for these comparisons, we use the OxCal combine function to test the age overlaps of probability functions between southern Cascadia at Trinidad and Eel channels, and the NSAF at Noyo Canyon. OxCal provides two functions, Combine and R_Combine for comparisons of radiocarbon ages. If two or more Radiocarbon determinations are from the same source (Radiocarbon reservoir) then they can be merged using R_Combine to result in a single calibrated date with a narrower uncertainty range. If two ages are thought to be coeval, but not from the same source, then merging by the Combine function is appropriate (Ramsey, 2010, Ward and Wilson, 1978, Wilson & Ward 1981). In this case we use the Combine function as the radiocarbon source is not the same. In this case we compare samples from different sources and compare the PDF's with a Chi^2 comparison and the OxCal Acombine function. The null hypothesis in the following examples is that the distributions have no connection. The Chi^2 test provides a test statistic that if smaller than the critical value at the 5% level (95% confidence) rejects the null hypothesis. The Acombine function measures the overlap of the PDF's. The minimum criteria for this test is $1/\sqrt{(2n)}$, with n = the number of ages. These comparisons will use two ages, thus N=2 and the criteria will be = 0.7071. This value is expressed as a percent, and may exceed 100%.

Cascadia T1

To compare the Cascadia T1 age with potential correlative Noyo event T3-4, we use several T1 ages from southern Cascadia to Noyo Canyon ages. Figure 67 shows two such comparisons, Cascadia sample 39 and Cascadia sample 38 to the Noyo age for T3-4, sample 50b. Two OxCal combines were done and each of the Cascadia and Noyo ages are compared. The combines yielded a rejection of the null

hypothesis that there is no relation between the distributions at well above the 95% confidence limit, shown in the lower right of each panel. The overlap of the PDF's is expressed as between 110% and 117% for these ages. Individual agreements are shown in the panels.

Cascadia T2g

To compare the Cascadia T2g age with potential correlative Noyo event T5, we use a T2g age from southern Cascadia at the Trinidad plunge pool for comparison to Noyo Canyon ages. Figure 68 shows two such comparisons, Cascadia sample 211 is compared to the Noyo age for NT5, sample 87-87b, and another to Noyo sample 51-51b. The combines yielded a rejection of the null hypothesis that there is no relation between the distributions at well above the 95% confidence limit, shown in the lower right of each panel in Figure 68. The overlap of the PDF's is expressed as the Acomb statistic of 110 and 118% respectively. Individual agreements are shown in the panels. A third comparison would include Cascadia sample 215 to Noyo Canyon, but this sample is likely contaminated, and is ~ 70 years older than the preferred sample 211. These comparisons have at least one complication making them more problematic. The age range (~ 800BP) includes a time for which Goldfinger et al. (2012) inferred a reservoir excursion from the 20th century value. We include this excursion of ~ 100 years for the Trinidad age. Omitting this reservoir excursion results in a mismatch of the Trinidad P-sequence age

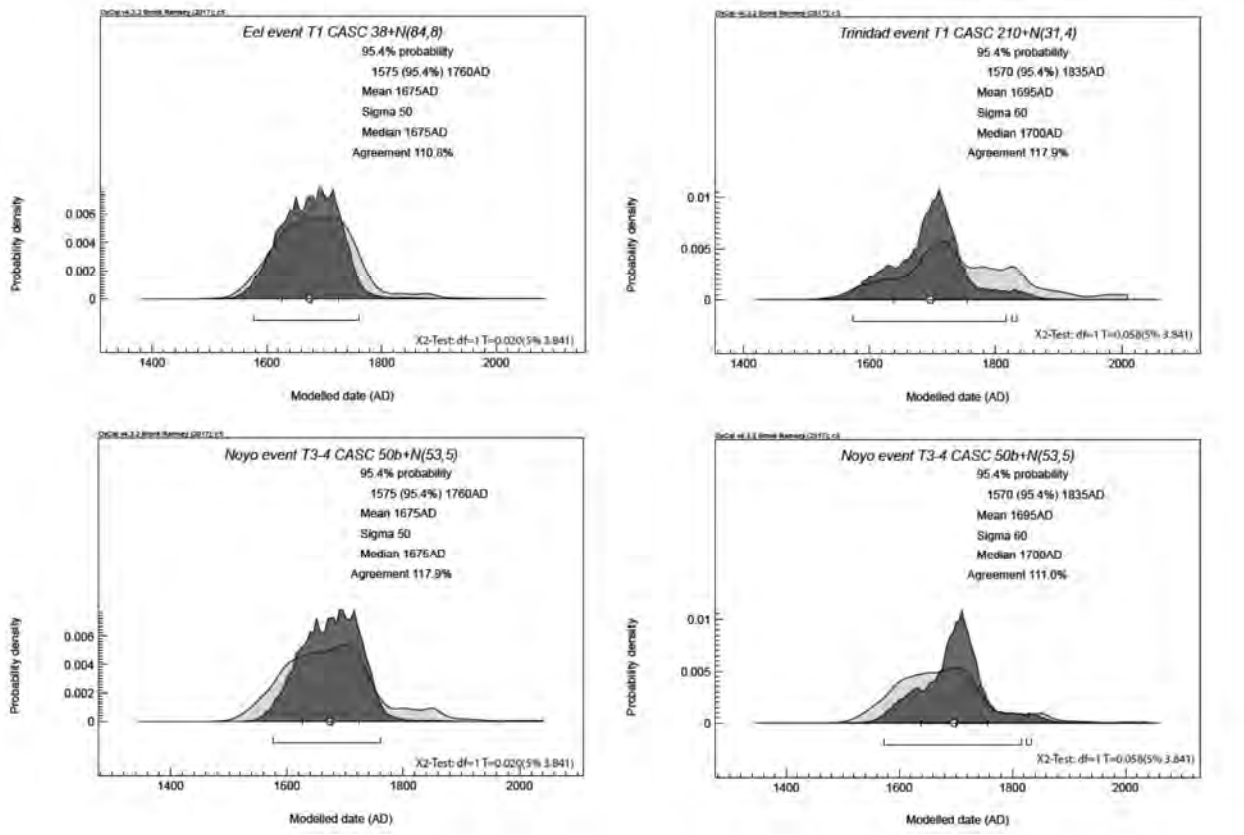

Figure 67. Comparisons of Cascadia T1 ages and Noyo Canyon T3-4 ages. A and B. Comparisons of T1 age Casc. 38 vs. the combined age of Casc 38 and Noyo 50b (dark shade). C and D. Comparisons of T1 age Casc. 210 vs. the combined age of Casc. 210 and Noyo 50b (dark shade).

model and the individual age of T2g. At Noyo Canyon, 200 km to the south, we see no evidence of this reservoir excursion, though constraints are limited. The primary constraint is the good match of the age model as shown in Figure 68, and the single radiocarbon age for sample 87-87b. With a lack of evidence for it, and this good fit, we did not apply the southern CSZ reservoir excursion to the Noyo age for sample 87-87b. This may or not be correct. We note that such a reservoir excursion of limited spatial range may well fall within the variability of the upwelling driven by the California current as discussed in Goldfinger et al 2012). Including this correction results in a strong match between the two events, while omitting the correction results in a Cascadia event age inconsistent with any known event on either the CSZ or the NSAF. Considering that Cascadia event T2g is a significant event, this latter possibility is not considered likely, but cannot be excluded.

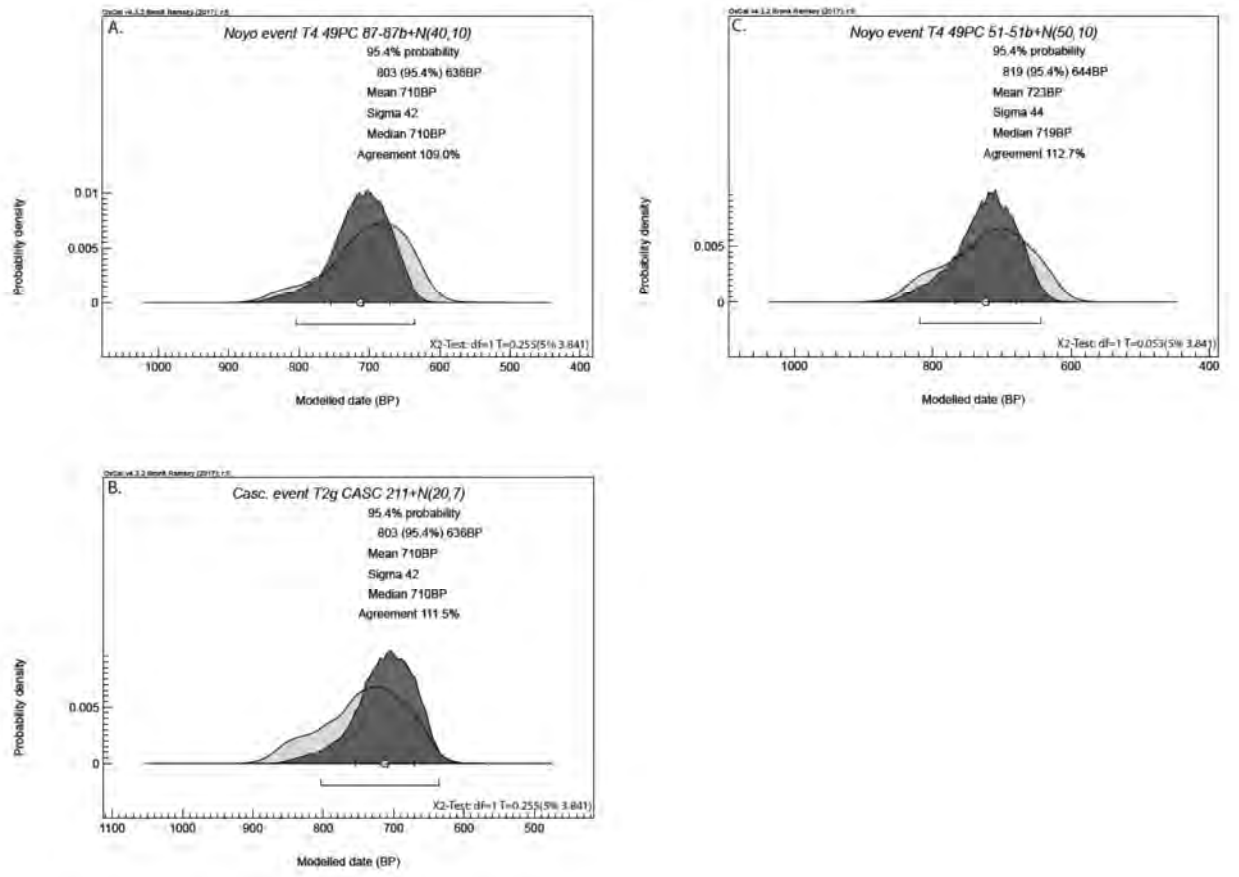

Figure 68. Comparisons of Cascadia T2g ages and Noyo Canyon NT5 age. A. Comparisons of Cascadia age T2g (sample Casc. 211) vs. the combined age of Casc 211 and Noyo 87-87b (dark shade). B. Comparisons of Noyo age T5 (sample 87-87b) vs. the combined age of Casc 211 and Noyo 87-87b (dark shade). C. Comparisons of Noyo age T5 (sample 51-51b) vs. the combined age of Casc 211 and Noyo 51-51bb (dark shade).

Cascadia T3

To compare the Cascadia T3 age with potential correlative Noyo event T6, we use a two T3 ages from southern Cascadia at the Trinidad plunge pool for comparison to the available Noyo Canyon ages. Figure

69 shows two such comparisons, Cascadia samples 213 and 278 are compared to the Noyo age for T6, sample 59. Another Noyo age, sample 33 is ~ 100 years older sample 59, and is rejected. The combines yielded a rejection of the null hypothesis that there is no relation between the distributions at well above the 95% confidence limit, shown in the lower right of each panel in Figure 69. The overlap of the PDF's is expressed as the Acomb statistic of 130%, with Amodel agreement at 125% . Individual agreements are shown in the panels. These two comparisons the same reservoir excursion as discussed above for Cascadia T2g. Omitting this reservoir excursion results in a mismatch of the Trinidad P-sequence age model and the individual age of T3. At Noyo Canyon, 200 km to the south, we see no evidence of this reservoir excursion, though constraints are limited. The primary constraint is the good match of the age model as shown in Figure 69, and the single radiocarbon age for sample 59. With a lack of evidence for it, and this good fit, we did not apply the southern CSZ reservoir excursion to the Noyo age for sample 59. Including this correction results in a strong match between the two events, while omitting the correction results in a Cascadia event age inconsistent with any known event on either the CSZ or the NSAF. Considering that Cascadia event T3 is a major correlated event, this latter possibility is not considered likely, but cannot be excluded.

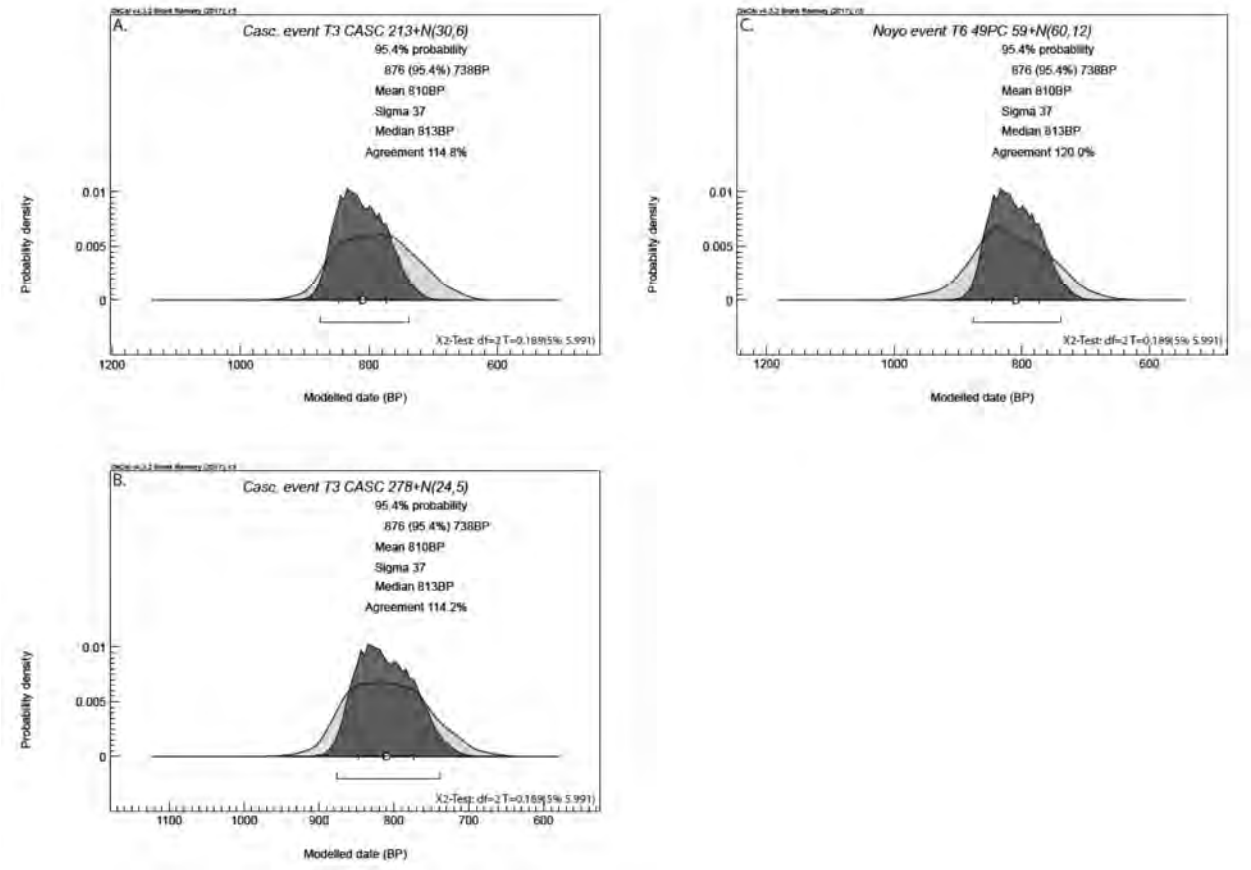

Figure 69. Comparisons of Cascadia T3 ages and the Noyo Canyon NT6 age. A. Comparisons of the Cascadia T2g age (sample Casc. 213) vs. the combined age of Casc 213, 278 and Noyo 59 (dark shade). B. Comparisons of Cascadia age of T3 (sample 278) vs. the combined age of Casc 278, 213 and Noyo 59 (dark shade). C. Comparisons of the Noyo T6 age (sample 59) vs. the combined age of Casc 213 and 278 and Noyo sample 59 (dark shade).

Cascadia T4

To compare the Cascadia T4 age with potential correlative Noyo event T7, we use the T4 age from southern Cascadia at the Trinidad plunge pool for comparison to the available Noyo Canyon age from RR0207 54 KC. Figure 70 shows one such comparison, Cascadia sample 283 is compared to the Noyo age for T7, sample 76. The combine yielded a rejection of the null hypothesis that there is no relation between the distributions at well above the 95% confidence limit, shown in the lower right of each panel in Figure 70. The overlap of the PDF's is expressed as the Acomb statistic of 125%, with Amodel agreement at 125% . Individual agreements are shown in the panels.

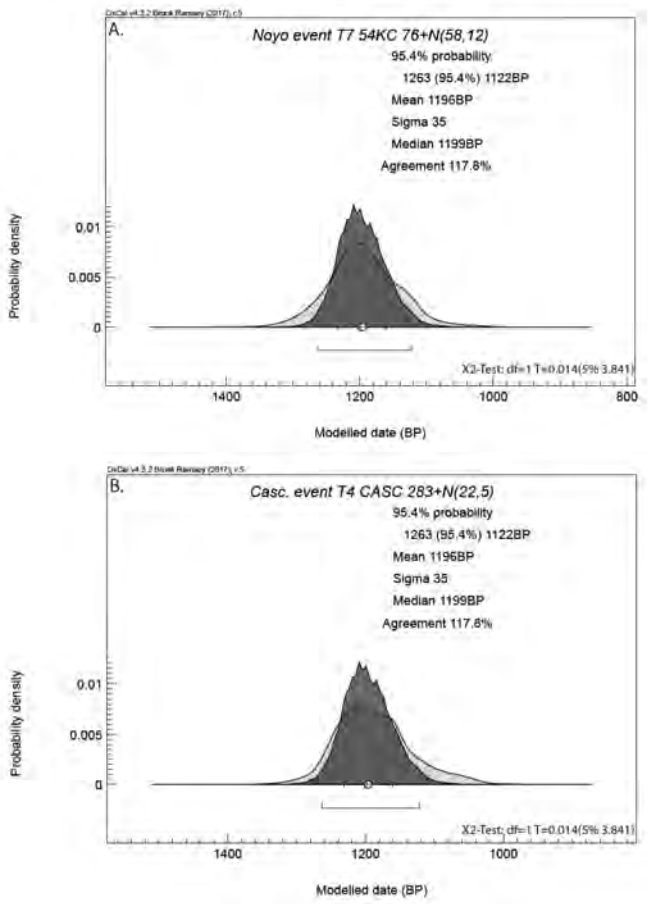

Figure 70. Comparisons of the Cascadia T4 age and the Noyo Canyon NT7 age. A. Comparison of the Cascadia T4 age (sample Casc. 283) vs. the combined age of Noyo sample 76 and Casc. 283 (dark shade). B. Comparisons of the Cascadia age of T4 (sample 283) vs. the combined age of Casc 283 and Noyo sample 76 (dark shade).

Cascadia T4a

In the high-resolution Trinidad record, there are multiple events for which model ages exist between T4 and T5. The regional model age of 1370 (1260-1500) for T4a is based on age model at Rogue Canyon. The age model at Trinidad has an event of similar age (T4a2: 1350 (1250-1460)), and this event is shown in the age model and space time diagram, however it cannot be reliably correlated to T4a as observed at Rogue Apron. The similar age from Noyo Canyon for event T8 is 1370 (1230-1500). Individual agreements are shown in the panels.

Cascadia T5

Cascadia T5 is an easily correlated major event in the southern CSZ, and also has a time equivalent in the form of a major event doublet in Noyo Canyon. The Cascadia T5 age, represented by sample Casc. 284 is compared to the age of T9 on Noyo canyon, best represented by the OxCal model age for that event, as it has not been dated directly. Figure 71 shows this comparison. The combine yielded a rejection of the null hypothesis that there is no relation between the distributions at well above the 95% confidence limit, shown in the lower right of each panel in Figure 71. The overlap of the PDF's is expressed as the Acomb statistic of 122%, with Amodel agreement at 120%. Individual agreements are shown in the panels.

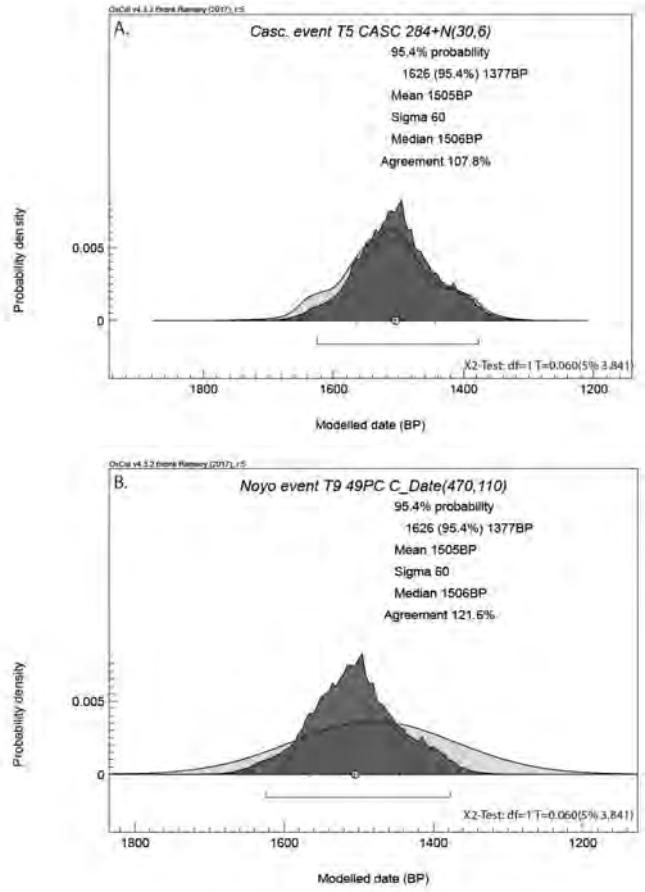

Figure 71. Comparison of the Cascadia T5 age and the Noyo Canyon NT9 age. A. Comparison of the Cascadia T5 age (sample Casc. 284) vs. the combined age of Noyo T9 model age and Casc. 284 (dark shade). B. Comparisons of the Noyo T9 model age vs. the combined age of Casc 284 and Noyo T9 model age (dark shade).

Cascadia T5b

Cascadia T5b is an easily correlated major event in the southern CSZ, and also has a time equivalent in the form of a major event doublet in Noyo Canyon. The Cascadia T5b age, represented by sample Casc. 33 is compared to the age of T10 in Noyo canyon, best represented by the OxCal model age for that event, as it has not been dated directly. Figure 72 shows this comparison. The combine yielded a

rejection of the null hypothesis that there is no relation between the distributions at well above the 95% confidence limit, shown in the lower right of each panel in Figure 72. The overlap of the PDF's is expressed as the Acomb statistic of 124%, with Amodel agreement at 121%. Individual agreements are shown in the panels.

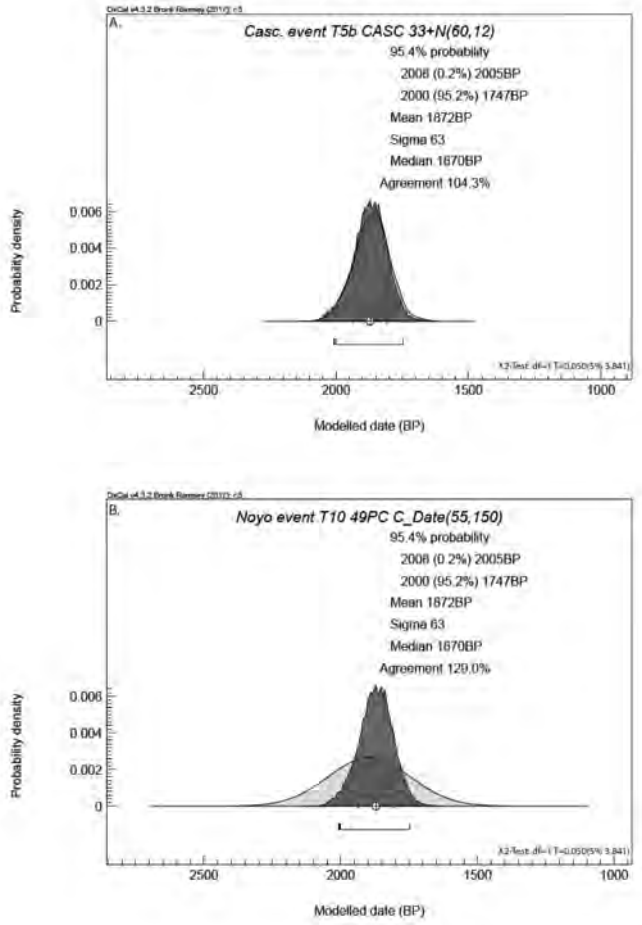

Figure 72. Comparison of the Cascadia T5b age and the Noyo Canyon NT11 age. A. Comparison of the Cascadia T5b age (sample Casc. 33) vs. the combined age of the Noyo T10 model age and Casc. 33 (dark shade). B. Comparisons of the Noyo T10 model age vs. the combined age of Casc 33 and Noyo T10 model age (dark shade).

Cascadia T5c

Cascadia T5c is an easily correlated major event in the southern CSZ, and also has a time equivalent in the form of a major event doublet in Noyo Canyon. The Cascadia T5c age, represented by sample Casc. 285 is compared to the age of T11 in Noyo canyon, best represented by the OxCal model age for that event, as it has not been dated directly. Figure 73 shows this comparison. The combine yielded a rejection of the null hypothesis that there is no relation between the distributions at the 95% confidence limit, shown in the lower right of each panel in Figure 73. The overlap of the PDF's is expressed as the Acomb statistic of 94%, with Amodel agreement at 91%. Individual agreements are shown in the panels. While these values are statistically acceptable, the fit is far less strong than shown for other pairings.

This is because the Cascadia T5c age (sample 285) is younger than expected for this event, and younger than other ages for this correlated event at Rogue Apron and other sites. The age for this event is corrected from benthic forams as discussed in Goldfinger et al. (2012), adding uncertainty, and there always remains the possibility of mis-correlation.

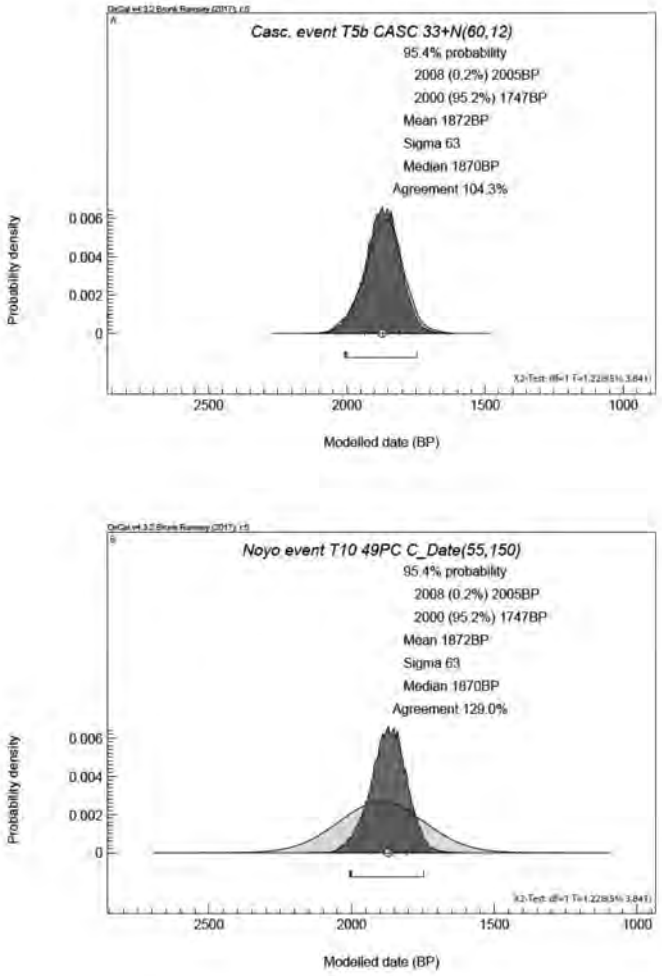

Figure 73. Comparison of the Cascadia T5c age and the Noyo Canyon NT11 age. A. Comparison of the Cascadia T5c age (sample Casc. 285) vs. the combined age of the Noyo T11 model age and Casc. 285 (dark shade). B. Comparisons of the Noyo T11 model age vs. the combined age of Casc 285 and Noyo T11 model age (dark shade).

Cascadia T6

Cascadia T6 is an easily correlated major event in the southern CSZ, and also has a time equivalent in the form of a major event doublet in Noyo Canyon. The Cascadia T6 age, represented by sample Casc. 66 is compared to the age of T12 in Noyo canyon, best represented by the OxCal model age for that event, as the radiocarbon age for that event is reversed. Figure 74 shows this comparison. The combine yielded a rejection of the null hypothesis that there is no relation between the distributions at well above the 95% confidence limit, shown in the lower right of each panel in Figure 74. The overlap of the PDF's is

expressed as the Acomb statistic of 120%, with Amodel agreement at 117%. Individual agreements are shown in the panels.

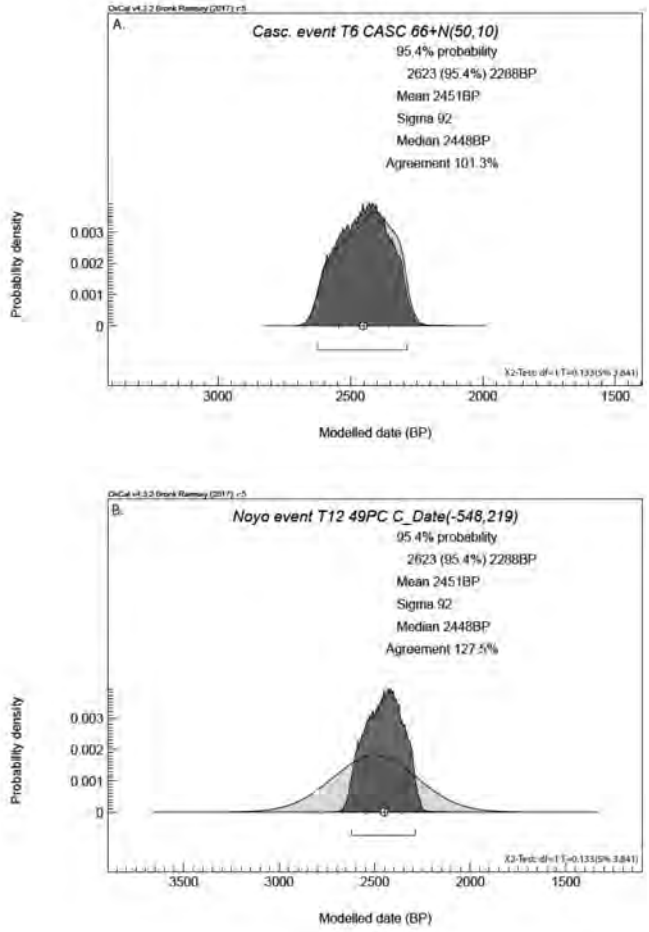

Figure 74. Comparison of the Cascadia T6 age and the Noyo Canyon NT12 age. A. Comparison of the Cascadia T6 age (sample Casc. 66) vs. the combined age of the Noyo T12 model age and Casc. 66 (dark shade). B. Comparisons of the Noyo T12 model age vs. the combined age of Casc 66 and Noyo T12 model age (dark shade).

Cascadia T6a

Cascadia T6a is faint event in much of the southern CSZ, and also has a time equivalent in the form of a major event doublet in Noyo Canyon. T6a is not dated directly, and its Trinidad model age is compared to the age of T13 in Noyo Canyon, best represented by the Noyo model age for Noyo T13. Figure 75 shows this comparison. The combine yielded a rejection of the null hypothesis that there is no relation between the distributions at well above the 95% confidence limit, shown in the lower right of each panel in Figure 75. The overlap of the PDF's is expressed as the Acomb statistic of 124%, with Amodel agreement at 121%. The correlation of T6b with other sites in the southern CSZ is less reliable that that for the major event beds. Individual agreements are shown in the panels.

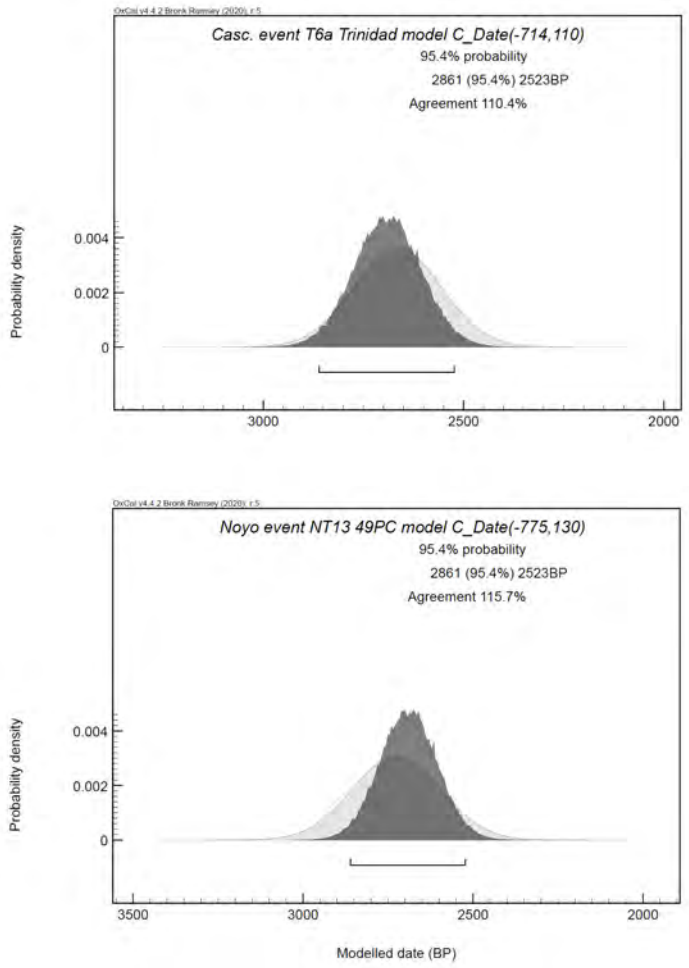

Figure 75. Comparison of the Cascadia T6a age and the Noyo Canyon NT13 age. A. Comparison of the Cascadia T6a model age vs. the combined age of the Noyo NT13 model age and Casc. 66 (dark shade). B. Comparisons of the Noyo NT13 model age vs. the combined age of Casc T6a and Noyo NT13 model age (dark shade).

Cascadia T6b

Cascadia T6b is faint event in much of the southern CSZ, and also has a time equivalent in the form of a major event doublet in Noyo Canyon. The Cascadia T6a age, represented by sample Casc. 287 is compared to the age of T14 in Noyo Canyon, best represented by Cascadia sample 18. Figure 76 shows this comparison. The combine yielded a rejection of the null hypothesis that there is no relation between the distributions at well above the 95% confidence limit, shown in the lower right of each panel in Figure 76. The overlap of the PDF's is expressed as the Acomb statistic of 124%, with Amodel agreement at 121%. The correlation of T6b with other sites in the southern CSZ is less reliable that that for the major event beds. Individual agreements are shown in the panels.

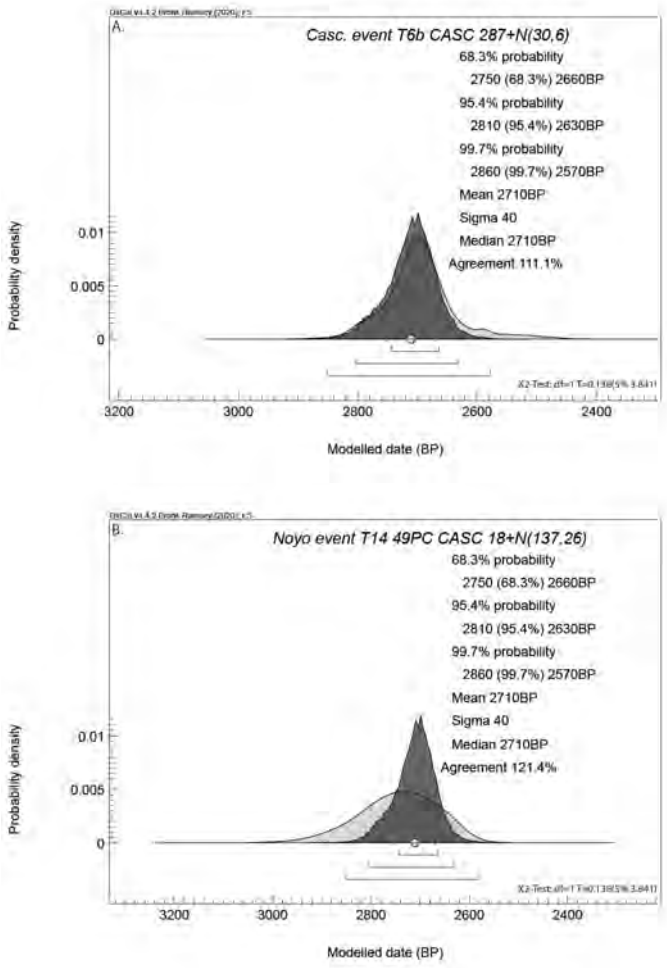

Figure 76. Comparison of the Cascadia T6b age and the Noyo Canyon T14 age. A. Comparison of the Cascadia T6b age (sample Casc. 287) vs. the combined age of the Noyo T14 model age and Casc. 287 (dark shade). B. Comparisons of the Noyo T14 model age vs. the combined age of Casc 287 and Noyo T14 model age (dark shade).

Cascadia T7

Cascadia T7 is an easily correlated major event throughout the CSZ, and also has an approximate time equivalent in the form of a major event doublet in Noyo Canyon event T15. At nether Trinidad nor Noyo was this event dated directly. To compare them we use the depositional model ages for both sites, and also compare to the regional model age from the OxCal combine presented in Goldfinger et al., (2012). In Figure 77, the Cascadia T7 age, represented by the Oxcal regional combined age is compared to the combination of that age and the Noyo model age in panel A, and the Noyo model age is compared to this combination in panel B. Panel C shows the T7 Trinidad model age compared to the combination of that age and the Noyo model age, and Panel D shows the Noyo model age as compared to this combination. The combine of the regional Trinidad age yielded a rejection of the null hypothesis that there is no relation between the distributions at well above the 95% confidence limit, shown in the lower right of each panel in Figure 77 A and B. The overlap of the PDF's is expressed as the Acomb statistic of 95%, with Amodel agreement at 90.4%. The combine of the Trinidad specific model age yielded a rejection of the null hypothesis that there is no relation between the distributions at well above the 95% confidence limit, shown in the lower right of each panel in Figure 77 C and D. The

overlap of the PDF's is expressed as the Acomb statistic of 123%, with Amodel agreement at 119%. Individual agreements are shown in the panels.

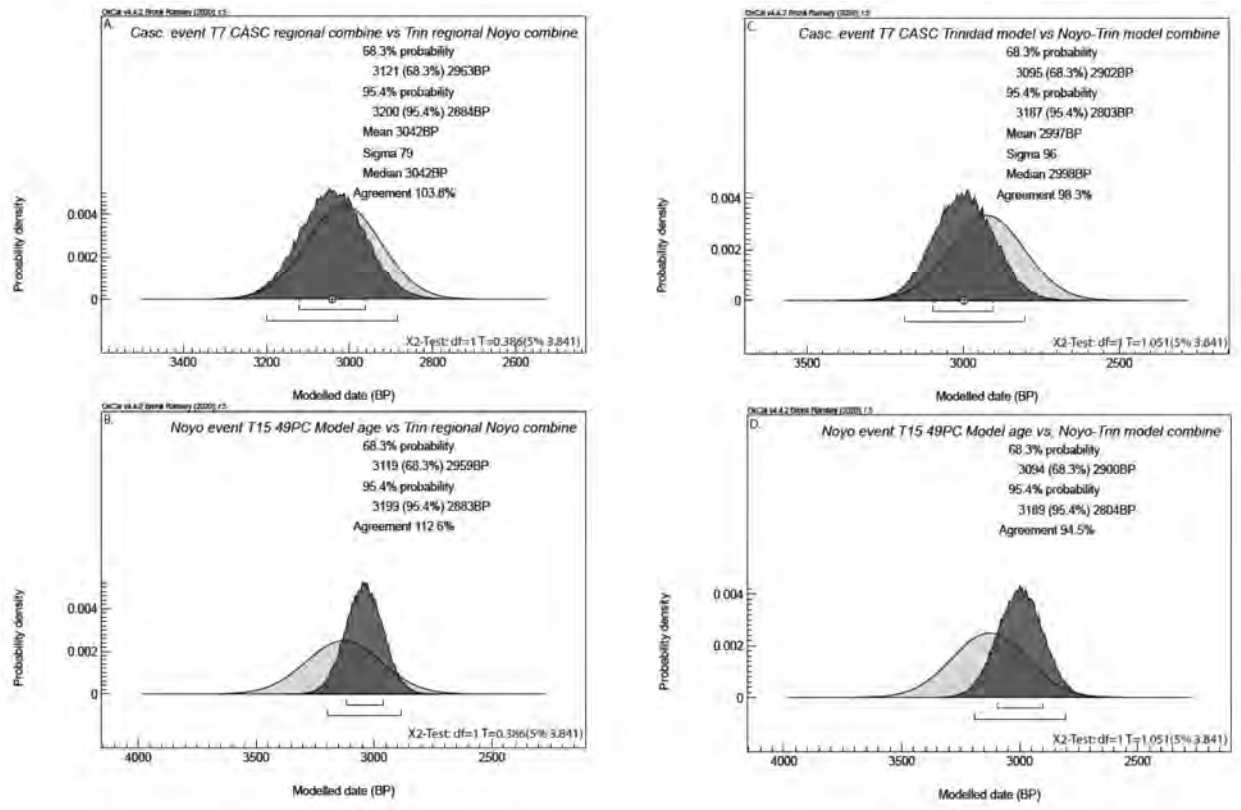

Figure 77. Comparisons of Cascadia T7 ages and Noyo Canyon T15 ages. A Comparison of the T7 age from the regional OxCal Combine of Goldfinger et al. (2012) vs. the combined Regional T7 age and Noyo T15 model age (dark shade). B. Comparison of the model age for T7 from the Trinidad M9907 36PC model vs. the combined regional T7 age and Noyo T15 model age (dark shade). C. Comparison of the model age for T7 from the Trinidad M9907 36PC model vs. the combined Trinidad model T7 age and Noyo T15 model age (dark shade). D. Comparison of the Noyo T15 model age vs. the combined Trinidad model T7 age and Noyo T15 model age (dark shade).

Cascadia T8

Cascadia T8 is an easily correlated major event throughout the CSZ, and also has a time equivalent in the form of a major event doublet in Noyo Canyon event T16. At Noyo Canyon the event was dated directly, but was not at Trinidad. To compare them we use the depositional model age for Trinidad, and a nearby age from Klamath apron (sample 75) and compare these to the Noyo Canyon sample 82 age. In Figure 78, the Trinidad model age for T8 is compared to the combination of that age and the Noyo sample 82 age in panel A, and the Noyo sample 82 age is compared to this combination in panel B. Panel C shows the T8 Klamath sample 75 age compared to the combination of that age and the Noyo sample 82 age, and Panel D shows the Noyo model age as compared to this combination. The combine of the regional Trinidad age yielded a rejection of the null hypothesis that there is no relation between the distributions at well above the 95% confidence limit, shown in the lower right of panels A and B. For the Trinidad model age comparison, the overlap of the PDF's is expressed as the Acomb statistic of 118%, with Amodel agreement at 115.8%. The combine of the Klamath sample 75 age yielded a rejection of the null hypothesis that there is no relation between the distributions at well above the 95% confidence limit,

shown in the lower right of each panel in Figure 78 C and D. The overlap of the PDF's is expressed as the Acomb statistic of 123%, with Amodel agreement at 119%. Individual agreements are shown in the panels.

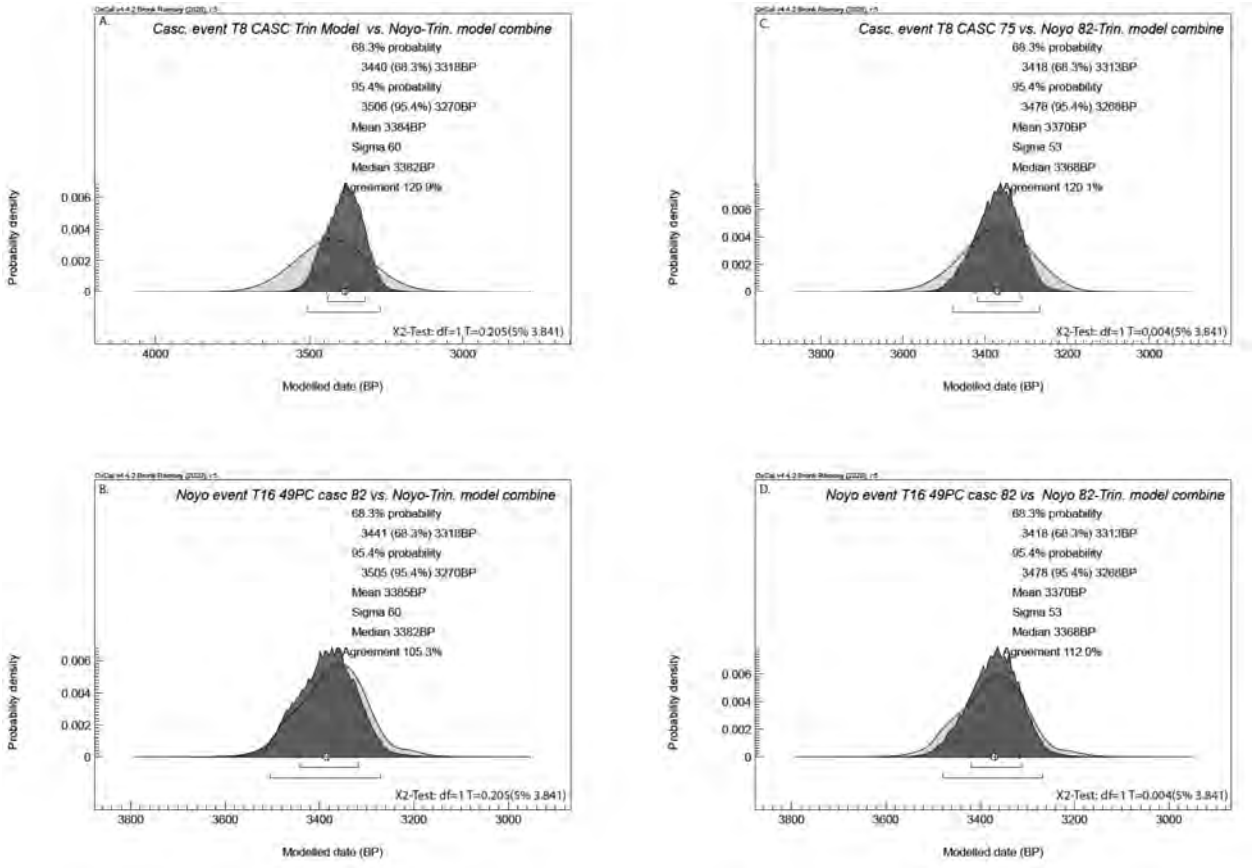

Figure 78. Comparisons of Cascadia T8 ages and Noyo Canyon T16 ages. A. Comparison of the T8 age from the Trinidad model age vs. the combined Trinidad model age and Noyo T16 sample 82 age (dark shade). B. Comparison of the Noyo sample 82 age vs. the combined Trinidad T8 model age and Noyo T16 sample 82 age (dark shade). C. Comparison of the Klamath T8 sample 75 age vs. the combined Klamath T8 sample 75 age and Noyo T16 sample 82 age (dark shade). D. Comparison of the Noyo T16 sample 82 age vs. the combined Klamath T8 sample 75 age and Noyo T16 sample 82 age (dark shade).

Depositional Model

We propose a depositional model for the southern Cascadia and northern NSAF turbidites that satisfies the observations in terms these elements: 1) The likely close timing between Cascadia and NSAF events; 2) The doublet stratigraphy observed in southern Cascadia and the northernmost NSAF, with strongly inverted doublets the norm in Noyo Canyon; 3) The rapid fading of doublet stratigraphy north and south of the triple junction; 4) The tendency for expanded thickness of the beds that have the doublet character; and 5) The lack of a doubling of the turbidite frequency that would result in independent rupture of the two faults, but the demonstrated ability to trigger turbidity currents at sites along the opposing fault. Figure 79 shows this sequence. In the first stage, a Cascadia earthquake occurs, triggering a robust turbidity current on the Cascadia side systems, and depositing a coarse bed. A weaker turbidity current is triggered simultaneously on the NSAF, at 90 km from the southern boundary of Cascadia deposit a silty bed. In the second stage an NSAF earthquake occurs a short time later,

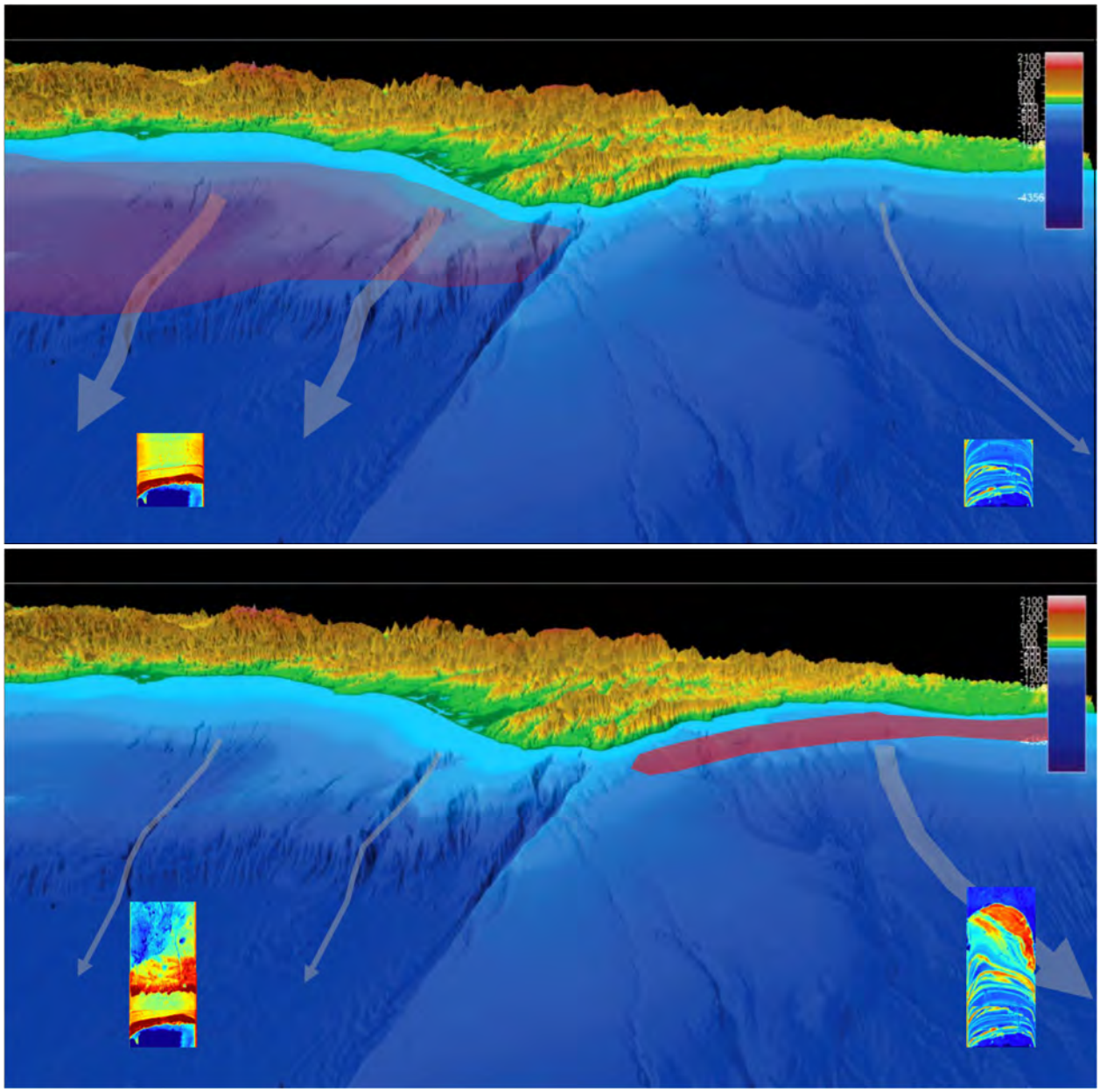

Figure 79. Two stage depositional sequence proposed for a Cascadia-NSAF stress interaction. In the first panel, a Cascadia earthquake occurs, triggering a robust turbidity current on the Cascadia side systems, and depositing a coarse bed. A weaker turbidity current is triggered simultaneously on the NSAF, at 90 km from the southern boundary of Cascadia, depositing a silty bed. In the second panel, an NSAF earthquake occurs a short time later, triggering a weak turbidity current in Cascadia, at 90 km range, depositing a silty bed, and generates a robust sand-bearing turbidity current in Noyo Canyon, creating the upper parts of the doublets. The results is a normally graded doublet on the Cascadia side, and an inverted doublet on the Noyo side.

triggering a weak turbidity current in Cascadia, at 90 km range, depositing a silty bed, and a robust sand-bearing turbidity current in Noyo Canyon, creating the upper parts of the doublets. The results is a normally graded doublet on the Cascadia side, and an inverted doublet on the Noyo side. The consistency of the stratigraphy is strong on the Noyo side, with the inverted doublets strongly similar in most cases, and much less so on the Cascadia side with greater variability. The concept follows that

proposed by Goldfinger et al. (2008, 2012) in which the turbidity currents are capable depositing a record that may record some of the basic characteristics of the triggering earthquake. This was proposed in order to explain the regional correlation of Cascadia turbidites based on their unique depositional sequences. The "paleoseismogram" hypothesis was subsequently testing in Sumatra, where samples of the 2004 triplet turbidite closely matched the seismograms and three patch rupture (Patton et al., 2015). Similarly, Howarth et al. (2021) were able to match the 2016 Kaikoura turbidites to the corresponding seismograms. In this case, the sequence includes two fault ruptures closely spaced in time as opposed to a multi-patch large rupture as first proposed for Cascadia, but otherwise, the concept is much the same.

Conclusions

Lake Merced results have established that site as a viable paleoseismic site on the northern San Francisco peninsula. The lake records ~ 2300 years of event beds, 17 in total. Prior to that the lake was open to the ocean and contains marine shells consistent with an estuarine environment, and less tenable as a paleoseismic site, although that remains unexamined at present. Historic results from Lake Merced using bomb-carbon based age models show the site recorded three historic events, 1906, the 1957 Daly City earthquake, and Loma Prieta in 1989 with no intervening event beds. During the 20th century, these earthquakes resulted in the only three event beds in the lake during that time, providing a good test of the fidelity of the lake as an earthquake recorder. These results also show that this site records not only NSAF events, likely along the north coast and the peninsula, but also related earthquakes in the Santa Cruz Mountains, events in the probable pull apart basin at Daly City, and possibly others as well. The event bed corresponding to 1906 is ~ 1m thick, much greater than any other bed in the lake during the past 2200 years. Pb isotope data show this bed is contaminated with isotopes consistent mostly with lead based paint, and additionally tetraethyl Pb from gasoline. We interpret the thick Pb laden deposit as likely anthropogenic material from the early development of San Francisco, and the great thickness of the bed may have been deposited over several decades as a hillslope effect following the earthquake. The Lake Merced record is largely compatible with onshore and offshore records for the north coast segment of the NSAF, and potentially with the lesser known peninsula segment. The lack of numerous "extra" events at Lake Merced relative to the north coast segment record may suggest that many, but not all north coast and peninsula segment events are one in the same, as was 1906.

Detailed analysis of cores near the northern limit of the NSAF at Noyo Canyon and in Southern Cascadia primarily at Trinidad Canyon, have yielded improved detailed records, age models, and evidence of historic earthquakes. In southern Cascadia, several significant event beds overlie the 1700 CE earthquake bed. High-resolution age models supported by bomb-carbon ages suggest that the significant 20th century beds likely include 1906 NSAF, 1980 Eureka, and 1992 Petrolia earthquake event beds. The presence of the 1906 beds in southern Cascadia suggests that others from the NSAF should be present as well, and also suggests that event beds from Cascadia earthquakes should be expected at similar ranges south of Cascadia in Noyo Canyon. In both Trinidad plunge pool and Noyo Canyon cores, a number of unusual doublet event beds are observed. The Noyo Canyon doublets are nearly all inverted, with the coarsest components at the top. In detail. These beds are composed of two stacked fining upward sequences, with the upper unit having greater density and coarser grain size. These unusual beds are unlikely to be the result of hydrodynamic transport effects or storm or climatic events. On the Cascadia side they are somewhat more subtle, but nonetheless unusual. The unusual doublet beds are not observed elsewhere in the Cascadia basin, or along the NSAF. The doublet beds correspond to times when both the NSAF, and Cascadia have both had had significant earthquakes at similar times. In all, of the 9 major earthquakes in

the Cascadia record younger than 4100 years, 7 of them have a corresponding inverted doublet bed in Noyo Canyon with significant temporal overlap with Cascadia event timings. One other has a corresponding bed, but is not a doublet. Of these 7, 4 of them have possible correlatives at other land sites including some or all of those available: Point Arena, Fort Ross, Bodega bay, Bolinas lagoon, Vedanta Marsh, Dogtown, and Lake Merced, the other events are older than the available land data. Three of the southern segmented Cascadia events have similar evidence for a matching doublet on the NSAF, and five others have temporal equivalents, some of which do not correlate southward along the NSAF. For most of the doublet beds, time intervals above and below commonly do not allow enough time for Cascadia beds to be present in Noyo Canyon, but mis-correlated on the basis of radiocarbon. We infer that the earthquake recurrence sequence that best explains the data is that for most Cascadia events < 3500 BP, a corresponding NSAF earthquake occurred shortly thereafter, producing the doublet stratigraphy in Noyo Canyon, and in Cascadia. This would explain both the inverted doublets in Noyo, and the non-inverted doublets in Cascadia. In Noyo Canyon, the site would feel the shaking from Cascadia first, initiating a turbidity current and starting the depositional sequence. Subsequently, the NSAF ruptures, initiating a much more robust current in Noyo Canyon, as the fault crosses the canyon head, forming the upper part of the doublet. In Cascadia, the sequence is the same, but the distant NSAF forms the weaker upper part of the non-inverted doublet. The time separation between the Cascadia and NSAF ruptures is not known. We observe no interevent hemipelagic sedimentation between the two parts of the Noyo doublets. However, in most cases on the Noyo Canyon side, the upper event could easily erode and erase any interevent sediment, which is not observed in the cores. For the youngest event, the ~ 1700 CE doublet, this erasure would have to have been replicated at all core sites, 13 samples in all, but is possible. On the Cascadia side, the doublet for that event, and several others appears to be embedded in the tail of the first event, implying a very short time separation where the second event is settling into the still moving, waning turbidity current from the first event. This would imply hours of separation at most. For other events, the time separation cannot be as definitively deduced with present data, but several of them are closely spaced and likely do not exceed ~ 30 years. In conclusion, a hypothesis of a stress-triggering interaction, and even partial synchronization of the NSAF with Cascadia is supported by new stratigraphic and radiocarbon evidence of occurrence and timing. The data suggest that Cascadia ruptures first, and the NSAF thereafter. In Holocene times prior to ~ 4100 BP, the doublet stratigraphy is rare to absent, and the weaker timing constraints available do not suggest such a relationship during that period. The 1906 event may have either ended a period of stress interactions, or is one of a small number of NSAF events unrelated to Cascadia in the past ~ 4100 years in a scenario of partial synchronization of the two faults.

Acknowledgements

We would like to thank the Pacific Rowing Club and in particular Joe Mees for his help, loaning boats, motors, and the Club facilities to the project. This help was invaluable, and made field work simple for our crew. Thanks are extended to the San Francisco Recreation and Parks Department and Dana Ketcham in particular for making the permitting process for sampling Lake Merced simple and efficient. Many thanks to Liam Reidy who persevered through serious illness to work with us coring Lake Merced. Thanks to undergraduate student Rachel Hausmann for her long hours processing the cores, XRF, CT data, and shepherding the radiocarbon dating work at Lake Merced. Thanks to Maureen Davies Walczak (OSU), Madeline Hille and Bruce Nelson of University of Washington for their help running Pb isotopic samples. Thanks to Mike Mutchler of Seahorse Geomatics for spending many hours training the crew on the Norbit multibeam sonar system, and to some very nice work by Josh mode also of Seahorse Geomatics for processing through some troublesome issues with the bathymetry data. Thanks to Joel Gutierrez who added Mazama ash data for Rogue Canyon and additional pmag and CT data for Trinidad

cores. Many thanks to the field crew that included Rachel Hausmann, Liam Reidy, Jeff Beeson, Bran Black and Brad Pitcher.

REFERENCES

Abdeldayem, A. L., Ikehara, K., and Yamazaki, T., 2004, Flow path of the 1993 Hokkaido-Nansei-oki earthquake seismoturbidite, southern margin of the Japan sea north basin, inferred from anisotropy of magnetic susceptibility: Geophysical Journal International, v. 157, p. 15-24.

Anderson RS, Ejarque A, Brown PM et al., 2013, Holocene and historical vegetation change and fire history on the north-central coast of California, USA. The Holocene v. 23, p. 1797–1810.

Baldwin, J. N. (1996). Paleoseismic investigation of the San Andreas Fault on the north coast segment, near Manchester, California, Master's Thesis, San Jose State University, San Jose, California, 127 pp.

Baldwin, J. and Prentice, C., 2008, Earthquake records of the Peninsula segment of the San Andreas fault, Portola Valley, California: Collaborative research with William Lettis & Associates, Inc. and U.S. Geological Survey, Final Technical Report, U. S. Geological Survey National Earthquake Hazards Reduction Program Award Number 05HQGR0073.

Baldwin, J. Kozacl, O., Zachariasen, J., and Prentice, C., 2011, Paleoseismic investigations of Holocene earthquake recurrence on the peninsula segment of the San Andreas Fault, Woodside, CA: collaborative research with Fugro William Lettis & Associates and the United States Geological Survey, joint project with Judy Zachariasen, URS Corporation, Final Technical Report, U. S. Geological Survey National Earthquake Hazards Reduction Program Award Number 05HQGR0073.

Beeson, J.W., Goldfinger, C., Johnson, S.Y., 2017, The Offshore Section of the Northern San Andreas Fault: Fault Zone Geometries, Shallow Deformation Patterns, and Asymmetric Basin Growth, Geosphere, v13 (3).

Bell, T., Campbell, S., Liverman, D., Allison, D., and Sylvester, P. J., 2010, Environmental and potential human health legacies of non-industrial sources of lead in a Canadian urban landscape - The case study of St John's, Newfoundland: International Geology Review, v. 52, no. 7, p. 771-800.

Berquist, J. R., 1978, Depositional history and fault-related studies, Bolinas Lagoon, California. U. S. Geological Survey Open-file Report 78-802, 160 pp.

Black, B., 2014, Stratigraphic correlation of seismoturbidites and the integration of sediment cores with 3.5 kHz chirp subbottom data in southern Cascadia [MS Thesis] Oregon State University, Corvallis, 211 p.

Blott, S. J., and Pye, K., 2006, Particle size distribution analysis of sand-sized particles by laser diffraction: an experimental investigation of instrument sensitivity and the effects of particle shape: Sedimentology, v. 53, no. 671-685, p. 671-685.

Bonilla, M.G., 1959, Geologic observations in the epicentral area of the San Francisco earthquake of March 22, 1957: California Division of Mines Special Report 57, p. 25-37.

Bonilla, M.G. 1960, Landslides in the San Francisco South quadrangle, California: U.S. Geol. Survey open file report, 44 p. 10 figs.

Bonilla, M.G., 1964, Bedrock-surface map of the San Francisco South Quadrangle, California: U.S. Geological Survey Open File Report, scale 1:20,000.

Bonilla, M.G., 1965, Geologic map of the San Francisco South Quadrangle, California: U.S. Geological Survey Open-File Map, scale 1:20,000.

Bonilla, M.G., 1971, Preliminary geologic map of the San Francisco South Quadrangle and part of the Hunters Point Quadrangle, California: U.S. Geological Survey Miscellaneous Field Studies Map MF-311, 2 sheets, scale 1:24,000.

Bonilla, M.G., 1988, Preliminary Geological Map of the San Francisco South 7.5' Quadrangle and Part of the Hunters Point 7.5' Quadrangle, San Francisco Bay Area, California: A Digital Database. United States Geological Survey (USGS) Open-File Report 98-354. Scale 1:24,000.

Bonilla, M.G., 1994a, Surface faulting studies *in* Jacobson , M.L., compiler, Summaries of technical reports volume XXXV, prepared by Participants in National Earthquake Hazards Reduction Program, U.S. Geological Survey Open-File Report 94-176, p. 241-242.

Bonilla, M.G., 1994b, Serra Fault Zone, San Francisco Peninsula, California (abstract): EOS, Transactions, American Geophysical Union, v. 75, no. 44, Supplement, p. 681.

Bonilla, M. G., Jachens, R. C., Jayko, A. S., Wentworth, C. M., and McGarr, A. F., 2000, The Demise of the San Bruno Fault: California Geology, v. 53, no. 02, p. 4-19.

Brocher, T. M. (2019). Was the 23 November 1873 California-Oregon border earthquake an inslab earthquake? Seismological Society of America Annual Meeting, April 2019, Seattle WA.

Bruns, T.R., Cooper, A.K., Carlson, P.R., McCulloch, D.S., 2002. Structure of the submerged San Andreas and San Gregorio fault zones in the Gulf of the Farallones as inferred from high-resolution seismic-reflection data. In: Parsons, T. (Ed.), Crustal Structure of the Coastal and Marine San Francisco Bay region, California. U. S. Geological Survey Professional Paper 1658, pp. 77–117.

Boatwright J, Bundock H, Seekins LC. Using Modified Mercalli Intensities to Estimate Acceleration Response Spectra for the 1906 San Francisco Earthquake. Earthquake Spectra. 2006;22(2_suppl):279-295. doi:10.1193/1.2186348

Bürgmann, R., Hilley, G., Ferretti, A., and Novali, F., 2006, Resolving vertical tectonics in the San Francisco Bay Area from permanent scatterer InSAR and GPS analysis: Geology, v. 34, no. 3, p. 221-224.

Camp Dresser & McKee. 1999, Lake Merced water sanitary survey November 1999 Report, San Francisco Public Utilities Commission.

Carver, G. A., Paleoseismic geology of the southern part of the Cascadia subduction zone *in* Proceedings Penrose conference "Great Cascadia earthquake tricentennial"; program summary and abstracts Seaside, OR January 1, 2000 2000, Oregon Department of Geology and Mineral Industries p. 38-39.

Carver, G. A., and Plafker, G., 1999, Cascadia Subduction Zone Segmentation in the Mendocino Triple Junction Region: Seismological Research Letters, v. 70, no. 2, p. 245-246.

Caskey, S.J., Grove, K., Li, C., Berger, G.W., 2005, Constraints on Late Pleistocene and Active Uplift Rates Along the Serra Fault and the Timing of Late Pleistocene Transpressional Deformation Along the San Andreas Fault, Northern San Francisco Peninsula, NEHRP Final Report, USGS, Reston VA.

Chaytor, J. D., Goldfinger, C., Dziak, R. P., and Fox, C. G., 2004, Active deformation of the Gorda plate: Constraining deformation models with new geophysical data: Geology, v. 32, no. 4, p. 353-356.

Chow, T.J., Earl, J.L., 1972, Lead isotopes in North American coals, Science, v. 176, p. 510–511.

Chow, T.J., Johnstone, M.S., 1965, Lead isotopes in gasoline and aerosols of Los Angeles Basin, California, Science, v. 147, p. 502–503.

Clifton, H.E., 1988. Sedimentologic approaches to paleobathymetry, with applications to the Merced Formation of central California. Palaios v. 3, p. 507– 522.

Clifton, H.E. and Hunter, R.E., 1999, Depositional and other features of the Merced Formation in sea cliff exposures south of San Francisco, California, *in* Wagner, D.L. and Graham, S.A., eds., Geologic field trips in Northern California; centennial meeting of the Cordilleran Section of the Geological Society of America: California Department of Conservation, Division of Mines and Geology Special Publication 119, p. 89-100.

Clifton, H.E. and R.E. Hunter, 1987, "The Merced Formation and related beds: A mile-thick succession of late Cenozoic coastal and shelf deposits in the sea cliffs of San Francisco, California". In: Geological Society of America Centennial Field Guide—Cordilleran. Section. pp. 257-262.

Clifton, H. E., Hunter, R.E., and Gardner, J.V., 1988, "Analysis of eustatic, tectonic, and sedimentologic influences on transgressive and regressive cycles in the late Cenozoic Merced Formation." In: Cordilleran Section of Geological Society of America Centennial Field Guide. Volume 1. Paola, C., and Kleinspehn, K.L. Boulder, CO (Eds.): Geological Society of America. p.27-262.

Coffman, J.L., and von Hake, C. A., 1973, Earthquake history of the United States (rev. ed.): U.S. Environmental Data Service, Pub. 41-1, 208 p.

Cooper, A.K., 1973, Structure of the continental shelf west of San Francisco, California. U. S. Geological Survey Open-file Report 1907. 65 pp.

d'Alessio, M. A., I. A. Johanson, R. Bürgmann, D. A. Schmidt, and M. H. Murray, 2005, Slicing up the San Francisco Bay Area: Block kinematics and fault slip rates from GPS-derived surface velocities, Journal of Geophysical Research, 110, B06403, doi:10.1029/2004JB003496.

Dettinger, M.D., and F. M. Ralph, F.M., 2011, Storms, Floods, and the Science of Atmospheric Rivers, Eos, Vol. 92, No. 32, page 265; 2011.

Dickinson, W.R., and Snyder, W.S., 1979, The geometry of the triple junctions related to San Andreas transform, Journal of Geophysical Research, v. 84, p. 561-572.

Dixon, K., 2006, “StarFire: A Global SBAS for Sub-Decimeter Precise Point Positioning”, Proceedings of ION GNSS 2006.

Enkin, R. J., Dallimore, A., Baker, J., Southon, J. R., and Ivanochko, T., 2013, A new high-resolution radiocarbon Bayesian age model of the Holocene and Late Pleistocene from core MD02-2494 and others, Effingham Inlet, British Columbia, Canada; with an application to the paleoseismic event chronology of the Cascadia Subduction Zone: Canadian Journal of Earth Sciences, v. 50, no. 7, p. 746-760.

Fahy, Neil E., 1974. Origin of Lake Merced. California Geology Vol. 27, No. 8, p. 171-174.

Fukuma, K., 1998, Origin and applications of whole-core magnetic susceptibility of sediments and volcanic rocks from Leg 152: Proceedings of the Ocean Drilling Program: Scientific Results, v. 152, p. 271-280.

Fuller, C.C., van Geen, A., Baskaran, M., Anima, R.J., 1999, Sediment chronology in San Francisco Bay, defined by 210 Pb, 234Th, 137Cs, 239,240Pu. Mar. Chem. v. 64, p. 7–27.

Fumal, T. E., T. E. Dawson, R. Flowers, J. C. Hamilton, G. F. Heingartner, J. Kessler, and L. Samrad, 2003, Photomosaics and logs of trenches on the San Andreas fault at Mill Canyon near Watsonville, California, U. S. Geological Survey Open-File Report 03-469, 1 sheet.

Fumal, T. E., 2012, Timing of Large Earthquakes during the Past 500 Years along the Santa Cruz Mountains Segment of the San Andreas Fault at Mill Canyon, near Watsonville, California: Bulletin of the Seismological Society of America, v. 102, no. 3, p. 1099-1119.

Fumal, T.E. Heingartner, G.F. Samrad, L., Dawson, T.E., Hamilton, J.C., and Baldwin, J.N., 2003, Photomosaics and Logs of Trenches on the San Andreas Fault at Arano Flat near Watsonville, California: U.S. Geological Survey Open-File Report 03-450, Version 1.0.

Geo/Resource Consultants, Inc., 1993. Lake Merced Water Resources Planning Study, San Francisco Water Department in association with Montgomery/Watson, Jones and Stokes Asso., Inc. Public Affairs Management. San Francisco, CA GRC Project No. 1756-00.

Garrison-Laney, C. E., Abramson, H. F., and Carver, G. A., 2002, Late Holocene tsunamis near the southern end of the Cascadia Subduction Zone: Seismological Research Letters, v. 73, no. 2, p. 248.

Goldfinger, C., Morey, A. E., Black, B., Beeson, J., Nelson, C. H., and Patton, J., 2013, Spatially limited mud turbidites on the Cascadia margin: segmented earthquake ruptures?: Nat. Hazards Earth Syst. Sci., v. 13, no. 8, p. 2109-2146.

Goldfinger, C., Nelson, C. H., Johnson, J. E., Erickson, D., Winkler, M., Kalk, P., Pastor, J., Camarero, A., Morri, C., Dunhill, G., Ramos, L., Raab, A., Pisias, N., Pourmanoutscheri, M., van Rooij, D., Amy, L., and Liu, C.-C. C., 2003, Holocene earthquake records from the Cascadia subduction zone and northern San Andreas Fault based on precise dating of offshore turbidites Annual Review of Earth and Planetary Sciences v. 31, p. 555-577.

Goldfinger, C., Grijalva, K., Burgmann, R., Morey, A.E., Johnson, J.E., Nelson, C.H., Gutierrez-Pastor, J., Karabanov, E., Chaytor, J.D., Patton, J., and Gracia, E., 2008, Late Holocene Rupture of the Northern San Andreas Fault and Possible Stress Linkage to the Cascadia Subduction Zone, Bulletin of the Seismological Society of America, v. 98, p. 861-889.

Goldfinger, C., Morey, A. E., Nelson, C. H., Gutierrez-Pastor, J., Johnson, J. E., Karabanov, E., Chaytor, J., and Ericsson, A., 2007, Rupture Lengths and Temporal History of Significant Earthquakes on the Offshore and North Coast Segments of the Northern San Andreas Fault Based on Turbidite Stratigraphy: Earth and Planetary Science Letters, v. 254, p. 9-27.

Goldfinger, C., Nelson, C.H., Morey, A., Johnson, J.E., Gutierrez-Pastor, J., Eriksson, A.T., Karabanov, E., Patton, J., Gracia, E., Enkin, R., Dallimore, A., Dunhill, G., and Vallier, T., 2012, Turbidite Event History: Methods and Implications for Holocene Paleoseismicity of the Cascadia Subduction Zone, USGS Professional Paper 1661-F, Reston, VA, U.S. Geological Survey, p. 184 p, 64 Figures. http://pubs.usgs.gov/pp/pp1661f/

Goldfinger, C., Morey, A., Galer, S., Beeson, J., Erhardt, M.E., 2014, A paleoseismic transect of Forearc Lakes at the Latitude of Seattle, Washington, Seismological Society of America Annual Meeting, Anchorage Alaska, April 30, 2014.

Goldfinger, C., Hausmann, R., Black, B., Beeson, J., Galer, S., Collins, T., 2016, Estimating Inland Ground Motions from Lake Turbidite Sequences, Northern Cascadia margin, USA., AGU Fall meeting Abstract , San Francisco, Dec. 11-16, 2016.

Goldfinger, C., Galer, S., Beeson, J., Hamilton, T. S., Black, B., Romsos, C., Patton, J., Nelson, C. H., Hausmann, R., and Morey, A., 2017, The importance of site selection, sediment supply, and hydrodynamics: A case study of submarine paleoseismology on the northern Cascadia margin, Washington USA: Marine Geology, v. 384, p. 4-46.

Goldfinger, C., Black, B., Patton, J.R., Beeson, J. , Morey, A.E., Nelson, C.H., 2020, Calibrating the Smallest Southern Cascadia Earthquakes with Historic Turbidite Stratigraphy, American Geophysical Union Fall Meeting, Abstract NH004-04.

Hall, N. T., R. H. Wright, and K. B. Clahan (1999). Paleoseismic studies of the San Francisco Peninsula segment of the San Andreas Fault zone near Woodside, California, J. Geophys. Res. V. 104, p. 23,215–23,236.

Hall, N. T., and Niemi, T. M., 2008, The 1906 Earthquake Fault Rupture and Paleoseismic Investigation of the Northern San Andreas Fault at the Dogtown Site, Marin County, California: Bulletin of the Seismological Society of America, v. 98, no. 5, p. 2191-2208.

Hall, N.T., Wright, R.H., and, C.S. Prentice, 2001, Studies along the peninsula segment of the San Andreas fault, San Mateo and Santa Clara Counties, California *in* Ferriz, H., and Anderson, R., eds., Engineering Geology Practice in Northern California: California Division of Mines and Geology, Bulletin 210, Special Publication 12, p. 193 - 210.

Hall, N.T., Wright, R.H., and Clahan, K.B., 1999, Paleoseismic studies of the San Francisco peninsula segment of the San Andreas fault zone near Woodside, California: Journal of Geophysical Research, v. 104, no. B10, p. 23,215-23,236.

Hamilton, T. S., Enkin, R. J., Riedel, M., Rogers, G. C., Pohlman, J. W., and Benway, H. M., 2015, Slipstream: an early Holocene slump and turbidite record from the frontal ridge of the Cascadia accretionary wedge off western Canada and paleoseismic implications: Canadian Journal of Earth Sciences, v. 52, no. 6, p. 405-430.

Hengesh, J.V., Wakabayashi, J., 1995, Dextral translation and progressive emergence of the Pleistocene Merced basin and implications for timing of initiation of the San Francisco Peninsula segment of the San Andreas fault. In: Sangines, D.W., Andersen, D.W., Buising, A.W. (Eds.), Recent Geologic Studies in the San Francisco Bay Area. Pacific Section, SEPM (Society for Sedimentary Geology), Book, vol. 76, pp. 47– 54.

Henkart, P., 2006, Chirp Sub-Bottom Profiler Processing - A review: Sea Technology, October, 2006, p. 35-38.

Hill, J. C., Watt, J. T., Brothers, D. S., and Kleusner, J. W., 2020, Submarine canyons, slope failures and mass transport processes in southern Cascadia: Geological Society Special Publication, v. 500, p. 453-475.

Hirao, Y., Patterson, C.C., 1974, Lead aerosol pollution in the high Sierra override natural mechanisms which exclude lead from a food chain, Science, v. 184, p. 989–992.

Holden, E. S., 1898, A catalogue of earthquakes on the Pacific Coast, 1769-1897: Smithsonian Inst. Misc. Colln., v. 37, no. 5, 253 p.

Howarth, J.D., A.R. Orpin, Y. Kaneko, et al. (2021). Calibrating the marine turbidite palaeoseismometer using the 2016 Kaikōura earthquake. *Nature Geoscience*, doi:10.1038/s41561-021-00692-6.

Holzman, B.A., 2005, http://online.sfsu.edu/bholzman/LakeMerced/Default.htm

Iwaki, H., Hayashida, A., Kitada, N., Ito, H., Suwa, S., and Takemura, K., 2004, Stratigraphic correlation of samples from the Osaka Bay off Kobe based on magnetic properties and its implication for tectonic activity of the Osaka-wan fault for the last 6300 years: Eos Transactions American Geophysical Union, v. 84, p. GP41C-0053 F0554.

Jachens, R.C., Roberts, C.R. and Zoback, M.L., 1996, Total offset and right-stepping geometry of the San Francisco Peninsula segment of the San Andreas Fault, California, defined by aeromagnetic anomalies (abstract): EOS, Transactions, American Geophysical Union, v. 77, no. 46, Supplement, p. F742.

Jachens, R. C., and Zoback, M. L., 1999, The San Andreas fault in the San Francisco Bay region, California: Structure and kinematics of a Young plate boundary: International Geology Review, v. 41, no. 3, p. 191-205.

Jaffe, B.E., Smith, R.E., Zink, L., 1998, Sedimentation and bathymetry changes in San Pablo Bay: 1865 1983, U.S. Geological Survey Open-File Report 98–759.

Jennings, C.W., 1994, Fault activity map of California and adjacent areas with locations and ages of recent volcanic eruptions: California Division of Mines and Geology, Geologic Data Map No. 6, scale 1:750,000.

Johnson, S. Y., Hartwell, S. R., Sliter, R. W., Watt, J. T., Phillips, E. L., Ross, S. L., and Chin, J. L., 2015, Local (Offshore of San Francisco Map Area) and Regional (Offshore from Bolinas to Pescadero) Shallow-Subsurface Geology and Structure, California: U.S. Geological Survey Open-File Report 2015-1068.

Karlin, R. C., and Abella, S. E. B., 1992, Paleoearthquakes in the Puget Sound region recorded in sediments from Lake Washington, U.S.A.: Science, v. 258, p. 1617-1620.

Karlin, R. E., Holmes, M., Abella, S. E. B., and Sylwester, R., 2004, Holocene landslides and a 3500-year record of Pacific Northwest earthquakes from sediments in Lake Washington: Geological Society of America Bulletin, v. 116, no. 1-2, p. 94-108.

Kelsey, H. M., Witter, R. C., and Hemphill-Haley, E., 2002, Plate-boundary earthquakes and tsunamis of the past 5500 yr, Sixes River estuary, southern Oregon: Geological Society of America Bulletin, v. 114, no. 3, p. 298-314.

Kelsey, H. M., Nelson, A. R., Hemphill-Haley, E., and Witter, R. C., 2005, Tsunami history of an Oregon coastal lake reveals a 4600 yr. record of great earthquakes on the Cascadia subduction zone: GSA Bulletin, v. 117, no. 7-8, p. 1009-1032.

Kelson, K., A. Strieg, R. Koehler, and K. Kang, 2006, Timing of Late Holocene Paleoearthquakes on the Northern San Andreas Fault at the Fort Ross Orchard Site, Sonoma County, California, Bulletin of the Seismological Society of America, v. 96 (3), p. 1012-1028.

Kennedy, D.G., 2002, Neotectonic character of the Serra fault, northern San Francisco Peninsula, California [M.S. Thesis]: San Francisco State University, 117 p.

Kioka, A., Schwestermann, T., Moernaut, J., Ikehara, K., Kanamatsu, T., McHugh, C. M., dos Santos Ferreira, C., Wiemer, G., Haghipour, N., Kopf, A. J., Eglinton, T. I., and Strasser, M., 2019, Megathrust earthquake drives drastic organic carbon supply to the hadal trench: Scientific Reports, v. 9, no. 1, p. 1553.

Kitman, J., 2000, "The Secret History of Lead." The Nation. March 2, 2009.

Kneller, B., 2003, The influence of flow parameters on turbidite slope channel architecture: Turbidites; models and problems, v. 20, no. 6-8, p. 901-910.

Knudsen, K.L., R.C. Witter, C.E. Garrison-Laney, J.N. Baldwin, G.A. Carver, L.B. Grant, and W.R. Lettis, 2002, Past earthquake-induced rapid subsidence along the northern San Andreas Fault; a paleoseismological method for investigating strike-slip faults, Bulletin of the Seismological Society of America, *v.* 92, p. 2612-2636.

Komar, P. D., 1985, The hydraulic interpretation of turbidites from their grain sizes and sedimentary structures: Sedimentology, v. 32, no. 3, p. 395-407.

Kozaci, O., J. Zachariasen, and C. Prentice (2015). Paleoseismic investigations of Holocene earthquake recurrence on the peninsula segment of the San Andreas Fault, Woodside, CA, Joint Project between Fugro Consultants Inc., AECOM and the United States Geological Survey, Final Technical Report Submitted to the U.S. Geological Survey National Earthquake Hazards Reduction Program, Award Numbers G12AP20060 and G12AP20061, 43 pp.

Kraus, N. C., Militello, A., and Todoroff, G., 2002, Barrier breaching processes and barrier spit breach, Stone Lagoon, California: Shore & Beach, v. 70, no. 4, p. 21-28.

Lawson, A.C., 1895, Sketch of the geology of the San Francisco peninsula: U.S. Geological Survey Annual Report 15, p. 399-476.

Lawson, A.C., 1908, The California earthquake of April 18, 1906, report of the State Earthquake Investigation Commission: Carnegie Institution of Washington, Publication 87 Volumes I and II, (reprinted 1969). Washington, D. C.

Lawson, A.C., 1914, San Francisco Folio: Washington, D.C, U.S. Geological Survey Geological Atlas of the United States, Folio 193, 24 p.

Lay, T.; Given, J. W.; Kanamori, H. *(1982),* "Long-period mechanism of the 8 November 1980 Eureka, California, earthquake", Bulletin of the Seismological Society of America, v. **72**(2), p. 439, 440, 455, 456.

Lee SE, Talling PJ, Ernst GCJ, Hogg AJ. 2002. Occurrence and origin of submarine plunge pools at the base of the US continental slope. *Mar. Geol.* 185:363–77

Lees, J. A., Flower, R. J., Ryves, D., Vologina, E., and Sturm, M., 1998, Identifying sedimentation patterns in Lake Baikal using whole core and surface scanning magnetic susceptibility: Journal of Paleolimnology, v. 20, p. 187-202.

Leithold, E. L., Wegmann, K. W., Bohnenstiehl, D. R., Smith, S. G., Noren, A., and O'Grady, R., 2018, Slope failures within and upstream of Lake Quinault, Washington, as uneven responses to Holocene earthquakes along the Cascadia subduction zone: Quaternary Research, v. 89, no. 1, p. 178-200.

Li, Wen-Hao, 1992, Evidence for the late Holocene coseismic subsidence in the lower Eel River Valley, Humboldt County, northern California: An application of foraminiferal zonation to indicate tectonics submergence, M.S. thesis, Humboldt State University, Arcata California, 87 p.

Lovlie, R., and van Veen, P., 1995, Magnetic susceptibility of a 180 m sediment core: reliability of incremental sampling and evidence for a relationship between susceptibility and gamma activity, *in* Turner, P., and Turner, A., eds., Palaeomagnetic applications in hydrocarbon exploration and production: Special Publication, 98, Geological Society, London, p. 259-266.

Lowe, D., 1982, Sediment gravity flows; II, Depositional models with special reference to the deposits of high-density turbidity currents: Journal of Sedimentary Research, v. 52, no. 1, p. 279-297.

McCubbin, D. G., 1982, Barrier-island and strand-plain facies, *in* Scholle, P. A., and Spearing, D., eds., Sandstone Depositional Environments, Memoir 31, AAPG, p. 247-258.

McGuire, T., 2009, Stratigraphic Investigation of the North Westside Basin of San Francisco and Northern San Mateo County [MS Thesis]: San Francisco State University, 94 p.

McKay, C. P., Long, A., and Friedmann, E. I., 1986, Radiocarbon dating of open systems with bomb effect: Journal of Geophysical Research: Solid Earth, v. 91, no. B3, p. 3836-3840.

Melgar, D., 2021, The 26 January 1700 Cascadia Earthquake as Part of an Event Sequence, Seismological Society of America Annual Meeting, April 20, 2021, online meeting.

Moernaut, J., Daele, M. V., Heirman, K., Fontijn, K., Strasser, M., Pino, M., Urrutia, R., and De Batist, M., 2014, Lacustrine turbidites as a tool for quantitative earthquake reconstruction: New evidence for a variable rupture mode in south central Chile: Journal of Geophysical Research: Solid Earth, v. 119, no. 3, p. 1607-1633.

Morales, Y., and Tsubouchi, T., 2007, DGPS, RTK-GPS and StarFire DGPS performance under tree shading environments, IEEE International Conference on Integration Technology, 2007. ICIT '07.

Morey, A. E., Goldfinger, C., Briles, C. E., Gavin, D. G., Colombaroli, D., and Kusler, J. E., 2013, Are great Cascadia earthquakes recorded in the sedimentary records from small forearc lakes?: Nat. Hazards Earth Syst. Sci., v. 13, no. 10, p. 2441-2463.

Morey, A.E., 2020, Cascadia earthquakes disturb sediment in small Oregon and California lakes, PhD Dissertation, Oregon State University, Corvallis, OR, 232p.

Morton-Thompson, D., and Woods, A. M., 1992, Development Geology Reference Manual: AAPG Methods in Exploration Series, No. 10.

Mountjoy, J. J., Howarth, J. D., Orpin, A. R., Barnes, P. M., Bowden, D. A., Rowden, A. A., Kane, T. 2018, Earthquakes drive large-scale submarine canyon development and sediment supply to deep-ocean basins. Science Advances, 4, eaar3748. https://doi.org/10.1126/sciadv.aar3748

Mulder, T., Migeon, S., Savoye, B., and Jouanneau, J.M., 2001, Twentieth century floods recorded in the deep Mediterranean sediments: Geology, v. 29, no. 11, p. 1011-1014.

Mulder, T., Syvitski, J.P.M., Migeon, S., Faugeres, J.C., and Savoye, B., 2003, Marine hyperpycnal flows; initiation, behavior and related deposits; a review: Turbidites; models and problems, v. 20, no. 6-8, p. 861-882.

Nelson, A. R., Jennings, A. E., and Kashima, K., 1996, An earthquake history derived from stratigraphic and microfossil evidence of relative sea-level change at Coos Bay, southern coastal Oregon: GSA Bull., v. 108, no. no. 2, p. 141-154.

Nelson, A. R., Kelsey, H. M., Hemphill-Haley, E., Witter, R. C., and Anonymous, 1998, AMS 14C dating of a 7300-year earthquake history from an Oregon coastal lake Geological Society of America, 1998 annual meeting v. 30, no. 7, p. 162.

Nelson, A.R., Christopher B. DuRoss, C.B., Robert C. Witter, R.C., Harvey M. Kelsey, H.M., Simon E. Engelhart, S.E., Shannon A. Mahan, S.A., Harrison J. Gray, H.J., Andrea D. Hawkes, A.D., Benjamin P. Horton, B.P., Jason S. Padgett, J.S., 2021, A maximum rupture model for the central and southern Cascadia subduction zone—reassessing ages for coastal evidence of megathrust earthquakes and tsunamis, Quaternary Science Reviews, Volume 261,106922,ISSN 0277-3791.

Niemi, T.M., and Hall, N.T., 1992, Late Holocene slip rate and recurrence of great earthquakes on the San Andreas Fault in northern California: Geology, v. 20, p. 195-198.

Niemi, T. M., 2010, Variable earthquake recurrence on the Northern San Andreas fault over the past 3,000 years at the Vedanta marsh site, Olema, CA, American Geophysical Union, Fall Meeting: San Francisco, Abstract T41C-01.

Nittrouer, C. A., and Sternberg, R. W., 1981, The formation of sedimentary strata in an allochthonous shelf environment: The Washington continental shelf: Marine Geology, v. 42, no. 1-4, p. 201-232.

Nriagu, J. O., 1990, The rise and fall of leaded gasoline: Science of The Total Environment, v. 92, p. 13-28.

Okutsu, N., Ashi, J., Yamaguchi, A., Irino, T., Ikehara, K., Kanamatsu, T., Suganuma, Y., and Murayama, M., 2019, Evidence for surface sediment remobilization by earthquakes in the Nankai forearc region from sedimentary records: Geological Society, London, Special Publications, v. 477, no. 1, p. 37.

Oppenheimer, D., Beroza, G., Carver, G., Dengler, L., Eaton, J., Gee, L., Gonzalez, F., Jayko, A., Ki., W.H., Lisowski, M., Magee, M., Marshall, G., Murray, M., McPherson, R., Romanowicz, B., Satake, K., Simpson, R., Somerille, P., Stein, R., and Valentine, D., The Cape Mendocino, California, Earthquakes of April, 1992: Subduction at the Triple Junction in Science, v. 261, no. 5120, p. 433-438.

Gutiérrez-Pastor, J., Nelson, C. H., Goldfinger, C., and Escutia, C., 2013, Sedimentology of Seismo-Turbidites off the Cascadia and Northern California Active Tectonic Continental Margins, Northwest Pacific Ocean: Marine Geology, v. 336, p 91-119.

J.S. Padgett, S.E. Engelhart, H.M. Kelsey, R.C. Witter, N. Cahill, E. Hemphill-Haley, 2021, Timing and amount of southern Cascadia earthquake subsidence over the past 1,700 years at northern Humboldt Bay, California, Geological Society of America Bulletin, USA (2021), 10.1130/B35701.1

Patton, J.R., Goldfinger, C., Morey, A., Romsos, C., Black, B., Djadjadihardja, Y.S., and Udrekh, U., 2013, Seismoturbidite Record as Preserved at Core Sites at the Cascadia and Sumatra-Andaman Subduction Zones, Natural Hazards and Earth System Sciences, v. 13,p. 833–867.

Patton, J. R., Goldfinger, C., Morey, A. E., Ikehara, K., Romsos, C., Stoner, J., Djadjadihardja, Y., Udrekh, Ardhyastuti, S., Gaffar , E. Z., and Vizcaino, A., 2015, A 6600 year earthquake history in the region of the 2004 Sumatra-Andaman subduction zone earthquake: Geosphere.

Paull, C. K., McGann, M., Sumner, E. J., Barnes, P. M., Lundsten, E. M., Anderson, K., Gwiazda, R., Edwards, B., and Caress, D. W., 2014, Sub-decadal turbidite frequency during the early Holocene: Eel Fan, offshore northern California: Geology, v. 42, no. 10, p. 855-858.

Prentice, C.S., 1989, Earthquake Geology of the Northern San Andreas Fault near Point Arena, California, [Ph.D. thesis], California Institute of Technology, Pasadena, California, 252 p.

Prentice, C. S., R. Langridge, and D. J.Merritts (2000). Paleoseismic and Quaternary tectonic studies of the San Andreas Fault from Shelter Cove to Fort Ross, in Tectonic Problems of the San Andreas Fault System, G. Bokelman and R. Kovachs (Editors), Geological Sciences XXI, Stanford University Publications, 349–351.

Prentice, C. S., D. J. Merritts, E. C. Beutner, P. Bodin, A. Schill, and J.R. Muller (1999). Northern San Andreas fault near Shelter Cove, California, Geol. Soc. Am. Bull. 111, no. 4, 512–523.

Prentice, C.S., Bartow, G., Hall, T.N., Liapes, M., 2006, The San Andreas fault on the San Francisco Peninsula, Geological Society of America Field Guide 7, San Francisco Earthquake Centennial Filed Guides, Field Trips Associated with the 100th Anniversary Conference, 18-23 April, 2006.

Prentice, C. S., Zachariasen, J. A., Kozaci, O., Clahan, K., Sickler, R. R., Rosa, C. M., Hassett, W., Feigelson, L., Haproff, P. J., DeLong, S., Perkins, A., Brooks, B. A., Delano, J., and Baldwin, J. N., 2013, Paleoseismic Studies of the Peninsula San Andreas Fault near Crystal Springs Reservoir,

Woodside, California, AGU Fall Meeting, Volume T43A-2620: San Francisco, American Geophysical Union.

Prentice, C. S., Sickler, R. R., Clahan, K., Pickering, A., and DeLong, S., 2016, Preliminary Results from Paleoseismic Excavations across the San Andreas Fault at the Scarp Creek Site on the San Francisco Peninsula, California, American Geophysical Union Fall Meeting: San Francisco, CA, American Geophysical Union, Abstract T41B-2922.

Prentice, C. S., Sickler, R. R., Clahan, K., Pickering, A., and DeLong, S., 2019, Prehistoric Earthquakes on the Peninsula San Andreas Fault, Woodside, California, Geological Society of America Abstracts with Programs. Vol. 51, No. 4, ISSN 0016-7592 doi: 10.1130/abs/2019CD-329381, Geological Society of America Cordilleran Meeting: Portland OR, Abstract 16-7.

Priest, G.R., Zhang, Y., Witter, R.C., Wang, K., Goldfinger, C., and Stimely, L., 2014, *Tsunami impact to Washington and northern Oregon from segment ruptures on the southern Cascadia subduction zone*, Natural Hazards, v. 72, p, 849–870.

Puig, P., Ogston, A. S., Mullenbach, B. L., Nittrouer, C. A., and Sternberg, R. W., 2003, Shelf-to-canyon sediment-transport processes on the Eel continental margin (northern California): Marine Geology, v. 193, p. 129-149.

Rabinowitz, M.B., Wetherill, G.W., 1972, Identifying sources of lead contamination by stable isotope techniques. Environ. Sci. Technol. v. 6, p. 705–709.

Ramirez-Herrera, T., Sowers, J. M., Richard, C., and Grossinger, R., 2007, Creek & Watershed Map of San Francisco: Oakland Museum of California.

Ramsey, C. B., 2001, Development of the Radiocarbon Program OxCal: Radiocarbon, v. 43, p. 355-363.

Ramsey, C. B., 2009, Bayesian analysis of radiocarbon dates, Radiocarbon, v. 51(1), p. 337 360.

Ramsey, C.B., Dee, M., Lee, S., Nakagawa, T., & Staff, R., 2010, Developments in the calibration and modelling of radiocarbon dates. Radiocarbon, v. 52, (3), p. 953-961.

Reimer, P. J., Brown, T. J., and Reimer, R. W., 2004, Reporting and Calibration of Post-Bomb14C Data, Radiocarbon, v. 46, p. 1229-1304.

Ritson, P.I., Esser, B.K., Niemeyer, S., Flegal, A.R., 1994, Lead isotopic determination of historical sources of lead to Lake Erie, North America. Geochim. Cosmochim. Acta v. 58, p. 3297–3305.

Ritson, P. I., Bouse, R. M., Flegal, A. R., and Luoma, S. N., 1999, Stable lead isotopic analyses of historic and contemporary lead contamination of San Francisco Bay estuary, Marine Chemistry, v. 64, no. 1, p. 71-83.

Rong, Y., Jackson, D. D., Magistrale, H., and Goldfinger, C., 2014, Magnitude Limits of Subduction Zone Earthquakes: Bulletin of the Seismological Society of America, v. 104, no. 5, p. 2359-2377.

Rothwell, R. G., and Rack, F., 2006, New techniques in sediment core analysis, New techniques in sediment core analysis, Volume Geological Society Special Publication 267: London, UK, Geological Society of London, p. 1-29.

Ryan, H. F., Parsons, T., and Sliter, R. W., 2008, Vertical tectonic deformation associated with the San Andreas fault zone offshore of San Francisco, California: Tectonophysics, v. 457, no. 3-4, p. 209-223.

Satake, K., Wang, K., and Atwater, B. F., 2003, Fault slip and seismic moment of the 1700 Cascadia earthquake inferred from Japanese tsunami descriptions: Journal of Geophysical Research, B, Solid Earth and Planets, v. 108, p. 2,325.

Scheuhammer, A., and Templeton, D., 1998, Use of stable isotope ratios to distinguish sources of lead exposure in wild birds: Ecotoxicology, v. 7, no. 1, p. 37-42.

Schnellmann, M., Anselmetti, F. S., Giardini, D., McKenzie, J. A., and Ward, S. N., 2002, Prehistoric earthquake history revealed by lacustrine slump deposits: Geology, v. 30, no. 12, p. 1131-1134.

Schwartz, D. P., D. Pantosti, K. Okumura, T. Powers, and J. Hamilton, 1998, Paleoseismic investigations in the Santa Cruz Mountains: Implications for the recurrence of large magnitude earthquakes on the San Andreas Fault, J. Geophys. Res. 103, 17,985–18,001.

Schwartz, D. P., Lienkaemper, J. J., Hecker, S., Kelson, K. I., Fumal, T. E., Baldwin, J. N., Seitz, G. G., and Niemi, T. M., 2014, The Earthquake Cycle in the San Francisco Bay Region: A.D. 1600–2012: Bulletin of the Seismological Society of America pre-press online article.

Segall, P., 2002, Integrating geologic and geodetic estimates of slip rate on the San Andreas Fault system, International Geology Review, v. 44 (1) p. 62-82.

Shirahata, H.R., Ellias, R.W., Patterson, C.C., 1980. Chronological variations in concentrations and isotopic compositions of anthropogenic atmospheric lead in sediments of a remote subalpine pond. Geochim. Cosmochim. Acta v. 44, p. 149–162.

Shoup, L. H. and Baker, S. D., 1981 Cultural Resource Overview: Lake Merced Transport, San Francisco, Clean Water Management Program, San Francisco, California.

Song, S. G., Beroza, G. C., and Segall, P., 2008, A Unified Source Model for the 1906 San Francisco Earthquake: Bulletin of the Seismological Society of America, v. 98, no. 2, p. 823-831.

Soulé, F., Gihon, J. H., and Nisbet, J., 1855, The Annals of San Francisco: Containing a Summary of the History of the First Discovery, Settlement, Progress, and Present Condition of California, and a Complete History of all the Important Events Connected with Its Great City; to Which Are Added, Biographical Memoirs of Some Prominent Citizens: New York, D. Appleton and Company.

St-Onge, G., Chapron, E., Mulsow, S., Salas, M., Viel, M., Debret, M., Foucher, A., Mulder, T., Winiarski, T., Desmet, M., Costa, P. J. M., Ghaleb, B., Jaouen, A., and Locat, J., 2012, Comparison of earthquake-triggered turbidites from the Saguenay (Eastern Canada) and Reloncavi (Chilean margin) Fjords: Implications for paleoseismicity and sedimentology: Sedimentary Geology, v. 243–244, p. 89-107.

St-Onge, G., Mulder, T., Piper, D. J. W., Hillaire-Marcel, C., and Stoner, J. S., 2004, Earthquake and flood-induced turbidites in the Saguenay Fjord (Québec): a Holocene paleoseismicity record: Quaternary Science Reviews, v. 23, p. 283-294.

Stover, C.W., and Coffman, J.L., 1993, Seismicity of the United States, 1568-1989 (Revised), U.S. Geological Survey Professional Paper 1527, 424 p.

Strasser, M., Anselmetti, F. S., Fäh, D., Giardini, D., and Schnellmann, M., 2006, Magnitudes and source areas of large prehistoric northern Alpine earthquakes revealed by slope failures in lakes: Geology, v. 34, p. 1005-1008.

Streig, A. R., Dawson, T. E., and Weldon, R. J., 2014, Paleoseismic Evidence of the 1890 and 1838 Earthquakes on the Santa Cruz Mountains Section of the San Andreas Fault, near Corralitos, California: Bulletin of the Seismological Society of America, v. 104, no. 1, p. 285-300.

Streig, A., Weldon, R. J., Biasi, G., Dawson, T. E., Gavin, D. G., Guilderson, T. P. 2020, New Insights into Paleoseismic Age Models on the Northern San Andreas Fault: Charcoal Inbuilt Ages and Updated Earthquake Correlations. Bulletin of the Seismological Society of America; v. 110, no. 3, p. 1077–1089. doi: https://doi.org/10.1785/0120190307

Sternberg, R. W., 1986, Transport and accumulation of river-derived sediment on the Washington continental shelf: J. Geol. Soc. London, v. 143, p. 945-956.

Stevenson, C. J., Talling, P. J., Wynn, R. B., Masson, D. G., Hunt, J. E., Frenz, M., Akhmetzhanhov, A., and Cronin, B. T., 2013, The flows that left no trace: Very large-volume turbidity currents that bypassed sediment through submarine channels without eroding the sea floor: Marine and Petroleum Geology, v. 41, p. 186-205.

Stuvier, M., and Braziunas, T. F., 1993, Modeling atmospheric 14C influences and 14C ages of marine samples to 10,000 BC: Radiocarbon, v. 35, p. 137-189.

Stuvier, M., Reimer, P. J., Bard, E., Beck, J. W., Burr, G. S., Hughen, K. A., Kromer, B., McCormack, F. G., Plicht, J., and Spurk, M., 1998, INTCAL98 Radiocarbon age calibration 24,000 - 0 cal BP: Radiocarbon, v. 40, p.1041-1083.

Todt, W., Cliff, R. A., Hanser, A., and Hofmann, A. W., 1996, Evaluation of a 202Pb - 205Pb double spike for high - Precision lead isotope analysis, Geophysical Monograph, Volume 95, American Geophysical Union. 10 p.

Toppozada, T. R., and G. Borchardt, 1998, Re-evaluation of the 1836 "Hayward fault" and the 1838 San Andreas Fault earthquakes Bull. Seismol. Soc. Am., v. 88, p. 140-159.

Townley, S. D., and Allen, M. W., 1939, Descriptive catalog of earthquakes of Pacific Coast of the United States 1769 to 1928: Seismol. Soc. America Bull., v. 29, no. 1, p. 21-252.

U.S. Geological Survey, 1997, Investigation of the San Bruno Fault near the proposed extension of the Bay Area Rapid Transit Line from Colma to San Francisco International Airport, San Mateo County, California: U.S. Geological Survey Open-File Report 97-429, 73 p.

Valentine, D. W., Keller, E. A., Carver, G., Li, W. H., Manhart, C., and Simms, A. R., 2012, Paleoseismicity of the Southern End of the Cascadia Subduction Zone, Northwestern California: Bulletin of the Seismological Society of America, v. 102, no. 3, p. 1059-1078.

van Geen, A., Vallette-Silver, N.J., Luoma, S.N., Fuller, C.C., Baskaran, M., Tera, F., Klein, J., 1999, Constraints on the sedimentation history of San Francisco Bay from ^{14}C and ^{10}Be. Mar. Chem. v. 64, p. 29–38.

Völz, H. G. et al., 2006, Pigments, Inorganic, Ullmann's Encyclopedia of Industrial Chemistry. Weinheim, doi 10.1002/14356007.a20_243.pub2: Wiley-VCH.

Wakabayashi, J., Hengesh, J. V., and Sawyer, T. L., 2004, Four-dimensional transform fault processes: Progressive evolution of step-overs and bends, Tectonophysics, v. 392, no. 1, p. 279-301.

Walker, R. G., 1965, The Origin and Significance of the Internal Sedimentary Structures Of Turbidites: Proceedings of the Yorkshire Geological Society, v. 35, no. 1, p. 1.

Ward, G. K., and Wilson, S. R., 1978, Procedures for comparing and combining radiocarbon age determinations: a critique: Archaeometry, v. 20, p. 19-34.

Weber, M. E., Niessen, F., Kuhn, G., and Wiedicke, M., 1997, Calibration and application of marine sedimentary physical properties using a multi-sensor core logger: Marine Geology, v. 136, no. 3-4, p. 151-172.

Weldon, R. J., T. E. Dawson, G. Biasi, C. Madden, and A. R. Streig, 2013, Appendix G, Paleoseismic Sites Recurrence Database, in Uniform California earthquake rupture forecast, version 3 (UCERF3)—The time-independent model, U.S. Geol. Surv. Open-File Rept. 2013-1165, 97 pp., California Geological Survey Special Report 228, and Southern California Earthquake Center Publication 1792, available at http://pubs.usgs.gov/of/2013/1165/ (last accessed April 2021).

Wells, M. G., 2007, Influence of Coriolis forces on turbidity currents and sediment deposition, *in* Proceedings Particle-Laden Flow, Dordrecht, Springer Netherlands, p. 331-343.

Wetzel, A., and Balson, P., 1992, Sedimentology of fine-grained turbidites inferred from continuously recorded physical properties data Source, Marine Geology, v. 104, p. 165-178.

Wilson, S. R., and Ward, G. K., 1981, Evaluation and Clustering of Radiocarbon Age Determinations: Procedures and Paradigms: Archaeometry, v. 23, no. 1, p. 19-39.

Witter, R. C., Kelsey, H. M., and Hemphill-Haley, E., 2003, Great Cascadia earthquakes and tsunamis of the past 6700 years, Coquille River estuary, southern coastal Oregon: Bulletin of the Geological Society of America, v. 115, no. 10, p. 1289–1306.

Witter, R. C., Zhang, Y., Wang, K., Priest, G. R., Goldfinger, C., Stimeley, L., English, J.T., and Ferro, P.A., 2013, Simulated tsunami inundation for a range of Cascadia megathrust earthquake scenarios at Bandon, Oregon, USA: Geosphere, v. 9, no. 6, p. 1783-1803.

Working Group on California Earthquake Probabilities (2003). Earthquake Probabilities in the San Francisco Bay Region: 2003 to 2032, U.S. Geological Survey Open-File Report 03-214, 235 p.

Wilson, S. R., and Ward, G. K., 1981, Evaluation and Clustering of Radiocarbon Age Determinations: Procedures and Paradigms: Archaeometry, v. 23, no. 1, p. 19-39.

Youd, T. L., and Hoose, S. N., 1978, Historic ground failures in northern California triggered by earthquakes, U.S. Geological Survey professional paper 993, U.S. GPO., Washington, IV, 177 p.

Zachariasen, J. A., Prentice, C. S.; Kozaci, O., Sickler, R. R., Baldwin, J. N., Sanquini, A., Knudsen, K. L., 2010, Paleoseismic Study on the Peninsula Section of the San Andreas Fault South of Crystal Springs Reservoir, San Mateo County, California, American Geophysical Union, Fall Meeting 2010, abstract #S21C-2048

Zhang, H., T. Niemi, and T. Fumal, 2006, A 3000-year Record of Earthquakes on the Northern San Andreas Fault at the Vedanta Marsh Site, Olema, California, Seismological Research Letters, v. 77 (2) p. 248.

Zoback, M.L. and Jachens, R.C., 1996, Right stepping geometry of the San Andreas and San Gregorio faults and persistent normal faulting in the 1906 San Francisco earthquake epicentral area (abstract): EOS, Transactions, American Geophysical Union, v. 77, no. 46, Supplement, p. F742.

Zoback, M. L., Jachens, R. C., and Olson, J. A., 1999, Abrupt along-strike change in tectonic style: San Andreas Fault zone, San Francisco Peninsula, Journal of Geophysical Research: Solid Earth, v. 104, no. B5, p. 10719-10742.

APPENDICES

Appendix 1. Lake Merced OxCal P-Sequence model input

```
Plot()
 {
  Curve("IntCal20","IntCal20.14c");
  P_Sequence("Merced 04-27-2021 composite", 1)
  {
   Boundary ("Estuarine Contact",-405)
   {
    z=59.08;
   };
   Date("Merced 17")
   {
    z=57.58;
   };
   Date("Merced 16")
   {
    z=53.58;
   };
   R_Date("5Li_5_1b offset 2.5", 1975, 20)
   {
    z=53.58;
   };
   Date("Merced 15")
   {
    z=51.08;
```

```
};
Date("Merced 14")
{
 z=48.08;
};
Date("Merced 13")
{
 z=45.08;
};
R_Date("2Li_5_203 offset 3", 1540, 15)
{
 z=43.08;
};
Date("Merced 12")
{
 z=40.08;
};
Date("Merced 11")
{
 z=33.58;
};
R_Date("6Li_3_54-54.5 offset 2", 1150, 20)
{
 z=32.08;
};
Date("Merced 10")
{
 z=30.08;
};
Date("Merced 09")
{
 z=27.58;
};
Date("Merced 08")
{
 z=25.08;
};
R_Date("7Li_2_7 offset 3", 645, 15)
{
 z=23.58;
};
Date("Merced 07")
{
 z=20.58;
};
Date("Merced 06")
{
 z=15.58;
};
Date("Merced 05")
{
 z=13.08;
};
Date("Merced 04")
{
 z=8.08;
};
C_Date(1906)
{
 z=3.08;
};
Date("Merced 02")
```

```
  {
   z=1.2;
  };
  Boundary("1989", 1989)
  {
   z=0;
  };
 };
};
```

Appendix 2. Lake Merced OxCal P-Sequence results

Name Show all Show structure	Unmodelled (BC/AD)							Modelled (BC/AD)							Indices A_{model}=97.3 $A_{overall}$=97.1					Select All Visible	Page break
	from	to	%	from	to	%	m	from	to	%	from	to	%	m	A_{comb}	A	L	P	C		
	Warning! Function not found - # Warning! Function not found - #																				
1989																				27	
▲ Boundary 1989	1980	1990	68.3	1980	1990	95.4	1990	1980	1990	68.3	1980	1990	95.4	1990		100			100	26	
Merced 02								1940	1990	68.3	1870	2000	95.4	1960					99.9	25	
Merced 03								1850	1960	68.3	1780	1980	95.4	1900					99.8	24	
Merced 04								1660	1810	68.3	1590	1870	95.4	1730					99.7	23	
Merced 05								1590	1750	68.3	1520	1820	95.4	1670					99.8	22	
Merced 06								1510	1660	68.3	1440	1740	95.4	1590					99.7	21	
Merced 07								1360	1480	68.3	1320	1550	95.4	1420					99.7	20	
R_Date 7Li_2_7 offset 3	1290	1390	68.3	1290	1400	95.4	1360	1290	1390	68.3	1290	1390	95.4	1310		94.1			99.8	19	
Merced 08								1200	1320	68.3	1140	1380	95.4	1270					99.8	18	
Merced 09								1060	1220	68.3	990	1280	95.4	1140					99.7	17	
Merced 10								950	1080	68.3	890	1160	95.4	1020					99.8	16	
R_Date 6Li_3_54 54.5 offset 2	770	960	68.3	770	980	95.4	920	880	960	68.3	830	980	95.4	930		105			99.8	15	
Merced 11								830	940	68.3	760	960	95.4	880					99.7	14	
Merced 12								580	700	68.3	510	770	95.4	640					99.6	13	
R_Date 2Li_5_203 offset 3	530	570	68.3	430	590	95.4	550	480	570	68.3	430	590	95.4	550		94.8			99.9	12	
Merced 13								390	530	68.3	300	560	95.4	450					99.8	11	
Merced 14								210	380	68.3	140	450	95.4	300					99.7	10	
Merced 15								70	210	68.3	20	300	95.4	150					99.7	9	
R_Date 5Li_5_1b offset 2.5	10	80	68.3	-40	120	95.4	50	1	70	68.3	-50	120	95.4	30		99.4			97.5	8	
Merced 16								-30	70	68.3	-50	120	95.4	30					97.6	7	
Merced 17								400	250	68.3	410	130	95.4	300					99.7	6	
-405																				5	
▲ Boundary Estuarine Contact	-410	-400	68.3	-410	-400	95.4	-410	-410	-400	68.3	-410	-400	95.4	-410		100			100	4	
▲ P_Sequence Merced 04-27-2021 composite																				3	
Curve IntCal20																				2	

Appendix 3. Lake Merced OxCal P-Sequence Calibration Curve Plot

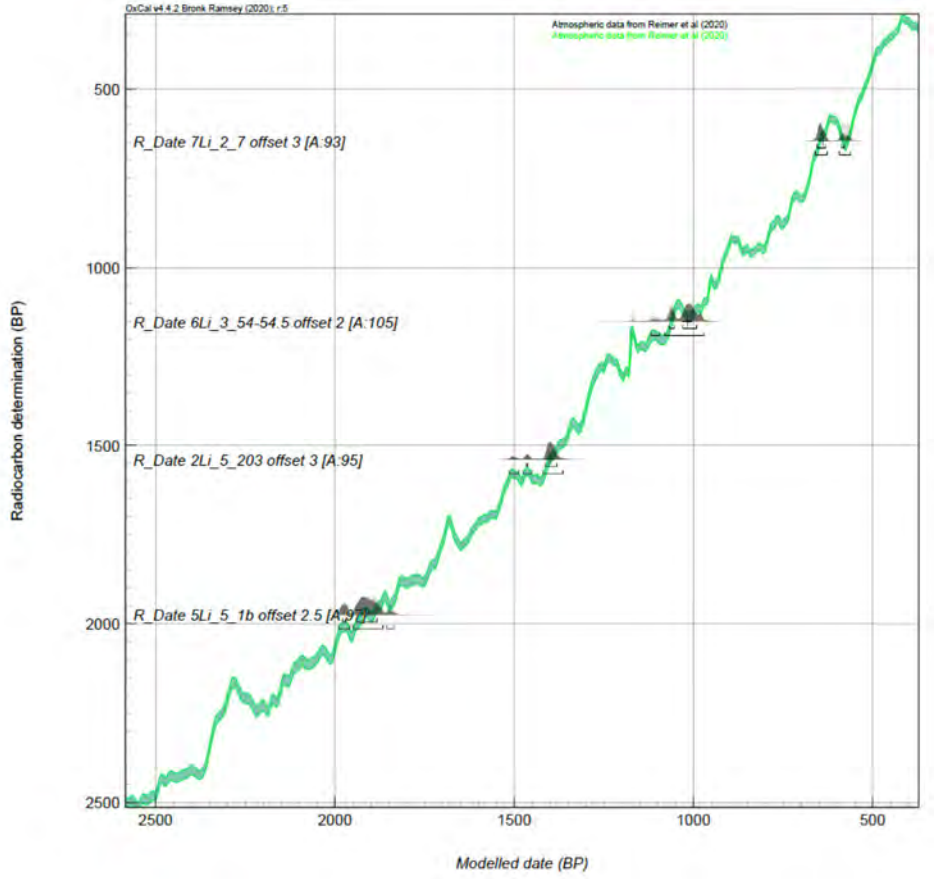

Appendix 4. S. Cascadia correlation plot, Rogue Apron to Trinidad plunge pool.

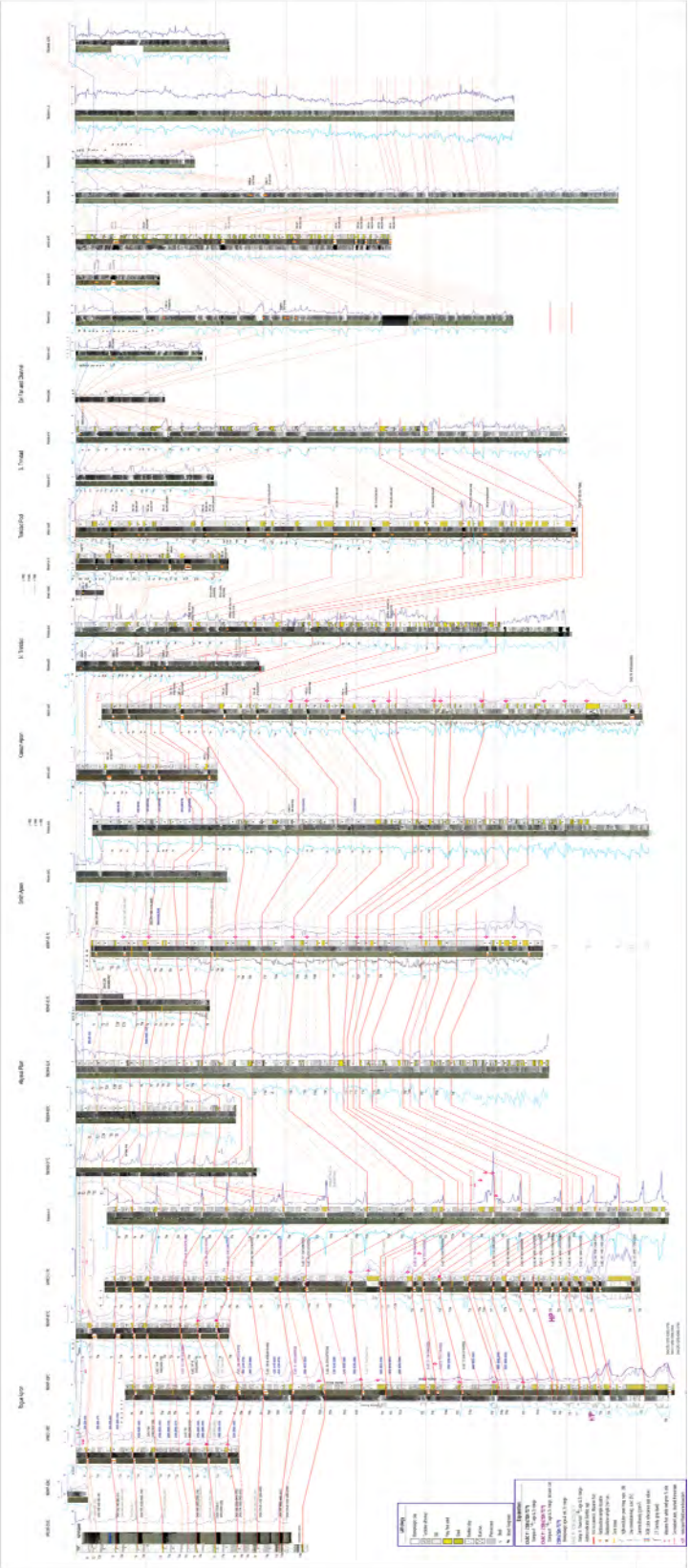

Appendix 5. Trinidad age model output

Name	Unmodelled (BP)						Modelled (BP)						Indices				
	from	to	%	mu	sigma	median	from	to	%	mu	sigma	median	Acomb	A	L	P	C
	1999.5																
Boundary surface	-40	-50	95.44997	-50	0	-50	-40	-50	95.44997	-50	0	-50			100		100
36TC T0a							0	-60	95.44997	-40	10	-40					100
36TC T0b							20	-60	95.44997	-30	20	-30					99.9
36TC T0c							50	-50	95.44997	-10	30	-10					99.9
36TC T0d							80	-40	95.44997	10	30	10					99.7
36TC T0e							100	-40	95.44997	30	30	30					99.5
36TC T0e1							110	-30	95.44997	40	30	30					99.5
36TC T0f							120	-20	95.44997	50	40	40					99.5
36TC T0h							160	0	95.44997	80	40	80					99.8
36TC T0i							200	40	95.44997	120	40	120					99.9
36TC T0j							240	100	95.44997	170	30	180					100
C_Date 36TC T1	260	250	95.44997	250	0	250	260	250	95.44997	250	0	250			100		100
36TC T1a0							290	240	95.44997	260	10	260					99.8
36TC T1e1							300	240	95.44997	270	20	260					99.7
36TC T1a2							340	250	95.44997	290	30	290					98.8
36TC T1a3							370	260	95.44997	320	40	310					98
36TC T1a							410	290	95.44997	350	50	350					92.5
36TC T2							420	290	95.44997	350	50	350					92.7
36TC T2a0							460	320	95.44997	390	50	390					98.2
36TC T2a000							490	340	95.44997	420	50	410					98.8
36TC T2a00							530	380	95.44997	460	50	450					99.1
36TC T2a							550	390	95.44997	470	50	470					99.1
36TC T2b							590	440	95.44997	520	50	520					99
36TC T2c							630	480	95.44997	560	40	560					98.8
R_Date Casc 214 T2c offset 1	660	500	95.44997	580	40	580	660	520	95.44997	590	40	590			107		98.3
Delta_R Pub_DR	278.5	403.5	95.44997	341	31	341	279	395	95.44997	336.772	29.0879	337.5			104.4		99.3
36TC T2c0							700	540	95.44997	630	40	620					99.1
36TC T2d							730	560	95.44997	650	40	650					99.2
36TC T2e							760	590	95.44997	670	40	670					99.2
36TC T2e0							770	600	95.44997	690	40	690					99.3
36TC T2f							820	640	95.44997	730	40	730					99.3
36TC T2fa							850	670	95.44997	770	40	770					99.3
36TC T2g							910	730	95.44997	830	40	830					99.3
R_Date Casc 211 planktic T2g	920	660	95.44997	790	70	790	950	780	95.44997	870	40	870			78.9		99.2
Delta_R Pub_DR	349	589	95.44997	469	60	469	325	496.5	95.44997	414.545	41.948	417.5			90.1		99.3
36TC T3							970	790	95.44997	890	40	890					99
36TC T3a0							1080	880	95.44997	980	50	980					98
36TC T3a1							1120	910	95.44997	1020	50	1020					97.3
36TC T3a2							1150	940	95.44997	1040	50	1050					96.8
36TC T3a3							1180	970	95.44997	1080	50	1080					96
36TC T3a4							1250	1050	95.44997	1150	50	1150					92.9
36TC T3a5							1280	1100	95.44997	1190	40	1190					81.9
36TC T4							1290	1100	95.44997	1190	40	1190					81.9
R_Date Casc 283 T4 offset 1.	1290	1070	95.44997	1190	60	1200	1320	1140	95.44997	1230	40	1240			101		92.8
36TC T4a0							1350	1160	95.44997	1260	40	1260					94.5
36TC T4a1							1420	1210	95.44997	1320	50	1320					96.4
36TC T4a2							1470	1250	95.44997	1360	50	1360					97.1
36TC T4a3							1570	1340	95.44997	1450	50	1450					98
36TC T5							1610	1380	95.44997	1490	50	1490					98.3
36TC T5a0							1650	1430	95.44997	1540	50	1540					98.4
R_Date Casc 284 T5 offset 1.	1670	1380	95.44997	1520	70	1520	1690	1480	95.44997	1580	50	1580			88.4		98.5
36TC T5a1							1710	1490	95.44997	1600	50	1600					98.6
36TC T5a							1760	1530	95.44997	1640	60	1640					98.8
36TC T5a2							1870	1620	95.44997	1750	60	1750					99
36TC T5b							1970	1720	95.44997	1840	60	1840					99.1
R_Date Casc 33 T5b offset 2.	2050	1770	95.44997	1910	70	1900	2050	1820	95.44997	1940	50	1940			100.3		99
36TC T5c							2250	2000	95.44997	2120	60	2120					99.1
R_Date Casc 285 T5c offset 1	2290	1980	95.44997	2120	80	2120	2290	2040	95.44997	2160	60	2160			100.7		99.1
36TC T6							2630	2360	95.44997	2500	70	2500					99.1
R_Date Casc 66 T6 offset 2.0	2660	2320	95.44997	2470	90	2460	2690	2430	95.44997	2560	70	2570			77.6		99.1
36TC T6a0							2750	2500	95.44997	2630	70	2630					99.1
36TC T6a							2780	2540	95.44997	2660	60	2660					99.1
36TC T6b							2840	2610	95.44997	2720	60	2720					99.2
R_Date Casc 287 T6b offset 1	2830	2540	95.44997	2700	60	2710	2870	2670	95.44997	2760	60	2760			77		98.8
36TC T7							3080	2800	95.44997	2930	80	2930					85.1
36TC T7ao							3080	2800	95.44997	2930	80	2930					85.3
36TC T7a							3170	2870	95.44997	3010	80	3020					97.1
36TC T7b							3300	2990	95.44997	3140	80	3140					98.8
36TC T7c							3370	3060	95.44997	3210	80	3210					99.2
36TC T7d							3440	3140	95.44997	3290	70	3300					99.5
36TC 8							3560	3290	95.44997	3420	70	3420					99.7
Delta_R pub_DR	295.5	420.5	95.44997	358	31	358	267	387	95.44997	325.679	30.878	324			74		97.7
R_Date 36TC T8 casc 75	3660	3380	95.44997	3520	70	3520	3640	3410	95.44997	3520	50	3520			109.3		99.8
Delta_R T8_DR	-4.5	120.5	95.44997	58	31	58	-2	117	95.44997	57.8391	29.1209	58			103.2		99.9
36TC T8a							3670	3430	95.44997	3550	60	3550					99.8
36TC T8b							3800	3520	95.44997	3660	70	3660					99.9
36TC T8c							3890	3600	95.44997	3750	70	3750					99.9
36TC T8d							4020	3730	95.44997	3880	70	3880					99.9
C_Date regional T9 age oxca	4260	3970	95.44997	4110	70	4110	4160	3900	95.44997	4030	60	4030			70.5		99.8
Boundary below regional T9 age							4160	3900	95.44997	4030	60	4030					99.8
P_Sequence M9907-36TC 8-19-20																	
Delta_R pub_DR	295.5	420.5	95.44997	358	31	358	295.5	420.5	95.44997	357.981	31.0194	358			100		99.9
Curve Marine13																	

Appendix 6. Trinidad Oxcal code.

```
Plot()
 {
  Curve("Marine13","marine13.14c");
  Delta_R("pub_DR", 358, 31);
  P_Sequence("M9907-36TC 8-19-20", 2)
  {
   Boundary (" below regional T9 age");
   C_Date("regional T9 age oxcal combine", -2160, 70)
   {
    z=127.7;
   };
   Date("36TC T8d")
   {
    z=124.2;
   };
   Date("36TC T8c")
   {
    z=121.2;
   };
   Date("36TC T8b")
   {
    z=119.2;
   };
   Date("36TC T8a")
   {
    z=116.68;
   };
   Delta_R("T8_DR", 58, 31);
   R_Date("36TC T8 casc 75", 3680, 40)
   {
    z=115.98;
   };
   Delta_R("pub_DR", 358, 31);
   Date("36TC 8")
   {
    z=113.68;
   };
   Date("36TC T7d")
   {
    z=110.68;
   };
   Date("36TC T7c")
   {
    z=108.68;
   };
   Date("36TC T7b")
   {
    z=107.18;
```

```
};
Date("36TC T7a")
{
 z=104.18;
};
Date("36TC T7ao")
{
 z=102.18;
};
Date("36TC T7")
{
 z=102.18;
};
R_Date("Casc 287 T6b offset 1.25", 3290, 40)
{
 z=98.43;
};
Date("36TC T6b")
{
 z=97.18;
};
Date("36TC T6a")
{
 z=95.38;
};
Date("36TC T6a0")
{
 z=94.38;
};
R_Date("Casc 66 T6 offset 2.0", 3095, 50)
{
 z=92.38;
};
Date("36TC T6")
{
 z=90.38;
};
R_Date("Casc 285 T5c offset 1.25", 2825, 40)
{
 z=79.63;
};
Date("36TC T5c")
{
 z=78.38;
};
R_Date("Casc 33 T5b offset 2.95", 2650, 40)
{
 z=72.33;
};
Date("36TC T5b")
{
 z=69.38;
```

```
};
Date("36TC T5a2")
{
 z=66.38;
};
Date("36TC T5a")
{
 z=63.08;
};
Date("36TC T5a1")
{
 z=61.58;
};
R_Date("Casc 284 T5 offset 1.5", 2325, 40)
{
 z=61.08;
};
Date("36TC T5a0")
{
 z=59.58;
};
Date("36TC T5")
{
 z=58.08;
};
Date("36TC T4a3")
{
 z=56.58;
};
Date("36TC T4a2")
{
 z=53.48;
};
Date("36TC T4a1")
{
 z=51.88;
};
Date("36TC T4a0")
{
 z=49.78;
};
R_Date("Casc 283 T4 offset 1.5", 1995, 40)
{
 z=48.98;
};
Date("36TC T4")
{
 z=47.48;
};
Date("36TC T3a5")
{
 z=47.48;
```

```
};
Date("36TC T3a4")
{
 z=46.08;
};
Date("36TC T3a3")
{
 z=43.38;
};
Date("36TC T3a2")
{
 z=42.18;
};
Date("36TC T3a1")
{
 z=41.18;
};
Date("36TC T3a0")
{
 z=39.68;
};
Date("36TC T3")
{
 z=36.42;
};
Delta_R("Pub_DR", 469, 60);
R_Date("Casc 211 planktic T2g offset 1.8", 1710, 25)
{
 z=35.82;
};
Date("36TC T2g")
{
 z=34.02;
};
Date("36TC T2fa")
{
 z=31.27;
};
Date("36TC T2f")
{
 z=29.68;
};
Date("36TC T2e0")
{
 z=27.68;
};
Date("36TC T2e")
{
 z=27.07;
};
Date("36TC T2d")
{
```

```
 z=25.93;
};
Date("36TC T2c0")
{
 z=24.88;
};
Delta_R("Pub_DR", 341, 31);
R_Date("Casc 214 T2c offset 1.5", 1335, 40)
{
 z=23.38;
};
Date("36TC T2c")
{
 z=21.88;
};
Date("36TC T2b")
{
 z=19.9;
};
Date("36TC T2a")
{
 z=17.55;
};
Date("36TC T2a00")
{
 z=16.98;
};
Date("36TC T2a000")
{
 z=14.98;
};
Date("36TC T2a0")
{
 z=13.78;
};
Date("36TC T2")
{
 z=12.0;
};
Date("36TC T1a")
{
 z=11.999;
};
Date("36TC T1a3")
{
 z=10.299;
};
Date("36TC T1a2")
{
 z=9.209;
};
Date("36TC T1a1")
```

```
{
 z=8.069;
};
Date("36TC T1a0")
{
 z=7.750;
};
C_Date("36TC T1", 1700)
{
 z=7.29;
};
Date("36TC T0j")
{
 z=5.41;
};
Date("36TC T0i")
{
 z=4.04;
};
Date("36TC T0h")
{
 z=3.18;
};
Date("36TC T0f")
{
 z=2.30;
};
Date("36TC T0e1")
{
 z=2.05;
};
Date("36TC T0e")
{
 z=1.90;
};
Date("36TC T0d")
{
 z=1.53;
};
Date("36TC T0c")
{
 z=1.00;
};
Date("36TC T0b")
{
 z=.51;
};
Date("36TC T0a")
{
 z=0.23;
};
Boundary("surface", 1999.5)
```

```
   {
    z=0;
   };
  };
 };
```